TRANS **NOW**

TRANSPORTATION NORTHWEST

Final Report TNW2012-18

Research Project Agreement No. 62-0936

Long-Term and Seismic Performance of Concrete-Filled Steel Tube Columns with Conventional and High-Volume SCM Concrete

Árni Kristinn Gunnarsson, Dawn Lehman, Charles Roeder and Katherine Kuder

Civil and Environmental Engineering

University of Washington

A report prepared for

Transportation Northwest (TransNow)
University of Washington
112 More Hall, Box 352700
Seattle, Washington 98195-2700

and

Washington State Department of Transportation

June 2012

TECHNICAL REPORT STANDARD TITLE PAGE

1. REPORT NO. TNW2012-18	2. GOVERNMENT ACCESSION NO.	3. RECIPIENT'S CATALOG NO.
4. TITLE AND SUBTITLE Long-Term and Seismic Performance of Concrete-Filled Steel Tube Columns with Conventional and High-Volume SCM Concrete		5.REPORT DATE 6/2012 6. PERFORMING ORGANIZATION CODE 62-0936
7. AUTHOR(S) Árni Kristinn Gunnarsson, Dawn Lehman, Charles Roeder and Katherine Kuder		8. PERFORMING ORGANIZATION REPORT NO. TNW2012-18
9. PERFORMING ORGANIZATION NAME AND ADDRESS Transportation Northwest Regional Center X (TransNow) Box 352700, 112 More Hall University of Washington Seattle, WA 98195-2700		10. WORK UNIT NO. 11. CONTRACT OR GRANT NO. DTRT07-G-0010
12. SPONSORING AGENCY NAME AND ADDRESS United States Department of Transportation Office of the Secretary of Transportation 1200 New Jersey Ave, SE Washington, D.C. 20590		13. TYPE OF REPORT AND PERIOD COVERED Final Technical Report 14. SPONSORING AGENCY CODE
15. SUPPLEMENTARY NOTES		

ABSTRACT

Production of Portland Cement for concrete is a major source of CO2 emission. Concrete can be made more sustainable by replacing a large volume of the cement with Supplementary Cementitous Materials (SCMs) such as fly ash and slag. The amount of cement that can be replaced with SCMs in conventional concrete structures is limited due to slow strength gain, of such concretes.

Concrete-Filled Tubes (CFT) are composite structural elements that consist of a steel tube with concrete infill. In CFT sections, neither formwork nor rebar is needed since the steel tube serves as both, which can reduce construction time and cost. In bridge construction, the steel tube itself has strength to support some dead weight of the superstructure prior to casting of the concrete. This can significantly reduce delays for concrete curing and eliminates the need for high early strength of the concrete, making slow-curing concrete, such as SCM concrete a realistic alternative. In this research program, two 20-inch diameter CFT columns were tested for creep and shrinkage behavior under sustained axial loading. Subsequently, the specimens were tested until failure under combined loading consisting of constant axial load and increasing cyclic lateral load to evaluate seismic performance. One tube was filled with conventional self-consolidating concrete (SCC), while self-consolidating SCM concrete was used in the other specimen. The objective was to determine if the performance of CFTs filled with SCM concrete is comparable to the performance of CFTs with conventional concrete. In the SCM concrete, 80% of the cement was replaced with fly ash and slag, which reduces the carbon footprint of the mixture greatly. Sealed and unsealed cylinders were made from both concrete mixtures and tested for creep and shrinkage behavior as a comparison. The results indicate that the long-term performance of CFTs filled with low early-strength concrete, such as SCM concrete, is fully comparable to performance CFTs filled with conventional concrete. Slightly more load was shed to the steel in the SCM specimen, but the concrete core of the SCM specimen was shown to creep considerably less.

The results from the long-term tests were compared to four existing models for creep and shrinkage, to determine if these models provided acceptable predictions for the long-term behavior of structural CFT components. Some models captured the behavior quite well in some cases, while other models provided inferior predictions. Results from the seismic performance tests were compared to results from two specimens previously tested for seismic performance. One was identical to the SCC specimen tested in this research program, apart from the embedment depth of the tube, which was slightly smaller. The other specimen was 30 inches in diameter but the steel tube was of the same thickness. The results showed that the seismic performance of the CFT SCM specimen was almost identical to the seismic performance of CFTs filled with conventional concrete. Observed damage, Force-Displacement response, and Moment-Drift ratio were all very similar for all 20 in. specimens compared.

17. KEY WORDS		18. DISTRIBUTION STATEMENT	
Concrete, seismic performance		No restrictions.	
19. SECURITY CLASSIF. (of this report)	20. SECURITY CLASSIF. (of this page)	21. NO. OF PAGES	22. PRICE
None	None	236	

DISCLAIMER

The contents of this report reflect the views of the authors, who are responsible for the facts and the accuracy of the information presented herein. This document is disseminated under the sponsorship of the Department of Transportation University Transportation Centers Program, in the interest of information exchange. The U.S. Government assumes no liability for the contents or use thereof.

Acknowledgement

The author wishes to express his sincere appreciation to the faculty and staff of the Department of Civil and Environmental Engineering at University of Washington and Seattle University for their support. The research was funded by the Valle Scholarship Program and Transportation Northwest, a Regional University Transportation Center (UTC). This support is gratefully acknowledged. I would also like to thank my family and friends for their support. My three sons; Róbert Elí, Birkir Ísak, and Gunnar Bergvin, have been very understanding and wonderful through the whole process and deserve much gratitude for that. Finally, I cannot express enough gratefulness to my amazing wife Regína for her immense support, encouragement, patience and strength during my studies here in Seattle.

Table of Contents

List of Figures

List of Tables

Chapter 1: Introduction

Concrete-filled tubes (CFT) are composite structural elements comprised of a steel tube with concrete infill. In CFT components, the steel tube serves as the reinforcing steel and the formwork. This can reduce construction time and cost. In addition, the hollow tube has the strength to support some dead weight prior to casting of the concrete. This facilitates rapid construction by eliminating both delays for concrete curing and need for high early strength of the concrete, making concrete with high cement replacement a realistic option. (Lee, 2011)

Concrete filled tubes are effective structural components due to their strength-to-size efficiency and facilitation of rapid construction. The flexural stiffness of the steel is maximized by placing it along the perimeter of the cross-section resulting in a large moment of inertia relative to the area of steel. Although hollow tubes also have this benefit, the concrete infill provides additional strength to the member as well as improving stability by delaying local buckling of the steel tube. Confinement of the concrete infill improves its strength and prevents spalling that might occur in a traditionally reinforced concrete component under cyclic lateral loading such as an earthquake. The confinement also reduces the creep and shrinkage of the concrete greatly. The component that results is a slender member with high strength, good ductility, and small long-term deflections. (Lee, 2011)

Cement production is one of the major sources of CO_2 emissions in the world. Portland cement has so far been the primary content in the binder of concrete. Lowering the amount of cement in the binder therefore reduces concrete's carbon footprint and facilitates greener construction. (CEMBUREAU, 2009)

Materials that are commonly used as cement replacement in concrete are fly ash and slag. Fly ash is the inorganic, noncombustible residue of powdered coal after burning in power plants, and is widely available in the world. Slags are residues from metallurgical processes, either from production of metals from ore or refinement of impure metals. (Hannesson, 2010)

SCMs are commonly used in concrete at replacement levels less than 30% because they improve both durability and the interface with aggregate. However, concrete containing SCMs at high replacement levels tends to have slower strength development. As mentioned above, high early

strength is not as important in concrete-filled tubes as it is in regular reinforced concrete structures, making high-replacement SCM concrete a viable alternative.

1.1 Structural applications and research objective

The specimens model a footing and a column that can potentially be used as the foundation and column supporting a bridge structure. The purpose of this research is to study the creep and shrinkage of the concrete inside the steel tubes under sustained loading applied to the concrete core only, and to examine the effect that these factors have on the tube. Large increase in compressive strain in the tube can facilitate local buckling at the bottom of the tube due to combined axial and lateral loading.

The performance was compared to that of unreinforced concrete cylinders, both sealed with epoxy coating and unsealed. Two different types of concrete were observed; regular self-consolidating concrete (SCC) and self-consolidating SCM concrete in which 80% of the cement has been replaced with the Supplementary Cementitious Materials (SCMs) fly ash and slag. Since this is the first research known to the author that tests creep and shrinkage in large-scale specimens, and the first research to study SCM in CFTs, the results can only be compared to previous research done on small-scale specimens.

The two specimens were tested under combined constant axial and increasing cyclic lateral loading to compare seismic performance of a tube filled with the SCM concrete and a tube filled with the conventional SCC concrete. Their response was compared to two specimens previously tested for seismic performance.

SCC has advantages in reinforced concrete and composite construction by facilitating rapid construction. Possible composite components include aforementioned concrete-filled tubes for structural columns, and dual skin composite shear walls to resist gravity and seismic loadings. As mentioned in the introduction, an advantage of using a high-volume SCM concrete in these applications is that high early strength is not required from the concrete, since the steel tube is capable of supporting the initial construction loads, and formwork is not removed, as would be required for a conventional reinforced concrete component. Therefore, concrete containing high volume of SCMs can be more readily used in composite constructions, even though a low early strength is often associated with such concrete.

Creep and shrinkage strains are in general higher in concrete that is given only a short time to cure before loading. However, the steel tube may confine the concrete and prevent water evaporation, therefore providing resistance against both creep and shrinkage. This research will explore the differences in response between tubes filled with the two different types of concrete mentioned above.

1.2 Scope of report

Chapter 2 provides a summary of the experimental research that has been done on concrete-filled tubes to evaluate their performance under long-term axial loading representing the dead load of a structure.

Chapter 3 presents an overview of the materials that were used in the experiments, as well as instrumentation, test setup and test procedure for both the creep and shrinkage tests, and the seismic performance tests.

Chapter 4 presents the results of the testing program. The tests were performed in two parts. The first part consisted of 126-day long creep and shrinkage tests on two large-scale concrete-filled tubes and sixteen standard ASTM test cylinders. The second part consisted of seismic performance tests of the two large-scale CFT under combined constant axial and increasing cyclic lateral loading.

Chapter 5 includes an evaluation of four existing models for shrinkage and creep. The experimental data from the long-term test is compared to the predictions of these models. The models are then calibrated to best fit the experimental curves.

Chapter 6 presents the findings from the seismic performance tests. Experimental results, Force-Displacement response and Moment-Drift response are examined. Comparison between the two specimens is provided. The specimens are also compared with two specimens previously tested for seismic performance; specimen 5-50, tested by Lee and specimen 30”-50, tested by O’Neill.

Chapter 7 concludes the report with a brief summary of the tests performed, observations, research conclusions, and recommendations for future research.

Chapter 2: Previous research of CFTs under sustained loading

This chapter provides a summary of the experimental research that has been performed on concrete-filled tubes tested to evaluate their performance under long-term axial loading representing the dead load of a structure. Only research data that focuses on creep and shrinkage is included in this chapter. For each research program, the objective, test setup, experimental results and conclusions are provided.

2.1 Literature review

Limited research has been done on creep and shrinkage of small-scale (≤ 6-in. diameter) concrete filled tubes. There has been no research on long-term performance of large-scale CFTs and none on CFTs that contain SCMs. Following is an overview of tests that have been done on CFTs under long-term axial loading.

2.1.1 Overview

Furlong (1967) tested 22 circular and 17 square CFT columns for strength but mentioned the effect of creep. However, he provided no creep data. Tan et al., (1987) monitored creep on 16 circular CFT columns with a different steel-to-concrete ratio. Various levels of stress were applied to the specimens and the differences were observed. Nakai et al., (1991) constructed specimens and monitored them for 6 months under sustained loading. Two were CFT columns with a different steel-to-concrete ratio and one was a plain concrete column. The aforementioned research programs are not covered in this chapter due to lack of information.

Terrey et al., (1994) conducted creep experiments of four CFT columns with different tube thicknesses for about 130 days. One column for each tube thickness was greased to remove as much bond between the steel and the concrete as possible, while the other two were not. Plain and painted concrete cylinders were also tested at the same time, and shrinkage strains were monitored for all three types. Morino et al., (1997) tested six square CFT columns of different lengths, diameters and tube thicknesses under sustained axial loading for 100 - 200 days. Shrinkage of CFTs was considered negligible in this research.

A few research programs investigated creep and shrinkage of CFTs in the last decade. Ichinose et al., (2001) examined the influence of steel-to-concrete ratio, as well as loading condition, on the

creep of CFT columns. Four specimens where loaded through the concrete only, while two were loaded through the steel pipe and two through both. Four plain uncoated columns were also monitored for creep. Five shrinkage specimens were constructed for this experiment; three CFT's and two plain concrete.

Uy, (2001) examined the time-dependent behavior of four CFT columns subjected to axial compression loading. Creep strains in plain concrete cylinders were also monitored, as well as shrinkage strains for both.

Han et al., (2003) had four rectangular CFT specimens under sustained loading for about 180 days and four identical specimens to measure shrinkage. All specimens had the same tube thickness but a different perimeter.

Han et al., (2004) then repeated the experiment from the previous year for about 120 days, using square tubes instead of rectangular ones. Six specimens were made, of which two were shrinkage samples.

Yang et al., (2008) measured long-term strains of five rectangular and five circular CFT specimens, six of which were under sustained loading and two unloaded shrinkage samples. One creep specimen of each cross section had conventional concrete while two had concrete in which 50% of the coarse natural aggregate was replaced with recycled aggregate. Comparable shrinkage specimens were also monitored.

Zhou et al., (2009) constructed thirteen circular specimens, including four CFT columns, three reinforced concrete columns and six plain concrete columns. Two specimens of CFT and RC, and four specimens of PC, were placed in a creep rig for 864 days. The remaining specimens were monitored for shrinkage strain only, two of PC and CFT, and one of RC.

Wang et al., (2010) performed creep testing of eleven nearly identical tubes filled with concrete which with an expansive additive mixture. The experiment lasted for about 150 days. The CFTs were subject to different levels of axial stress applied at different time since concrete casting.

2.1.2 Terrey, Bradford, & Gilbert, 1994

Creep and shrinkage in concrete-filled steel tubes

2.1.2.1 Research objective

Terrey, et al. tested the long-term effects on four CFTs of different thicknesses to determine appropriate values for the creep coefficient and shrinkage strains in such members, so that a rational time-dependent analysis may be established. Sealed and unsealed cylinders were also tested for comparison.

2.1.2.2 Specimens

The sealed and unsealed cylinders had a diameter of 150 mm and a height of 300 mm (denoted as S1 and P1, respectively). The CFTs were 200 mm in diameter with an H/D ratio of 3 and tube thicknesses of 1.0 mm and 1.5 mm. The inside surface of one tube of each thickness was greased to minimize the bond between the steel and the concrete, the other tube was untreated. The 1.0 mm thick tubes are denoted as CFST1 and the 1.5 mm as CFST2. Demec gauges were used to measure the concrete strains. Small square pieces were cut out of the steel tubes so that the targets could be glued to the concrete. All exposed concrete surfaces in the CFTs were then painted with sealant to minimize the effect of moisture escaping from the concrete. Steel strains were also measured to verify the debonding between the steel and the concrete.

2.1.2.3 Test setup

The CFTs were loaded to a constant 350 kN force ($P/P_0 = 0.35$). This was done by placing the specimens in the creep rigs shown in Figure 2.1 and Figure 2.2. All specimens were loaded at eighteen days. The load was maintained by adjusting the hydraulic jack on a regular basis. As can be seen in Figure 2.1 each greased specimen was paired with a bonded specimen. The specimens with the greased tubes were loaded through the concrete core only, while the bonded CFTs had steel plates on the ends, which transferred the load to both the core and the tube. Steel strains in the bonded tube were compared to those in the concrete to determine the degree of bonding. The sealed and unsealed concrete cylinders were loaded to 280 kN ($P/P_0 = 0.35$) in a standard creep rig and the load was maintained by the hydraulic jack, as for the CFT specimens. Identical specimens were constructed for all three types to measure shrinkage strains only. These

were therefore not subjected to any load. The shrinkage specimens were placed in the same environmental conditions as the creep specimens.

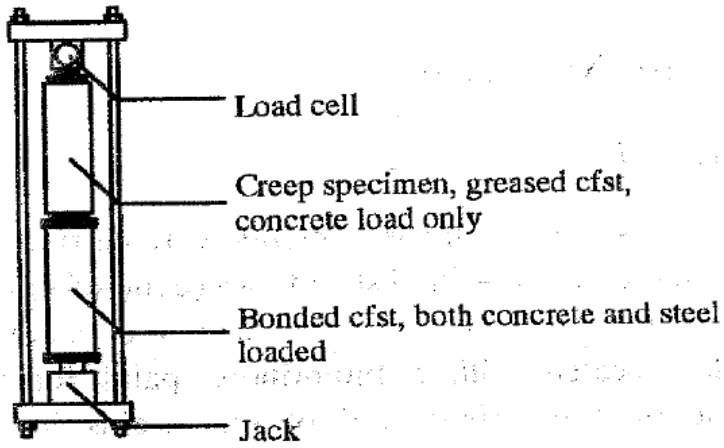

Figure 2.1. Arrangement of cfst specimens in rig (Terrey, Bradford, & Gilbert, 1994)

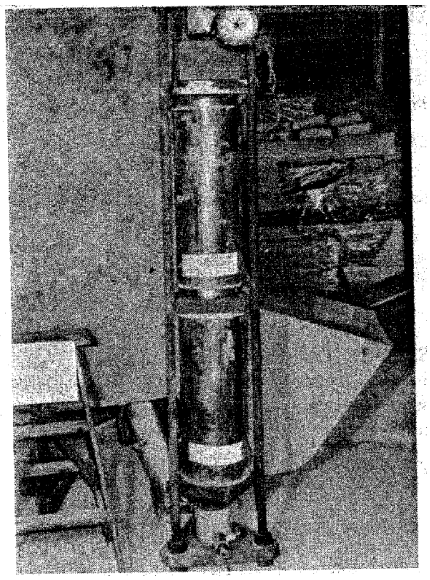

Figure 2.2. Arrangement of cfst specimens in rig (Terrey, Bradford, & Gilbert, 1994)

2.1.2.4 Experimental results

Figure 2.3 and Figure 2.4 show the average change in shrinkage strain over time for specimens P1 and S1, respectively. Two coatings of sealant usually reduce the moisture loss of concrete drastically. However, only one coat was applied to the sealed cylinders for this experiment, which seems to have very little effect on the shrinkage.

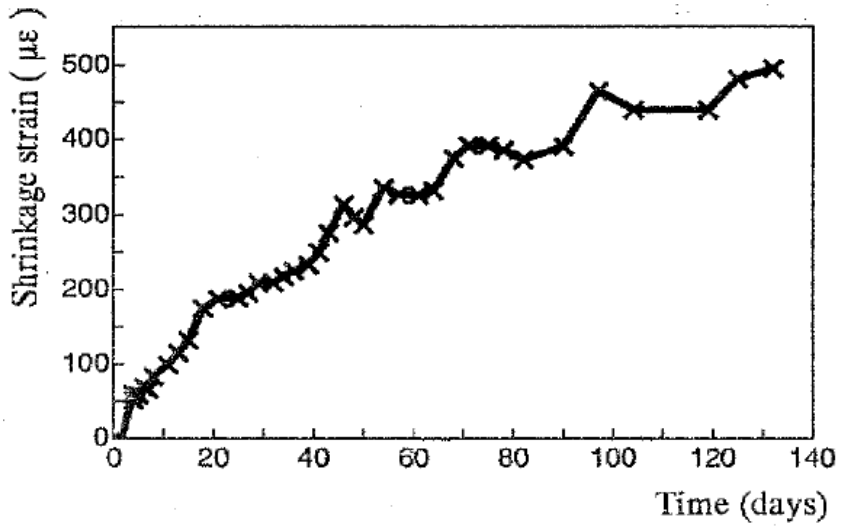

Figure 2.3. Shrinkage strain for specimen P1 (Terrey, Bradford, & Gilbert, 1994)

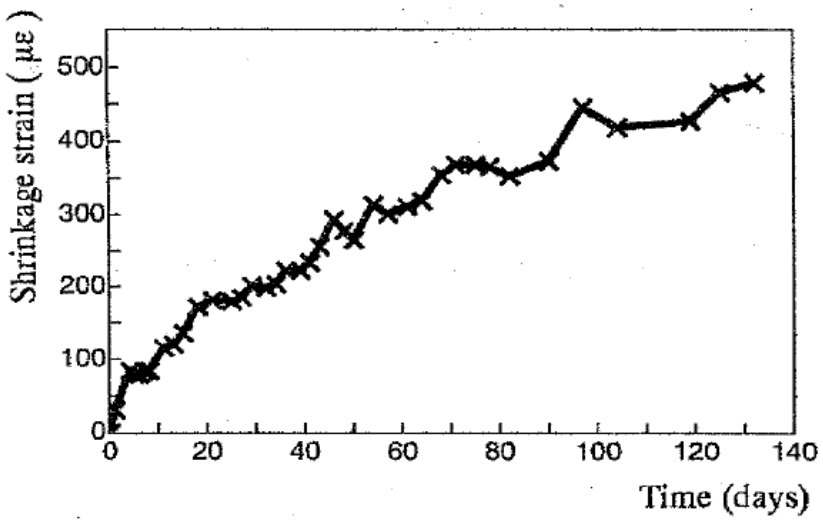

Figure 2.4.. Shrinkage strain for specimen S1 (Terrey, Bradford, & Gilbert, 1994)

Figure 2.5 shows the shrinkage strain of specimen CFST1. Shrinkage of specimen CFST2 was similar, but it was not presented. The three curves represent shrinkage in the concrete core of an unbonded specimen and the strains in steel of both unbonded and bonded specimens. The coefficient of thermal expansion α is usually very similar for steel and concrete and is often taken as 11.7×10^{-6}/°C for steel and 10.0×10^{-6}/°C for concrete. Therefore, a value of 11×10^{-6}/°C

was considered appropriate for the CFTs. The temperature at the start of the test was 26°C and at the end it was 17°C. This temperature drop results in shortening of the specimens of approximately 100 με, which is only about 30 με less than the data from the shrinkage tests show. Comparing this with the shrinkage strains of the sealed and unsealed cylinders, and considering the much higher strain a structure would endure from initial loading and creep, shrinkage strain in CFT members can be considered negligible.

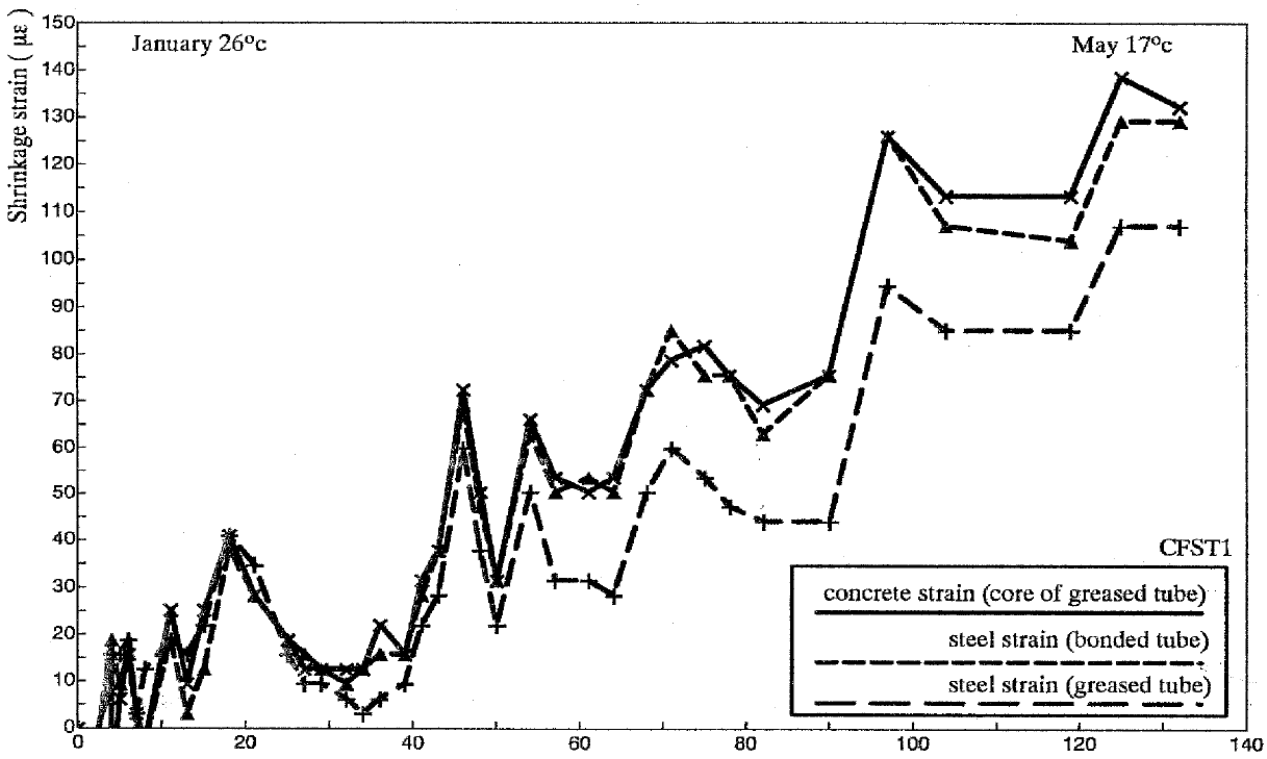

Figure 2.5. Shrinkage strain for specimen CFST1 (Terrey, Bradford, & Gilbert, 1994)

The creep coefficients are plotted in Figure 2.6 and Figure 2.7 for specimens P1 and CFST1, respectively. CFST2 gave similar results as CFST1, but they were not published. A prediction of the creep coefficient used in the creep model given by ACI committee 209 (ACI Committee 209, 2008) is also shown. This creep model is discussed in section chapter 5. Good consistency seems to be between the predictive model and the experimental results when the model has been calibrated to a final creep coefficient of 2.2 for the plain concrete and 1.2 for the greased CFT specimens.

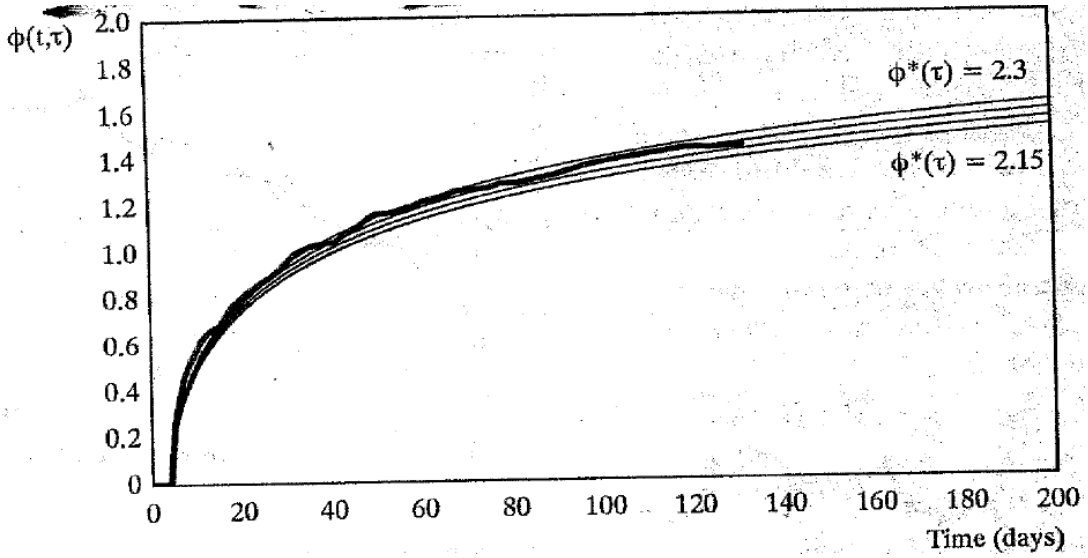

Figure 2.6. Creep coefficient for specimen P1 (Terrey, Bradford, & Gilbert, 1994)

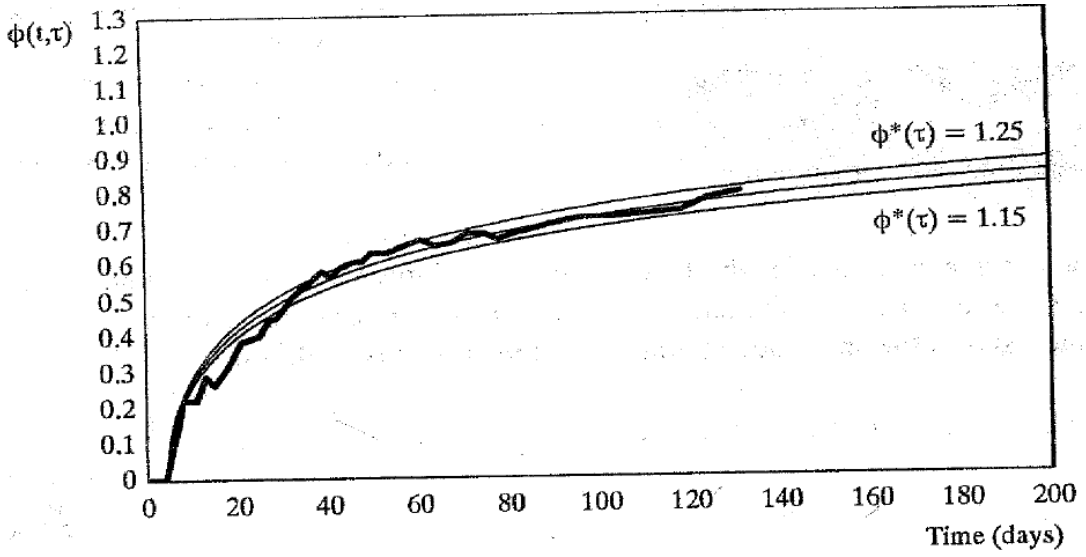

Figure 2.7. Creep coefficient for specimen CFST1 (Terrey, Bradford, & Gilbert, 1994)

Figure 2.8 shows the total concrete and steel stains for a greased specimen, as well strains in a companion bonded specimen. The steel strain in the bonded tube is compared with a theoretical analysis, which uses the same creep and shrinkage data as that obtained from the CFST1, which is a greased specimen.

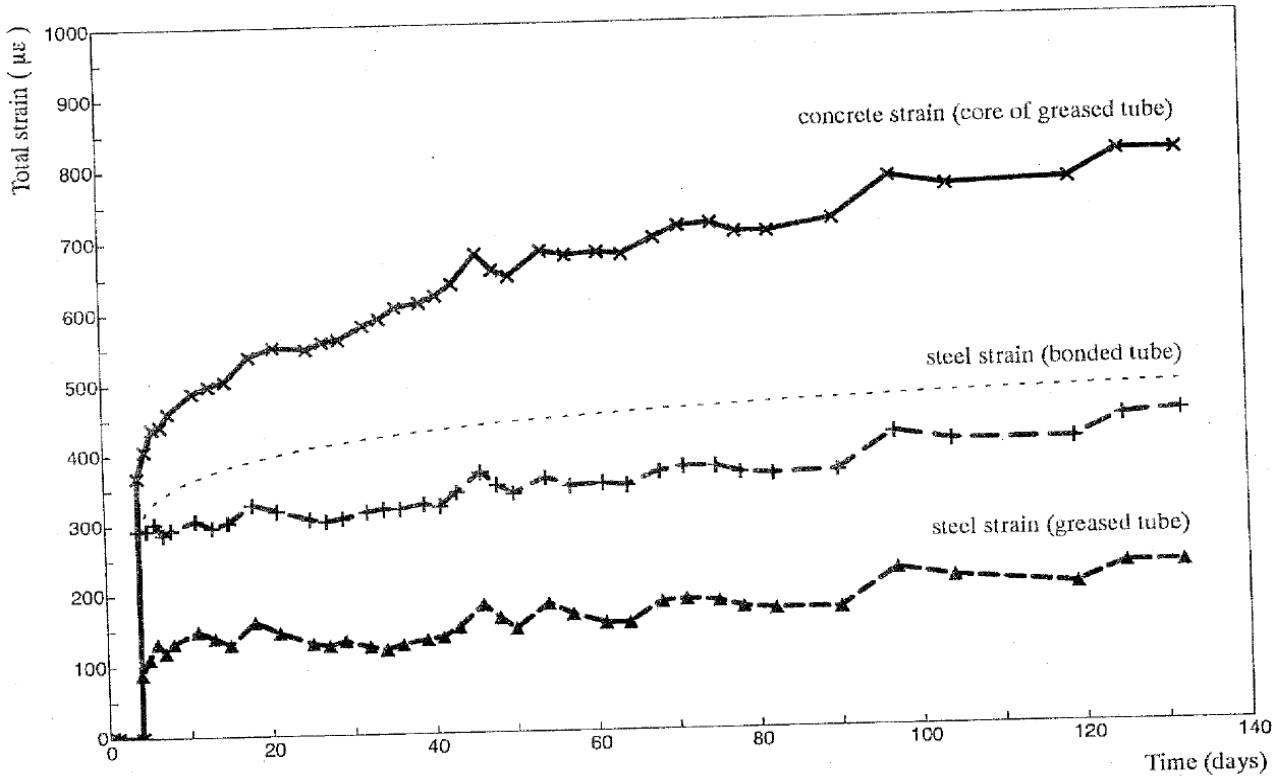

Figure 2.8. Concrete and steel strains (Terrey, Bradford, & Gilbert, 1994)

The AAEM (age-adjusted effective modulus) method (Gilbert, 1988) was used to calculate the time-dependent steel strains in the bonded CFT specimen. Full strain compatibility at the concrete/steel interface is assumed. The strains of the bonded steel tube obtained from this analysis are also shown in Figure 2.8 as a dashed line. The figure indicates that there is good agreement between the predicted and measured steel strains in the ungreased CFT specimens. It can also be seen that the initial strains in the greased tube are only about a quarter of those in the untreated tube. Creep strains of the concrete are much larger than the increase in steel strain over time in the greased tube, so the strain of concrete seems to be independent of the strains of steel. If the aforementioned thermal strains are taken into account, it can be concluded that the steel strains hardly change at all over time.

2.1.2.5 Conclusions

From this research the following conclusions were made:

1. Drying creep and shrinkage in normal exposed concrete are the main contributors to the long-term behavior of concrete structures. When concrete is encased in a steel tube, the loss of moisture from the concrete may be small enough to be neglected, with a consequent decrease of creep and shrinkage and its adverse effects on structures.

2. This experiment revealed that creep coefficients between 50 and 60 percent of those for unsealed concrete are appropriate for CFTs. Moreover, results indicate that shrinkage strains in the concrete may be neglected when such members are considered.

2.1.3 Morino, Kswaguchi, & Cao, 1994

Creep behavior of concrete-filled steel tubular members

2.1.3.1 Research Objective

Morino et al. tested the long-term effects on square concrete-filled tubes of different thicknesses and lengths under axial stress so that the creep coefficient could be obtained quantitatively. The purpose was also to evaluate if the stress transfer from the concrete to the steel tube may cause the steel yielding or local buckling of the steel tube.

2.1.3.2 Specimens

Concrete was poured into six cold-formed 100 x 100 mm steel tubes with nominal thicknesses of 2.3, 3.2 and 4.5 mm, and lengths of 200, 300, 400, 800, and 1200 mm. Steel plates were welded to both ends of each specimens and load was applied through the steel plates. Table 2.1 provides a list of the specimens.

Daily measurements of axial strain were taken with wire strain gauges on the steel surface. Some load drop was inevitable so measurements were taken before and after adjusting the load. The location of gauges is shown in Figure 2.10.

Table 2.1. List of specimens and dimensions of steel tube (Morino, Kswaguchi, & Cao, 1997)

Specimen name	Length (mm)	Thickness (mm)	Tube width (mm)
C-40-4.5	396.0	4.36	100.12
C-40-3.2	396.6	3.12	100.12
C-80-3.2	796.5	3.12	99.96
C-20-2.3	194.3	2.14	99.98
C-30-2.3	294.6	2.14	99.98
C-120-2.3	1203.3	2.14	99.98

2.1.3.3 Test setup

The specimens were placed in a creep rig which consisted of 60 mm thick end plates, four threaded steel rods with a diameter of 12 mm, a pin to remove eccentricity, a load cell, and a 20-ton hydraulic jack. No springs were used, but the small diameter steel rods prevented too much load drop. The test setup is shown in Figure 2.9. Two 400 mm long specimens were tested together in one rig and two 800 mm long specimens were tested in another. Axial load of 103.9 kN was applied to these specimens. The load was decided based on the average of the loads that would induce a stress of one third of f'_c in the concrete. Other specimens were loaded to 114.0 kN by the same testing method.

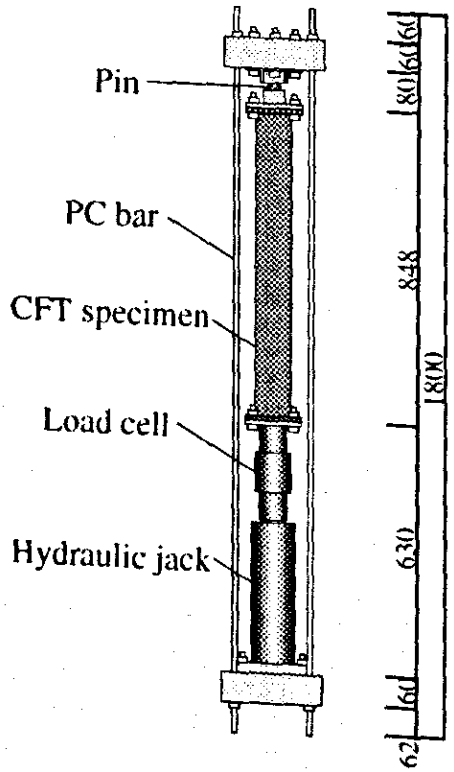

Figure 2.9. Test setup for compression members (Morino, Kswaguchi, & Cao, 1997)

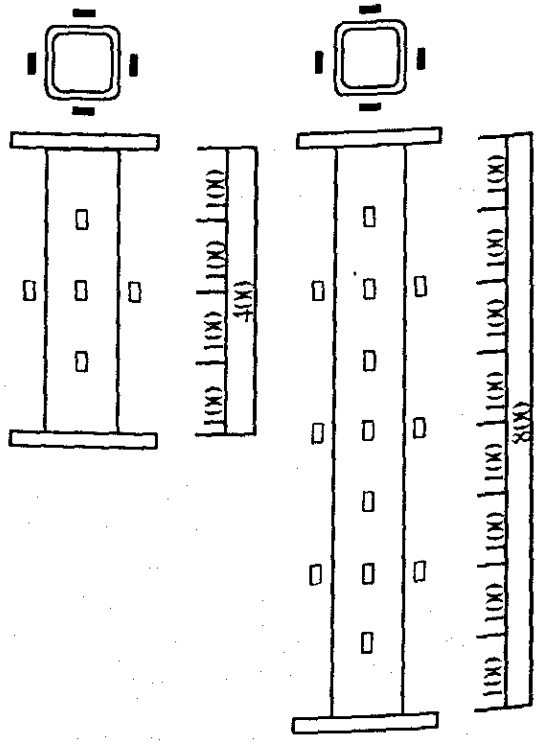

Figure 2.10. Location of W.S.G (Morino, Kswaguchi, & Cao, 1997)

2.1.3.4 Experimental results

Total strains of all specimens are shown in Figure 2.11, where ε_0 is the strains at mid height of the steel tube. All specimens showed similar behavior, which suggests that the length of the specimen is irrelevant. However, initial strain of the 1200 mm long specimen is larger than other that of other specimens with 2.3 mm wall thickness. This discrepancy is not explained.

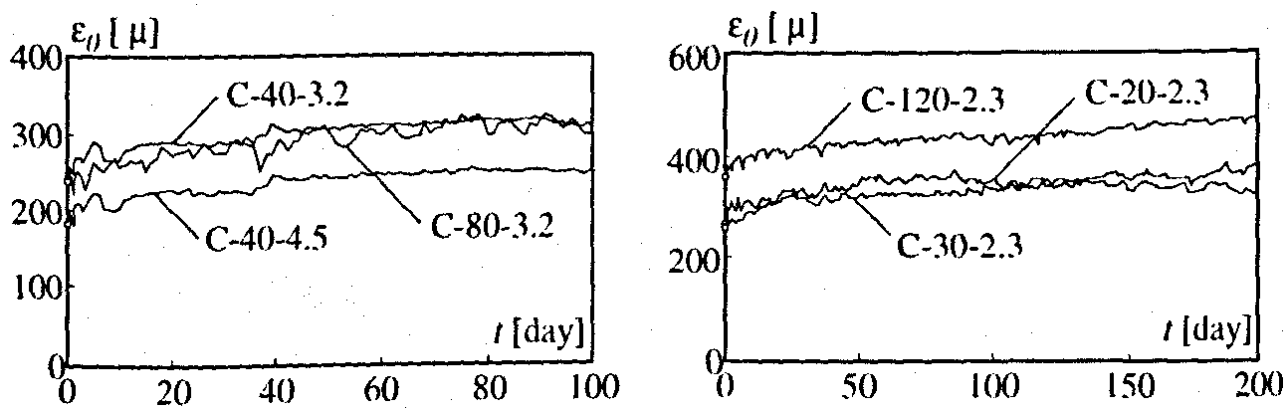

Figure 2.11. Time-history of axial strain ε_0 of centrally-loaded compression members (Morino, Kswaguchi, & Cao, 1997)

The total load carried by the specimens is shown in Figure 2.12. It is separated into load carried by concrete and load carried by steel. The steel load is found by calculating the steel stress from the steel strains and the Young's modulus of steel. The concrete load is then found by subtracting the steel load from the total load measured by the load cell. All specimens show a slight decrease in the load on the concrete over time, and an increase in the load on the steel. The test was stopped after 100 days for thee of the six specimens since the wire strain gauges started to deteriorate at that time.

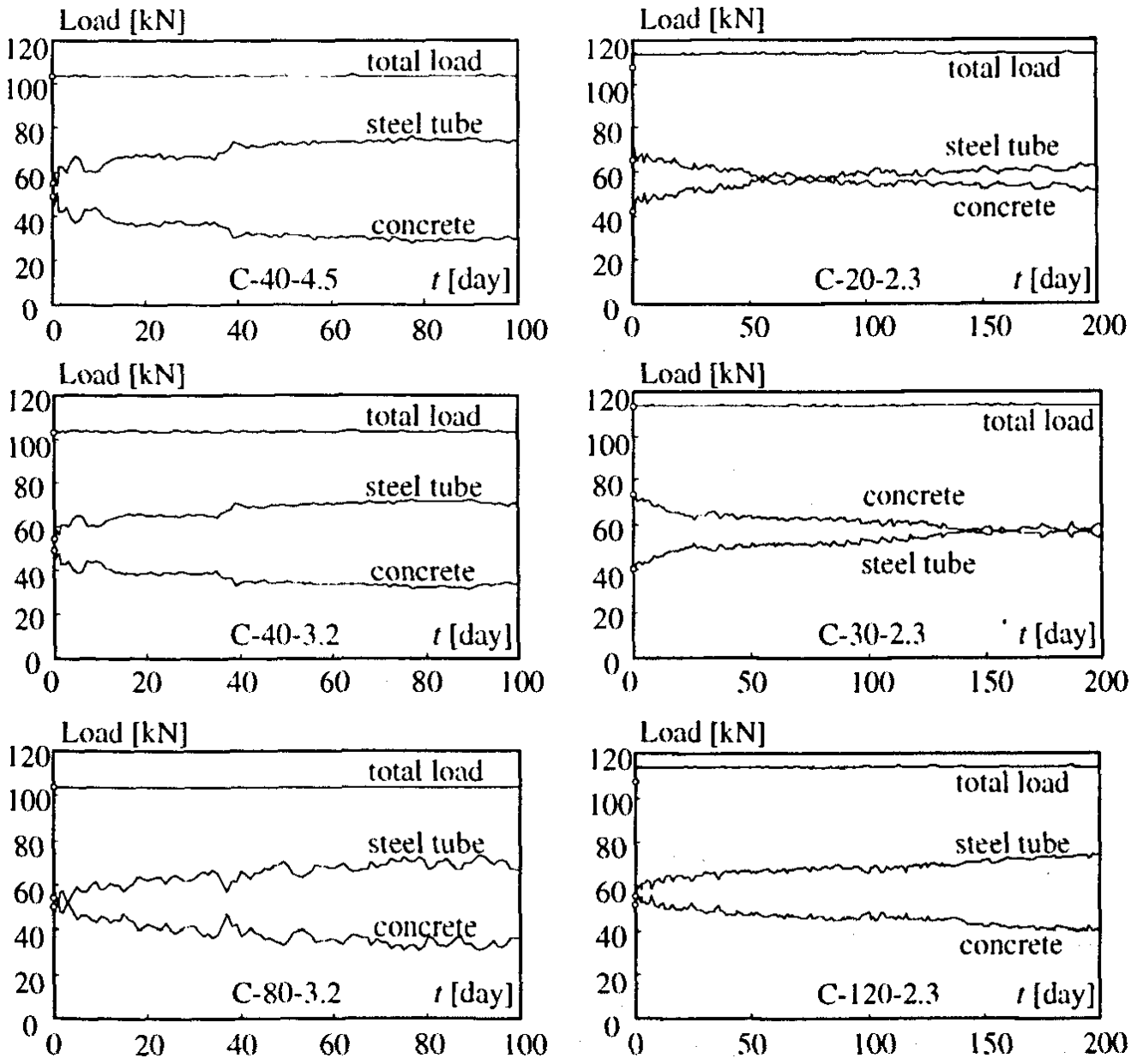

Figure 2.12. Time-history of axial loads of centrally-loaded compression members (Morino, Kswaguchi, & Cao, 1997)

Figure 2.13 and Figure 2.14 show the fitted curves used to determine the creep coefficient, φ. The value of the creep coefficient was reported to range from 0.18 to 0.39 in the six specimens after 100 days of loading, and from 0.26 to 0.44 after 200 days in the three specimens for which the test lasted that long. (Ichinose, Watanabe, & Nakai, 2001)

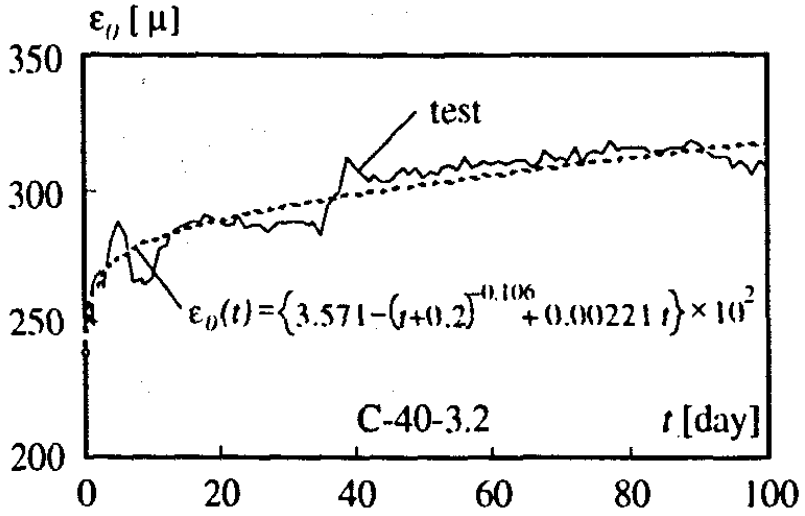

Figure 2.13. Time-history of axial strain ε_0 of centrally-loaded compression members and fitted curve (Morino, Kswaguchi, & Cao, 1997)

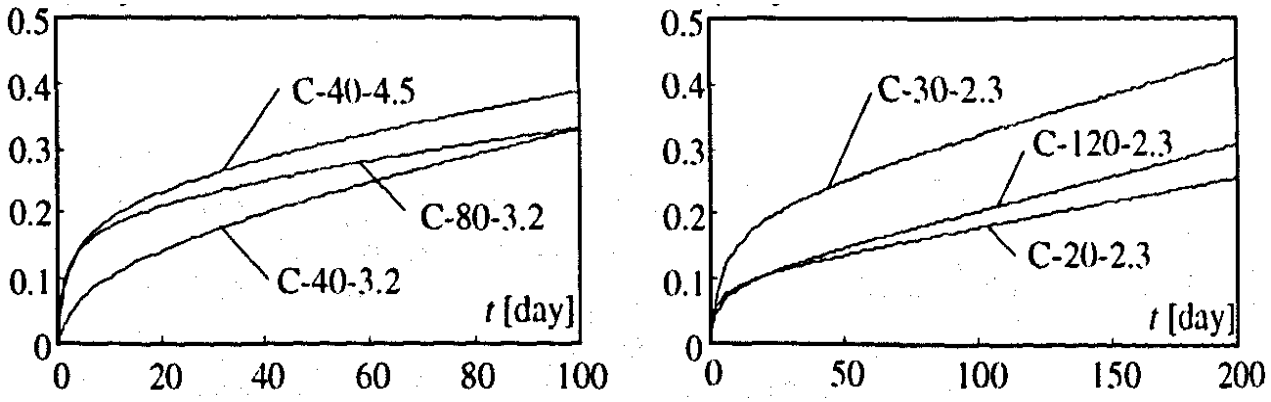

Figure 2.14. Creep coefficient of centrally-loaded compression members (Morino, Kswaguchi, & Cao, 1997)

2.1.3.5 Conclusions

From this research the following conclusions were made:

1. The creep coefficient of CFT members is considerably smaller than the values used for conventional reinforced concrete columns
2. The length of the column did not impact creep in CFTs in this study, where
3. More work needs to be done on methods of time-dependent analysis of CFT columns.

2.1.4 Ichinose, Watanabe, & Nakai, 2001

An experimental study on creep of concrete filled steel pipes

2.1.4.1 Research objective

Ichinose, et al. carried out continuous measurements of eleven concrete filled steel tubes and six plain concrete columns of same sizes, to obtain visco-elastic parameters of the Kelvin model which characterize the time-dependent behavior. Three different kinds of loading conditions were applied to the specimens; load applied to the concrete core (case C), load applied to the steel tube (case S), and load applied uniformly to both (case V). The results show that creep strains are largest when the load is applied to the concrete and smallest when the load is applied to the steel tube.

2.1.4.2 Specimens

Table 2.2. Specimen types Table 2.2 shows the specimen types and how they are loaded. The steel tubes were 1.0 m long and had an external diameter of 165.2 mm. In order to examine the effect of the steel-to-concrete ratio, three specimen types were constructed; two CFTs with a different wall thickness and one with a zero wall thickness (plain concrete).

Table 2.2. Specimen types (Ichinose, Watanabe, & Nakai, 2001)

Specimen type	Experiment	Loading section	Applied stress (kgf/cm^2)	Tube thickness (mm)	Specimen name
Concrete filled steel tube	Creep (CR)	Concrete (C)	60	4.5	CR-C-60-4.5
				5	CR-C-60-5
			80	4.5	CR-C-80-4.5
				5	CR-C-80-5
		Steel tube (S)	80	4.5	CR-S-80-4.5a
				4.5	CR-S-80-4.5b
		Composite (V)	80	4.5	CR-V-80-4.5a
				4.5	CR-V-80-4.5b
Concrete filled steel tube	Shrinkage (SH)	-	-	4.5	SH-4.5a
				4.5	SH-4.5b
				5	SH-5
Plain concrete column	Creep (CR)	Plain concrete	60	0	CR-60-0
				0	CR-80-0a
			80	0	CR-80-0b
				0	CR-80-0c
Plain concrete column	Shrinkage (SH)	-	-	0	SH-0a
				0	SH-0b

2.1.4.3 Test setup

Both creep and shrinkage strains were measured in the experiment. Total strain measurements were taken on specimens under sustained axial loading and shrinkage of concrete was measured in unloaded specimens, which had identical materials, size and age as the loaded specimens, and stored in the same environmental conditions. All specimens were kept in a laboratory where the temperature and humidity changed very little throughout the year. Figure 2.15 shows how the load was applied. The nuts on the PC bars were tightened until the desired load, which was measured through a load cell, was reached. No adjustments were made to the load after initial stressing of the specimens, and the time-dependent behavior of the load was modeled analytically. Strain measurements were taken on the mid-height of the column. A gauge was embedded inside the concrete core and four foil gages were attached to external surface of the steel pipe with 90° angles between them.

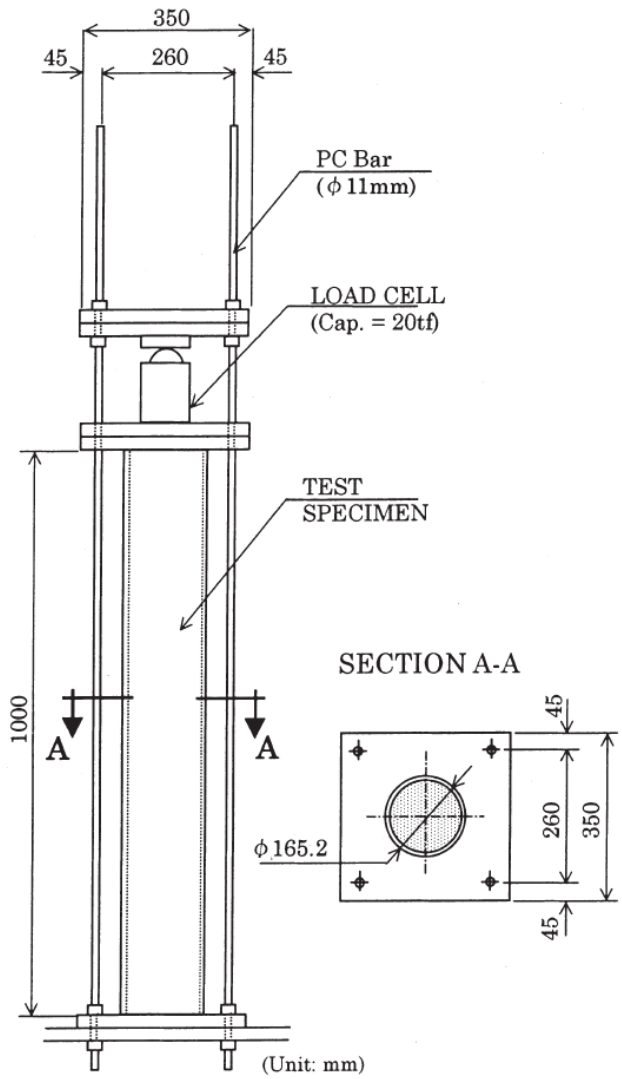

Figure 2.15. Loading system (Ichinose, Watanabe, & Nakai, 2001)

2.1.4.4 Experimental results

The effects of the steel tube on shrinkage can be clearly seen in Figure 2.16, where the strains in CFT specimens SH-4.5 and SH-5 are only about 9% of the values measured in specimens SH-0a and SH-0b, which are plain, unsealed concrete columns. The prevention of moisture loss and the corresponding prevention of reduction in concrete volume, may have improved the confinement effects on the encased concrete, allowing the column to behave as a composite section instead of the concrete shrinking away from the steel.

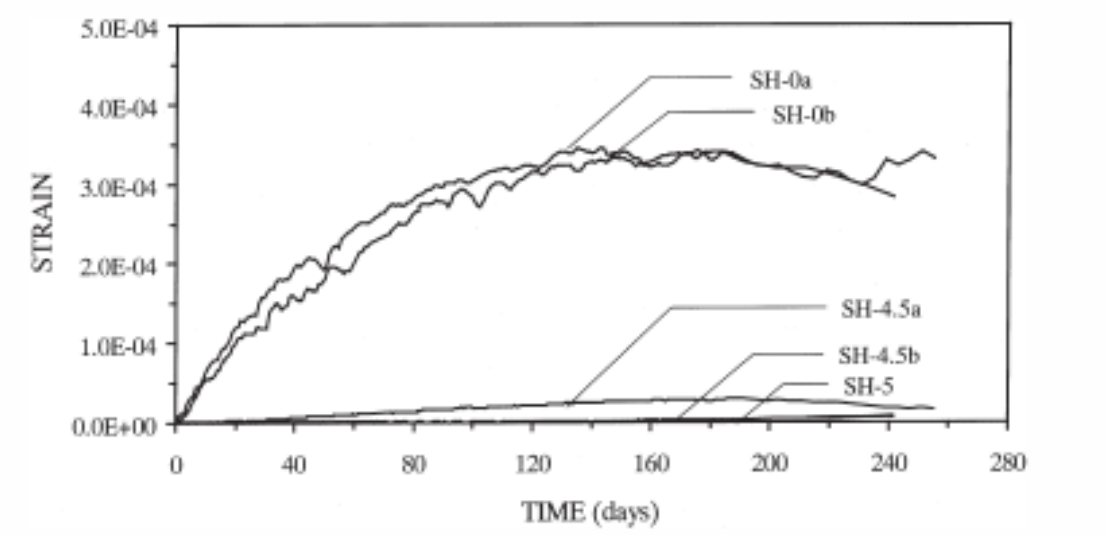

Figure 2.16. Concrete shrinkage (Ichinose, Watanabe, & Nakai, 2001)

Figure 2.17 and Figure 2.18 show examples of the experimental results for the axial creep strain in the concrete and the corresponding increase in strain in the steel tube, respectively. The values take into account the effects of the concrete shrinkage and temperature. For comparison, the curves resulting from an analytical evaluation were plotted on the same graphs. The curve seems to fit well for the concrete axial strain.

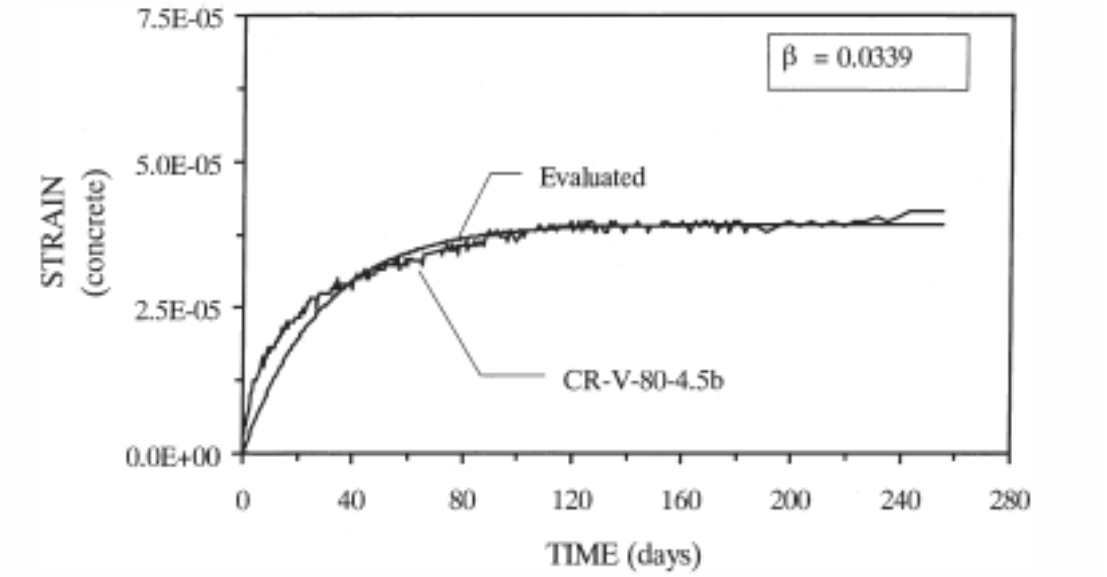

Figure 2.17. Concrete axial strain due to creep (Ichinose, Watanabe, & Nakai, 2001)

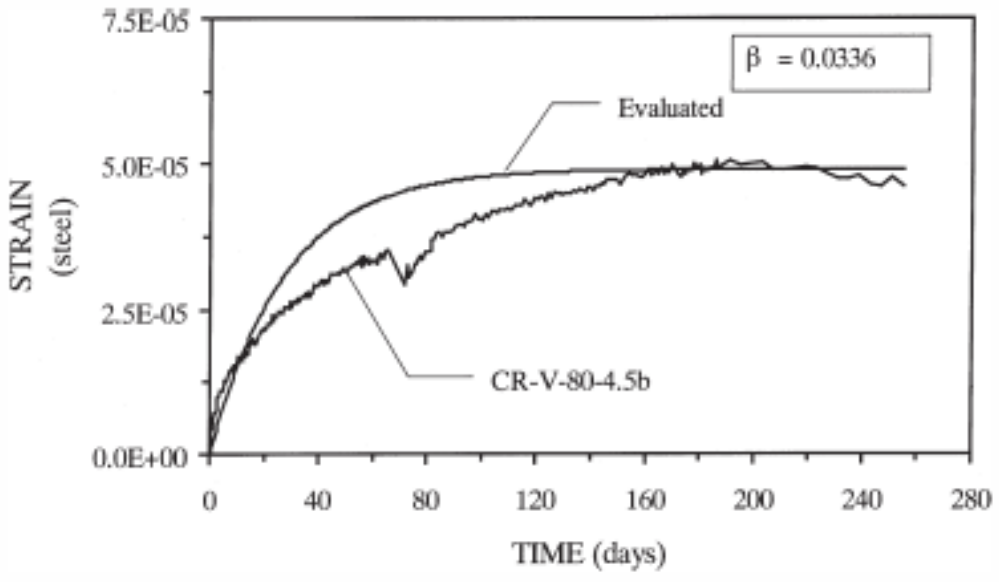

Figure 2.18. Steel tube axial strain due to creep (Ichinose, Watanabe, & Nakai, 2001)

Table 2.3 gives the experimental values of the final creep coefficient of each specimen. The creep coefficient is taken as the ratio between the creep strain and the initial elastic strain at any point in time. At t = ∞ the creep coefficient equals the final creep coefficient. The table shows that creep strains are considerably higher when CFT is loaded through the concrete only than when the steel and concrete are both loaded. The average values of the creep coefficients are 0.40 and 0.28, respectively. These are less than half of the values obtained for the plain concrete specimens, for which the average is 0.87.

Table 2.3. Experimental values of creep coefficients φ (Ichinose, Watanabe, & Nakai, 2001)

Specimen name	ε (με)	f_0 (x 10^{-6})	$\varphi = f_0/\varepsilon$
CR-60-0	592	542	0.92
CR-80-0a	474	424	0.89
CR-80-0b	494	372	0.75
CR-80-0c	739	676	0.91
CR-C-60-4.5	148	55	0.37
CR-C-60-5	136	54	0.40
CR-C-80-4.5	227	91	0.40
CR-C-80-5	166	69	0.42
CR-S-80-4.5a	65	4	0.06
CR-S-80-4.5b	68	10	0.15
CR-V-80-4.5a	161	53	0.33
CR-V-80-4.5b	162	39	0.24

ε = initial elastic strain
f_0 = predicted final strain

2.1.4.5 Conclusions

From this research the following conclusions were made

1. Excluding the initial parts of the curves, a good evaluation of the time-dependent behavior seems to have been provided, especially when predicting the final creep strain. This can be considered sufficient in design, where creep is usually evaluated in the form of creep coefficient.
2. This experiment indicates that the current JSHB values of creep coefficient are conservative, suggesting a value of 1.88. A value of 0.87, 0.40 and 0.28 were determined for the plain concrete column, the core-loaded CFT and the uniformly loaded CFT, respectively.
3. Shrinkage measurements show that the shrinkage strain in the CFT specimens was about 9% of that of the plain concrete specimen and that, which is a number of less than 30 microstrain. Thus, the shrinkage strain can be considered negligible when designing CFT members.

2.1.5 Uy, 2001

Static Long-Term Effects in Short Concrete-Filled Steel Box Columns under Sustained Loading

2.1.5.1 Research objective

Uy conducted long-term tests on 23 high-strength concrete cylinders and seven square concrete-filled steel tubes to compare the differences in shrinkage and creep and to compare them with the ACI 209 (ACI Committee 209, 2008) models for shrinkage and creep. The ACI models were then modified with re-calibrated creep coefficients to fit the data. The ACI models are discussed in Chapter 5.

2.1.5.2 Specimens

The CFT specimens were 90 mm on each side and had a length of 270 mm. The thickness of the tubes was 3.0 mm. None of the seven specimens were greased and load was applied uniformly to the concrete and the steel, so perfect strain compatibility between the steel and the concrete was assumed. Three specimens were left unloaded and monitored for shrinkage strain only. The ends

of the CFT specimens were sealed with polyethylene to simulate the conditions in practice, where moisture egression from the ends is prevented as well as from the sides. All strains were measured with mechanical demec gauges which had a gauge length of 50 mm. Holes for strain gauge targets were made in the steel so that direct measurements of concrete strains could be taken. Initial readings were taken immediately after the instrumentation.

The concrete cylinders were 100 mm in diameter and 200 mm in length. After casting, they were moist-cured for 14 days and then prepared as either shrinkage or creep specimens. Three specimens were left unloaded and subject to shrinkage strains only. Demec strain gage targets were attached to the surface of the cylinders, and initial readings were taken immediately after that.

2.1.5.3 Test setup

Both concrete cylinders and CFTs were subject to a sustained load in a conventional creep rig. The creep test setup is illustrated in Figure 2.19, which shows a steel rig with a hydraulic jack. High strength plaster on the surfaces of the specimens enabled uniform loading. The stress applied to the specimens was about a quarter of the assumed concrete strength of 60 MPa. This resulted in an initial strain of about 350 με for both the CFT and the cylinder specimens.

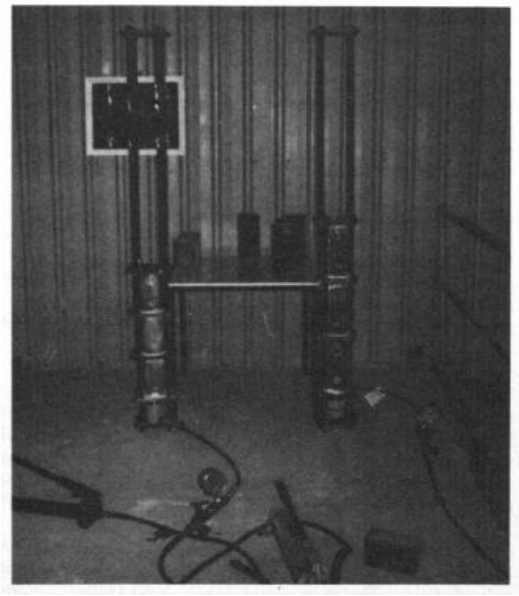

Figure 2.19. Creep specimens (Uy, 2001)

2.1.5.4 Experimental results

Figure 2.20 and Figure 2.21 show the shrinkage strains for the CFTs and the high-strength concrete cylinders, respectively. These results show the low shrinkage in CFT relative to plain concrete. The shrinkage strains after 140 days of testing were 160 and 600 με for the CFT and concrete cylinders, respectively. Variations in temperature were quite large during the test, especially in the CFTs, and, as a result, the temperature-induced strains were a larger portion of the total strain. These strain changes are not accounted for in the results, but were noted by the significant variations in total strains measured.

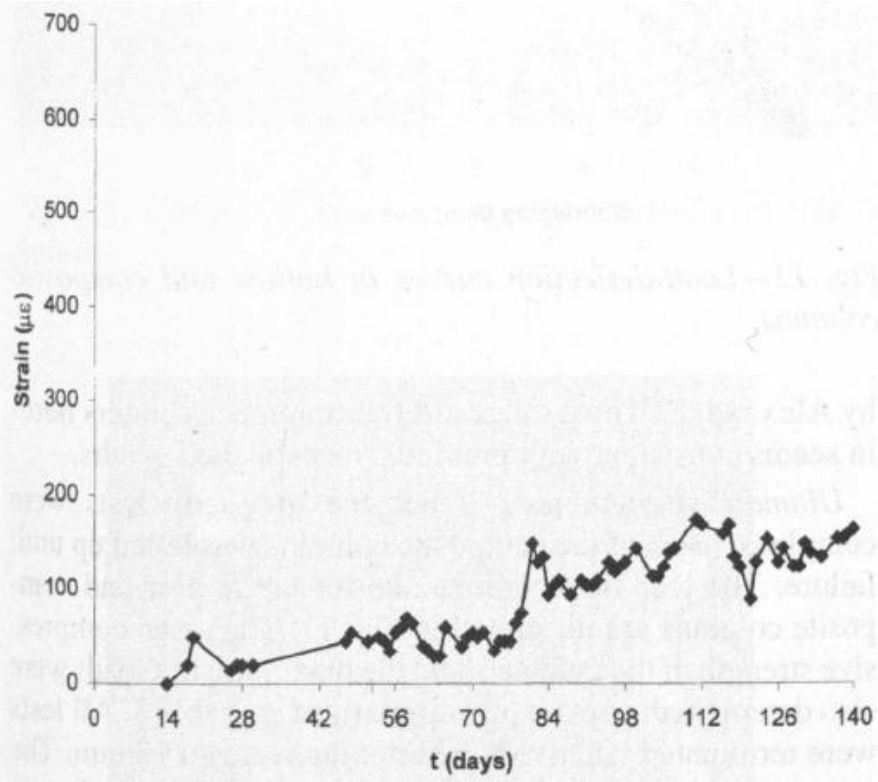

Figure 2.20. Average shrinkage strains (concrete-filled columns) (Uy, 2001)

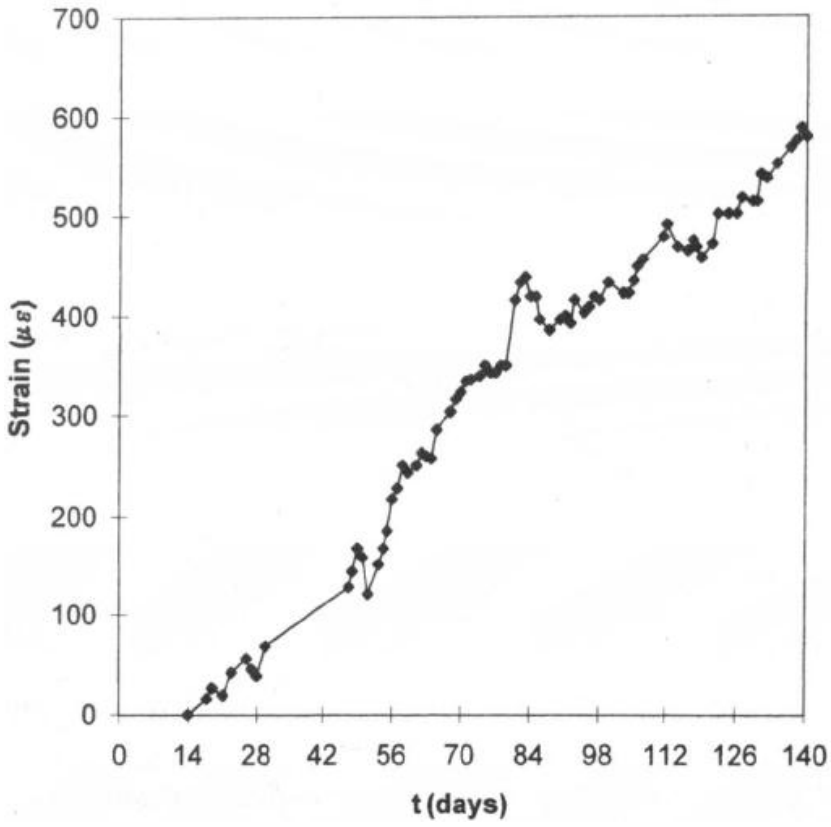

Figure 2.21. Average shrinkage strains (high-strength concrete cylinders) (Uy, 2001)

Figure 2.22 and Figure 2.23 show the average total strains for the CFT and the concrete cylinders, respectively. The final creep coefficient of CFTs was lower than that of the plain concrete cylinders.

The high-strength concrete also had a significantly lower creep coefficient than the plain normal-strength concrete. The final creep coefficients were 1.0 and 2.0 for the CFTs and concrete cylinders, respectively, while normal concrete has values that range between 2.0 and 3.0 when it is plain and unsealed. The final creep coefficient was defined as the ratio of final predicted creep strain to initial elastic strain.

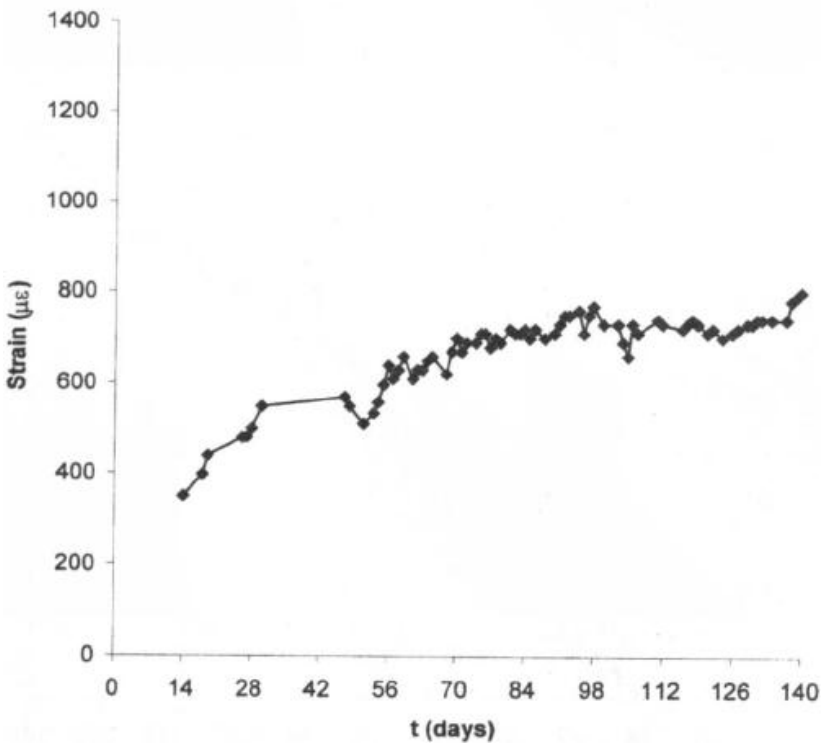

Figure 2.22. Average total strains (concrete-filled columns) (Uy, 2001)

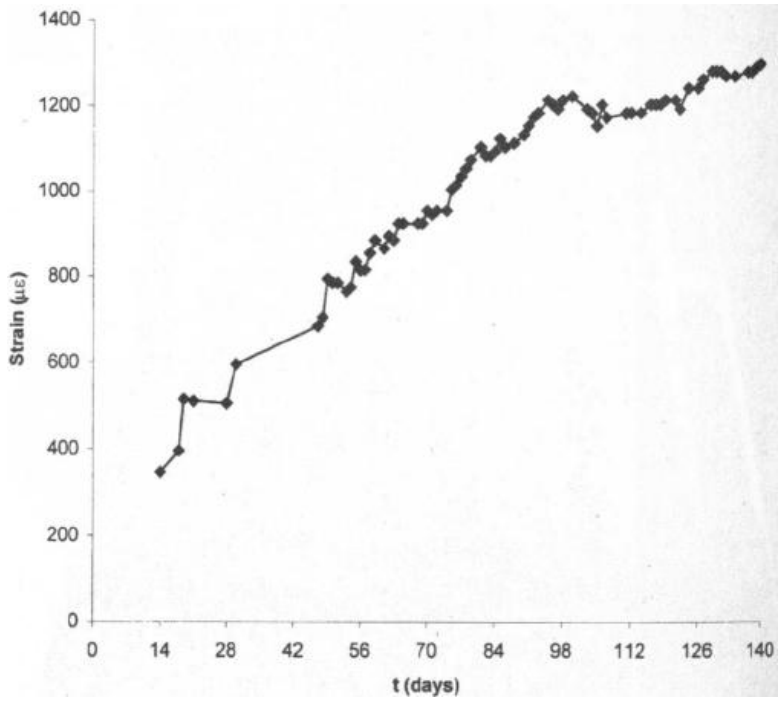

Figure 2.23. Average total strains (high-strength concrete cylinders) (Uy, 2001)

After determining the time-dependent strains, it is important to establish models that best predict the variation of those strains with time. Proper calibration then permits improvements of these models for use in design. The models suggested by ACI Committee 209, previously calibrated for normal-strength concrete, were calibrated to fit the experimental results. The creep model requires the prediction of the final creep coefficient at infinite time and the shrinkage model requires that the final shrinkage strain be predicted. These models were calibrated for both the CFTs and the high-strength concrete cylinders tested in this research program. Good agreement seems to have been established for the creep model. The expressions for the ACI Model are given in Chapter 5.

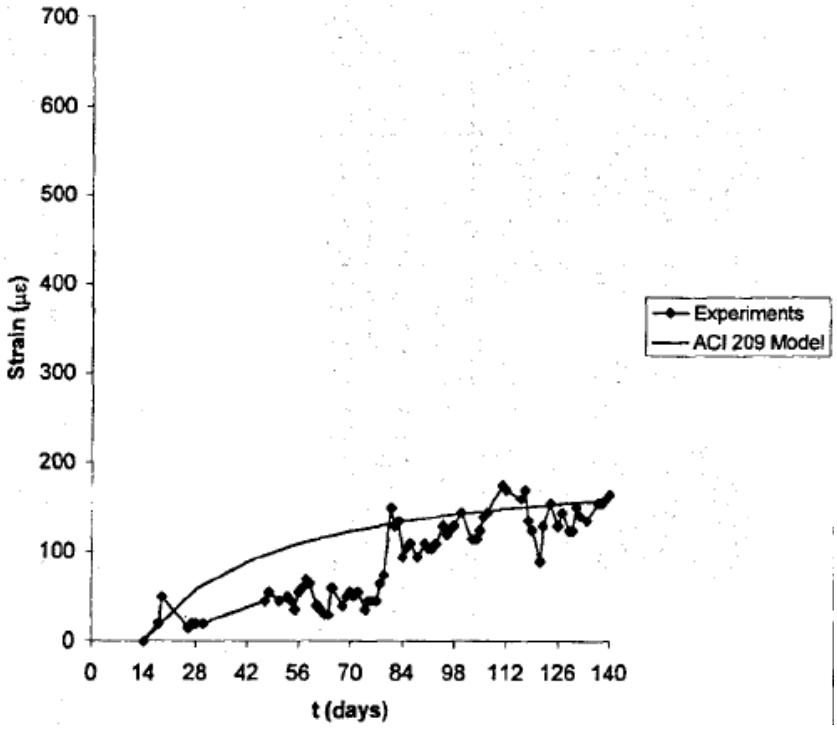

Figure 2.24. Comparison of shrinkage strains for composite columns (Uy, 2001)

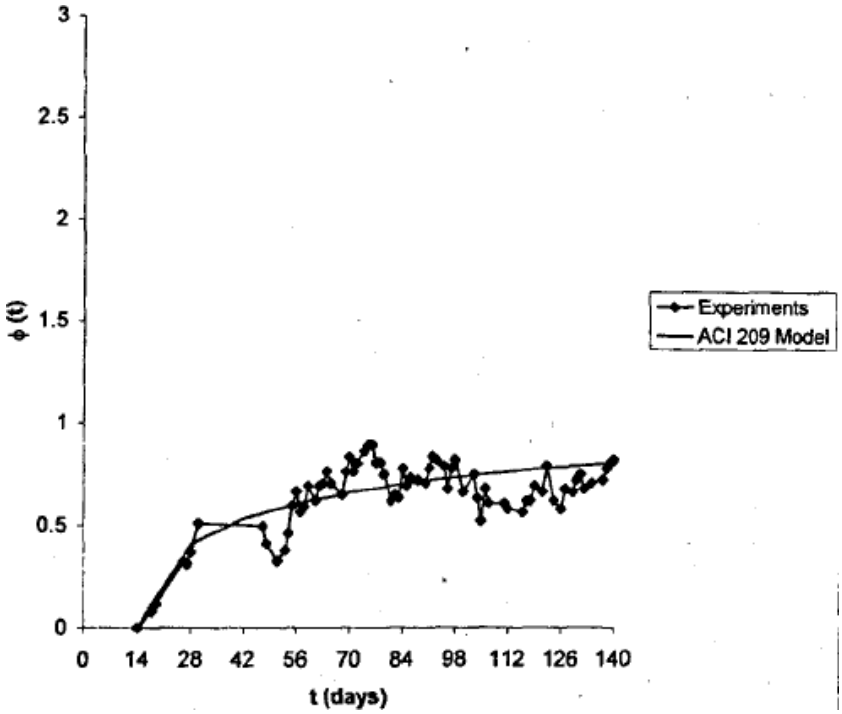

Figure 2.25. Comparison of creep coefficients for composite columns (Uy, 2001)

The models are very sensitive to the prediction of the final values mentioned above. Final shrinkage strain of 200 με was assumed for the CFTs and the final creep coefficient was predicted as 1.25. The shrinkage and creep models for the CFTs are plotted with the experimental results in Figure 2.24 and Figure 2.25, respectively. The predicted values for the high-strength concrete cylinders were 700 με for final shrinkage strain and 2.5 for final creep coefficient. The creep and shrinkage models for the high-strength concrete are plotted with the experimental results in Figure 2.26 and Figure 2.27, respectively.

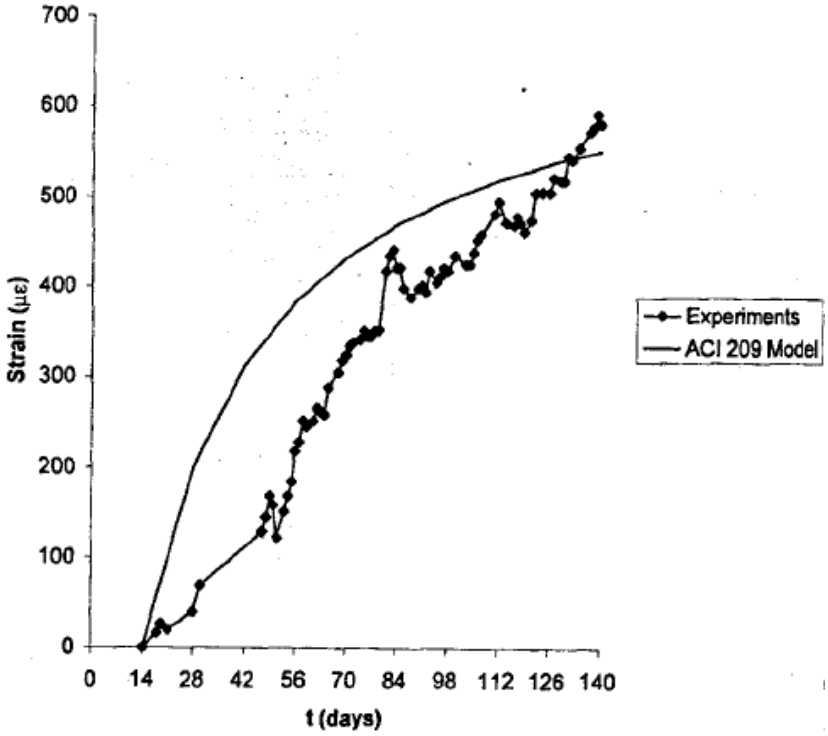

Figure 2.26. Comparison of shrinkage strains for high-strength concrete cylinders (Uy, 2001)

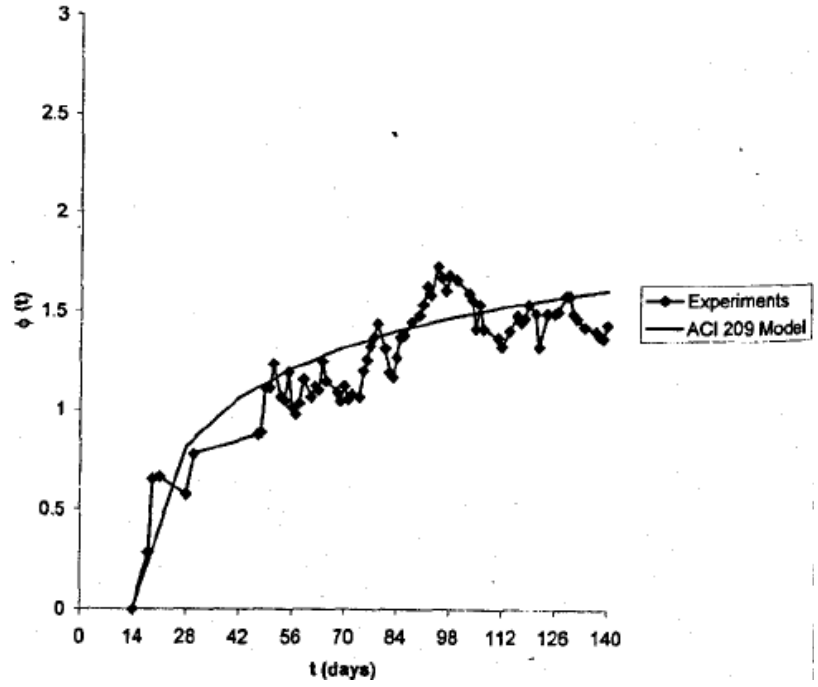

Figure 2.27. Comparison of creep coefficients for high-strength concrete cylinders (Uy, 2001)

2.1.5.5 Conclusions

From this research the following conclusions were made:

1. The experimental results enabled final shrinkage strains and final creep coefficients to be determined in CFTs and high-strength concrete for ACI committee 209 models for time-dependent behavior of shrinkage and creep.

2. Both creep and shrinkage of concrete are significantly reduced when concrete is enclosed in a steel tube.

2.1.6 Han & Yang, 2003

Analysis of thin-walled steel RHS columns filled with concrete under long-term sustained loads

2.1.6.1 Research Objective

Han & Yang conducted a research program in which long-term strains of eight rectangular concrete-filled steel tubes with different depth-to-breadth ratios were monitored for about 180 days to examine the creep behavior of CFTs. Also, the time-dependent behavior is predicted by means of a theoretical model developed for shrinkage and creep.

2.1.6.2 Specimens

The CFT specimens had a length of 600 mm and thickness of 2.93 mm, but were of four different rectangular cross-sections. The load was applied uniformly and the concrete was assumed to develop same strain changes as the steel. Four specimens were left unloaded and monitored for shrinkage strains only. After welding a square 25 mm thick plate on one end, the tube was filled with concrete and cured. A high-strength epoxy was then applied to the top of the specimens. All surfaces were ground flat and smooth using a grinding wheel with diamond cutters to ensure that the load would be equally distributed to the steel and the concrete. An identical plate was then welded to the other end.

2.1.6.3 Test setup

The sustained load vas initially applied 28 days after concrete casting, by tightening the nuts of eight pre-stressing bars. The load was monitored by a load cell and kept constant by tightening

the bars regularly. The value of the load and its intensity is shown for each specimen in Table 2.4. The creep rig setup is illustrated in Figure 2.28. The strain measurements were taken at mid-height of the steel tube by means of a deformation transducer.

Table 2.4 Summary of test information (Han & Yang, 2003)

No.	Specimen	Section dimension D x B x t_s (mm)	L (mm)	Sustained load N_L (kN)	Load level n
1	R-1	100 x 60 x 2.93	600	0	0.0
2	R-2	100 x 60 x 2.93	600	304	0.68
3	R-3	100 x 80 x 2.93	600	0	0.0
4	R-4	100 x 80 x 2.93	600	382	0.67
5	R-5	120 x 60 x 2.93	600	0	0.0
6	R-6	120 x 60 x 2.93	600	338	0.65
7	R-7	120 x 90 x 2.93	600	0	0.0
8	R-8	120 x 90 x 2.93	600	424	0.58

$n = N_L/N_u$, where N_u is the calculated ultimate capacity of the specimen

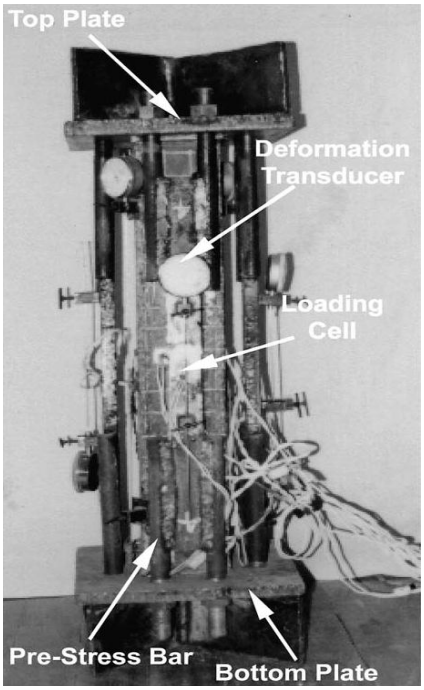

Figure 2.28. A general view of the long-term service load tests (Han & Yang, 2003)

2.1.6.4 Experimental results

The authors offer no experimental results from the shrinkage specimens, but the paper states that shrinkage was determined to be negligible. The authors do not report on variations in temperature and humidity, but state that these factors were almost constant during the whole year in the laboratory.

Figure 2.29 shows the total time-dependent strain for the loaded CFT specimens, plotted with a model that takes into account the initial elastic modulus of concrete, the change in load in the concrete resulting from creep, and the estimated final creep coefficient multiplied by an aging coefficient of concrete. This aging coefficient, however, is a function of time and the estimated final creep coefficient only. The author does not report these estimated values, but from Figure 2.29 it seems to range from 0.60 to 0.65. From the results presented in this paper, it seems like the author is investigating the effect of creep on axial load capacity. Therefore, limited results and discussions are provided on the creep experiments.

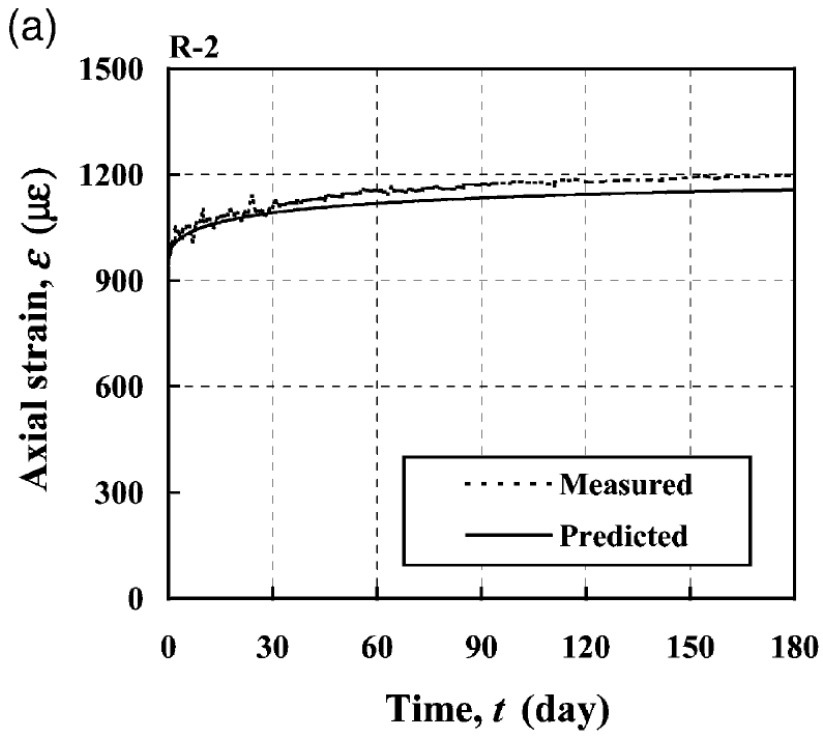

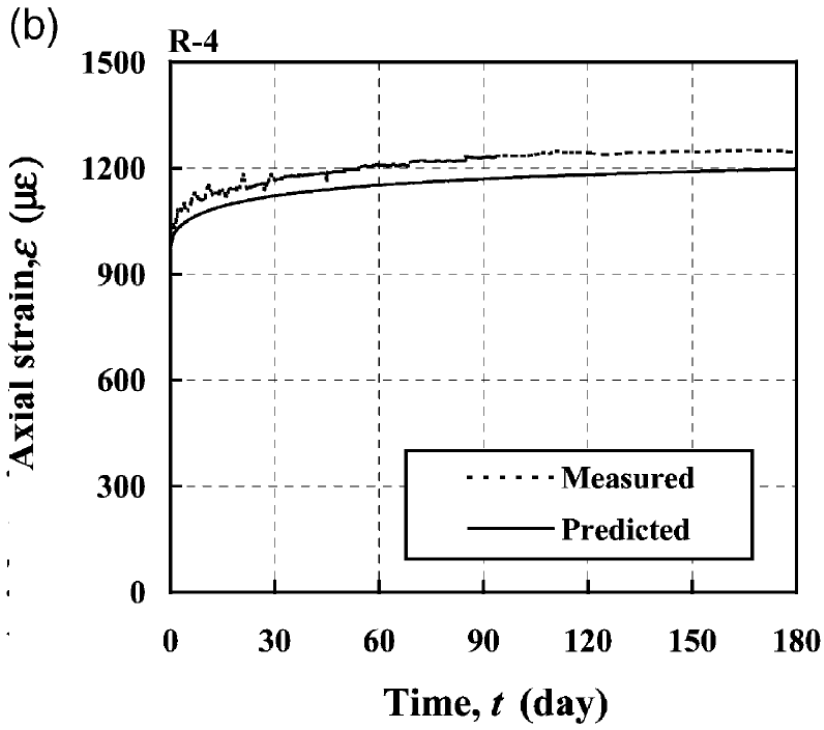
(b)
R-4
1500
1200
900
600
300
0
Axial strain,ε (με)
Measured
Predicted
0
30
60
90
120
150
180
Time, t (day)

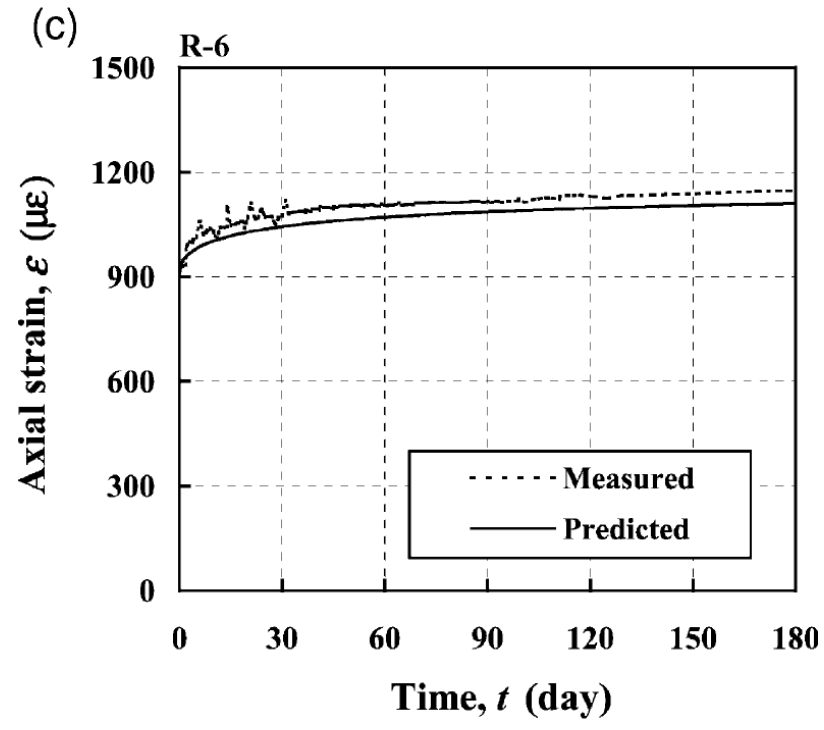
(c)
R-6
1500
1200
900
600
300
0
Axial strain, ε (με)
Measured
Predicted
0
30
60
90
120
150
180
Time, t (day)

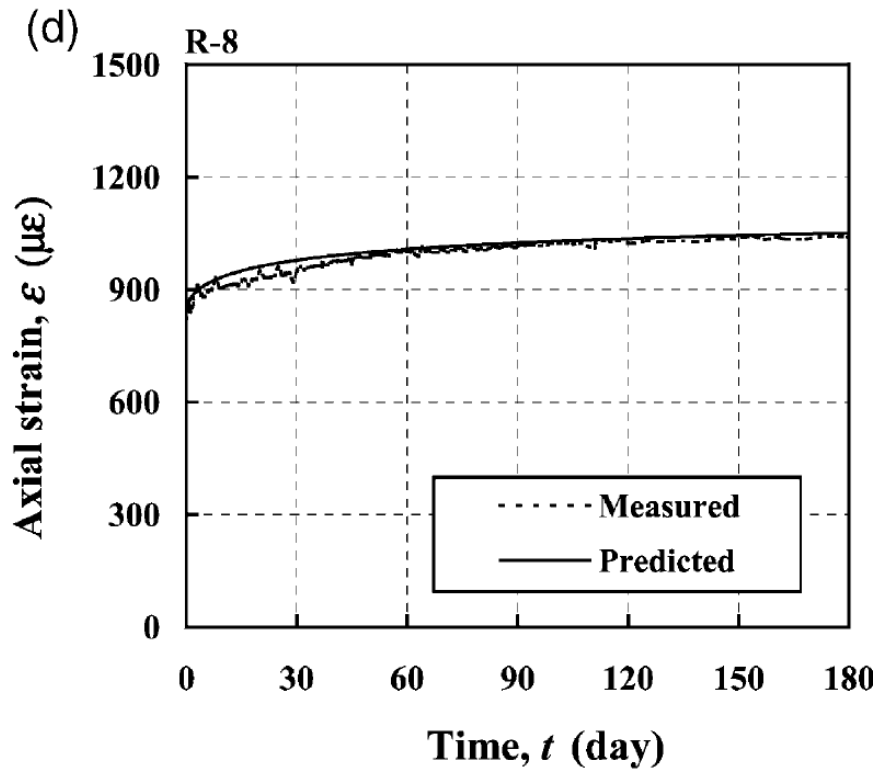

Figure 2.29. Measured time-history of the axial strain (ε) (Han & Yang, 2003)

2.1.6.5 Conclusions

From this research the following conclusions were made on creep of CFTs:

1. It was found that the creep process tends to stabilize after about 100 days of sustained loading.

2. The creep behavior of rectangular CFTs is similar to that of square CFTs.

2.1.7 Han, Tao, & Liu, 2004

Effects of Sustained Load on Concrete-Filled Hollow Structural Steel Columns

2.1.7.1 Research Objective

Han et al. conducted a similar research program as Han & Yang from the previous year, in which long-term strains of six square CFTs of two different cross sections were monitored for

approximately 120 days to examine the creep behavior of such columns. Also, the time-dependent behavior is predicted by means of a theoretical model developed for shrinkage and creep.

2.1.7.2 Specimens

The CFT specimens had a length of 600 mm and thickness of 2.93 mm. Three of the specimens had a 100 mm square cross-section and three had a 120 mm square cross-section. The load was applied uniformly and the concrete was assumed to develop same strain changes as the steel. Four specimens were left unloaded and monitored for 28 days shrinkage strains only. Rust and loose debris were removed from the insides of the tubes using a wire brush. After welding a square 25 mm thick plate on one end, the tube was filled with concrete and cured. A high-strength epoxy was then applied to the top of the specimens. All surfaces were ground flat and smooth using a grinding wheel with diamond cutters to ensure that the load would be equally distributed to the steel and the concrete. An identical plate was then welded to the other end.

2.1.7.3 Test setup

The sustained load was initially applied 28 days after concrete casting, by tightening the nuts of eight pre-stressing bars. The load was monitored by a load cell and kept constant by tightening the bars regularly. The value of the load and its intensity is shown for each specimen in Table 2.5. The creep rig setup is illustrated in Figure 2.30. The strain measurements were taken at mid-height of the steel tube by means of a deformation cell.

Table 2.5. Summary of test information (Han, Zhong, & Liu, 2004)

No.	Specimen	Section dimension D x t_s (mm)	L (mm)	Sustained load N_L (kN)	Load level n
1	S-1	□-100 x 2.93	600	-	-
2	S-1-L-1	□-100 x 2.93	600	360	0.62
3	S-1-L-2	□-100 x 2.93	600	360	0.62
4	S-2	□-120 x 2.93	600	-	-
5	S-2-L-1	□-120 x 2.93	600	470	0.62
6	S-2-L-2	□-120 x 2.93	600	470	0.62

$n = N_L/N_u$, where N_u is the calculated ultimate capacity of the specimen

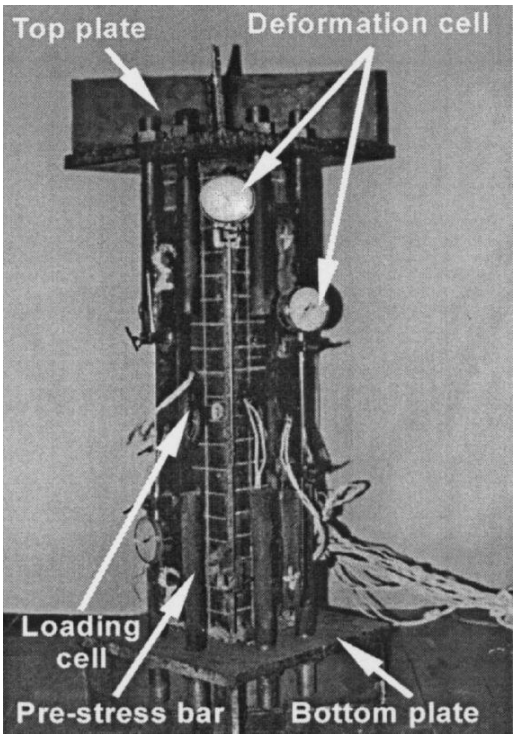

Figure 2.30. General view of the long-term service load tests (Han, Zhong, & Liu, 2004)

2.1.7.4 Experimental results

The authors offer no experimental results from the shrinkage specimens, but the paper states that shrinkage was determined to be negligible. It is also stated that the final shrinkage strain according to ACI 209 was estimated to be 42.7 με and 45.3 με for the 100 mm and 120 mm columns, respectively. The author does not report on variations in temperature and humidity, but states that these factors were almost constant during the whole year in the laboratory.

Figure 2.31 shows the total time-dependent strain for the loaded CFT specimens, plotted with a model that takes into account the initial elastic modulus of concrete, the change in load in the concrete resulting from creep, and the estimated final creep coefficient multiplied by an aging coefficient of concrete. This aging coefficient is a function of the estimated final creep coefficient only. The authors do not specify which specimen this figure refers to.

The author reports these estimated values to be 0.836 and 0.802 for the 100 mm and 120 mm columns, respectively but limited results and discussions are provided on the creep experiments.

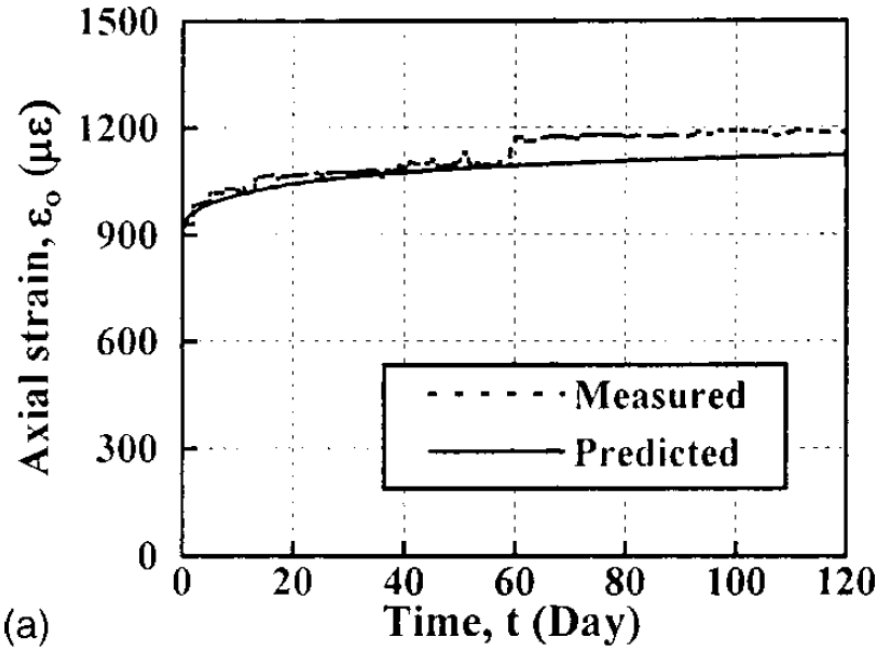
1500
1200
900
600
300
0
Axial strain, ε_o ($\mu\varepsilon$)
Measured
Predicted
0
20
40
60
80
100
120
Time, t (Day)

(a)

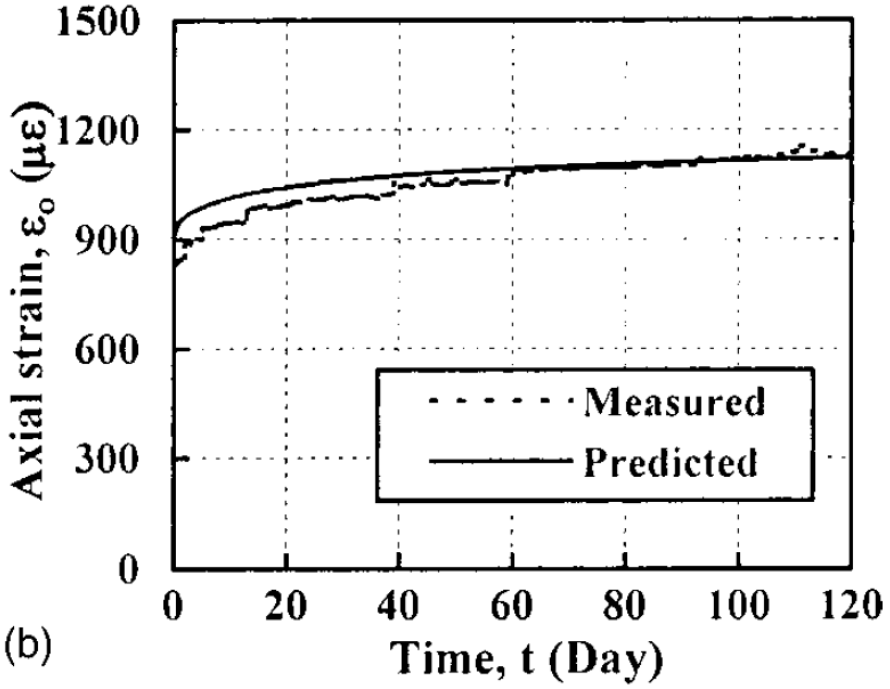
1500
1200
900
600
300
0
Axial strain, ε_o ($\mu\varepsilon$)
Measured
Predicted
0
20
40
60
80
100
120
Time, t (Day)

(b)

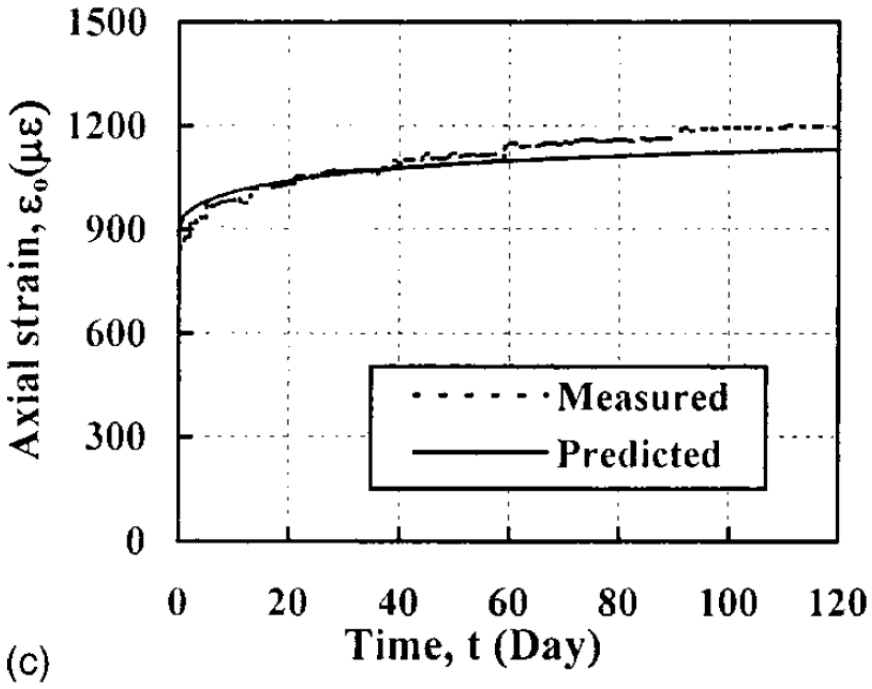

(c)

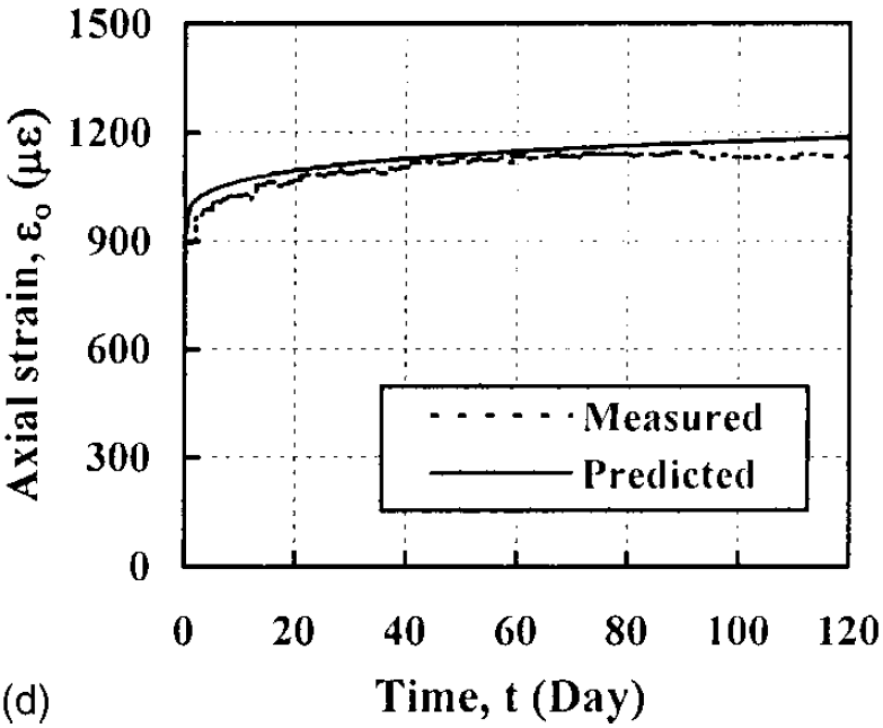

(d)

Figure 2.31. Tested time-history of axial strain (ε0) (Han, Zhong, & Liu, 2004)

2.1.7.5 Conclusions

From this research the following conclusions were made:

1. It was found that the creep process tends to stabilize after about 100 days of sustained loading.

2. The behavior of square CFTs is similar to that of rectangular CFTs.

2.1.8 Yang, Han, & Wu, 2008

Concrete Shrinkage and Creep in Recycled Aggregate Concrete-Filled Steel Tubes.

2.1.8.1 Research Objective

Yang, et al. evaluated the differences of the long-term behavior of concrete-filled tubes with Recycled Aggregate Concrete (RACFT) and conventional concrete (CFST), based on about 500 days of experimental testing of such columns. The responses for both types were predicted based on the ACI committee 209 models (ACI Committee 209, 2008), which are discussed in Chapter 5. Also, predictive models for the shrinkage, creep, and creep coefficient of the concrete core in concrete-filled tubes were suggested.

2.1.8.2 Specimens

Eight RACFST specimens and four corresponding normal CFT specimens of similar length and cross-sectional area were constructed. The steel tubes for the specimens were all cut from long cold-formed HSS columns, and the ends were machined to the desired length. Six of the specimens were circular, the other six were rectangular. The insides of the tubes were wire brushed to remove rust and loose debris. Grease and oil, if any, were cleaned from the inside surface of all specimens. A 16 mm thick steel plate was welded to both ends of each specimen. Table 2.6 and Table 2.7 summarize the shrinkage and creep specimens, respectively.

Table 2.6. Summary of specimens for shrinkage tests (Yang, Han, & Wu, 2008)

Sectional Type	No.	Specimen Label	D x t_s (mm)	L (mm)	$\varepsilon_{sh,u}$ ($\mu\varepsilon$)
Circular	1	C0	114 x 2.19	1140	115.5
	2	C1	114 x 2.19	1140	122.1
Square	3	S0	100 x 1.94	1155	108.7
	4	S1	100 x 1.94	1155	132.4

$\varepsilon_{sh,u}$ = Predicted final value of shrinkage strain
C0 and S0 are CFT specimens, C1 and S1 are RACFT specimens

Table 2.7. Summary of specimens for creep tests (Yang, Han, & Wu, 2008)

Sectional type	No.	Specimen Label	D x t_s (mm)	L (mm)	N_L (kN)	n
Circular	1	ccfst	114 x 2.19	1140	302.9	0.6
	2	cracfst-r	114 x 2.19	1140	-	-
	3	cracfst-1	114 x 2.19	1140	160.7	0.3
	4	cracfst-2	114 x 2.19	1140	321.4	0.6
Square	5	scfst	100 x 1.94	1155	299.1	0.6
	6	sracfst-r	100 x 1.94	1155	-	-
	7	sracfst-1	100 x 1.94	1155	158.9	0.3
	8	sracfst-2	100 x 1.94	1155	317.8	0.6

N_L = sustained axial force
$n = N_L/N_u$, where N_u is the calculated ultimate capacity of the specimen

2.1.8.3 Test setup

For the shrinkage tests, a rigid frame made of four rigid steel bars was designed. Two horizontal 10-mm diameter bars were embedded in the concrete through two circular holes that were drilled into the steel tubes near the top and near the bottom. Two sets were made that consisted of a deformation transducer attached to a vertical bar. The vertical bars were then attached to the bottom horizontal bars by welding and to the top horizontal bar with an adjustable nut. The shrinkage strain of concrete is then the mean value of the two values obtained from the deformation transducers divided by the standard gauge length, which was 900 mm for all specimens. The shrinkage test setup is shown in Figure 2.32. Strain measurements were taken daily to begin with, starting three days after concrete casting. This time interval was gradually reduced in accordance with decreasing shrinkage rate of the specimens.

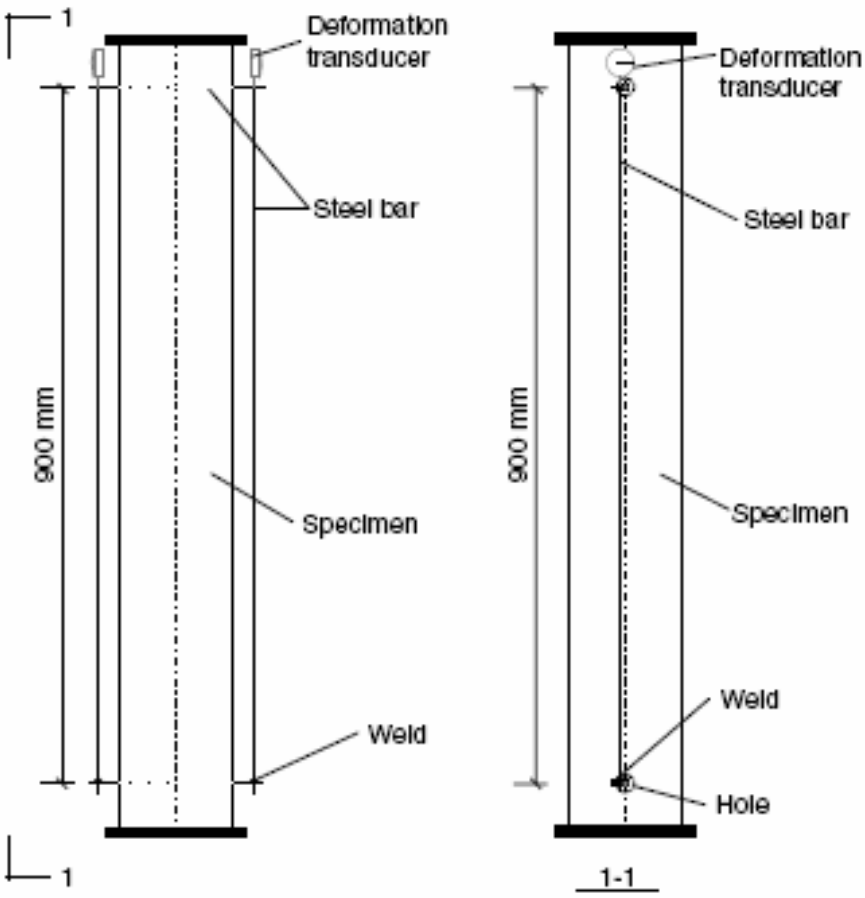

Figure 2.32. A schematic view of the shrinkage test set up (Yang, Han, & Wu, 2008)

Four RACFT columns and two normal CFT columns were placed in a creep rig 28 days after concrete casting and subject to sustained axial loading. The creep experiment was performed in the same laboratory as the shrinkage test to ensure the effect of environmental conditions would be minimal. Figure 2.32 shows a general view of the experimental setup. The sustained load was applied by post-tensioning the four steel bars of the rig; the load was monitored with a load cell. The load was kept as maintained by re-stressing these bars regularly throughout the duration of the test. Strain was measured on the mid-height of the column with four strain gauges spaced with 90° angles on the surface of the steel tube. Two displacement transducers were also attached a similar fashion as with the shrinkage specimens.

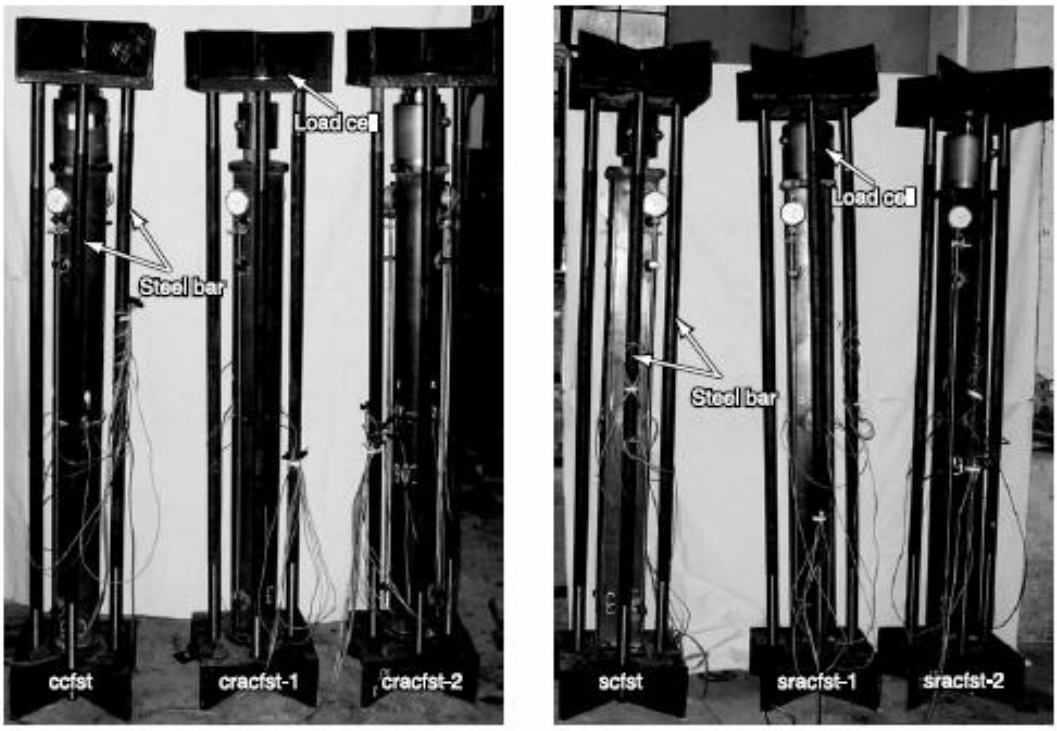

Figure 2.33. A general view of the long-term service load tests (Yang, Han, & Wu, 2008)

2.1.8.4 Experimental results

The time-dependent strain of the shrinkage specimens is shown in Figure 2.34. The figure suggests that the concrete shrinkage strain is similar for the RACFST and reference normal CFST specimen, but square sections show a bit more difference then circular sections. At the end of the test, the shrinkage strain of circular and square RACFST is about 6% and 22% higher than that of CFST with conventional concrete, respectively. The predicted curve of ACI committee 209 is shown to be significantly higher than the experimental results.

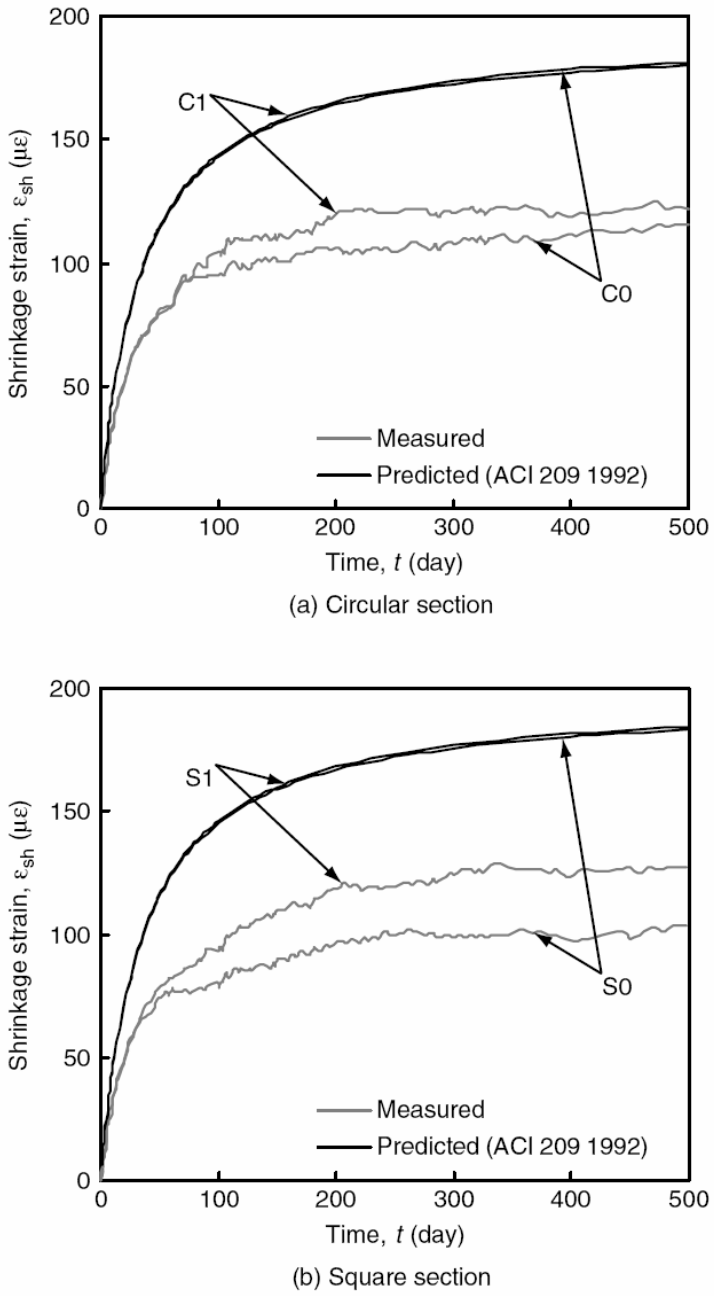

Figure 2.34. Time-history of the shrinkage strain (ε_{sh}) (Yang, Han, & Wu, 2008)

Figure 2.35 shows the creep strains of the loaded specimens. The predicted final creep coefficients of all specimens are given in Table 2.8, where the initial strains (ε_o) are the elastic strains measured immediately after initial loading. Figure 2.35 and Table 2.8 show that the creep strains of RACFST specimens are higher than those of the reference CFST specimens for the

same intensity of loading (n = 0.6). Circular and square RACFST specimens displayed about 23% and 22% higher creep strains than the reference normal CFST specimens, respectively. Examining the total axial strain measured in the RACFST columns indicates that the deformation process seemed to stabilize after approximately 200 days. However, the reference normal CFST columns seemed to be stabilizing sooner, or about 100 days after initial loading.

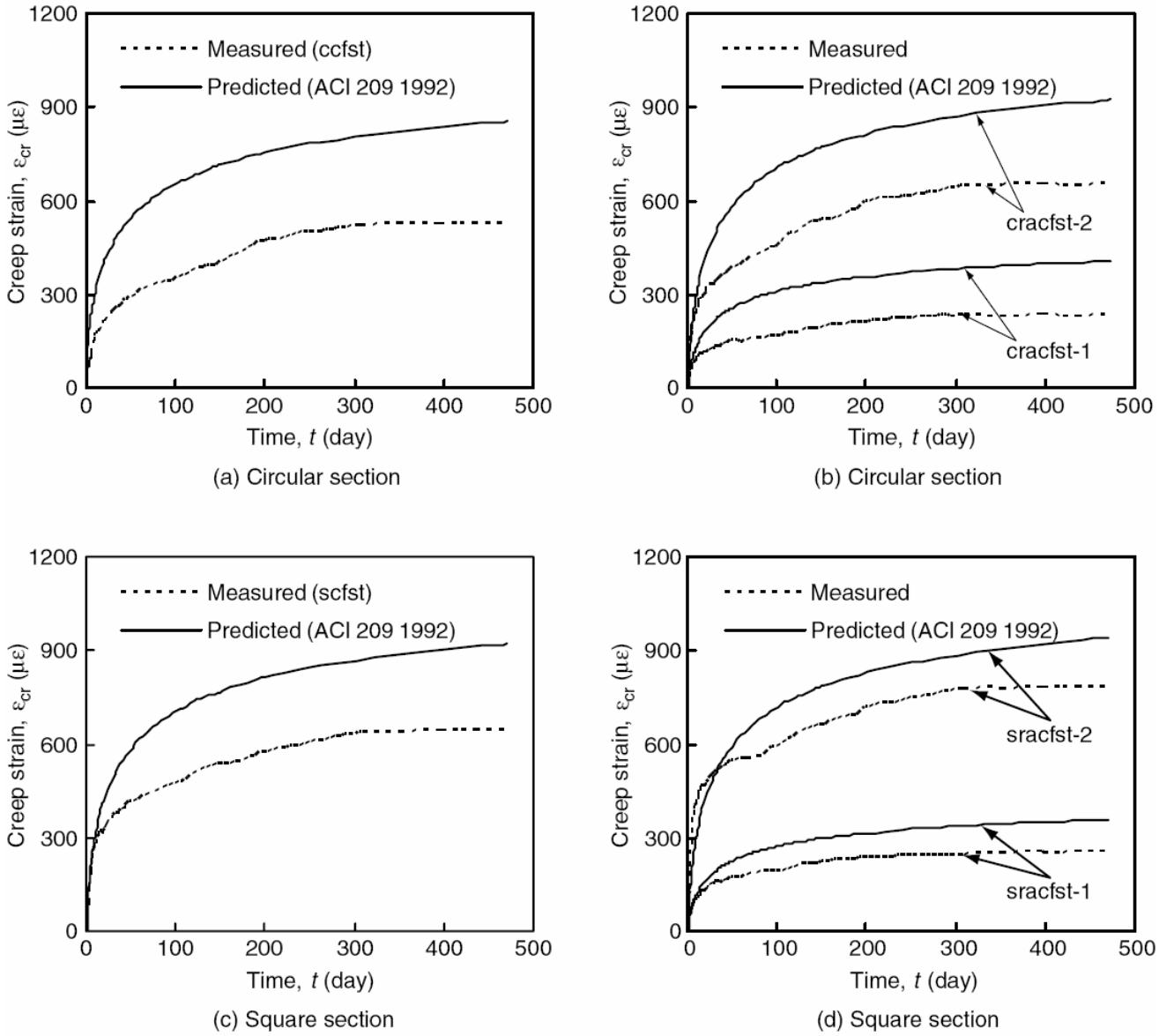

Figure 2.35. Time-history of the creep strain (ε_{cr}) (Yang, Han, & Wu, 2008)

Table 2.8 also demonstrates that the creep coefficient of RACFST specimens is about 30% higher than the value for the reference normal CFST specimens. In all cases, predicted results of ACI committee 209 are higher than the experimental results suggest.

Table 2.8. Creep coefficients of normal CFST and RACFST specimens (Yang, Han, & Wu, 2008)

Sectional type	Circular			Square		
Specimen label	ccfst	cracfst-1	cracfst-2	scfst	sracfst-1	sracfst-2
Long-term sustained load level	0.6	0.3	0.6	0.6	0.3	0.6
Initial strain ε_o (x 10^{-6})	885.5	306	885.5	968.5	332	960
Creep strain $\varepsilon_{cr,u}$ (x 10^{-6})	529.9	232.5	653.1	638.9	250.7	779.6
Creep coefficient $\varepsilon_{cr,u} / \varepsilon_o$	0.60	0.76	0.74	0.66	0.76	0.81

$\varepsilon_{cr,u} = \varepsilon_{final} - \varepsilon_0 - \varepsilon_{shrinkage}$

Figure 2.36 and Figure 2.37 show the experimental results of the concrete shrinkage strains and creep coefficients of the CFTs, respectively, plotted with the calibrated ACI Committee 209 (1992) models for shrinkage and creep. The calibration lead to values of total final shrinkage strain and final creep coefficient of RACFST that were 1.2 and 1.3 times of those of the reference normal CFST, respectively. The total final shrinkage strain was assumed to be 120 με and the final creep coefficient was set as 0.77 for normal CFST.

The temperature ranged between 10°C and 26°C, and the relative humidity was about 75% in the laboratory. The temperature changes are not taken into account in the results, but are evident through fluctuations in the time-dependent curves.

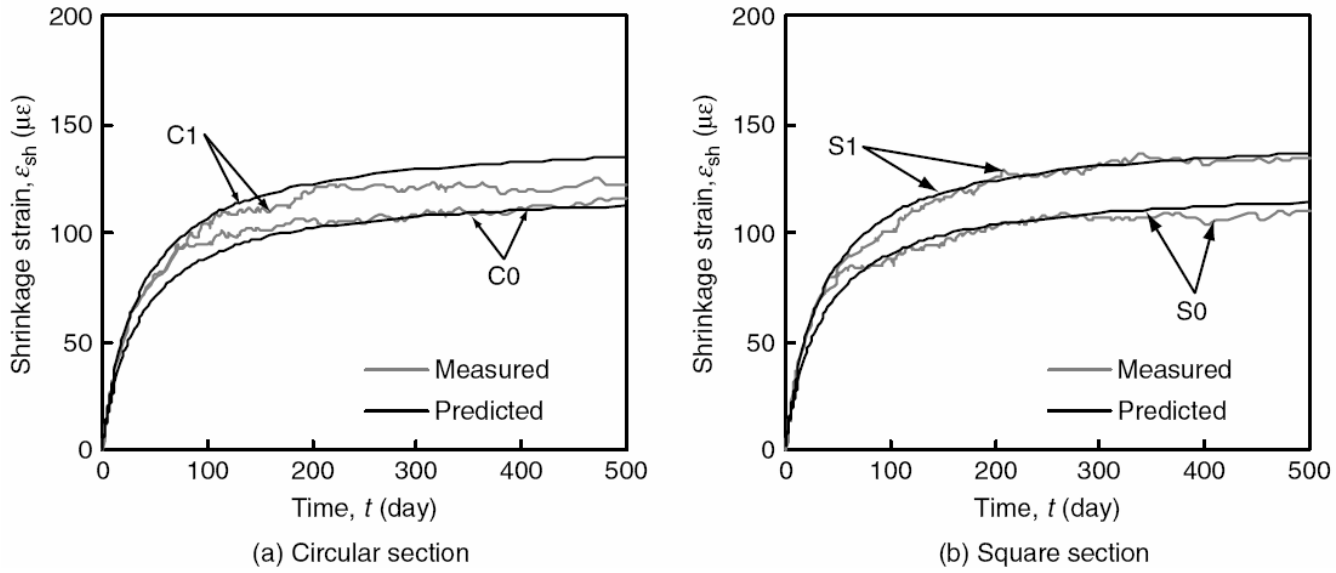

Figure 2.36. Comparisons of shrinkage strain for composite columns (Yang, Han, & Wu, 2008)

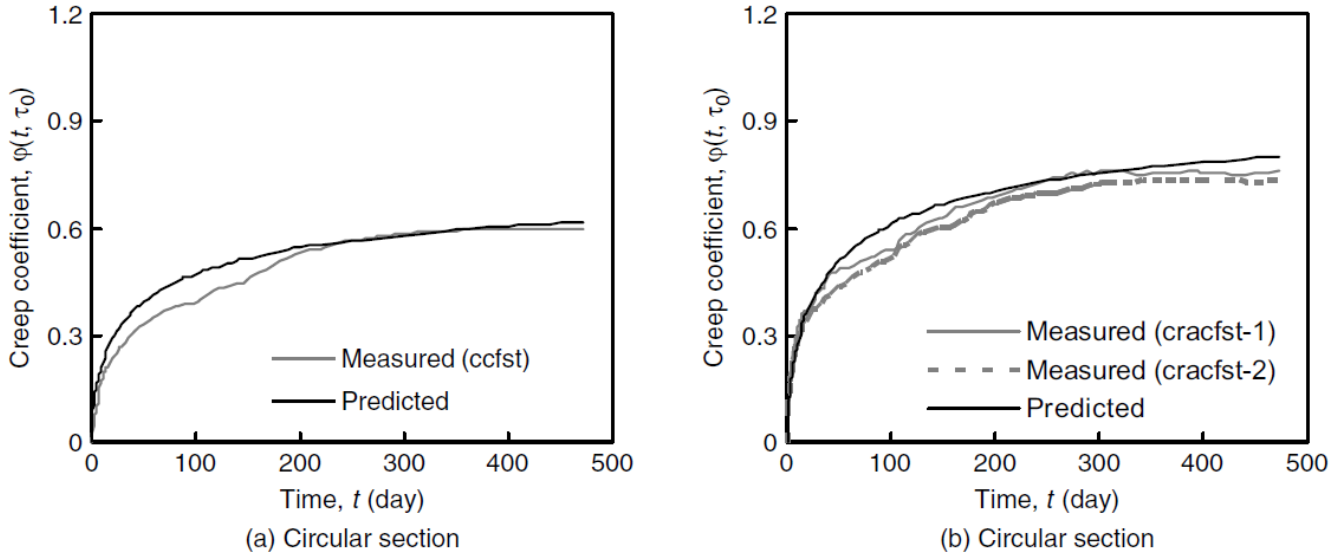

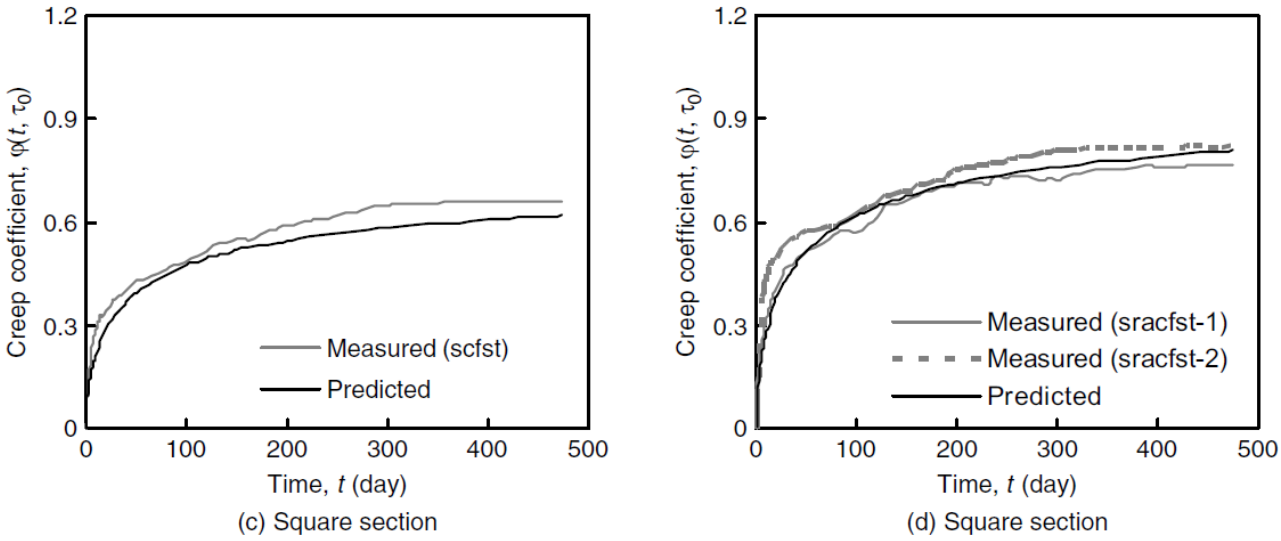

Figure 2.37. Comparisons of creep coefficient for composite columns (Yang, Han, & Wu, 2008)

2.1.8.5 Conclusions

From this research the following conclusions were made:

1. The concrete creep and shrinkage deformation behavior of RACFST is comparable to that of the reference normal CFST, so same prediction curves can be used.

2. The concrete shrinkage and creep strains in the RACFST specimens range from being 6% to 23% higher than the values obtained for the reference normal CFST specimens.

3. Good predictions of creep and shrinkage behavior of RACFST and normal CFST columns can be accomplished by the ACI committee 209 models for creep and shrinkage if they are calibrated with the suggested values of the total final shrinkage strain and final creep coefficient.

2.1.9 Zhou, Cao, He, & Liu, 2009

Study on Long-Term behavior and Ultimate Strength of CFST Columns

2.1.9.1 Research objective

Zhou, et al. studied three types of columns, including plain concrete (PC) columns, reinforced concrete (RC) columns and concrete-filled steel tube (CFST) columns. The shrinkage and creep performance and the ultimate strength of the columns were measured for more than two years and then analyzed. These factors were observed with respect to concrete age at initial loading and reinforcement ratio of CFST columns and RC columns.

2.1.9.2 Specimens

Thirteen circular short column specimens were constructed, including six PC columns, three RC columns, and four CFST columns. All specimens were 150 mm in diameter, with an L/D ratio of 4. The thickness of the steel tubes was 0.8 mm. Eight specimens were subject to sustained loading, and five specimens were monitored for shrinkage strains only. The basic parameters of specimens are given in Table 2.9. The mixing amount of expansion agent in the concrete was 6% and the reinforcement ratio in the RC columns is 1.49%.

2.1.9.3 Test setup

All creep specimens were subject to a sustained load in a conventional creep rig. The creep test setup is shown in Figure 2.38, which shows a steel rig with a hydraulic jack and a load cell in each rig. Embedded strain gauges for long-term tests were placed in specimens 1, 4, 11, and 13. All specimens were kept under the same environmental conditions. The temperature ranged from -1.2 to 39.4°C for the duration of the test, and the relative humidity ranged from 37% to 87%.

Table 2.9. Basic parameters of specimens (Zhou, Cao, He, & Liu, 2009)

Group	Specimen #	Specimen type	Age at loading (days)	Loading duration (days)	Initial stress (Mpa)	Expansion agent?
I	1	PC	14	864	11.6	no
	2		28	850	11.6	no
	*3		Monitoring started after 7 days			no
II	4	RC	14	864	11.6	no
	5		28	850	11.6	no
	*6		Monitoring started after 7 days			no
III	7	PC	7	846	10.5	no
	8					yes
	*9		Monitoring started after 7 days			yes
IV	10	CFST	7	846	10.5	no
	11					yes
	*12		Monitoring started after 7 days			no
	*13					yes

* shrinkage specimens

Figure 2.38. Loading device for creep test (Zhou, Cao, He, & Liu, 2009)

2.1.9.4 Experimental results

Figure 2.39 shows that the shrinkage strain of RC column #6 is about 88% of that of PC column #3. The two columns show very similar rate of shrinkage. For the PC column, the percentage of predicted final shrinkage strain completed in 1 month, 2 months, 3 months, 6 months, and 1 year was about 53%, 71%, 80%, 91%, 97%, respectively.

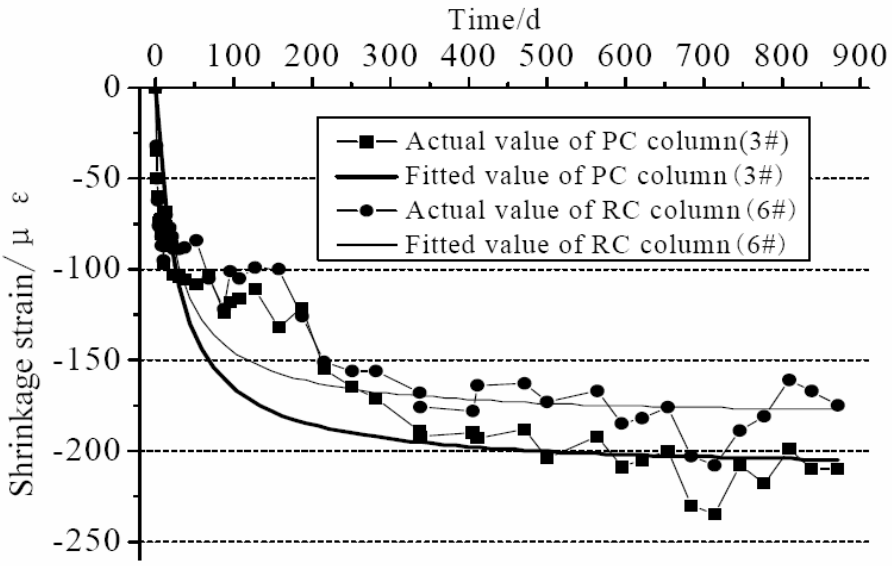

Figure 2.39. Shrinkage strain comparison of 3# and 6# columns (Zhou, Cao, He, & Liu, 2009)

Figure **2.40** shows the shrinkage strain of CFT column #13. The final shrinkage strain is about 35% of that of PC column #9. Concrete curing is different when it is encased in a steel tube. The tube hinders moisture loss, causing the small shrinkage deformation of the concrete of the CFT. Shrinkage of both columns develops quickly in earlier curing period, which contributes to the long-term stability.

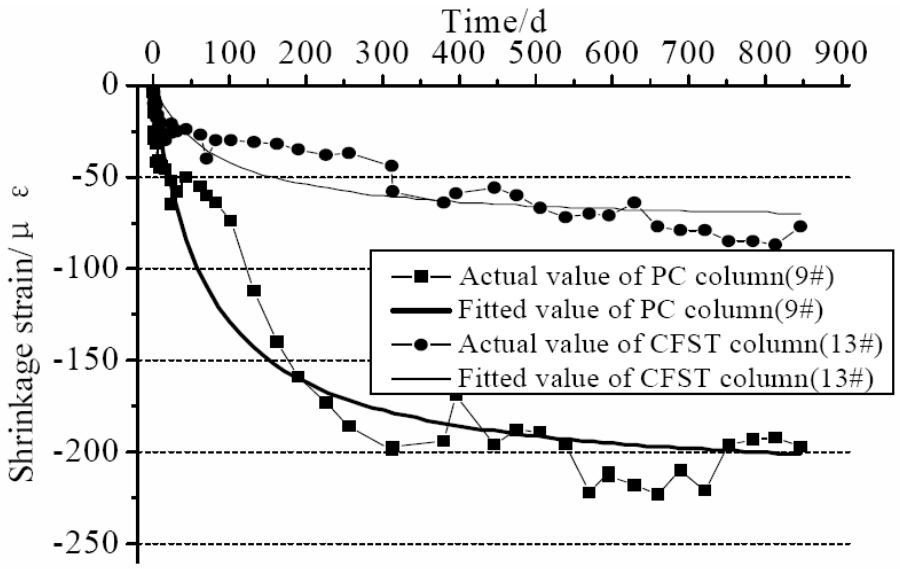

Figure 2.40. Shrinkage strain comparison of 9# and 13# columns (Zhou, Cao, He, & Liu, 2009)

Figure 2.41 shows that the creep curve of a PC column has similar changes in rate of creep for different times that pass between casting and initial loading. The shorter this time is, the greater the creep will be. Creep coefficient of the specimen loaded on the seventh day is about 20% higher that of the 14-day specimen and about 56% higher than the 28-day specimen.

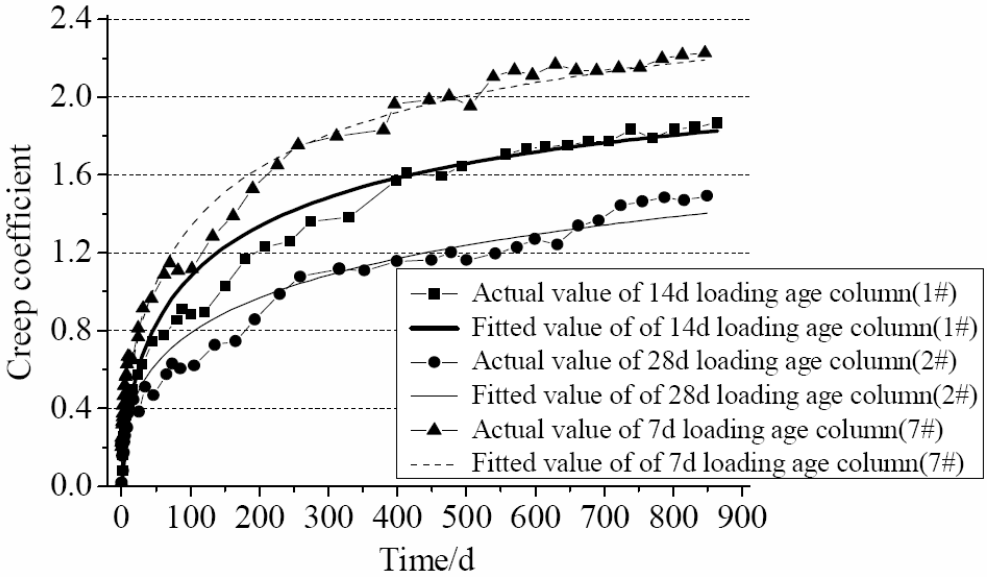

Figure 2.41. Effect of loading age on creep coefficient (Zhou, Cao, He, & Liu, 2009)

Figure 2.42 shows the significant effect that reinforcement has on creep deformation of concrete columns. Creep coefficient of the 14-day RC column is about 35% less than that of the PC column loaded at 14 days. This value is about 24% for the 28-day specimens.

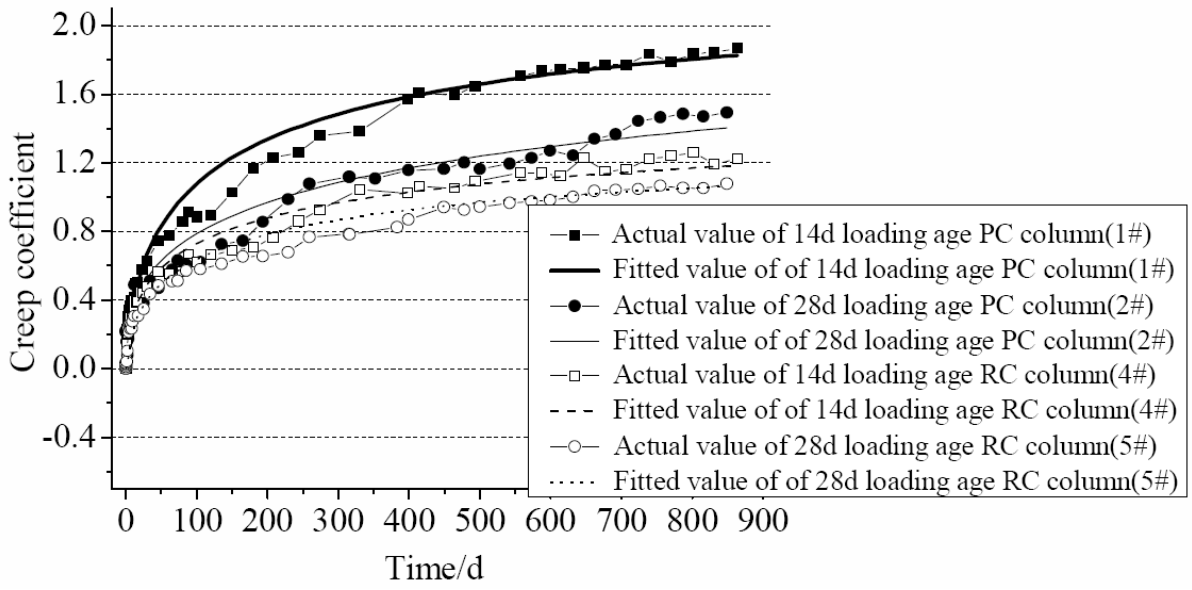

Figure 2.42. Effect of reinforcement on creep coefficient (Zhou, Cao, He, & Liu, 2009)

2.1.9.5 Conclusions

From this research the following conclusions were made

1. There is little difference in shrinkage strains between RC and PC columns. However, shrinkage in CFT columns is drastically lower than that of both RC and PC columns. The final value of shrinkage strain in CFST columns was about 80 microstrain.

2. The loading age has a quite large impact on the creep coefficient of PC columns but no data is presented for the RC and the CFT columns.

3. Reinforcement reduces the creep deformation of concrete columns.
4. The author claims that the creep coefficient of steel pipe surface is larger than that of inner concrete for CFST column, although the paper shows no evidence thereof.

2.1.10 Wang, Geng, Ranzi & Zhang, 2011

Time-dependent behaviour of expansive concrete-filled steel tubular columns

2.1.10.1 Research objective

Wang, et al. conducted a creep test of eleven concrete-filled steel tubes (ECFST) with expansive additive. The authors studied the impact of sustained axial loads, but shrinkage strain was assumed to be negligible. The specimens were loaded at early concrete ages to reflect construction site practice. The test lasted for approximately 150 days and the results were compared with four different existing creep models. The use of these models is based on the assumption that the magnitude of the creep strain increases linearly with the ratio between applied stress and ultimate compressive strength, which means that the creep coefficient is independent of the loading. The effect of a high axial load on creep was examined by subjecting identical specimens, loaded at approximately 28 days, to stress levels in the concrete core varying from 38% to 68% of compressive strength of cylinders measured at 28 days.

2.1.10.2 Specimens

The steel tubes were cut in 420 mm sections from one single 6 m long cold rolled circular tube with an outer diameter of 140 mm and a wall thickness of 2.6 mm. After welding a 160x160x10 mm plate on one end, the tube was filled with concrete and cured for one day. The surface of the specimens was ground plane and smooth. This was done to distribute the load equally to the steel and the concrete. An identical plate was then welded to the other end. Expansive additive was used in the concrete to minimize the shrinkage of the concrete. The specimens were divided into seven groups, based on loading age and sustained load level, as can be seen in Table 2.10.

Table 2.10. Details of the tested ECFST specimens (Wang, Geng, Ranzi, & Zhang, 2011)

Specimen	N_L (kN)	t_0 (days)	n_L	n_c (t_0)
I-1	303	5	0.38	0.52
I-2	303	5	0.38	0.52
II-1	304	7	0.38	0.61
II-2	304	7	0.38	0.61
III	290	27	0.33	0.38
IV	290	27	0.36	0.45
V	441	30	0.50	0.58
VI	441	30	0.55	0.68
VII-1	515	29	0.58	0.68
VII-2	515	29	0.58	0.68
VIII	0	-	0	0

N_L = sustained axial force
t_0 = concrete age initial of loading
$n_L = N_L/N_u$, where N_u is the calculated ultimate capacity of the specimen at 28 days
$n_C\ (t_0) = \sigma_c(t_0)/f_{cm}(t_0)$, where $\sigma_c(t_0)$ denotes the initial concrete stress of the time of first loading and $f_{cm}(t_0)$ defines the corresponding mean cylinder compression strength.

2.1.10.3 Test setup

Details and dimensions of the creep rig are shown in Figure 2.43. The sustained load was applied through prestressing bars. The nuts were screwed simultaneously to achieve the design load, and then tightened at given intervals to avoid reduction in load due to creep. At initial loading, the tensile force in each prestressing bar was obtained by electrical resistance strain gauges. The long-term loading was monitored with a dial gauge attached to the exterior surface of a steel plate. The gauge length was 200 mm. This arrangement is shown in Figure 2.43 (b). The initial elastic strain of the specimens was measured using two strain gauges and the time-dependent strain was monitored through two dial gauges. The four gauges were placed at 90° intervals at mid-height of the specimens as shown in Figure 2.44. These dial gauges also had a length of 200 mm.

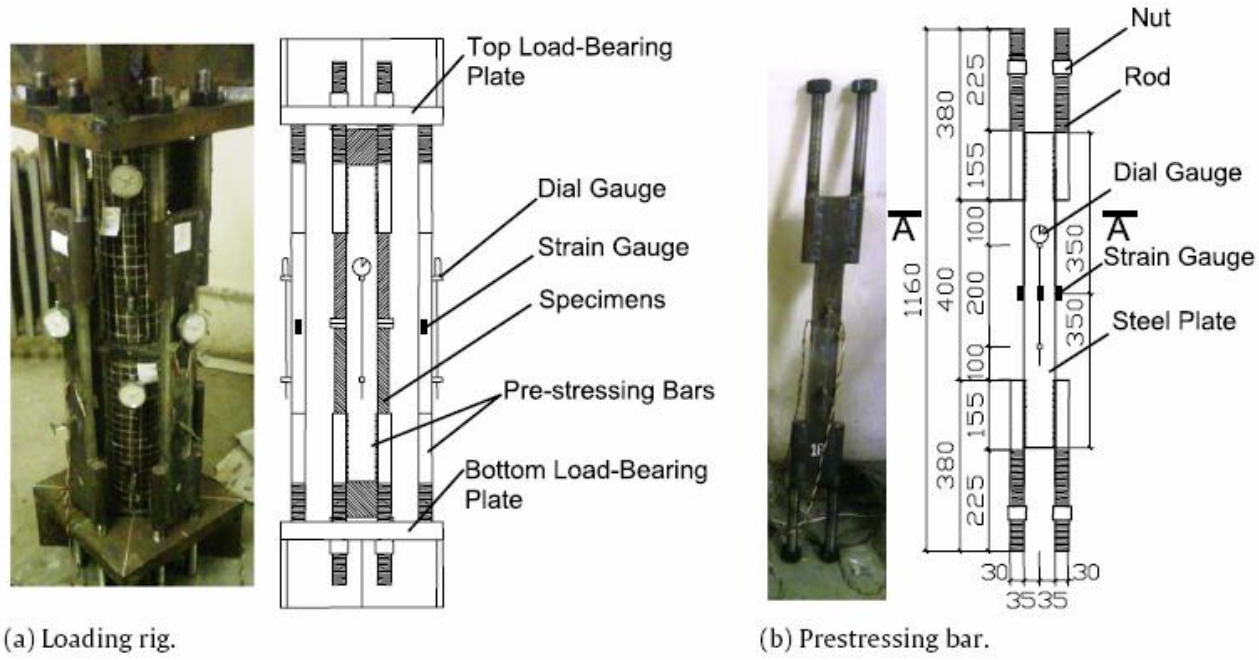

Figure 2.43. Testing set up (Wang, Geng, Ranzi, & Zhang, 2011)

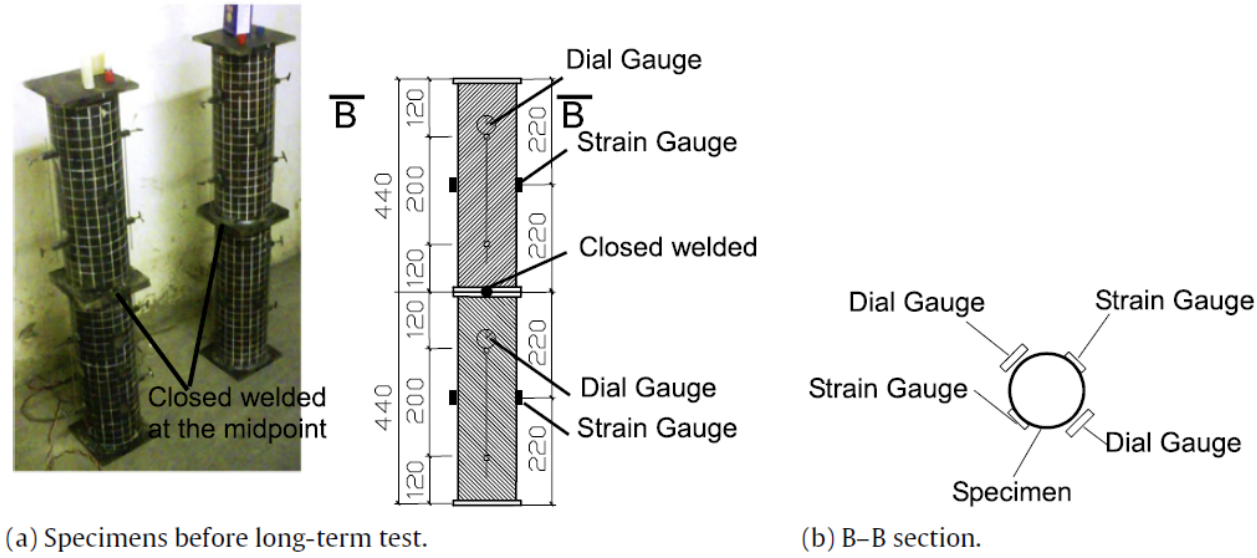

Figure 2.44. Instrumentation layout for the long-term test on ECFST specimens (Wang, Geng, Ranzi, & Zhang, 2011)

2.1.10.4 Experimental results

The rate of creep was high in the first few weeks of the test and then started to decrease, as shown in Figure 2.45. In one month, the time-dependent strains were about 60% of those recorded at the end of the experiment, and 80% after 50 days. The experimental results were compared with four existing creep models.

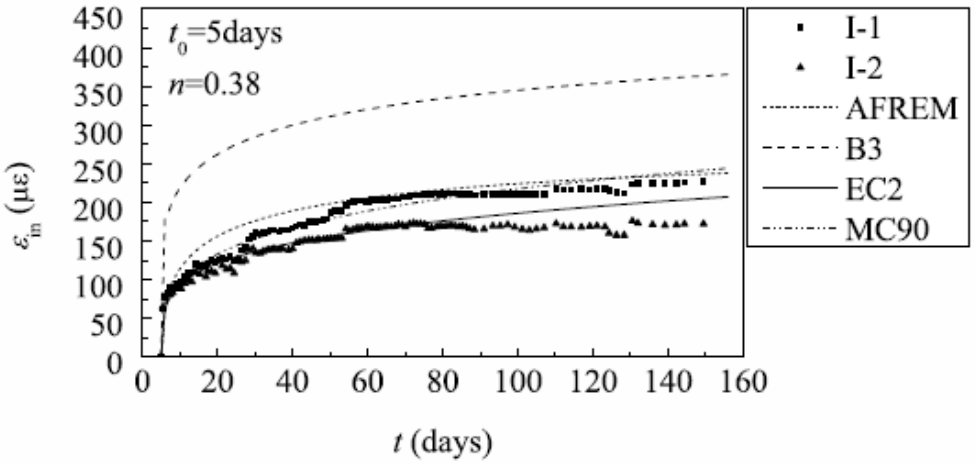

(a) Group I.

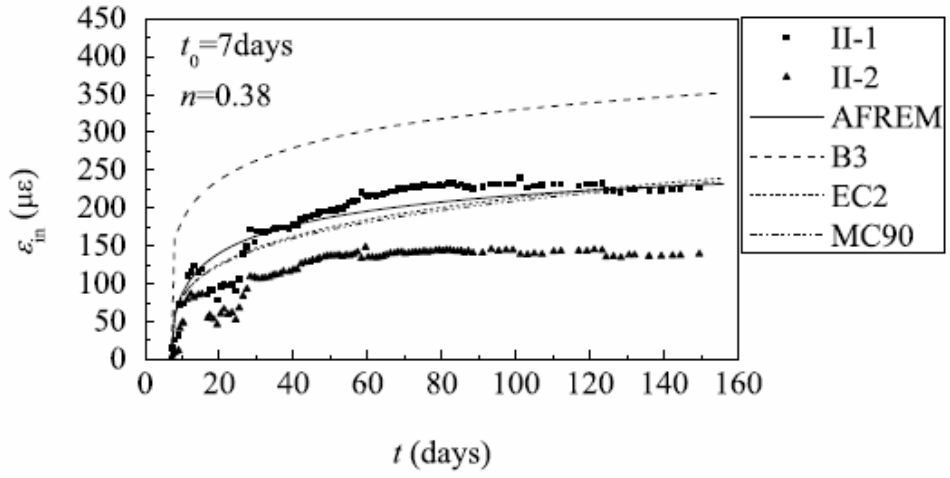

(b) Group II.

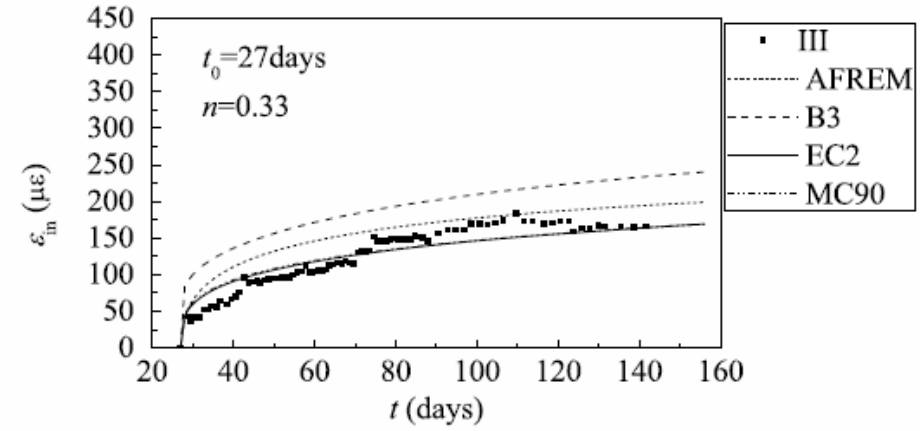

(c) Group III.

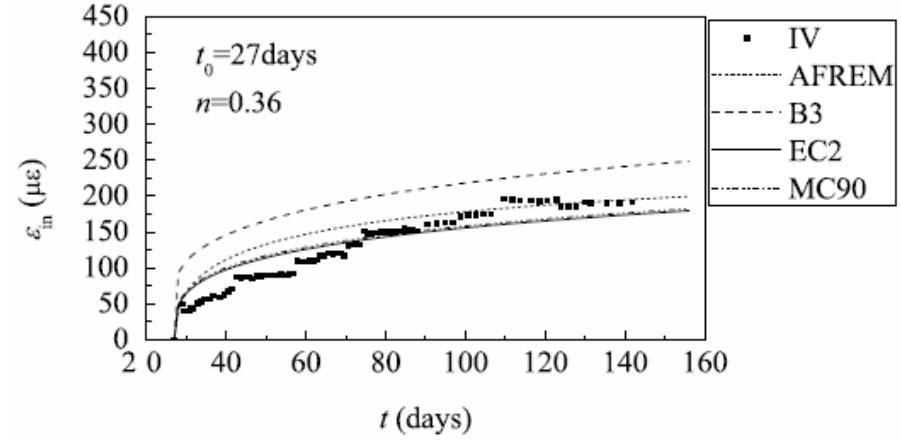

(d) Group IV.

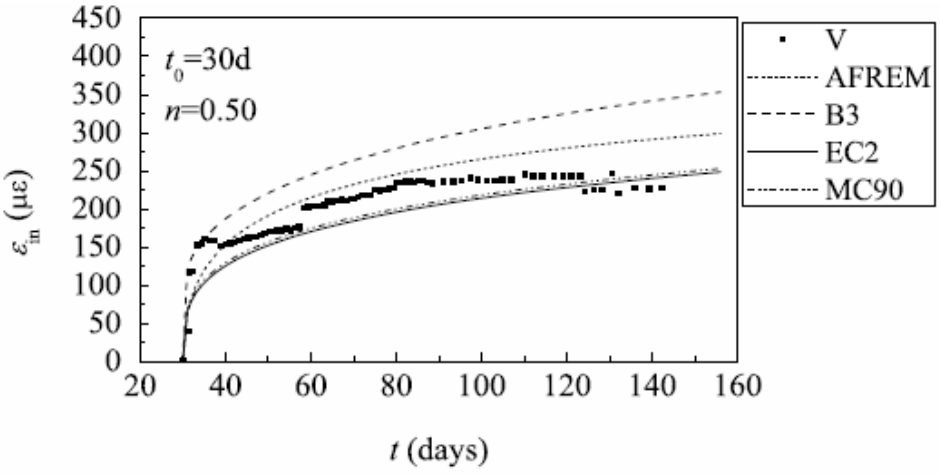

(e) Group V.

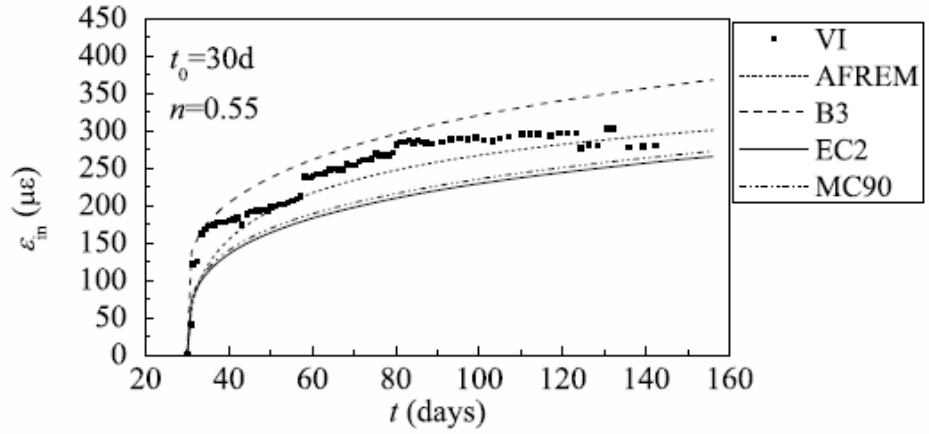

(f) Group VI.

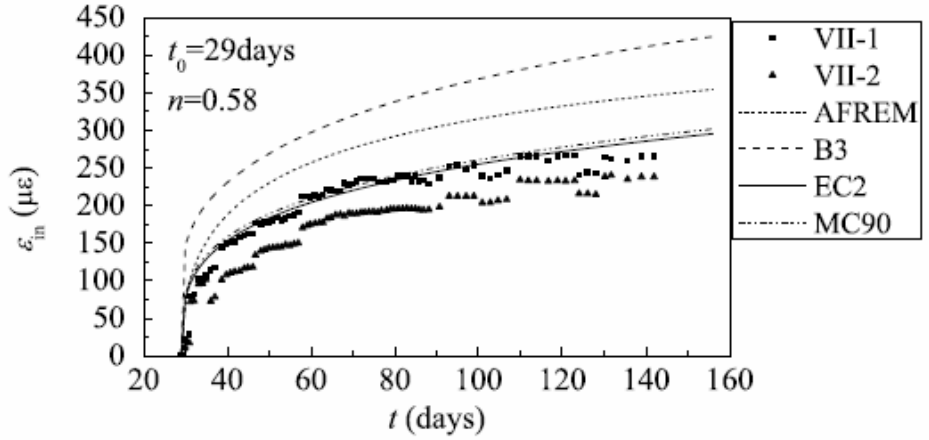

(g) Group VII.

Figure 2.45. Long-term deformations measured during the long-term tests and comparisons with calculated predictions (Wang, Geng, Ranzi, & Zhang, 2011)

The deformation of the specimens loaded at an earlier concrete age increased faster and reached a higher final value than companion specimens first loaded at a later time, as can be seen in Figure 2.46. The figure shows the final creep strains of the 5-day, 7-day and 27-day specimens, which were subject to approximately the same stress level. It indicates that the creep coefficient increases as the concrete is loaded sooner, as is assumed in most creep models.

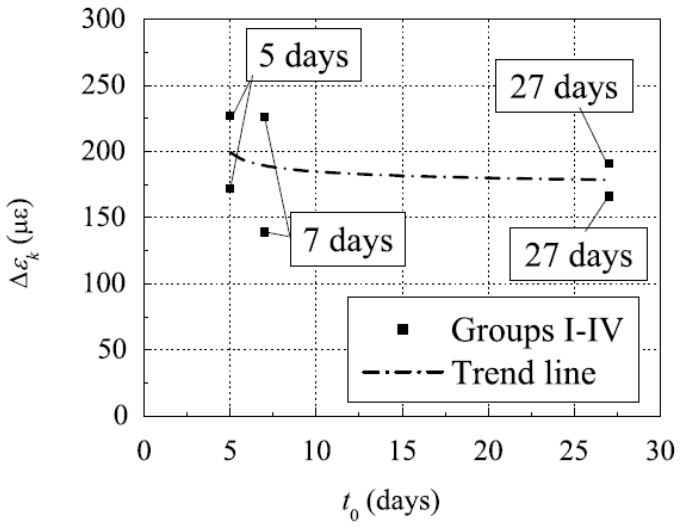

Figure 2.46. Variation of the incremental deformations as a function of the instant of first loading (t_0) (Wang, Geng, Ranzi, & Zhang, 2011)

The creep coefficient, shown in Table 2.11, provides an effective estimate of the time effect on the strain and stress distribution of ECFST specimens. As can be seen in the table, strain of expansive concrete encased in a steel tube increased 31% to 44% during the five months since initial loading, due to creep of the concrete. This is a change that cannot be neglected and should be considered in design.

Table 2.11. Long-term deformations measured after 5 months for specimens loaded at 28 days (Wang, Geng, Ranzi, & Zhang, 2011)

Specimen	III	IV	V	VI	VII-1	VII-2
ε_e	434	522	691	774	860	764
ε_{in}	191	166	227	280	265	238
$\varepsilon_{in}/\varepsilon_e$	0.439	0.318	0.328	0.361	0.308	0.311

ε_e = initial elastic strain of specimen
ε_{in} = incremental time-dependent strain of specimen after 5 months of constant loading
$\varepsilon_{in}/\varepsilon_e$ = creep coefficient after five months of loading

2.1.10.5 Conclusions

From this research the following conclusions were made

1. Experimental results showed that the assumption of creep strain increasing linearly as a function of applied load may be valid to ECFST with concrete stresses up to 80% of its compressive strength, rather than the normally accepted limit of 40-50%.

2. Four available models to predict the long-term response of the specimens were evaluated, i.e. EC2, MC 90, AFREM, and B3. The use of the EC2 and AFREM models was recommended for ECFST specimens loaded within 28 days of casting. The B3 model overestimated the deflections in all cases.

2.2 Summary

Most of the experiments show a fast increase in creep strain shortly after loading. The rate seems to decrease after about 60 days, and in one year more than 90% of the creep strains have been developed. Many factors influence the magnitude and rate of creep of CFT members, such as the age of concrete at initial loading, concrete mixture, shape of the cross section, steel-to-concrete ratio, and the ratio of stress to ultimate strength capacity. Results have also showed that the creep coefficient of CFT columns is less than half of that of concrete columns. (Ichinose et al., 2001; Terrey et al., 1994). Shrinkage strain is shown to be negligible in CFTs in most research programs, proving to be as low as 9% of the shrinkage strains of plain concrete columns. (Ichinose et al., 2001).

As can be seen, limited research has been conducted on creep and shrinkage of concrete-filled tubes and none on such members containing SCM concrete. The main focus of most of the prior research programs has been to compare long-time deformations of CFTs to those of regular concrete members and calibrate existing models to fit the experimental data obtained. Some programs have attempted to model the creep behavior based on steel ratio, load level, initial age of concrete, reduction in elastic modulus (AEMM), aging coefficient of concrete, and Kelvin model with experimentally evaluated parameters. This analytical work is not covered in this chapter. Most programs have applied load uniformly to the steel and the concrete, in which case

perfect strain compatibility can be assumed. The case of loading through the concrete core is much more complex, where slip between the steel and the concrete causes incompatible strains and factors such as confinement effect of the tube and friction between the steel and the concrete come into play. Table 2.12 is a summary of the research programs summarized herein.

Table 2.12. Summary of previous research programs

	Creep Tests								Shrinkage tests	
	Steel-to-concrete ratio, load level and concrete age			Load applied to concrete core only			Load applied uniformly			
Research Program	s/c ratio (%)	Load level, n	Age (days)	#	φ_{final}	φ_{steel}	#	φ_{steel}	#	$\varepsilon_{shrinkage}$ ($\mu\varepsilon$)
Terrey et al., 1994	2.7 - 4.1	0.45	18	2	1.2	≈ 0 (greased)	2	0.8	2	< 50
Morino et al., 1997	9.1 - 20.0	0.33	Not given	-	-	-	6	0.3 - 0.6	-	-
Ichinose et al., 2001	11.9 - 13.3	0.20 - 0.27	Not given	4	0.37 - 0.42	Not reported	2	0.24 - 0.33	3	< 50
Uy, 2001	14.8	0.25	14	-	-	-	4	1.25	3	200 (ends sealed)
Han&Yang, 2003	12.5 - 17.7	0.58 - 0.68	28	-	-	-	4	0.60 - 0.65	4	Not reported (negligible)
Han et al., 2004	10.5 - 12.8	0.62	28	-	-	-	4	0.80 - 0.84	2	43 - 45
Yang et al., 2008	8.2	0.3 - 0.6	28	-	-	-	6	0.60 - 0.81	4	109 - 132
Zhou et al., 2009	2.2	0.16	7	-	-	-	2	Not reported	2	180
Wang et al., 2010	8.0	0.52 - 0.68	7 - 30	-	-	-	10	0.5 - 0.7	-	-

s/c ratio = Area of steel divided by area of concrete
n = Load level N_L/N_u, where N_u is the calculated ultimate capacity of the specimen and N_L is the applied load
Age = Time between concrete casting and initial loading
# = number of specimens tested
φ_{final} = Predicted final creep coefficient of the concrete core
φ_{steel} = Predicted final creep coefficient of the column, based on strain measurements of the steel tube
$\varepsilon_{shrinkage}$ = Predicted final shrinkage strain of concrete

Chapter 3: Experimental test program

3.1 Overview

The research was conducted to investigate the performance of two large scale concrete-filled tubes containing two different concretes. Standard test cylinders were cast at the same time as the tubes. The CFT specimens were first subject to sustained loading for 110-130 days and then loaded to failure by constant axial and cyclic flexural loading combined. Results for a steel tube filled with self-consolidating SCM concrete with a high cement replacement were compared with the results from an identical specimen in which the steel tube was filled with conventional SCC concrete. One SCM mix was used, containing Class F fly ash and slag. The cement replacement level by weight was 80%, where half of the replacement material was fly ash and the other half was slag. One conventional SCC mix was used. This same SCC mix was used in the footings of both the CFTs, but the footings were cast eight weeks before the tubes. Standard test cylinders were cast at the same time as the footings. The material mix designs can be found in Table 3.3 and Table 3.4 for the SCM and SCC, respectively. The concrete cylinders from both mixes were tested for compressive strength, shrinkage and creep.

CFT specimens tested for combined axial and flexural loading by Kingsley (Kingsley, 2005), Williams, (Williams, 2006), and Chronister (Chronister, 2007) were all constructed with vanadium alloy steel tubes. The yield stress of these tubes was 75 ksi. This program investigates the response using a steel tube with a yield stress of 50 ksi, as was done in 2010 and 2011 by Lee (Lee, 2011). A summary of the study parameters for each test can be found in Table 3.1. Section 3.1 discusses the materials and layout of each specimen including detailed drawings of each component. Section 3.2 is a description of the construction of the specimens. Section 3.3 describes the experimental test setup and procedures, as well as the instrumentation used for each test including location and desired measurement for each instrument.

Table 3.1. Test matrix for complete program (Lee, 2011) (with additions)

Specimen	GSR	$\frac{l_e}{D}$	Connection	Test Loading	Study Parameter
1-75	Kingslev	0.6	Monolithic	Flexural	No Shear reinforcement
2-75	Kingsley	0.6	Monolithic	Flexural	Embedment Depth
3-75	Kingsley	0.9	Monolithic	Flexural	Embedment Depth
4-75	Kingsley	0.6	Isolated	Flexural	Connection Type
5-75	Williams	0.9	Monolithic	Flexural	Flexible Underlay
6-75	Williams	0.75	Isolated	Flexural	Flexible Underlay, Embedment
7-75	Williams	0.75	Isolated	Monotonic Axial	Punching Shear
8-75	Williams	0.75	Isolated	Cyclic Axial	Punching Shear
9-75	Chronister	0.9	Isolated	Flexural	Galvinization
10-75	Chronister	0.9	Isolated	Flexural	Galvinization, Drift History
11-75	Chronister	0.9	Isolated	Flexural	Axial Load P/Po = 0.15
12-75	Chronister	0.9	Isolated	Flexural	Axial Load P/Po = 0.2
1-50	Lee	0.8	Monolithic	Flexural	Straight Weld
2-50	Lee	0.775	Isolated	Flexural	Straight Weld
3-50	Lee	0.775	Isolated	Flexural	Spiral Weld
4-50	Lee	0.8	Monolithic	Flexural	Spiral Weld
5-50	Lee	0.7	Isolated	Flexural	Spiral Weld
6-50	Lee	0.6	Isolated	Flexural	Spiral Weld
7-50	Gunnarsson	0.8	Isolated	Sustained, Flexural	Creep, SCM Concrete
8-50-SCM	Gunnarsson	0.8	Isolated	Sustained, Flexural	Creep, SCM Concrete
30”-50	O’Neill	0.6	Isolated	Flexural	D/t ratio

3.1.1 Specimen layout

The specimens model a cantilever bridge column anchored into the footing. The column consists of a steel tube filled with the self consolidating, low shrinkage concrete specified in Table 3.3 and Table 3.4. Figure 3.1 shows the dimensions for a typical specimen. The length between the

column-footing interface and the center of the applied lateral load is 72 in. The footing is 24 in. deep, 76 in long and 68 in wide.

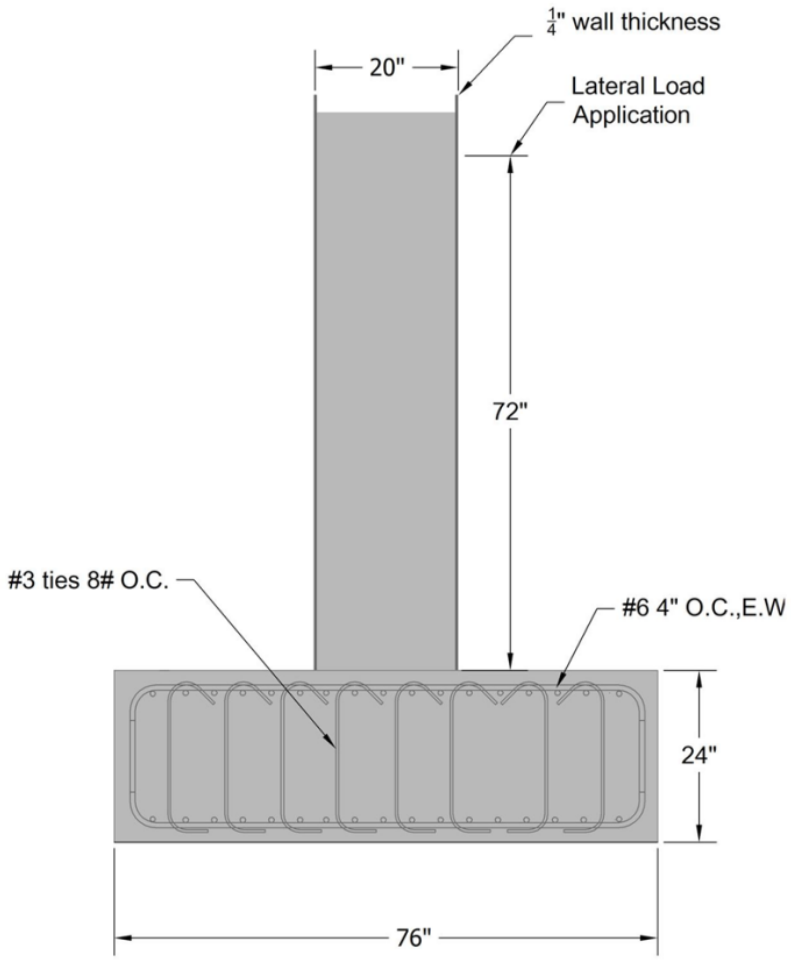

Figure 3.1. Typical specimen (Lee, 2011)

Two different concrete types were used for construction, as mentioned in Section 3.1. The connection used for Specimens 7-50 and 8-50-SCM is called an isolated connection and is shown in Figure 3.2. It is made by first creating a void in the footing with a 30 in. diameter corrugated galvanized steel pipe before casting the footing. The tube, with a welded steel flange on the end, is then placed into the void and grouted into place using fiber reinforced grout.

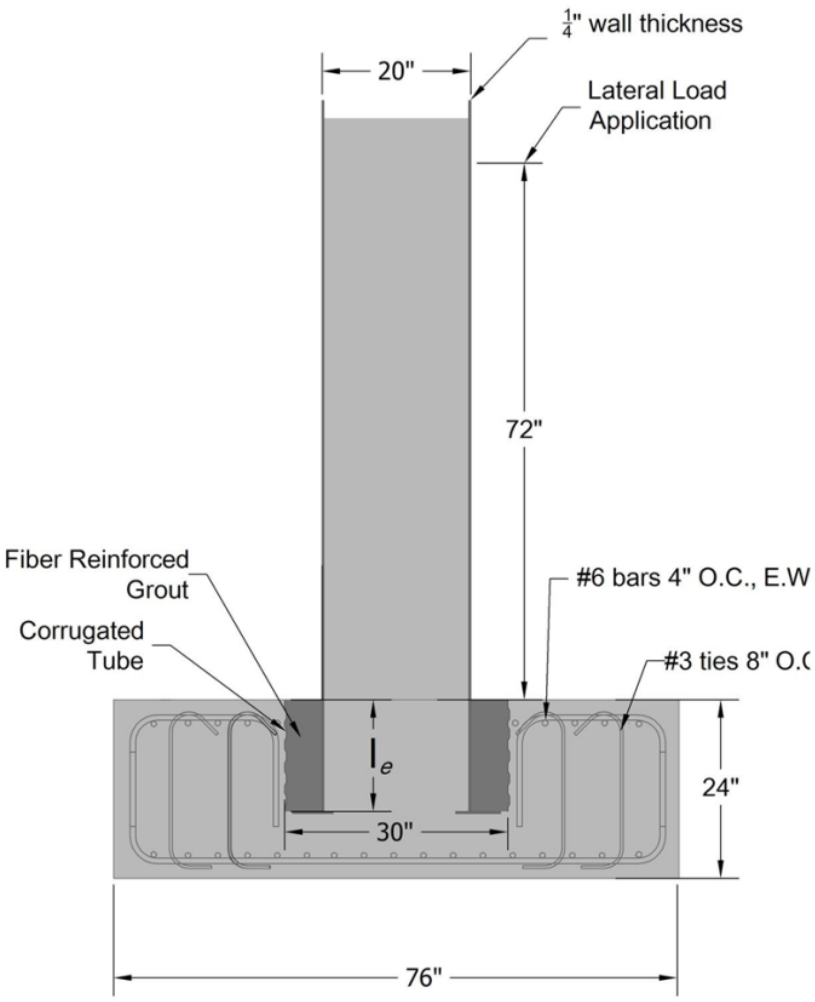

Figure 3.2. Typical specimen with isolated connection (Lee, 2011)

The reinforcement layout was the same for both specimens. The typical layout is shown in Figure 3.2. The footing was reinforced with No. 6 bars spaced at 4 in. intervals in both directions on the top and bottom. The upper reinforcement was bent 90^o down in the center of the specimen to leave space for the corrugated pipe to be placed. Vertical shear reinforcement was No. 3 bars detailed with seismic hooks spaced at 8-in. intervals along each longitudinal bar. (Lee, 2011)

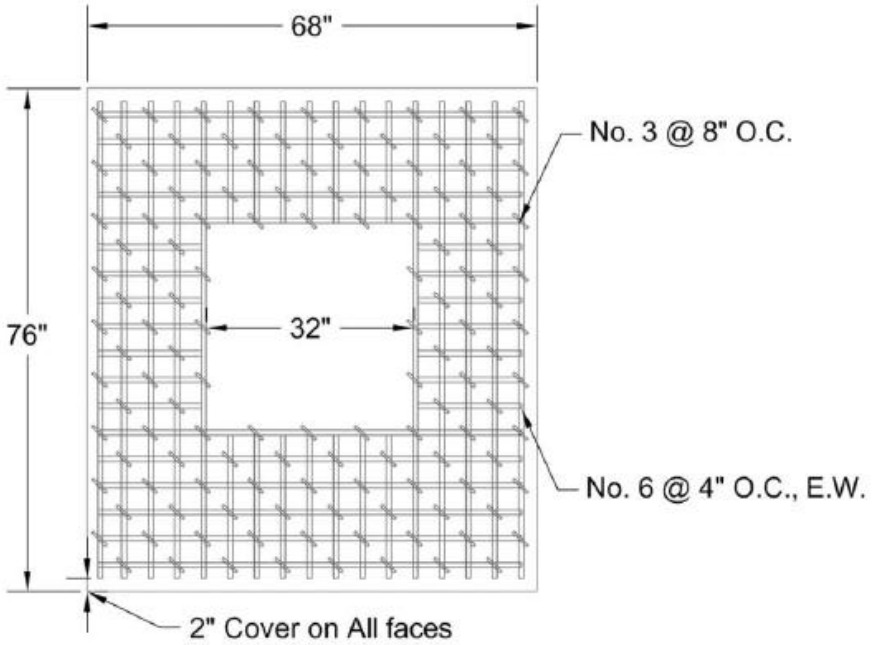

Figure 3.3. Layout of footing reinforcement (Lee, 2011)

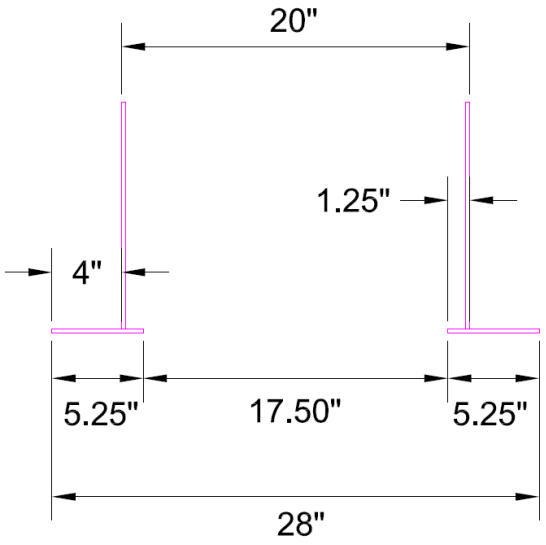

Figure 3.4. Steel tube connection detail

A 1/4 in. thick annular ring (steel flange) was welded to the embedded end of the tube to provide mechanical anchorage of the column. The ring had outer and inner diameters of 28 inches and 17.5 inches respectively and can be seen in Figure 3.4.

3.1.2 Materials

Each specimen required a variety of materials specified in design during construction. Table 3.2 outlines each material used, its required specifications and the supplying vendors.

Table 3.2 Material list (Lee, 2011) (with additions)

Item	Designation	Vendor
Spiral Seam Steel Tube	AWWA C200, ASTM A1018-07 SS	Northwest Pipe
Flange Plate	A572	Bloch Steel
Reinforcing Steel	ASTM A615M-08b Grade 60	Addison Supply
Formwork	Medium Dense Overlay Plywood	Dunn Lumber
Regular Concrete	Self Consolidating, Low Shrinkage, 6 ksi	Stoneway Concrete
SCM Concrete	Self Consolidating, Low Shrinkage, 6 ksi	Stoneway Concrete
High Strength Grout	ASTM C-1107	Mason Supply
Fiber Reinforcement	Polypropylene, Strux 85/50	Stoneway Concrete

3.1.3 Mix proportions

The mix designs of the SCM SCC concrete and the regular SCC concrete are given in Table 3.3 and Table 3.4, respectively. The w/b ratio for both concretes is 0.33. The binder in the SCM SCC concrete consists of 20% cement, 40% fly ash and 40% slag. The binder in the regular SCC concrete consists of 65% cement and 35% slag.

Table 3.3. Mix design of SCM SCC concrete (UW Test SCC)

Material	Description	ASTM	Spec. gravity	oz.	cu.ft	Weight (lb)
#8 coarse aggregate	AASHTO #8 (3/8)	C33	2.67	0.00	8.39	1399
Fine aggregate	Concrete Sand	C33	2.63	0.00	8.97	1473
Type I-II cement	Type I-II	C150	3.15	0.00	0.84	165
Type A Water Reducer	WRDA – 64	C494	1.21	33.00	0.00	-
Type F High Range Water Red.	ADVA – 170	C494	1.10	74.25	0.00	-

Fly Ash Class F	Fly Ash	C-618	2.20	0.00	2.40	330
Slag	Lafarge GGBFS	-	2.84	0.00	1.86	330
Water	Water	C94	1.00	0.00	4.32	270
Air	-	-	-	-	0.41	-

Table 3.4. Mix design of regular SCC concrete (SLSCC-6)

Material	Description	ASTM	Spec. gravity	oz.	cu.ft	Weight (lb)
#8 coarse aggregate	AASHTO #8 (3/8)	C33	2.67	0.00	8.76	1460
Fine aggregate	Concrete Sand	C33	2.63	0.00	9.37	1473
Type I-II cement	Type I-II	C150	3.15	0.00	2.73	536
Type A Water Reducer	WRDA – 64	C494	1.21	33.00	0.00	-
Type F High Range Water Red.	ADVA – 170	C494	1.10	74.25	0.00	-
Slag	Lafarge GGBFS	-	2.84	0.00	1.86	289
Water	Water	C94	1.00	0.00	4.32	270
Air	-	-	-	-	0.41	-

3.2 Specimen construction

The following section details construction of the specimens. The construction process has been separated into footing construction, tube construction, modifications made for test setup, specimen assembly and cylinder construction.

3.2.1 Footing construction

The formwork for the footing consisted of plywood defined as medium dense overlay (MDO) and 2x4s. The MDO was cut to meet the exterior dimensions of the footing. Each panel was reinforced using 2x4s at the perimeter (top and bottom) and vertically every 8 in. along the length. The panels were clamped together using steel rods and bearing plates as shown in Figure 3.5. The base of the formwork was constructed using two layers of plywood and extended beyond the vertical walls of the formwork. (Lee, 2011)

Figure 3.5. Steel bolt connection between formwork walls (Lee, 2011)

The reinforcing steel was sorted by bar length. There were four different bar sizes as well as one size tie as shown in Figure 3.6. Bar A and bar B shapes were used in the 72 in. long direction of the footing; Bar C and Bar D shapes were used in the 68 in. direction. The lower mat was comprised of the longer bars (Bar A and Bar C) spaced at 4 in. intervals. The top mat was comprised of longer bars where possible, but in the center of the footing two short bars (Bar B or Bar D) were used to create a space in the top mat for the column to be placed as shown at the bottom of Figure 3.6. (Lee, 2011)

.

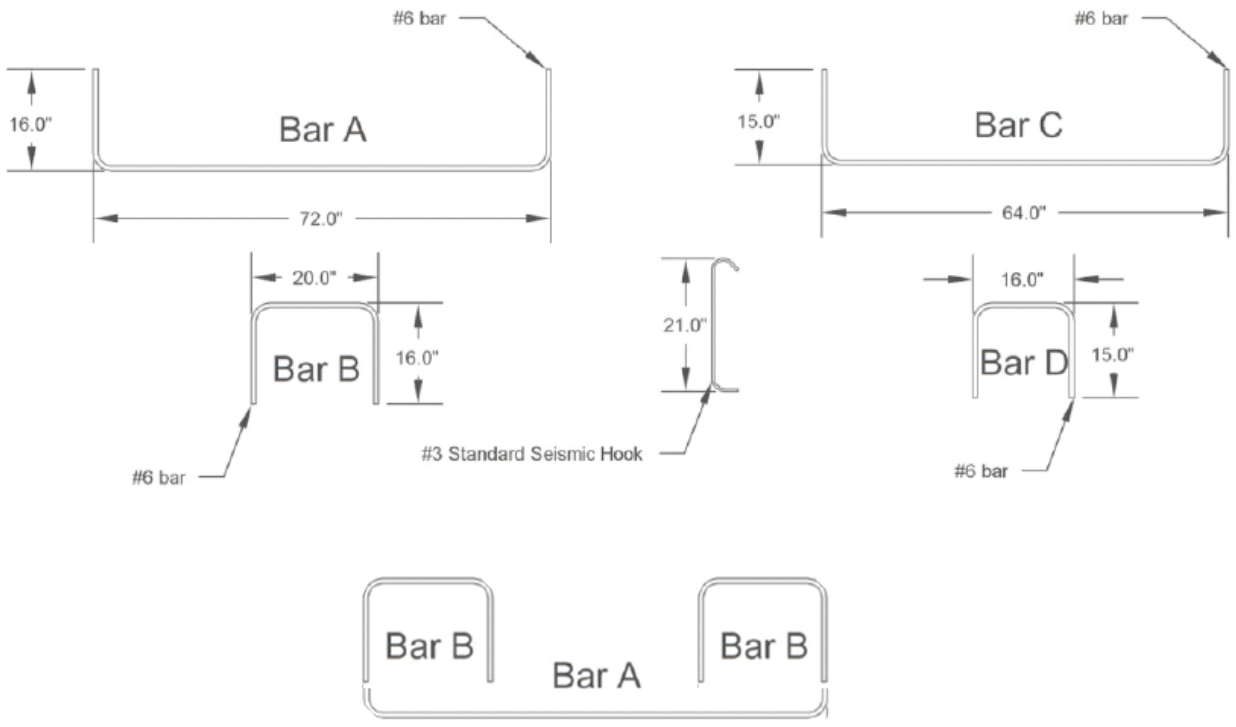

Figure 3.6. Reinforcing steel shapes and sizes for footing (Lee, 2011)

The cage was assembled as follows: (a) Tied all longitudinal bars used in the 72 in. direction (Bar A and Bar B) into hoops. (b) The hoops were hung from a large straight bar at 4 in. spacing and secured. (c) Hoops made from Bar C and Bar D were placed and tied into place. (d) #3 ties were placed every 8 in. in a checkerboard arrangement. e) 2 in. chairs were clipped to the underside of the ties and the large diameter spare bars were removed. f) PVC pipes were attached to the cage, creating a void in the concrete for the bolts that tie the footing to the reaction frame. g) Lifting hooks attached, completing the rebar cage shown in Figure 3.7. (Lee, 2011)

Figure 3.7. Finished rebar cage.

For the isolated connection, a corrugated pipe was used to create a void in the footing, as shown in Figure 3.8. The pipe was cut to 16 inches, using a grinder to get the smoothest cut possible. A plywood disc was then cut to fill the bottom of the pipe to prevent the flow of concrete. The disc was attached to the corrugated pipe with four 2x2x1/16-in. steel angles with staggered 1/4-in. holes already drilled. The angles were attached on the inside of the pipe so that they could be removed afterward the concrete in the footing had hardened. Two wood screws were used to attach each angle to the disc, but very short 1/8-in. diameter machine screws attached the angle to the pipe. One 3/32-in. hole was drilled into the tube for each angle to fit those screws. The screws themselves then made a thread in those holes because of the size difference, and therefore no nuts were needed. The joint was then caulked the whole way round to ensure a water tight seal. Four threaded rods were then attached to the disc, making sure they had enough embedment depth and would remain in the concrete after the disc was removed. A combination of 2x4s and 2x8s was then attached to the plywood so that the corrugated pipe could be easily positioned in its exact place, and to provide resistance to the buoyancy forces present when the pouring was finished and the concrete was still wet. This combination also allowed the plywood disc to be

removed easily after the concrete had hardened. The surface of the concrete was then kept moist for 7 days by covering it with burlap and plastic, making sure the burlap was constantly wet.

Figure 3.8. Corrugated pipe in place.

3.2.2 Tube construction

The 20 in. diameter tubes were fabricated offsite and delivered to the University in 20 ft. segments. The tube was cut to the desired length for each specimen. Each specimen was cut from an end of the original tube, using an acetylene torch track cutter, in order to preserve one quality end for welding. The tubes were prepped for welding of the annular ring by grinding the paint off the end using a wire brush to avoid any contamination of the weld. (Lee, 2011)

The flange ring was fabricated in house using A572 plate. The plate steel was cut into a flange ring using a stationary acetylene torch and a rotary table. Each ring had a 28 in. outer diameter and 17.5 in. inner diameter. Four 1/2-in. diameter holes for leveling rods, were then drilled in the flanges two inches away from the outer edge of the ring, spaced at 90°angles. (Lee, 2011) (with modifications)

Figure 3.9. Tube and flange after welding (Lee, 2011)

The flanges were welded to the tube using a 5/16-in. fillet weld on the interior and exterior side of the tube using E71T8. The welding was completed onsite by a certified welder. Each tube was placed on rollers and the flange plate was centered on the tube using angle brackets and C-clamps. The flange was then tack welded to the outside of the tube to prevent movement. Once tack welded into place, the angle brackets were removed and the inner fillet weld was placed. After the inner fillet weld was in place the tack welds were removed using a hand grinder before the outer fillet weld was placed. Figure 3.9 shows a tube following the placement of the annular ring. (Lee, 2011)

3.2.3 Modifications made for test setup

In order to test the specimen, a connection between the column and the lateral load actuator was required. Alterations to the column were completed to utilize the existing connection design for the actuator. Four 1 in. diameter steel rods extend from the actuator to mount to the column. Holes were made in the column so the actuator rods could run through the column and be anchored on the opposite side of the column with a bearing plate as shown in Figure 3.10. The holes were cut out of the steel tube using a handheld acetylene torch and 2-1/2 in. diameter PVC pipes were placed through the holes to create voids in the concrete for the actuator rods. After the PVC was removed, the end result was four cylindrical holes running through the column, centered at a point 72 inches above the surface. (Lee, 2011)

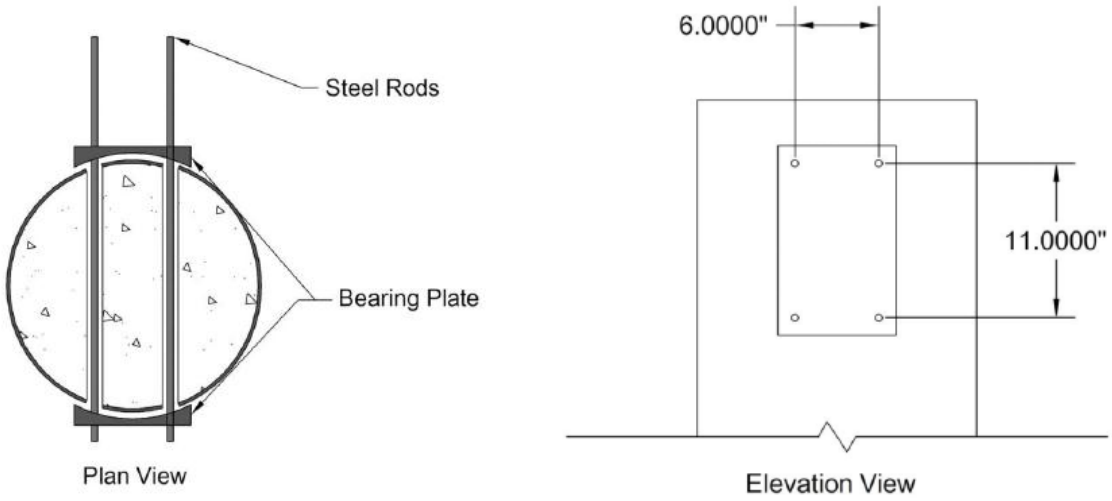

Figure 3.10. Actuator Anchor Rod Layout (Lee, 2011)

Proper anchorage of the footing was needed to prevent overturning of the footing during testing. Four steel Williams rods were selected to post-tension the footing to the concrete anchor block. Holes for the steel rods were made using four 2-1/2 in. diameter PVC pipes. Figure 3.11 shows the anchor rods in plan and elevation view. (Lee, 2011)

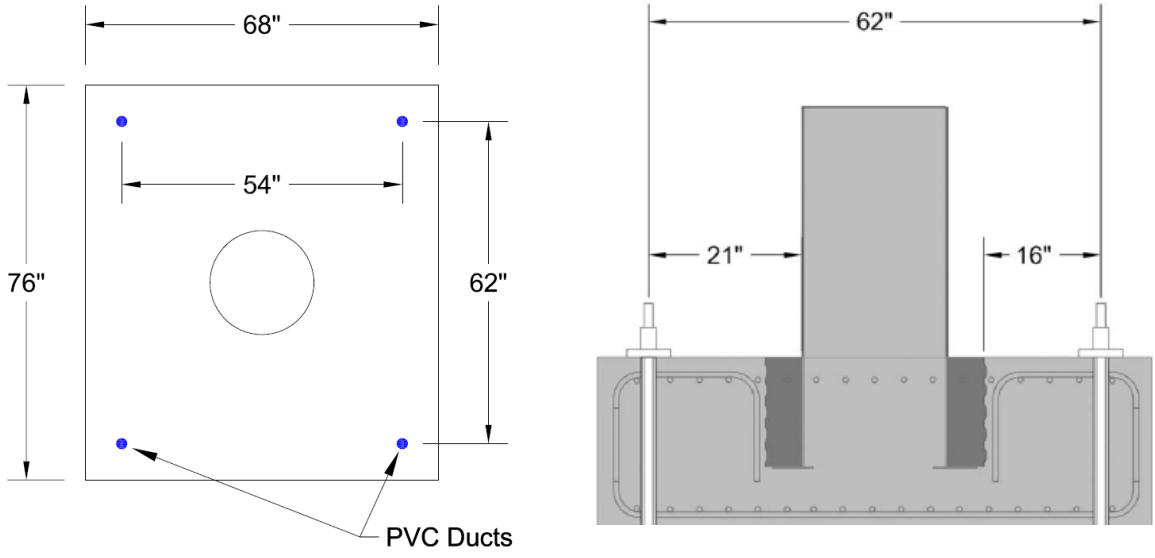

Plan View **Elevation View**

Figure 3.11. Anchor Rod Location (Lee, 2011) (with modifications)

Brackets were needed to allow a crane to lift the specimen after casting. Four straight No 6 bars were collected and bent into a u-shape. The ends of the bar were then bent orthogonal to the newly created plane. Four hooks were bent for each specimen. The ends of the hooks were placed inside the rebar cage with the crest of the hook exposed and pointing toward the top center of the tube. (Lee, 2011)

3.2.4 Specimen assembly

After the concrete in the footing had cured and the tube had been constructed and instrumented on the inside and on the outside beneath the surface of the grout, the finished tube was placed into the void and grouted into place. No leveling rods were needed to ensure the correct embedment depth, since that was already taken care of by setting the bottom of the plywood disc to match the embedment depth. After the disc had been removed, the tube was simply placed on the bottom of the void, fitting the holes in the annular ring onto the threaded rods in the void. Since the surface of the bottom of the void was not completely perfect, thin washers were placed under the annular ring as needed to set the pipe perfectly level. Nuts were then tightened down onto the annular ring to make sure the tube would remain level during the grouting of the void. Figure 3.12 shows the specimen after the first batch of grout had been poured in.

Figure 3.12. Specimen after first batch of grout

Each bag of grout required 3.1 liters of water resulting in a volume of 0.42 ft^3. Polypropylene fibers were used to reinforce the grout. A total of 0.75 oz of fibers was added to each bag of grout (3lb. of fiber per $yd.^3$). A total of eleven bags were used to cast the void and construct fourteen test cubes. The concrete mixer could not accommodate the entire batch; the grout was mixed in two-bag batches. The water and fiber for every bag was portioned prior to mixing. Once the batch was fully mixed it was poured into a wheel barrow and then poured into the void between the tube and the pipe. The next batch was mixed while the preceding batch was being poured. Two to three cubes for material testing were taken from each batch of grout. The surface of the grout was then kept moist for seven days in a similar fashion as the footing concrete. (Lee, 2011)

3.2.5 Cylinder construction

Both types of concrete used in the steel tubes and test cylinders were mixed at Stoneway Concrete and poured on the same day. The footings of the CFT specimens, however, were cast eight weeks earlier and only tested for compressive strenght. Samples were cast into 6x12 in. cylindrical molds (Figure 3.13) for determination of compressive strength, and creep and shrinkage strains. Once sufficient strength was reached, the specimens were demolded and stored at 100% relative humidity until testing. Both ends of the cylinders were sulfur capped before testing, to ensure flat surface. Flat surface of the cylinders is required to minimize stress concentration, which reduces the compressive strength. (Hannesson, 2010) (with modifications)

Figure 3.13. Photograph of casting of cylinders (Hannesson, 2010)

From each concrete mixture, twenty cylinders were cast for compressive strength test. Eight cylinders from each mix except the footing mix were cast for creep and shrinkage measurements. Finally, four extra cylinders of each mix were cast, in case some would turn out defected.

3.3 Experimental test program

3.3.1 Compressive strength

The objective of this test is to measure the compressive strength of concrete mixes by applying axial load. Compressive strength test is primarily used to determine if concrete mix meets the specified target strength, for certain application. Since concrete has very little tensile strength, it is mainly used in a compressive mode, and therefore the compressive strength is very important in engineering practice. Furthermore, compressive strength of concrete mixes increases with increasing curing period, it is therefore important to test concrete mix at different days to capture the strength development. Compressive strength was measured according to ASTM C 39. (ASTM C 39, 2009) The strength of the concrete mixtures was determined at age 7, 14, 28, 56, and 168 days. (Hannesson, 2010)

3.3.1.1 Instrumentation

Figure 3.14 shows the apparatus needed to determine the compressive strength. It is very difficult to make sure that the ends of the specimens are exactly perpendicular to direction of applied load. To ensure loading with no eccentricity, pivoting head (Figure 3.14a) is used; so small deviation from parallelism will not affect the strength. Safety door (Figure 3.14d) is kept closed during testing to prevent fly away particles to hit bystanders. The apparatus is connected to a hydraulic machine that records the load that is applied and a gauge needle stops on the maximum recorded load. (Hannesson, 2010)

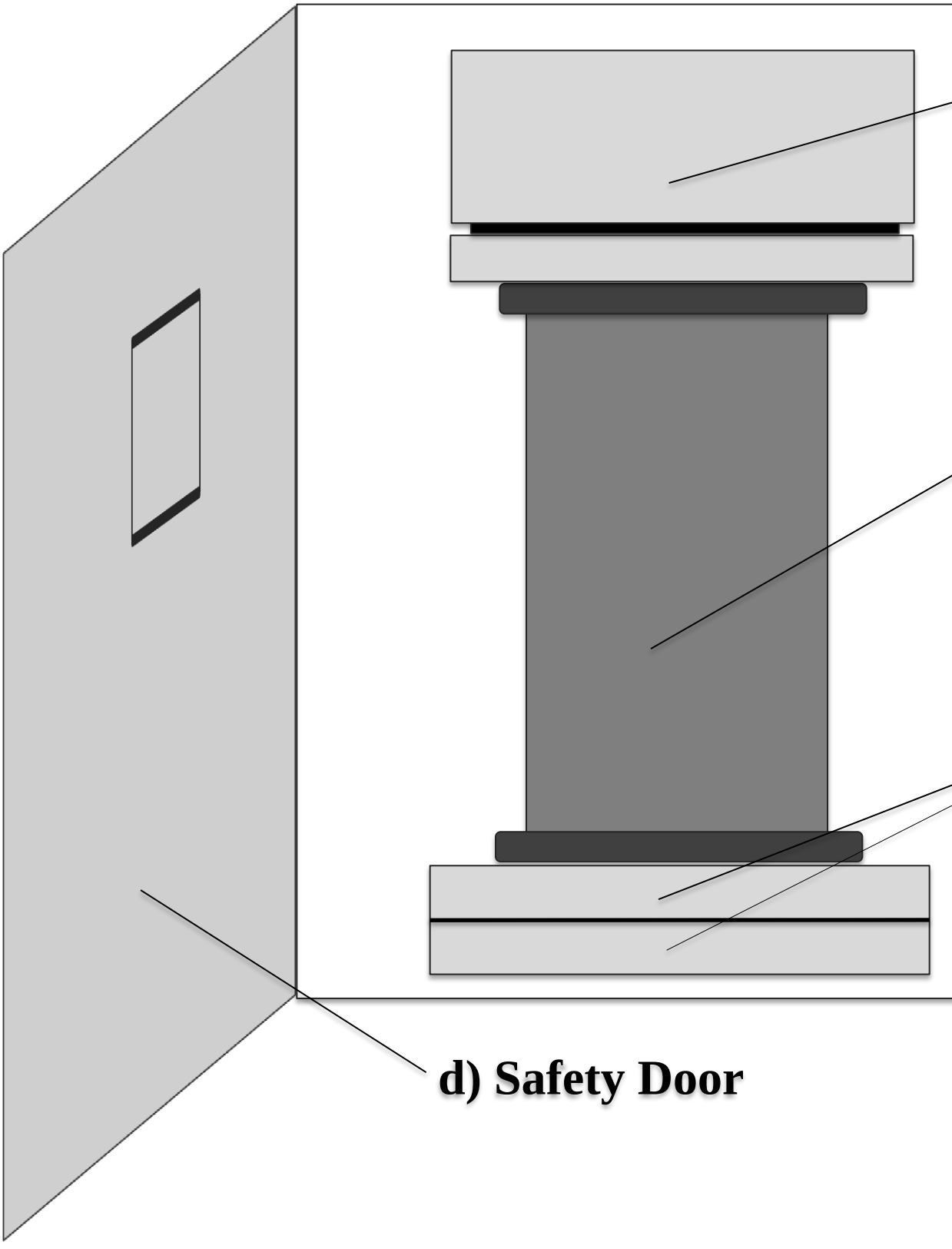

Figure 3.14. Compressive test setup (Hannesson, 2010)

3.3.1.2 Test setup

To set up the compressive test, 6x12 in. cylinder (Figure 3.14b) is placed in the apparatus (Figure 3.16). Steel plates (Figure 3.14c) are placed under the cylinder to elevate it, since the apparatus has limited axial displacement capacity. (Hannesson, 2010)

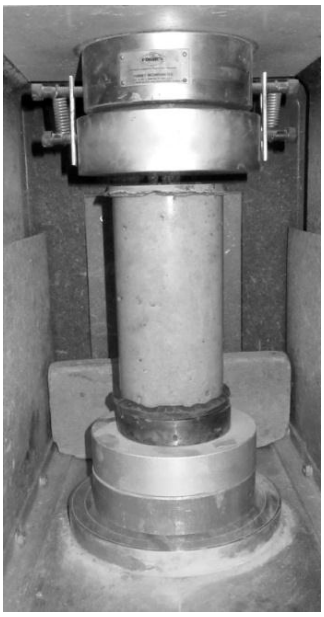

Figure 3.15. Photograph of the compressive strength set up (Hannesson, 2010)

3.3.1.3 Procedure

After completing the test set up, as described in Section 3.3.1.2, the apparatus is turned on and the load reader is set to zero. The apparatus is set to record the peak load. The cylinder is then loaded to failure, at a rate of (36 +/- 7 psi/s). The rate of loading is controlled by turning a knob (Figure 3.16a). Compression strength of the specimens is determined with equation (3-1):

$$f_c' = \frac{P}{A} \qquad \textbf{(3-1)}$$

Where f'_c is the compressive strength, P is the maximum applied load, and A is the original cross-sectional area of the specimen. At each age, three cylinders were tested for compressive strength. The strength of the mix was defined as average value of the three cylinders. (Hannesson, 2010)

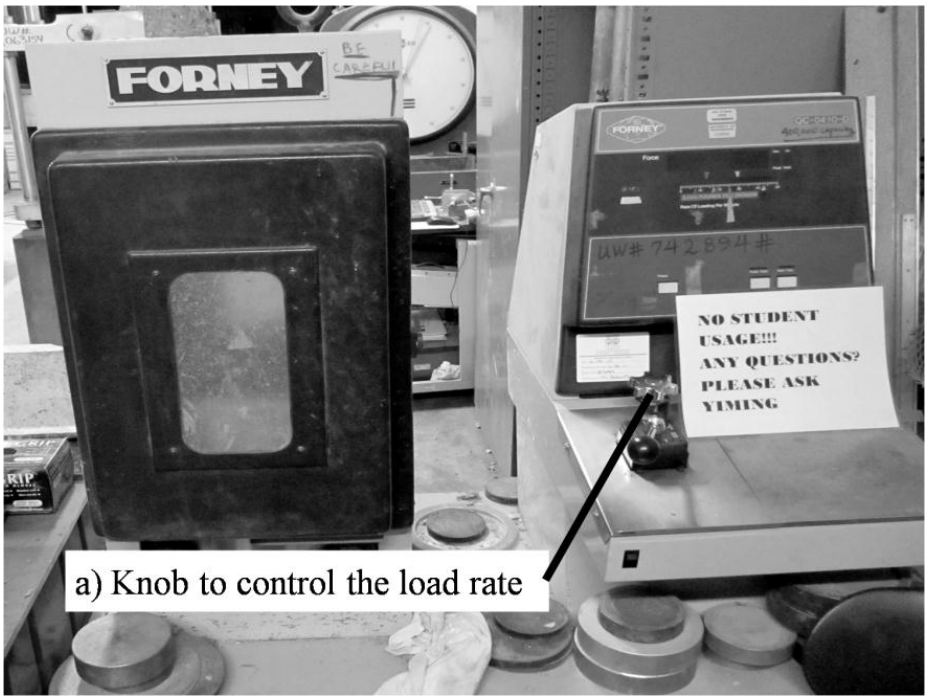

Figure 3.16. Photograph of the compressive test apparatus (Hannesson, 2010)

3.3.2 Creep and shrinkage tests

The objective of this test is to measure the creep and drying shrinkage strains of concrete mixes under three different conditions: Unsealed, sealed with epoxy, and encased in a steel tube. Creep is a time-dependent deformation under a load and drying shrinkage occurs in a hardened concrete when free water evaporates. Creep and shrinkage strains can affect the serviceability and durability of structures due to the fact that deflections increase over time, which can cause various problems. In CFT structures, shrinkage has proven to be very small and is usually considered to be negligible, as can be seen in many previous research programs in Chapter 2.

The strains were measured using vibrating wire strain gauges, both embedded and attached to concrete or steel surfaces. The gauges were attached to a data acquisition system that recorded microstrain readings at user-specified intervals. In addition, the creep and shrinkage of the sample cylinders was measured with a mechanical Whittemore strain gauge according to ASTM C 512 (ASTM C 512, 2010). The monitoring started after fourteen days of curing.

3.3.2.1 Instrumentation of CFT creep rigs

Figure 3.17 shows the CFT creep rig test setup. The rig is designed to apply constant load to the concrete-filled tube. It consisted of two parallel steel beams with a standard W24x94 cross-section with stiffener plates, two 1.75-in. diameter Williams bars with nuts and washers, one 18-in. diameter cotton duck bearing pad, one 18-in. diameter bearing plate on top of the pad, four spring washers, one 10x10x1.75-in. bearing plate under the spring washers, and two 8x8x1.5-in. bearing plates on top of them. In addition, the two W-sections were attached with plates and bolts so they could be placed on top of the CFT as a unit.

Each rig had two stacked Belleville spring washers to help maintain a nearly constant load as the specimens shortened. The washers were concentrically placed around the Williams bars and sat on top of the 10x10x1.75 in. bearing plate that was attached to the two steel beams with bolts through each of the four corner holes. A top view of this configuration is shown in and a side view in Each spring washer had a maximum compression of 0.1102 in. The outside-diameter of each washer was 7.87 in., the inside diameter was 4.41 in., and the thickness was 0.63 in. They had stiffness of 836 k/in each. Therefore the total stiffness of the four washers was 3344 kips/in. and the maximum load that could be applied to them was 369 kips.

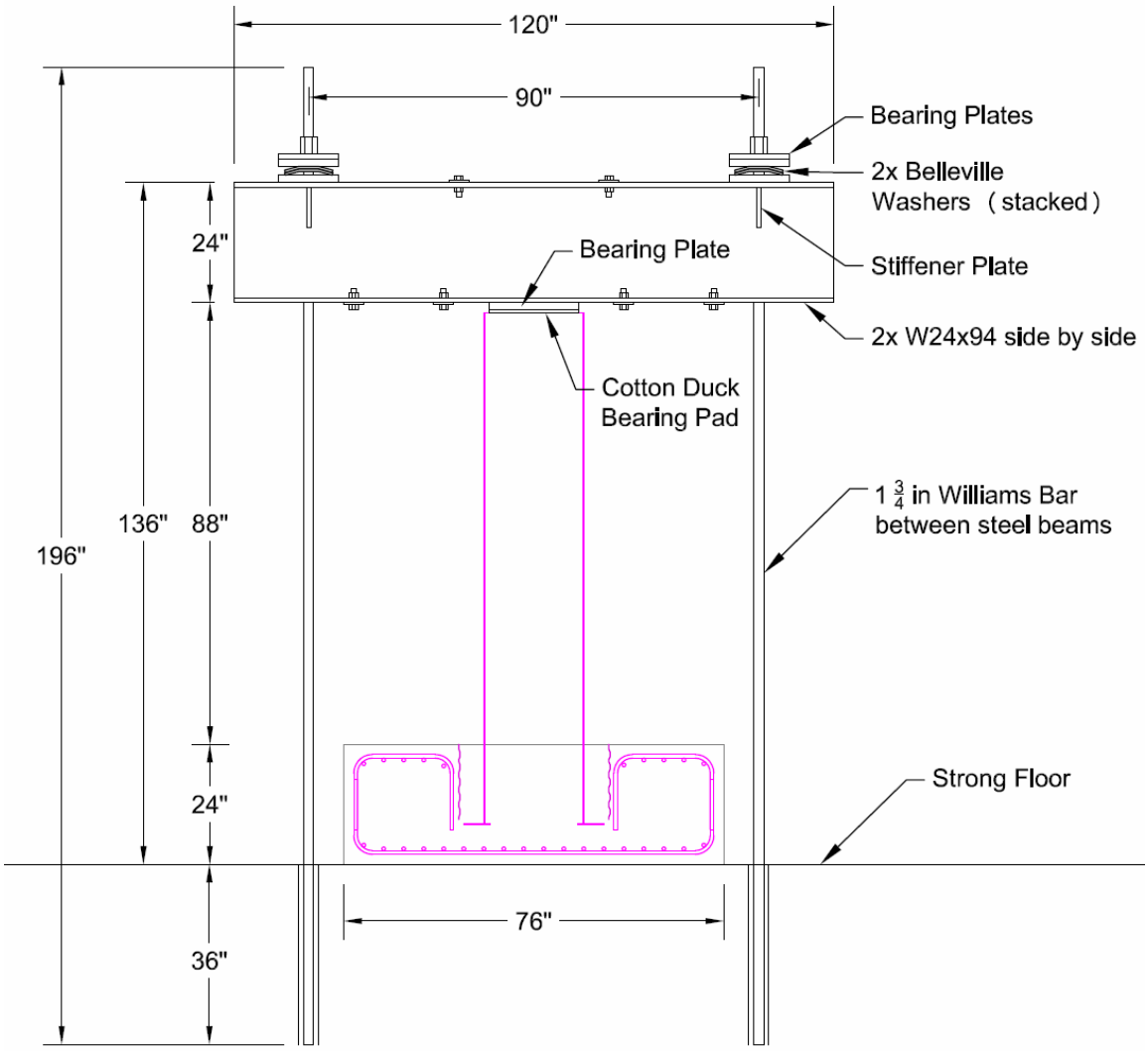

Figure 3.17. CFT creep rig test setup

The Williams bars were designed to reach 24 in. above the surface of the beams to accommodate a hydraulic ram on top of the rigs. A single 300-kip ram was used to apply the prescribed stress to the concrete inside the steel tube. A bearing unit for the ram was placed around the Williams bar and rested on the surface of the bearing plate below the nut. The ram was then placed around the Williams bar and on top of the bearing unit. Finally, a small bearing plate and a regular washer were placed around the Williams bar to rest on the surface of the ram and a Williams nut was hand tightened against the washer. A photograph of the ram ready to stress a specimen is shown in Figure 3.38, and a photograph of the CFT creep rigs is shown in Figure 3.20.

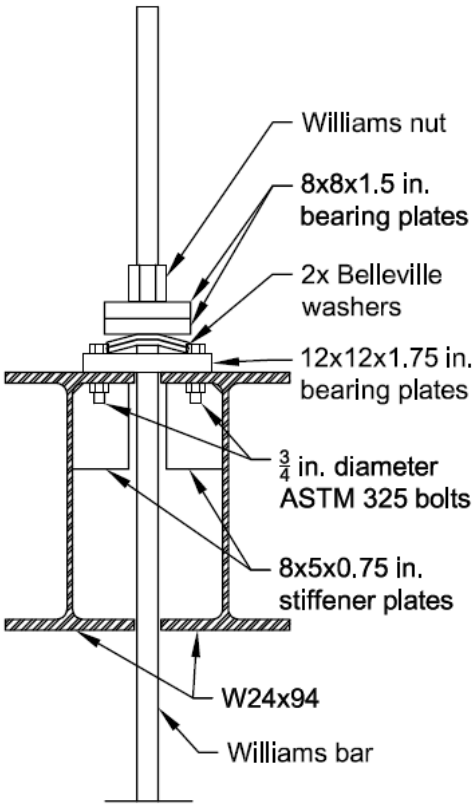

Figure 3.18. CFT creep rig test setup – Side view

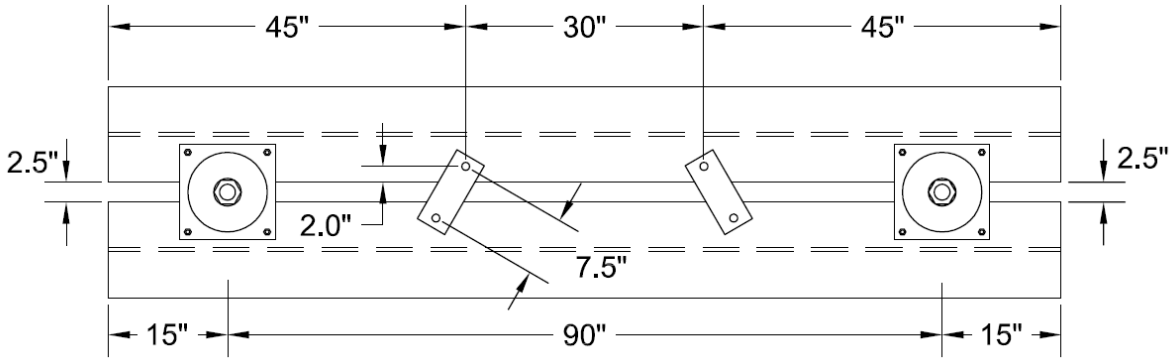

Figure 3.19. CFT creep rig test setup – Top view

Figure 3.20. Photograph of CFT creep rigs

Figure 3.21 shows the welded/glued vibrating wire strain gauges that were used to measure the strains of the steel tubes, concrete cylinder specimens, and Williams bars over time. Figure 3.22 shows the embedded vibrating wire strain gauges that were used to measure the strains of the concrete core of the CFT specimens over time.

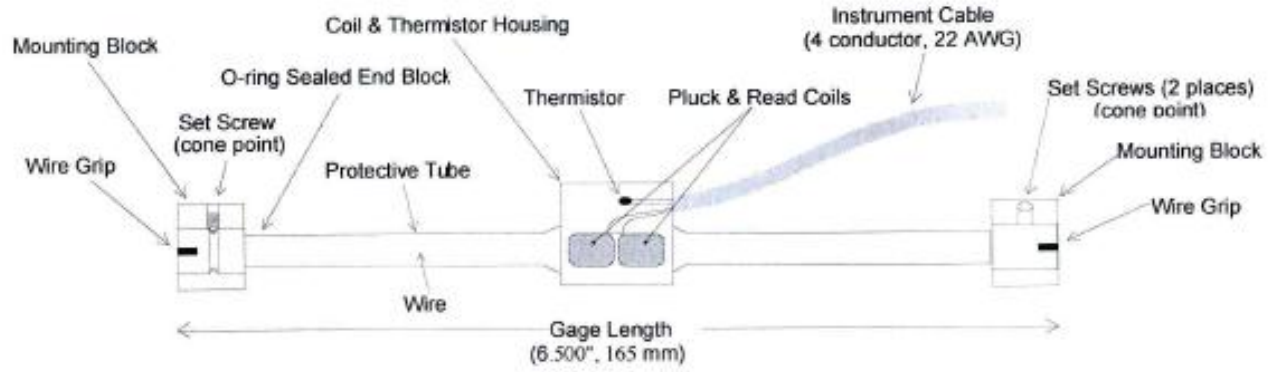

Figure 3.21. Model 4000 Weldable Vibrating Wire Strain Gauge (Geokon, 2010)

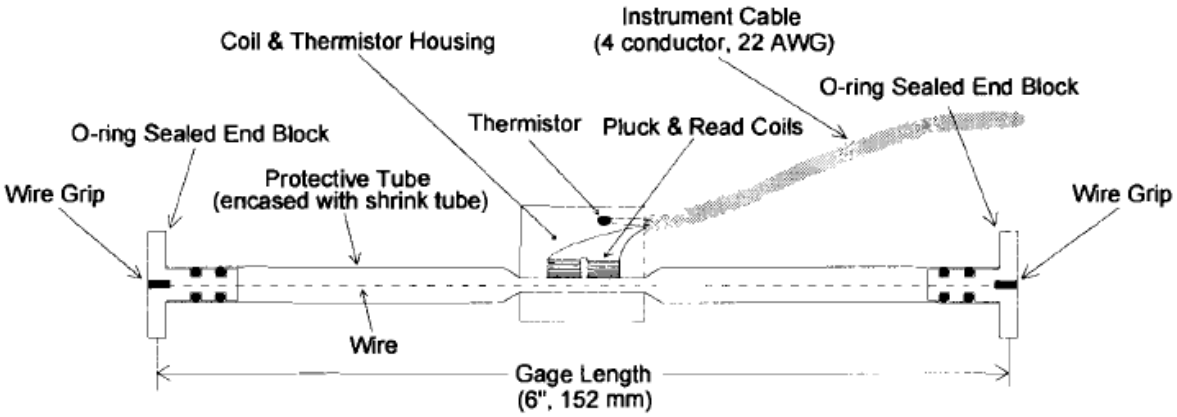

Figure 3.22. Model 4200 Embeddable Vibrating Wire Strain Gauge (Geokon, 2010)

Strains are measured using the vibrating wire principle: a length of steel wire is tensioned between two mounting blocks that are attached to the surface being studied. Deformations of the surface will cause the two mounting blocks to move relative to one another, thus altering the tension in the steel wire. The tension in the wire is measured by plucking the wire and measuring its resonant frequency of vibration. The wire is plucked, and its resonant frequency measured, by means of an electromagnetic coil positioned next to the wire. The data acquisition system, used in conjunction with the gauge, provides the necessary excitation to pluck the wire and converts the measured frequency so as to display the reading directly in microstrain. The useable range of the strain gauge runs from around 1000 to 4000 microstrains. The mid-range reading is 2500.

The reading can be adjusted by simply pulling or pushing on the free end of the strain gauge. (Geokon, 2010)

Figure 3.23 shows the location of the gauges within and on the surface of the CFT specimen. Six gauges were welded onto each tube. The two bottom gauges were glued on with high strength, quick curing epoxy in order to avoid welding in the plastic hinge region of the steel tube. Six gauges were then embedded in the concrete core.

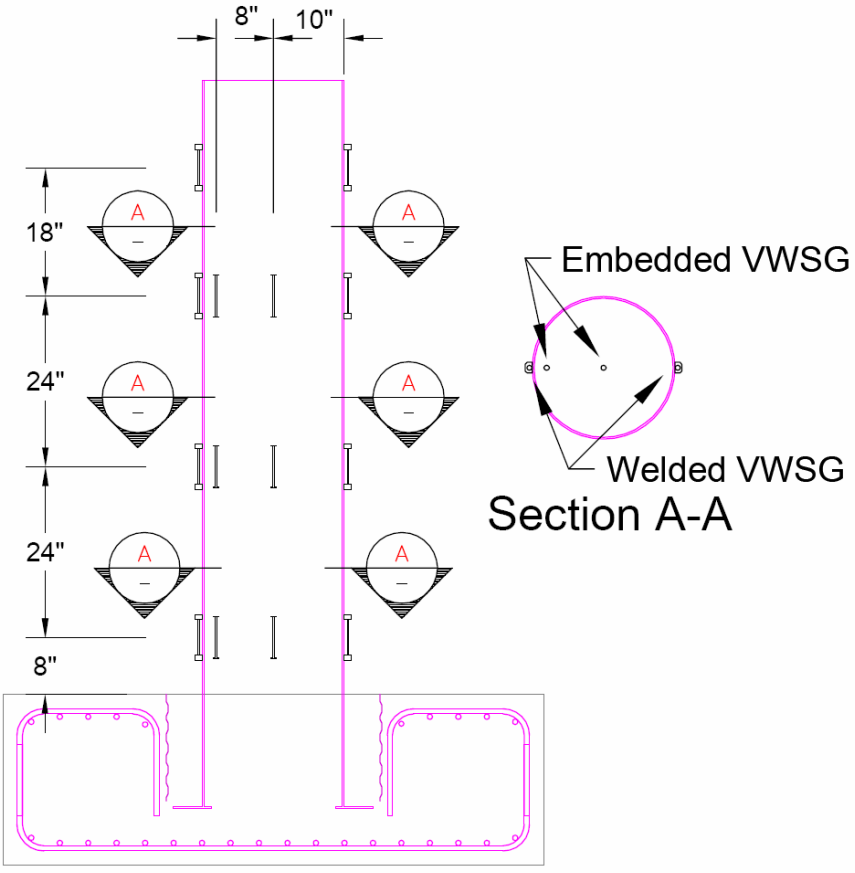

Figure 3.23. Instrumentation of the CFT creep rig

To embed the Model 4200 vibrating wire strain gauges in the concrete, two 1/8-inch diameter nylon strings were cut to a length of about 12 ft. and a 3/8-in. diameter steel pipe with a wall thickness of 1/16 inches was cut to six 18.5-in. segments. A 1/4-in. deep slot was then cut into each end of each pipe. The width of each slot was 3/32 inches and the distance between the two slots in each pipe was 17.5 inches. The pipes were attached to the two nylon strings at a 90°

angle to the strings, forming a sort of ladder. The nylon string was placed into each slot of each pipe and then the string was wrapped around the pipe once at each joint. The distance between a set of two pipes was 24 inches, and the distance between the two pipes in each set was 4 inches. Next, the ladder was strapped between two sawhorses that were placed about 10 ft apart. Enough tension was applied so that the strings remained nearly horizontal instead of sagging down. The distances between the pipes were then adjusted. The distance between the strings was 17.5 inches, since that is the distance between the two slots in each tube. This distance was used because it is the same as the inner diameter of the steel flange welded to the bottom of the tube. Hot glue was applied to each joint to help prevent the steel pipes from slipping on the nylon string.

The vibrating wire strain gauges were attached to the ladder simply by placing the gauges on top of the steel pipes of the ladder, while strapped between the two sawhorses, and tying them to the pipes with nylon straps. Four straps were used to attach each gauge, two at each gauge-pipe joint. A total of six concrete-embedded gauges were attached to the ladder. Two strain gauges were attached to each set of two pipes with 8 inches between them. One in the center and the other two inches away from the outermost fibers of the concrete-filled tube, which has an outer radius of 10 inches. A photograph of this configuration can be seen in Figure 3.24.

Figure 3.24. Embedded VWSG inside steel tube

To attach the ladder to the CFT, two 3/8-in. holes were drilled into the flange ring that had already been welded to the bottom of the tube. These holes were located so that the ladder would end up in the exact center of the tube. The inside diameter of the flange ring was 17.5 inches, hence the distance between the strings of the ladder. The bottom ends of the strings were then tied to those holes, making sure that the center of the bottom two strain gauges would end up 24 inches from the bottom of the flange ring, making the distance between the surface of the footing and the center of the bottom two strain gauges eight inches.

On top of the CFT, a 2x4 was attached flat. The 2x4 was attached to the CFT with two 2x2x1/16-inch steel angles with staggered 1/4-in. holes already drilled. Wood screws were used to attach the angle to the 2x4, but 3/16-in. diameter machine screws with accompanying nuts attached the angle to the tube. ¼-in. holes were drilled into the tube to fit those screws. After the 2x4 was securely fastened to the top of the tube, two 1/8-inch diameter holes were drilled in it 17.5 inches apart. These holes were also located so that the ladder would end up in the center of the tube. The 2x4 can be seen on the far end of the tube in Figure 3.24

Finally, the top ends of the nylon strings of the ladder were threaded through the holes in the 2x4 and tension applied to the string in a similar fashion as when they were attached to the sawhorses. The remaining slack of each string was then wrapped around the 2x4 and electric tape then wrapped around to secure the ends of the strings and make sure that they would remain in tension.

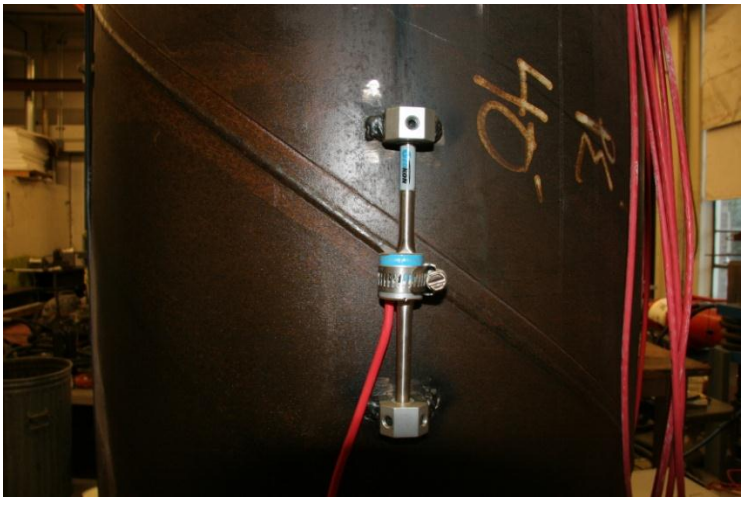

Figure 3.25. Weldable VWSG on surface of steel tube

To attach the Model 4000 vibrating wire strain gauges to the surface of the steel tube, the mounting blocks were first attached to spacer bars with the set screws and welded to the tube with small tack welds using low heat. A photograph of a gauge that has been welded on a tube is shown in Figure 3.25. The welding sequence is shown in Figure 3.26.

Figure 3.26. Welding sequence for the mounting blocks (Geokon, 2010)

Eight spacer bars were made instead of one to speed up the process. A 1/2-in. diameter, 1/16-in. thick steel pipe was cut to eight 6.5-in. segments, but any 1/2-in. steel rod can be used as a spacer bar. After loosening the spacer bar and making sure the blocks and welds had returned to room temperature, the Model 4000 vibrating wire strain gauges were inserted to the mounting blocks. In the case of the bottom two gauges, the spacer bars were not loosened until the expoxy had reached sufficient strength. The bottom end of the gauge was first slid through the top mounting block. The coil and thermistor housing were then attached to the center of the gauge. The housing was then secured to the gauge with a hose clamp which was tightened with a flat head screwdriver. The bottom end of the gauge was slid through the bottom mounting block, and at the same time the top end was slid through the top block. The end of the strain gauge which had a V-groove in it was inserted into the mounting block that only had one set screw, and the screw was tightened hard. After making sure all readings were and would remain in the useable range of the strain gauge, the other end of the strain gauge was secured to the other mounting block with the two set screws in that block. Finally, the mounting blocks were tapped with the handle of a screwdriver to remove any installation strains and stabilize the reading.

Figure 3.27. Weldable wire strain gauge to monitor load

Figure 3.27 shows how vibrating wire strain gauges were used to monitor the load in the CFT specimens. One gauge was used on each Williams bar. Two segments of 24-in. length were tested in a 300-kip Baldwin test machine to develop a load-strain curve for the Williams bars. A photograph of the setup for this test can be seen in Figure 3.28. The load in the specimens could then be monitored by converting the strain in each Williams bar to a load in the bar. Summing the load values of each bar then yielded the load in the CFT specimen.

Figure 3.28. Load test for Williams bars

Figure 3.29 shows the gauges that were used to measure humidity inside the CFT specimens, humidity inside the unsealed 20x40-in. plain concrete specimens, and the ambient humidity. LabView recorded the data from these gauges on 15-minute intervals throughout the whole test.

Figure 3.29. Humidity gauge

The humidity gauges were not suited for embedment in concrete, so a hole needed to be made in the concrete, into which the gauge was placed. Before the steel tubes and sonotubes were cast, four 5/8-in. holes were drilled into each tube, accommodating two 1/2-in. diameter rods with a length of 30 in. A total of eight rods were needed; two for each specimen. The rods were left in the holes during casting. After casting, the rods were rotated and moved back and forth every hour to prevent them from bonding with the concrete. After the concrete had cured sufficiently the rods were pulled out of the specimens, leaving a 1/2-in. diameter horizontal hole through the specimen. The humidity gauges were then inserted into the holes and the holes sealed from both ends. The process of inserting and removing a steel rod, followed by the insertion of a humidity gauge, was tested on a concrete cylinder before the experiment took place, and it seemed to work fine. A photograph of this test is shown in Figure 3.30.

Figure 3.30. A test for insertion of humidity gauges

3.3.2.2 Instrumentation of cylinder creep rigs

Figure 3.31 shows the cylinder creep rig test setup. The rig is designed to apply constant load to a stack of cylinders. It consisted of 3 steel plates; a top plate (Figure 3.31a), a middle plate (Figure 3.31e) and a bottom plate (Figure 3.31g). The dimension of the top plate was 15x15x2.5 in. and the dimensions of the middle and bottom plate were 20x20x2.5 in. Four threaded 1 in. diameter A449 steel rods (Figure 3.31c) with an axial stiffness of approximately 1000 kips/in. attached the steel plates to one another. (Hannesson, 2010)

Each rig had four coil springs (Figure 3.31f) to maintain a nearly constant load as the specimens shortened. Section A-A in Figure 3.31 shows the layout of the springs, which were concentrically placed around 1.024 in. holes (Figure 3.31l) that accommodate steel rods; to ensure even distribution of the spring stiffness. Each spring had a maximum compression of 2 in., the outside-diameter of each spring was 4-5/8 in. and they had a stiffness of 6.5 k/in. Therefore the total stiffness of the four springs was 26 k/in. and the maximum load that could be applied to them was 52 kips. (Hannesson, 2010)

Four C 127 x 0.098 mm steel supports (Figure 3.31k) were used to elevate the creep rigs to accommodate a hydraulic jack under the rigs. A single 60-kip jack (Figure 3.31i) was used to apply the prescribed stress to the concrete cylinders in the creep rigs. Jacking plate (Figure 3.31j)

with four 14-in. long threaded 1-in. diameter A449 steel rods and couplers (Figure 3.31h) was used elevate the jack. The dimension of the jacking plate was (14.5x14x2 in). (Hannesson, 2010)

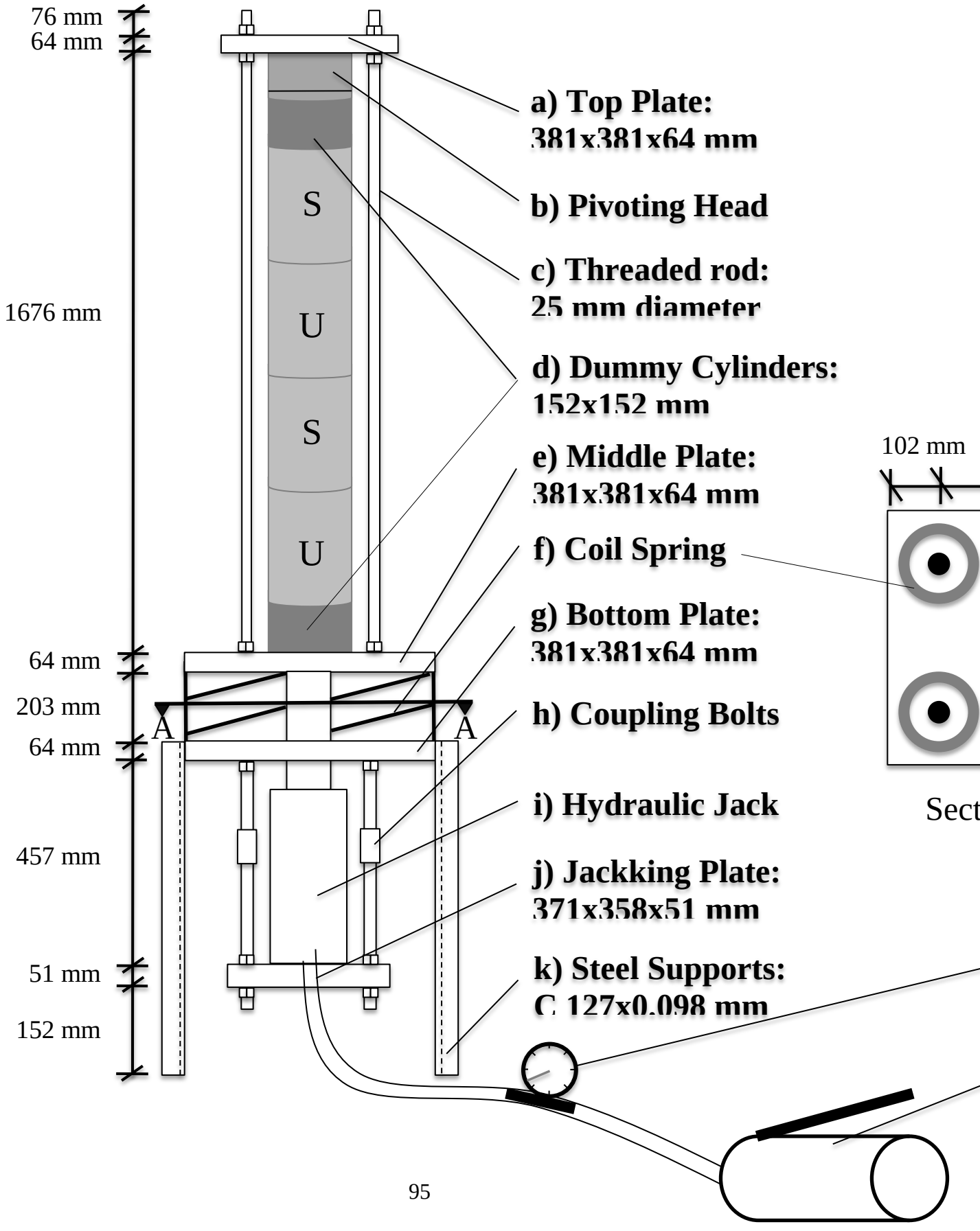
76 mm
64 mm
1676 mm
64 mm
203 mm
64 mm
457 mm
51 mm
152 mm
S
U
S
U
A
A
a) Top Plate:
381x381x64 mm
b) Pivoting Head
c) Threaded rod:
25 mm diameter
d) Dummy Cylinders:
152x152 mm
e) Middle Plate:
381x381x64 mm
f) Coil Spring
g) Bottom Plate:
381x381x64 mm
h) Coupling Bolts
i) Hydraulic Jack
j) Jackking Plate:
371x358x51 mm
k) Steel Supports:
C 127x0.098 mm
102 mm
Sect

Figure 3.31. Creep rig (Hannesson, 2010)

Figure 3.32 shows the detachable mechanical strain gauge (Whittemore Strain Gauge) that was used as a backup to measure the deformation of the specimens over time. The mechanical gauge reads increments of 0.0001 in. and has displacement capacity of 0.1 in. The mechanical gauge has two dial gauges. The larger dial gauge (Figure 3.32a) has scale from 0 to 100 in. and the smaller dial gauge (Figure 3.32b) has scale from 0 to 900 in. Targets (Figure 3.32f) were constructed to be glued on concrete cylinders to set gauge length that could change over time. Targets were designed to have rivets to accommodate the conical steel studs (Figure 3.32c) on the mechanical gauge. (Hannesson, 2010)

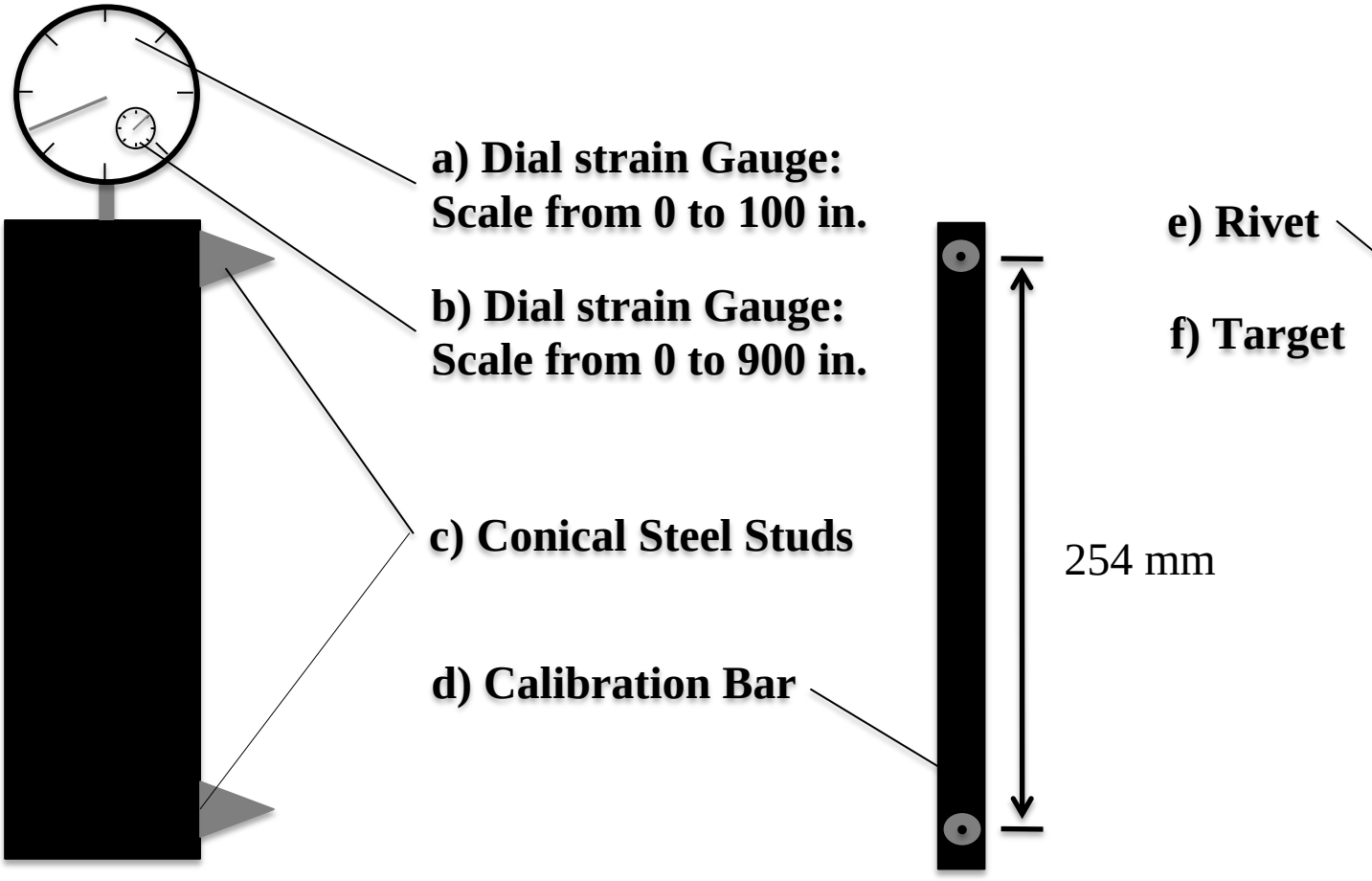

Figure 3.32. Whittemore strain gauge and target (Hannesson, 2010)

3.3.2.3 Test setup of CFT creep rigs

To create the creep rig, two 10 ft. segments were cut from a 60 ft. standard W24x94 steel beam section. The segments were then placed parallel to each other with 11.5 inches o/c, leaving a 2.5-in. gap between them since the flanges are 9 inches wide. The flanges of the two beams were then drilled with a 7/8 in. drill bit at prescribed locations and bolted together with a total of six 3x10x1/2-in. plates which each had two 7/8 in holes, spaced 7.5 inches o/c. Plates were placed diagonally on the flanges in alternating directions to brace the structure. Bolts used were standard ASTM A325 with a 3/4-in. diameter. (ASTM A325, 2009)

Two left-hand threaded Williams bars with a 2-in. outside thread diameter were cut to a length of 16 ft. After finding two suitable holes with 90 in. o/c in the strong floor, couplers that matched the selected Williams bars were screwed into the threads on the bottom of those holes. The Williams bars were then raised to a vertical position, placed in each hole, and screwed into the inner threads of the couplers. Four nuts were threaded on each bar to create two sets of two nuts tightened together. One mounting block was then welded onto each set of nuts and a vibrating wire strain gauge was placed between the blocks to monitor the load in the Williams bars. This configuration is shown in Figure 3.27. After pouring Hydrostone on top of the concrete in the tube and letting it cure for 24 hours, an 18-in. diameter, 3/4-in. thick steel bearing plate was placed on top, with an 18 in. diameter, 3/4 in thick cotton duck bearing pad in between the Hydrostone and the steel plate.

Figure 3.33. Belleville spring washer

The two steel beams were raised up with a crane and placed on top of the circular steel bearing plate with the two Williams bars inside the 2.5-in. gap between the beams. A 12x12x1.75-in. bearing plate with a 2.25-in. hole in the middle and a 7/8-in. hole in each corner was then placed around each bar and bolted onto the pre-drilled beams through the four corner holes. Bolts used were standard ASTM A325 with a 3/4-in. diameter. (ASTM A325, 2009). Two stacked Belleville spring washers, similar to the one shown in Figure 3.33, were then placed on top of each bearing plate and two 1.25-in. thick 8x8 in. bearing plates were placed on top of the washers. Those also had a 2.25-in. diameter hole in the center. Finally, a regular washer was placed on top of those bearing plates and a Williams nut threaded down to that washer and hand tightened. A drawing of the setup of bearing plates, Belleville washers and nut can be seen in Figure 3.18.

3.3.2.4 Test setup of cylinder creep rigs

Total of eight 6x12 in. cylinders were used in the creep and shrinkage test for each type of concrete. The specimens were prepared the day before testing so the epoxy would be fully cured at day of testing. The required gauge length was 10 in., since the mechanical gauge had displacement capacity limited to only 0.1 in. (Hannesson, 2010)

Each of the cylinders was instrumented with two vibrating wire strain gauges as well as four sets of targets located diametrically at opposite sides of the specimens. Figure 3.34 and Figure 3.35 shows layout of the targets and vibrating wire strain gauges. The blocks for the vibrating wire strain gauges were spaced 6.5 in. apart and the distance between the targets was 10 in. High viscous epoxy was used to glue the blocks and the targets on the cylinders.

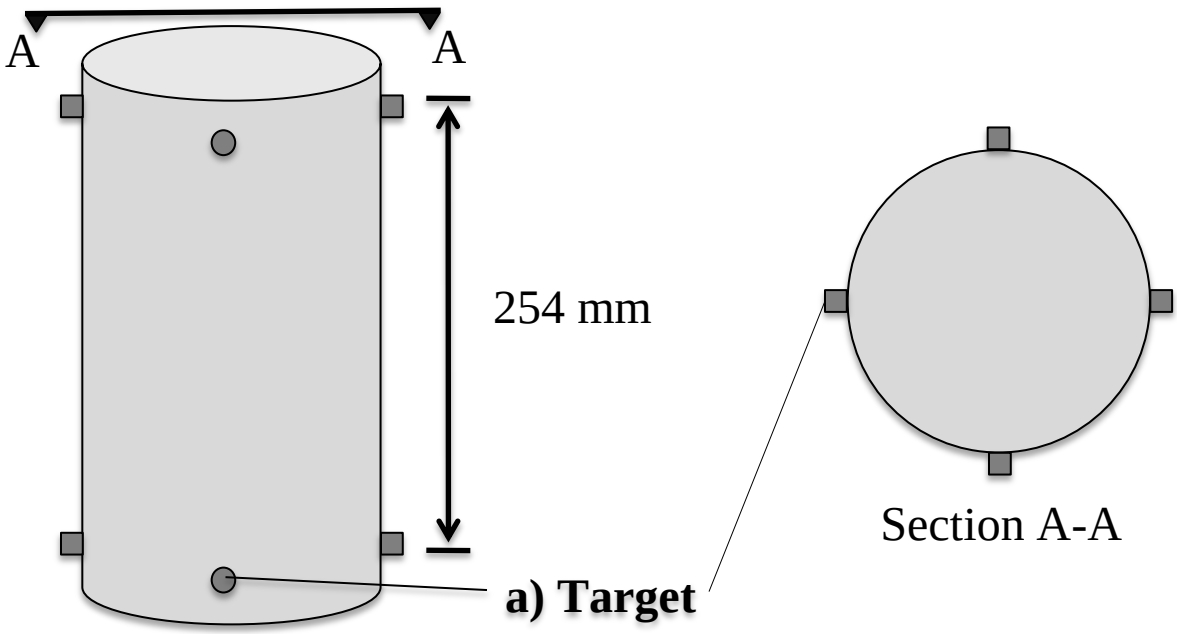

Figure 3.34. Target layout (Hannesson, 2010)

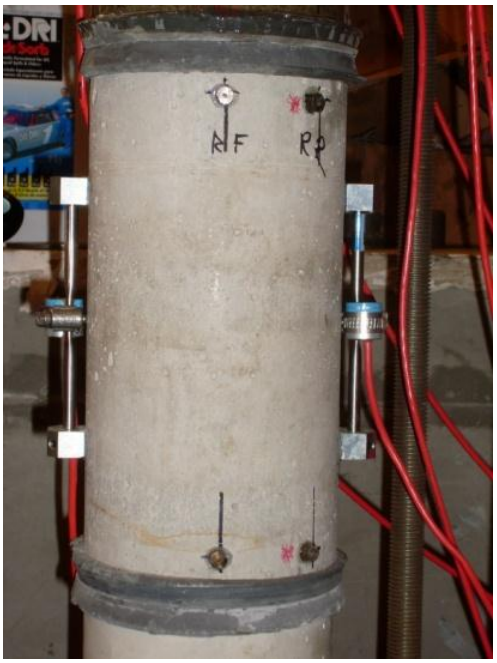

Figure 3.35. Photograph of the cylinder instrumentation

After gluing the targets and mounting blocks on the cylinders, four of the eight cylinders were sealed with two layers of low viscous clear coat epoxy (System three epoxy). The epoxy needs to cure for eight hours between layers. Low viscous epoxy was used to make the sealing of the

cylinder easier. The second layer was allowed to cure for 24 hours before the test began. (Hannesson, 2010)

Figure 3.36. Photograph of the creep rigs with the installed cylinders

At the day of testing, eight cylinders (two sealed and two unsealed of each type of concrete), were stacked in each creep rig (Figure 3.36). The cylinders are stacked from the bottom in the order unsealed, sealed, unsealed, sealed as shown in Figure 3.31. Before stacking the cylinders in the rig, 6x6 in. dummy cylinder (Figure 3.31d) was placed between the steel bearing plates and the test specimens at each end of the stack so the tested cylinders would not touch the steel plates. A pivoting head (Figure 3.31b) was placed on the top of the stack to avoid creating load eccentricity to the stack. Finally, the top plate (Figure 3.31a) was lowered until the plate was sitting on the stack. Then, the nuts on both sides of the top plate were incrementally hand tightened so the connection between the rod and the plate would be fixed. Since the connection is fixed, it provides increased bending resistance of the rods. The nuts below the middle plate

maintained the tension in the rods throughout the test. The nuts above the middle plate were kept loose, but close to the plate. Their purpose was to prevent the coil springs (Figure 3.31f) from extending in the event of unexpected cylinder failure. (Hannesson, 2010)

The other eight cylinders (two sealed and two unsealed from each type of concrete) were placed on the footings of the CFT specimens so they would be in similar height as the loaded cylinders. These cylinders remained unloaded throughout the test and were used to determine the drying shrinkage strain. Figure 3.37 shows a photograph of the SCM shrinkage cylinders.

Figure 3.37. SCM shrinkage cylinders

Environmentally controlled room was not available for the creep test. Instead, the creep rigs were placed in region as far away from windows and doors as possible, to minimize the change in temperature. The ambient temperature and humidity change during the test is graphically shown in **Error! Reference source not found.**.

3.3.2.5 Procedure - CFT creep rigs

After completing the test setup, as described in section 3.3.2.3, the CFT rigs were loaded. To apply stress to the concrete-filled tube, the 300-kip ram was positioned as described in section 3.3.2.1, and a pump connected to the ram with two hoses, one of which was connected to a pressure gauge. The pressure gauge had been calibrated with the ram in 20-kip increments, so

that the load in the Williams bars could be monitored both through the pressure gauge and the vibrating wire gauge connected to the double-nut configuration on the bar. Pressure was applied by a switch connected to the pump until the correct value on the pressure gauge was reached. The nuts on the Williams bar above the top bearing plate were hand tightened. Pressure was then released and the ram was moved to the second specimen. A photograph of the ram ready to stress a specimen is shown in Figure 3.38.

Figure 3.38. 300-kip ram ready to stress a CFT specimen

The Williams bar was loaded in 40-kip increments in four-minute intervals, since that is the shortest time interval available for the data acquisition system (Multilogger) with this many gauges. One Williams bar was stressed to 180 kips, resulting in about a 160-kip force in the other Williams bar and a 340-kip force in the concrete-filled tube. This discrepancy is discussed in Chapter 4. The load was later changed to 180 kips in each Williams bar by applying the ram to both bars of each specimen, resulting in a 360-kip force in the concrete-filled tube. The strain values were corrected to account for the change in load.

The Multilogger was set to take readings at four-minute intervals the first few weeks of the test. After that, the interval was changed to twelve hours, but changed again to four minutes during and for a few hours after restressing the specimens. The specimens had to be restressed quite frequently due to a rather high rate of drop in load. This is discussed in detail in Chapter 4. Figure 3.39 shows the Multilogger data window. The values in the white cells represent the channels. One vibrating strain gauge has two channels; one for microstrain readings and one for temperature readings. The values in the blue cells indicate those values for the corresponding channel.

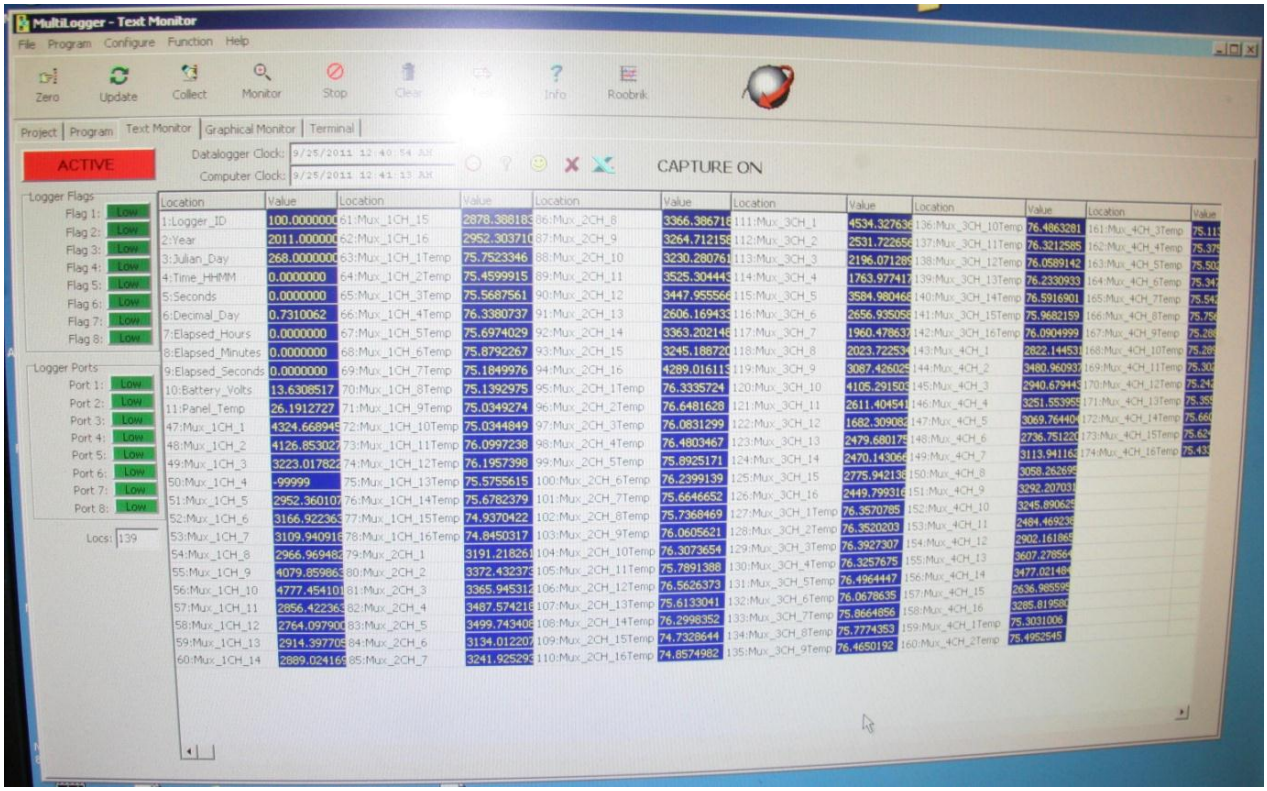

Figure 3.39. Multilogger data window

Strain in the steel tube at each height location was obtained by taking the average of the two gauges at that height. Strain in the concrete at each height location was obtained only from the center gauges at that height, due to the fact that the load differential mentioned above creates a moment in the specimen so that the concrete gauges close to the edge of the tube will always read a strain value that is too small or too large, depending on which Williams bar load is larger.

3.3.2.6 Procedure - Cylinder creep rigs

After completing the test set up, as described in section 3.3.2.3, the cylinder creep rigs were loaded. To apply stress to the cylinders, the hook of the crane above the strong floor was first positioned directly above the top plate of the rig. A long, wide strap was then placed under the rig and the ends elevated until they could be placed around the hook. The jacking plate (Figure 3.31j) was placed on the strap, so that it could be raised using the crane above the strong floor, since it is too heavy to lift by hand. The crane was raised and the four rods of the jacking plate were connected to the rig rods using the couplers (Figure 3.31h). The nuts under the jacking plate were then adjusted until the desired height of the plate, based on the height of the hydraulic jack (Figure 3.31i), was reached. Care was taken to make the plate perfectly level. The jack was then placed on the center of the jacking plate. The crane was lowered, and a pump (Figure 3.31n) fitted with a pressure gauge (Figure 3.31m) connected to the jack. The pressure gauge had been calibrated with the jack in 5-kip increments, so that the strains could be monitored in these increments during initial loading. Pressure was applied with the pump until the correct value on the pressure gauge was reached. The nuts under the bottom plate (Figure 3.31g) were then hand-tightened and pressure released from the jack.

Strain readings were automatically taken with the data acquisition system as described in section 3.3.2.5. However, backup readings were taken with a Whittemore mechanical strain gauge, shown in Figure 3.32.

To take the strain reading, the two conical steel studs (Figure 3.32c) of the mechanical gauge are placed in the rivets of the target. Before taking set of measurement, the mechanical gauge is calibrated with a mild steel calibration bar (Figure 3.32d). The calibration bar has the length 10 in. at 68°F, so if the ambient temperature is either higher or lower than 68°F the length must be corrected using the thermal expansion coefficient for mild steel. The correct length of the calibration bar can be evaluated using equation (3-2):

$$L_c = 10(1 + \Delta T\alpha) \quad \textbf{(3-2)}$$

Where L_c is the corrected length of the calibration bar, ΔT is the difference of ambient temperature from 68°F and α is the thermal expansion coefficient for mild steel and is equal to

0.0000070 1/°F. Equation (3-3) is used to find the distance between the targets relative to the calibration bar:

$$L_T = \frac{\varepsilon_T - \varepsilon_c}{10000} + L_c \quad \textbf{(3-3)}$$

L_T is the distance between the targets, ε_T is the strain value between the targets using the mechanical gauge and ε_c is the strain value of the calibration bar using the mechanical gauge. Figure 3.40 shows a photograph of the mechanical gauge used to measure the strains. (Hannesson, 2010)

Strain readings were taken immediately before and immediately after initial loading, and then again two hours later. Readings were taken daily for one week, then weekly for one month and then monthly after that. Before taking each strain reading, the applied load on the rig was adjusted with the hydraulic jack to prescribe the load. Strain readings on the shrinkage specimens were taken on the same schedule as for the specimens placed in the creep rig. (Hannesson, 2010)

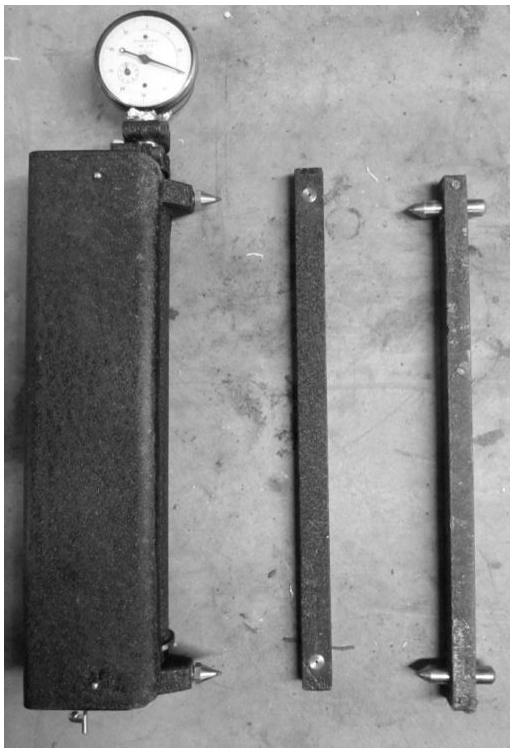

Figure 3.40. Whittemore mechanical strain gauge and calibration bar (Hannesson, 2010)

Strain for each cylinder was obtained by taking the average of the four sides. Drying shrinkage was obtained as the difference between total and autogenous shrinkage measured on unsealed and sealed specimens, respectively. Total creep was calculated as the difference between strains from the unsealed specimens under loading and the unsealed shrinkage samples. Similarly, basic creep was obtained as difference between sealed loaded and sealed shrinkage specimens. Finally drying creep was obtained as the difference between total and basic creep. (Hannesson, 2010)

3.3.3 Seismic performance tests

The experiments were implemented on a self reacting test rig developed by Angela Kingsley shown in Figure 3.41. The rig was centered underneath a Baldwin Universal Testing machine with a compressive capacity of 2400 kips. Each specimen was leveled and grouted into place

using Hydrostone. The 220 kip actuator was attached to the column 72 in. above the surface of the footing. (Lee, 2011)

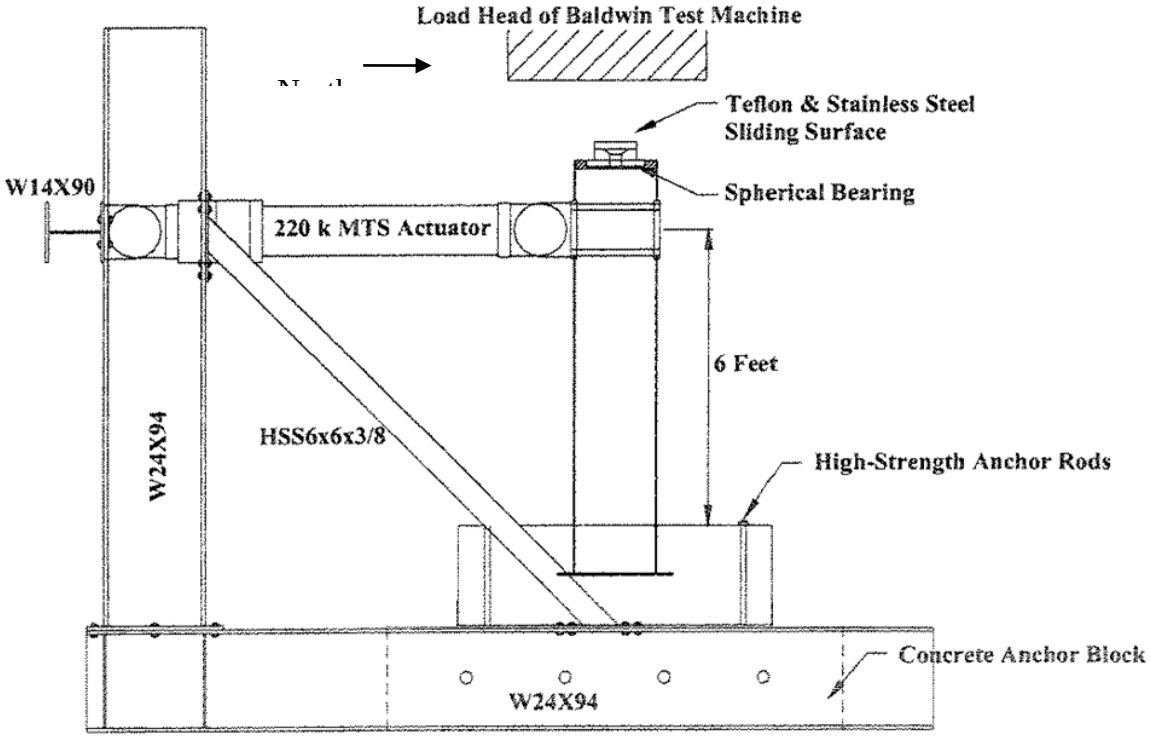

Figure 3.41. Self reacting rest rig (Kingsley, 2005)

Due to the expected lateral motion of the column and the high axial loads, special attention was paid to the bearing surface between the Baldwin crosshead and the column. Figure 3.42 illustrates the solution implemented to facilitate the necessary rotation. A spherical bearing with bearing plate was placed on the top of the column. Polytetrafluoroethylene (Teflon) was fixed to the top and sides of the bearing plate using epoxy. A channel was also fixed to the center of the Baldwin crosshead. Mirror finish stainless steel was placed inside the channel on all sides. Before lowering the crosshead, a silicone lubricant was placed on the Teflon surfaces. The purpose of this was to allow a near frictionless surface on the end of the column while restricting out of plane motion. (Lee, 2011)

In the presence of high axial pressure, such contact surfaces have been shown to have a coefficient of well below 0.01 (Cambell & Kong, 1988)

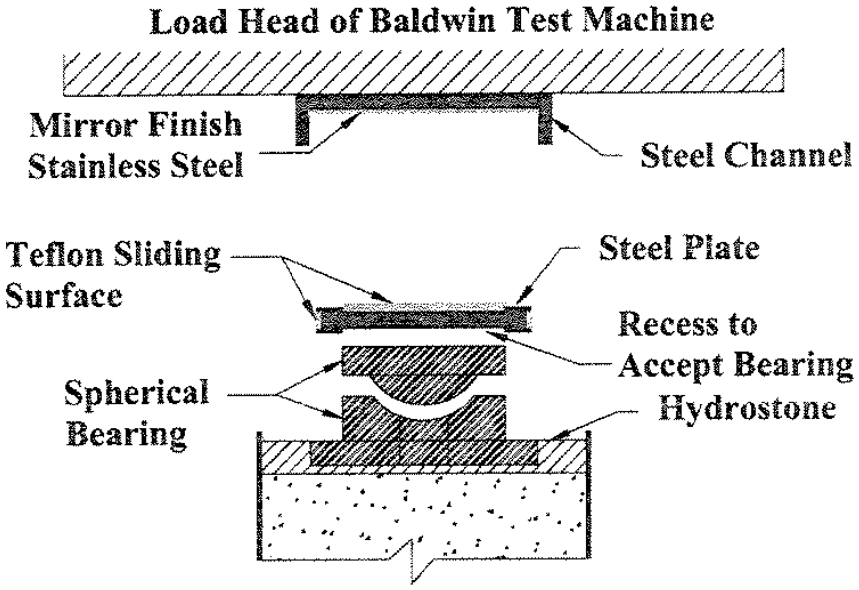

Figure 3.42. Axial load apparatus (Kingsley, 2005)

3.3.3.1 Load protocol

Ten percent of the gross axial capacity of the column was applied to each specimen using the Baldwin test machine. The axial load was applied before the horizontal loading protocol began and was held constant for the duration of the experiment. The horizontal load was displacement controlled using an internal linear variable differential transducer (LVDT) in the actuator. The lateral load protocol used was based on a previous tests completed by O'Neill, who used the ATC-24 protocol (Applied Technology Council (ATC), 1992). The low amplitude cycles were based on a yield displacement of 0.6 in. Post yield cycles were adjusted to match the history of the previous specimens tested. The protocol used for testing is shown in Table 3.5. The lateral load was oriented in the north-south direction where positive drift was considered south. (Lee, 2011)

Table 3.5. Lateral load protocol based upon 50 ksi nominal yield strength

Cycles	Target Column Increment (Δyield)	Target Column Displacement (inches)	Target Column Drift Ratio %	Approximate Lateral Load at Target Column Displacement (kips)	Estimated Back Rig Beam Displacement (inches)	Actuator Input Displacement (inches)
1-2	0.25	0.1494	0.21	65	0.18	0.33
3-4	0.5	0.2988	0.42	90	0.26	0.55
5-6	0.75	0.4482	0.62	120	0.34	0.79
7-9	1	0.5976	0.83	147	0.42	1.02
10-12	1.5	0.8964	1.25	175	0.50	1.39
13-15	2	1.1952	1.66	185	0.53	1.72
16-17	4	2.3904	3.32	200	0.57	2.96
18-19	6	3.5856	4.98	200	0.57	4.15
20-21	8	4.7808	6.64	200	0.57	5.35
22-23	10	5.976	8.30	200	0.57	6.54

3.3.3.2 Instrumentation of CFTs for seismic performance tests

A variety of instruments were used to capture information of interest: potentiometers, strain gauges, inclinometers and a positioning system called Optotrak. A list of which instruments were used on each test can be found in Table 3.6. This section briefly describes the location of each instrument and how it was used. (Lee, 2011)

Table 3.6. Specimen instrumentation

Specimen	Instrumentation used			
	Strain gauges	Inclinometers	Potentiometers	Optotrak
7-50	X	X	X	X
8-50-SCM	X	X	X	X

Three different types of potentiometers were used: string potentiometers, round potentiometers, and a small potentiometer made by Duncan Electronics. Locations for each potentiometer can be found in Figure 3.43 and cataloged in Table 3.8.

Small Duncan potentiometers were placed on the footing as well as the rig anchor block to account for any horizontal or vertical movement that might occur between the specimen footing and the anchor block or the anchor block and the laboratory floor. The average range of a Duncan potentiometer is 1.5 in. (Lee, 2011)

String potentiometers were used to measure horizontal movement of the column. The average range of these potentiometers is 10 in. with longer sting potentiometers reaching a 20 in. range. The housing of the potentiometers was fixed to a reference column bolted to the test floor, as can be seen in Figure 3.43. (Lee, 2011)

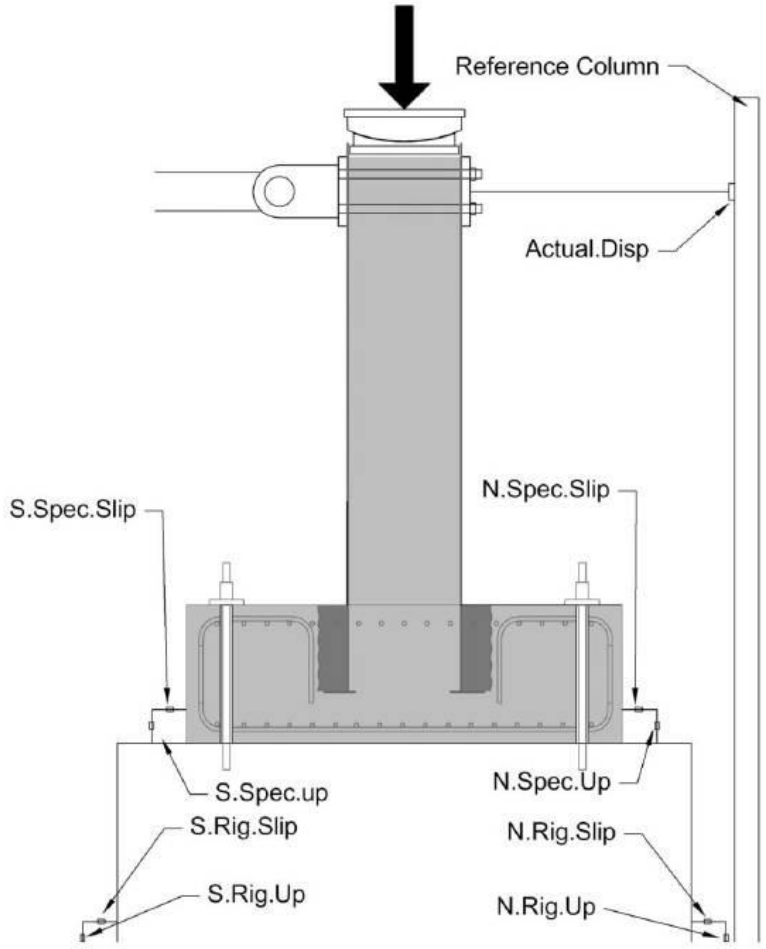

Figure 3.43. Potentiometer locations (Lee, 2011)

Inclinometers were glued to the tube in both tests. The inclinometers were placed on the east side of the columns of both specimens to be as close to the data acquisition system as possible. The inclinometers measure rotation and each have a range exceeding 40 degrees in each direction, but were calibrated to only a little more than the expected maximum rotation of the tube. Inclinometers were centered on the east side of the tube at locations 2 in., 8 in., 16 in., and 24 in. above the surface of the footing as shown in Figure 3.44 and cataloged in Table 3.8.

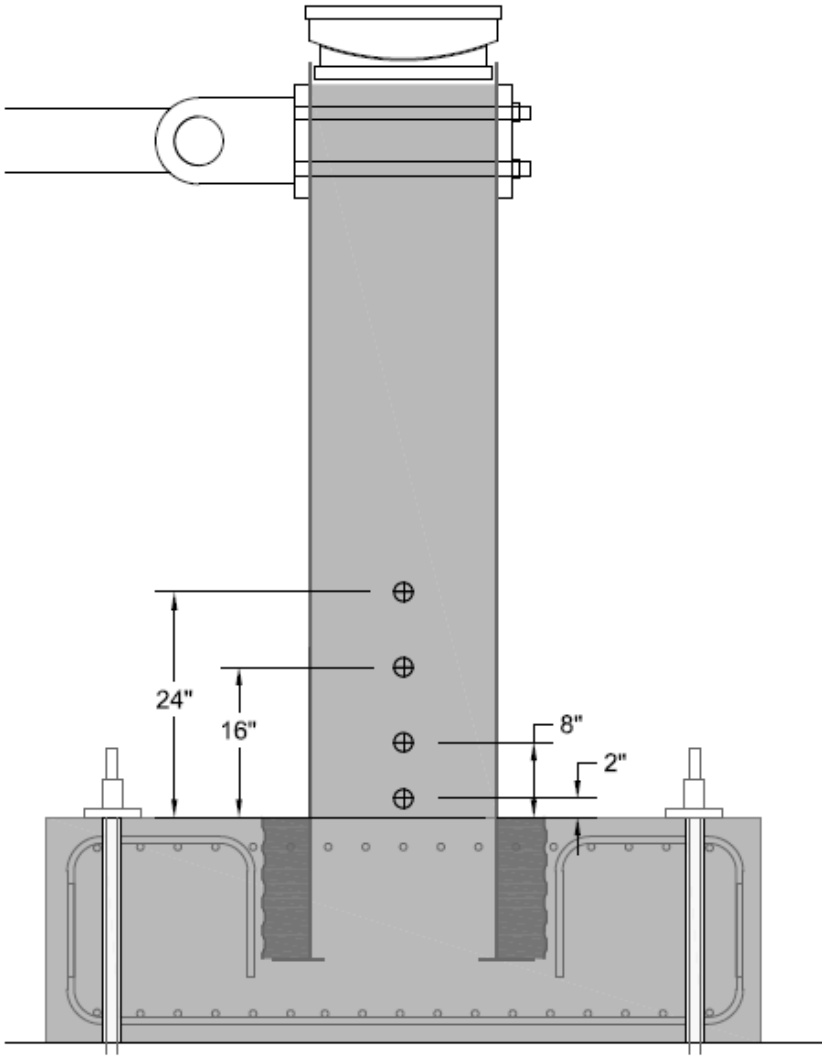

Figure 3.44. Inclinometer locations

Uniaxial strain gauges were placed longitudinally on the tube in several locations along the north and south ends of the column shown in Figure 3.45 and cataloged in Table 3.7. Ten gauges were also placed below the surface of the footing on the north side of the tube; two gauges in each cardinal direction except south, and two gauges at 45 degree angles from the cardinal directions. All gauges were placed longitudinally. Each gauge had a 5 mm gauge length and was manufactured by Tokyo Sokki Kenkyujo Co., Ltd with a manufacturer's designation of YFLA-5-5L.

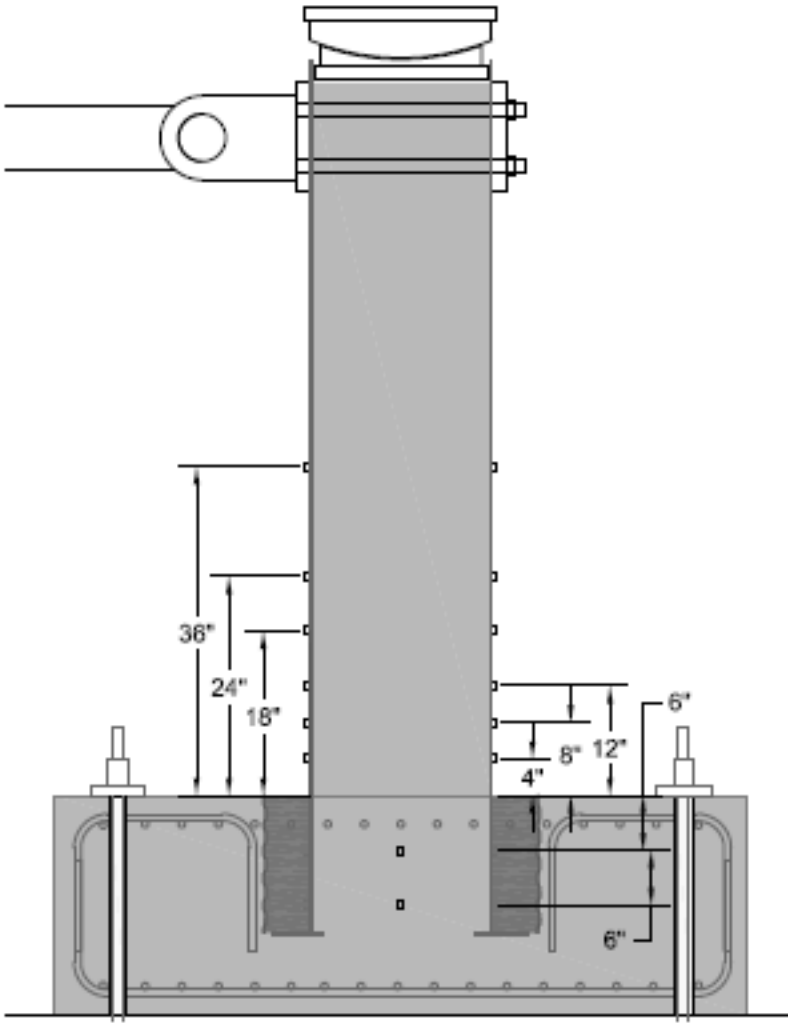

Figure 3.45. Strain gauge locations

The Optotrak Certus motion capture system was used to capture the shape of the tube. The primary goal of using this system was to better capture the buckled shape of the tube. The system was implemented by attaching small LED markers to the surface of the tube using adhesive foam. In conjunction with the markers, an Optotrak sensor was placed in the line of sight of the markers. Each Optotrak sensor contains three precision cameras. The sensor triangulates the position of each marker and reports it to recording software. Two sensors were available so markers were placed on the north and south side of the tube as shown in Figure 3.46. (Lee, 2011)

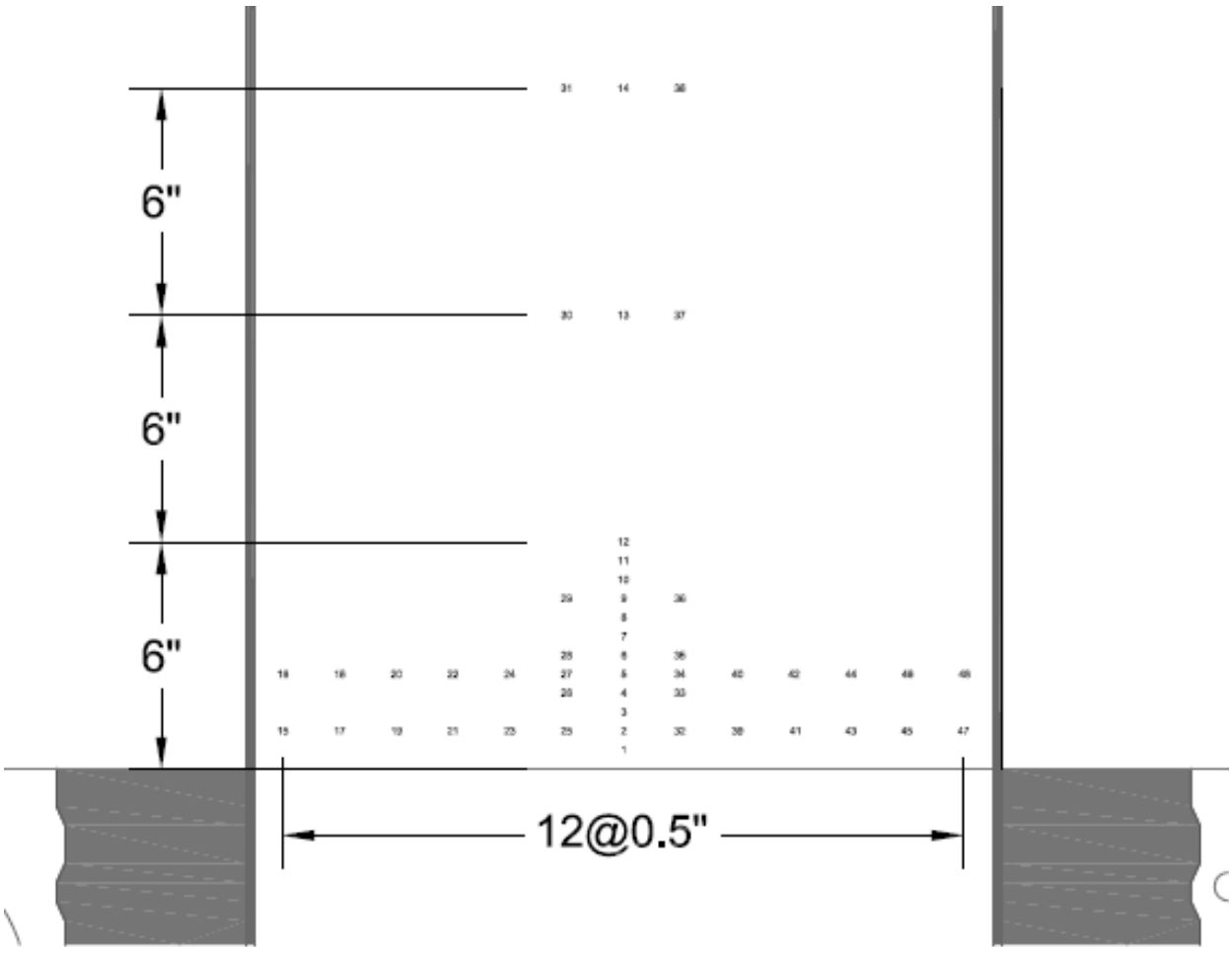

Figure 3.46. Optotrak marker layout for 7-50 & 8-50-SCM north & south faces

Table 3.7. Strain gauge identification

LabView Output Designation	Location
SG North -12 in.	North Side 12 inches below footing surface
SG North -6 in	North Side 6 inches below footing surface
SG North 4 in.	North Side 4 inches above footing surface
SG North 8 in.	North Side 8 inches above footing surface
SG North 12 in.	North Side 12 inches above footing surface
SG North 18 in	North Side 18 inches above footing surface
SG North 24 in	North Side 24 inches above footing surface
SG North 36 in	North Side 36 inches above footing surface
SG South 4 in	South Side 4 inches above footing surface
SG South 8 in	South Side 8 inches above footing surface
SG South 12 in	South Side 12 inches above footing surface
SG South 18 in	South Side 18 inches above footing surface
SG South 24 in	South Side 24 inches above footing surface
SG South 36 in	South Side 36 inches above footing surface
SG West -12in	West Side 12 inches below footing surface
SG West -6in	West Side 6 inches below footing surface
SG East -12in	East Side 12 inches below footing surface
SG East -6in	East Side 6 inches below footing surface
SG NW -12in	Northwest Side 12 inches below footing
SG NW -6in	Northwest Side 6 inches below footing
SG NE -12in	Northeast Side 12 inches below footing
SG NE -6in	Northeast Side 6 inches below footing surface

Table 3.8. Instrumentation data identification

Labview Output Designation	Abbreviated Designation	Instrument Type	Location
Actuator Beam Displ.	Beam.Disp.	Round	Center span of beam opposite the actuator
N Actual Displ.72 in	Actual Displ.	String	Fixed to North Tower 72 in above footing
S Horiz. Displacement 18 in	S.Horiz.72in	String	Fixed to South Tower 72 in above footing
N Specimen Uplift	N.Spec.Up	Duncan	Fixed to North Face of Footing
N Specimen Slip	N.Spec.Slip	Duncan	Fixed to Anchor Block Surface North Side
N Rig Slip	N.Rig.Slip	Duncan	Fixed to Laboratory Floor North Side
N Rig uplift	N.Rig.Up	Duncan	Fixed to North Face of Anchor Block
South Specimen Uplift	S.Spec.Up	Duncan	Fixed to South Face of Footing
South Specimen Slip	S.Spec.Slip	Duncan	Fixed to Anchor Block Surface South Side
S Rig Uplift	S.Rig.Up	Duncan	Fixed to South Face of Anchor Block
S Rig Slip	S.Rig.Slip	Duncan	Fixed to Laboratory Floor South Side
Inclinometer 2 in	Incl.2in	Inclinometer	2 inches above Footing Surface, east side
Inclinometer 8 in	Incl.8in	Inclinometer	8 inches above Footing Surface, east side
Inclinometer 16 in	Incl.16in	Inclinometer	16 inches above Footing Surface, east side
Inclinometer 24 in	Incl.24in	Inclinometer	24 inches above Footing Surface, east side

Chapter 4: Results from long-term experiments

Creep and shrinkage strain was determined for the concretes in the tubes and for the cylinders made from the same concrete mixes. Data was taken in four-minute intervals for the first three weeks and every twelve hours after that. The time interval was changed back to four minutes for a short period of time before, during, and after every restressing of the specimens. The reason for the frequent restressing is discussed in Section 4.1. The creep and shrinkage tests were performed as described in section 3.3.2.

Results from the two CFT specimens were compared, showing quite a difference in behavior. Initial elastic strains, total concrete strains, total steel strains, creep strains and creep coefficients were compared. Sealed and unsealed cylinder specimens were compared for total strain, shrinkage strain, creep strain and creep coefficient. Finally, total strain and creep coefficient of CFTs was compared to that of the cylinder specimens for both types of concrete.

4.1 Results from CFT specimens

Long-term tests were performed on the two large scale CFT specimens filled with the two different concretes specified in Table 3.3 and Table 3.4. The specimens had a steel-to concrete ratio of 5.2%. Shrinkage in CFTs was determined to be negligible, as discussed later in this chapter. Both specimens were loaded fourteen days after casting. The tests were performed as described in Section 3.3.2. Strain was data measured with the vibrating wire strain gauges and collected by the Multilogger data acquisition system.

The sum of the tensile load in the two Williams bars equals the compressive load in the CFT. Very early on in the creep experiment it became apparent from the data obtained from the load gauges on the bars, shown in Figure 3.27, that the load was decreasing at a higher rate than expected from the creep of the concrete alone. Furthermore, the vibrating wire strain gauges inside the specimens and on the tube surfaces showed elongation of the specimen instead of shortening because the decrease in elastic strain of the specimens, due to the decrease in load, was higher than the increase in time-dependent strain.

Inspection of the top of the specimens indicated that the cotton duck pad between the circular bearing plate and the hydrostone layer was creeping and causing this elongation. A visible amount of creep also occurred in the hydrostone layer.

The original thickness of the pad was 3/4 in. but at the end of the experiment the measured thickness was 5/8 in., or approximately 167.000 με. The axial stiffness of the pad was approximately 9500 k/in, which is less than 0.5% of the axial stiffness of the CFT specimen. Therefore, the initial deflection of the pad was higher than that of the CFT. Experiments on the cotton duck pads used in this research program (Lehman, Roeder, Larson, & Curtin, 2003) showed that at 1.4 ksi stress, the instantaneous strain of the pads is approximately 50.000 με, so the total instantaneous deflection of a 3/4-in. thick pad is around 0.0375 in. The average instantaneous deflection of the CFT specimens was less than 200 με, so the total instantaneous deflection of an 86-in. long specimen was approximately 0.017 in. The total deflection of the cotton duck pads was also found to have doubled after one week of sustained loading in the experiment; that is the creep strain had reached the same value as the initial strain. This is a much faster creep rate than can be expected in concrete. This behavior of the pad and the hydrostone was not considered in design of the CFT creep rig, so the rapid drop in load was the result. Therefore, the rig was restressed regularly. It was stressed above the initial value so that the average load throughout the experiment would be approximately the same as the initial load. Figure C-1 and Figure C-2 in **Error! Reference source not found.** show the actual measured load in each CFT specimen during the experiment.

The strain curves from the embedded vibrating wire strain gauges were adjusted for the load decrease by subtracting the change in elastic strain, due to the load decrease, from the total strain. First, a coefficient for change in elastic strain per force unit between two instances of restressing was found by:

$$C = \frac{\varepsilon_a - \varepsilon_b}{F_a - F_b} \qquad \textbf{(4-1)}$$

where:

ε_a = Total strain after restressing

ε_b = Total strain before restressing

F_a = Load in CFT after restressing

F_a = Load in CFT before restressing

This resulted in C = 0.58 με/kip and C = 0.66 με/kip on average for the SCM and the SCC concrete, respectively. In plain concrete specimens, a higher coefficient would be expected for the SCM than the SCC since the SCM is not as stiff. The reason for this difference is that the steel tube of the SCM specimen takes more load than the steel tube of the SCC specimen, as discussed later in this chapter.

The change in load at each time step was described by:

$$\Delta F(t) = F_i - F(t) \quad \textbf{(4-2)}$$

where:

F_i = Initial load in the specimen

F(t) = Load at a given time

If the load at a given time was lower than the initial load, the adjusted elastic strain at that time was higher than the measured. If the load at a certain time was higher than the initial load, the adjusted elastic strain was lower than the measured. This procedure can be quantified by the equation:

$$\varepsilon(t)_{adj.} = \varepsilon(t)_m - \Delta F(t) * C \quad \textbf{(4-3)}$$

where:

$\varepsilon(t)_{adj.}$ = adjusted value of the total strain

$\varepsilon(t)_m$ = measured value of the total strain

This procedure of adjusting the strains for load differential over time resulted in a smooth and continuous curve for the time-dependent strains, as can be seen in Figure 4.5 for example. Because of the decrease in load, the unadjusted curve was discontinuous and characterized by a large increase in strain at moments of restressing, as can be seen in Figure D-6 to Figure D-6 in **Error! Reference source not found.**. The steel strains were adjusted with a similar procedure.

At initial loading of the CFT specimens, one of the two Williams bar was stressed with the 300-kip ram shown in Figure 3.38. It was expected that equilibrium would result in approximately the same load in the other Williams bar. This was not the case, though the difference was not large. Stressing one Williams bar to 180 kips resulted in 161-kip and 154-kip loads in the other bar for the SCM and SCC specimen, respectively. This is equivalent to applying the load with about three inches of eccentricity and may have been caused by the rotation of the cotton duck pad. When the tube was restressed, care was taken to apply equal loads to both of the Williams bar to minimize eccentricity.

4.1.1 Total strain

Total strain in concrete is the sum of elastic, creep, shrinkage and thermal strains. Changes in thermal strain were accounted for by the VWSG, but they were very small due to the small variations in temperature in the testing area. In the CFT specimens, drying shrinkage was determined to be negligible, based on results from previous research programs and results from total time-dependent strain in CFT compared to drying shrinkage strain of sealed cylinders. However, autogeneous shrinkage may have taken place, which is a continuation of hydration process after the concrete hardens, rather than moisture loss. The majority of autogeneous shrinkage takes place within the first few days of curing and was assumed to be complete by the time the specimens were loaded. Strains were not monitored until the specimens were loaded, so autogenous shrinkage was not measured.

Time-dependent strains in steel are not a result of creep since steel does not creep unless it is loaded at a very high temperature. The steel strains are due to transfer of load from the concrete to the steel, resulting from concrete creep and bond between steel and concrete. For a specimen loaded through the concrete core only, there will always be both initial and time-dependent strains in the steel when the specimen is subject to sustained loading unless there is absolutely no

bond between the concrete and the steel, as some previous research programs ((Terrey, Bradford, & Gilbert, 1994), (Ichinose, Watanabe, & Nakai, 2001)) have tried to accomplish. The degree of these strains depends on how much bond there is, as mentioned before. Theoretically, no bond results in zero longitudinal strains in the steel (hoop strain only), while perfect bond results in steel strains identical to concrete strains. The latter is analogous to loading the steel and the concrete uniformly, as has been done in most previous research programs.

4.1.1.1 Strains at initial loading

Initial loading occurred in approximately 80-kip increments, apart from the last increment, which was smaller. Table 4.1 and Table 4.2 display the strain changes in the steel tube during the initial loading of the SCM and SCC specimens, respectively. The number in the subscript denotes the height level in inches above the footing surface. Figure 4.1 graphically illustrates the difference in behavior. As can be seen, the SCC concrete seems to react with the tube sooner than the SCM concrete which might indicate that the SCM concrete has experienced more autogeneous shrinkage prior to loading than the SCC concrete. This can be concluded from the strain per force unit that the steel in the SCC specimen displays after the first load increment, which is twice that of the SCM specimen. As the load increases, this difference decreases and in the last loading increment, the steel in the SCM specimen shows about 55% higher strain per unit force. As the concrete expands, the lateral pressure between the concrete and the steel increases. As a result, friction increases which leads to more bond. The SCM concrete therefore seems to expand more, and once it has overcome the small gap between itself and the steel due to autogenous shrinkage, it bonds more with the steel, which is evident from the last loading increment. More expansion in the SCM concrete may be due to the large amount of unreacted fly ash and slag. The excess water cannot escape through the steel, causing more expansion than in the SCC concrete.

Table 4.1. Steel strains at different heights in SCM specimen during initial loading

Load (kips)	ΔLoad (kips)	ε_{56} (με)	$\Delta\varepsilon_{56}$ (με)	$\Delta\varepsilon_{56}$/ ΔLoad (με/kip)	ε_{32} (με)	$\Delta\varepsilon_{32}$ (με)	$\Delta\varepsilon_{32}$/ ΔLoad (με/kip)	ε_{56} (με)	$\Delta\varepsilon_{8}$ (με)	$\Delta\varepsilon_{8}$/ ΔLoad (με/kip)	ε_{avg} (με)	$\Delta\varepsilon_{avg}$ (με)	$\Delta\varepsilon_{avg}$/ ΔLoad (με/kip)
83	83	36	36	0.43	36	36	0.43	40	40	0.48	37	37	0.45
161	78	70	34	0.44	76	40	0.52	81	41	0.53	76	39	0.49
241	80	102	33	0.41	116	40	0.50	120	39	0.48	113	37	0.46
315	74	130	27	0.37	156	40	0.54	160	40	0.54	149	36	0.49
341	26	143	13	0.51	177	21	0.78	181	21	0.78	167	18	0.69

*numbers in subscript indicate height above footing surface (inches)

Table 4.2. Steel strains at different heights in SCC specimen during initial loading

Load (kips)	ΔLoad (kips)	ε_{56} (με)	$\Delta\varepsilon_{56}$ (με)	$\Delta\varepsilon_{56}$/ ΔLoad (με/kip)	ε_{32} (με)	$\Delta\varepsilon_{32}$ (με)	$\Delta\varepsilon_{32}$/ ΔLoad (με/kip)	E_{8} (με)	$\Delta\varepsilon_{8}$ (με)	$\Delta\varepsilon_{56}$/ ΔLoad (με/kip)	ε_{avg} (με)	$\Delta\varepsilon_{avg}$ (με)	$\Delta\varepsilon_{avg}$/ ΔLoad (με/kip)
73	73	51	51	0.70	75	75	1.03	69	69	0.95	65	65	0.89
152	80	87	36	0.45	118	43	0.54	113	44	0.55	106	41	0.51
235	82	111	25	0.30	153	36	0.43	151	39	0.47	138	33	0.40
300	66	127	16	0.24	181	28	0.42	183	32	0.49	164	25	0.38
334	34	136	9	0.25	197	17	0.49	203	20	0.58	178	15	0.44

*numbers in subscript indicate height above footing surface (inches)

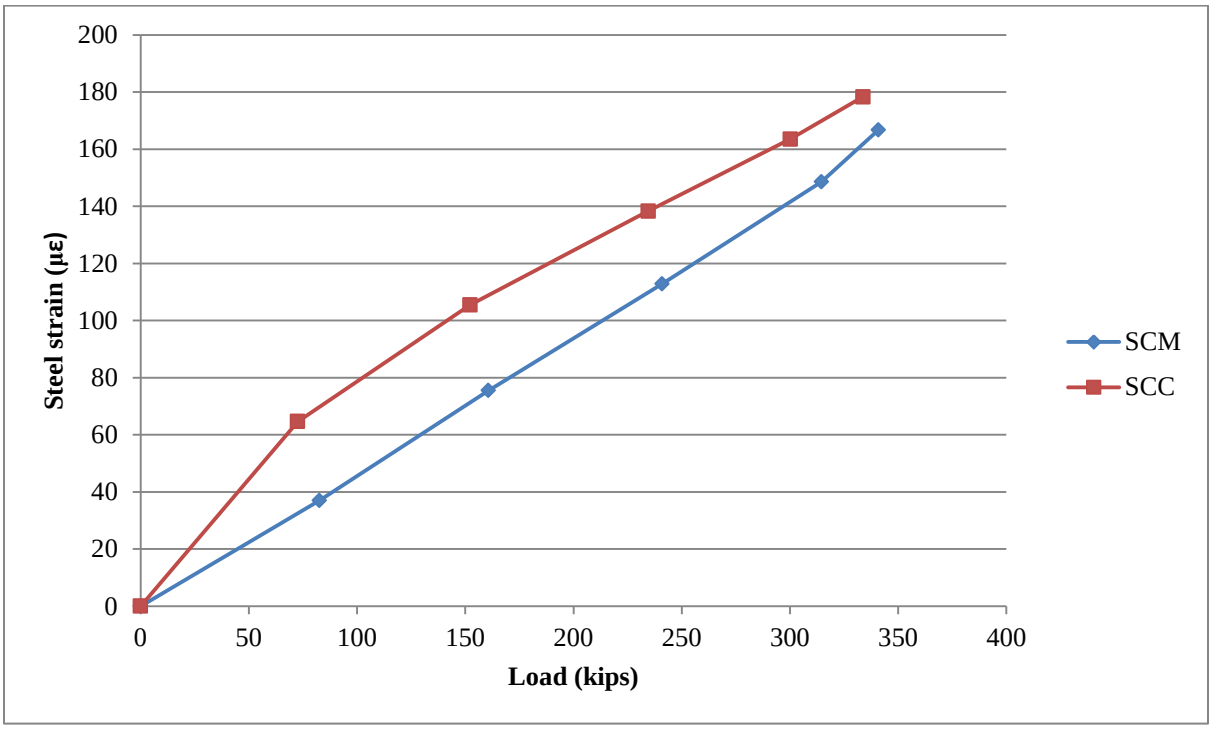

Figure 4.1. Average strain changes in steel tubes during initial loading

4.1.1.2 Total concrete strain

The total strains of the concretes of the CFT specimens are displayed in Figure 4.2 to Figure 4.5. As expected, the plots of total strain are characterized by initial strain followed by a gradual increase in strain with time. The large initial strain is the result of when load was first applied and is the elastic strain of the concrete.

The total strains of the concrete in the CFT specimens were much lower than those of the cylinder specimens, which are discussed in Section 4.2.1. The elastic strains were less because the steel takes about a fifth of the initial load, even though load is applied to the concrete core only. Another reason is that the tube confines the concrete, putting it in a tri-axial stress state that retards lateral expansion and therefore reduces compressive axial strain. The load is transferred to the steel by friction. Slip occurred, however, which was evident from the variation in strain between the concrete and the steel as can be seen in figures later in this chapter, but the degree of friction seems to be different for the two concretes, which may be due to a different level of confinement, as will also be discussed later in the chapter.

The assumption of negligible drying shrinkage in the CFTs seems to be valid, based on the fact that if the shrinkage strain of the sealed cylinders, displayed in Figure 4.19, was subtracted from the time-dependent strain of the CFTs, the result was a creep curve that sloped downwards, giving negative creep strain. In other words, the drying shrinkage strain of the sealed cylinders was larger than the total time-dependent strain of the CFTs.

Table 4.3 summarizes the average change in concrete stresses and strains in the CFT specimens after 126 days of loading.

Table 4.3. Average concrete stresses and strains in CFT specimens after 126 days of loading.

Specimen	Initial strain (με)	Initial stress (ksi)	% of total load	126 day strain (με)	126 day stress (ksi)	% of total load
SCM	208	0.89	79	289	0.78	68
SCC	159	0.85	78	308	0.78	73

The average stress in the concrete of the CFT core at a given time is found by:

$$\sigma_c(t) = \frac{F_i - \varepsilon_s(t) * E_s * A_s}{A_c} \quad \textbf{(4-4)}$$

where:

$\varepsilon_s(t)$ = average time-dependent steel strain

E_s = elastic modulus of steel, assumed to be 29,000 ksi

A_s = cross-sectional area of the steel tube

A_c = cross-sectional area of the concrete core

The initial strains of the CFT specimens were much lower than those of the sealed and unsealed cylinders, which are shown in Table 4.6. The ratio of the initial strain of the SCM CFT core to that of the unsealed cylinders was only 66%, while the ratio of concrete load to total load, taken from Table 4.3 was 79%. The difference between the two ratios indicates the confinement that the steel tube provides. The tube retards lateral expansion of the concrete, which results in less axial strains than in plain concrete, but there were no measurements of lateral strains to confirm

this. The ratio of the initial strain of the SCC CFT core to that of the unsealed cylinders was 60%, while the ratio of concrete load to total load, taken from Table 4.3 was 78%. This suggests more initial confinement effect in the SCC specimen than in the SCC specimen, and might indicate that more autogeneous shrinkage, discussed earlier in this chapter, had occurred in the SCM specimen prior to initial loading. This would cause the SCM concrete to engage less with the tube at initial loading, since it would have more room to expand.

Figure 4.2 shows the total strain in the concrete core of the CFT specimens 56 inches above the surface of the footing. The initial strain was lower in the SCC specimen at this height level, but the increase in strain over time was faster.

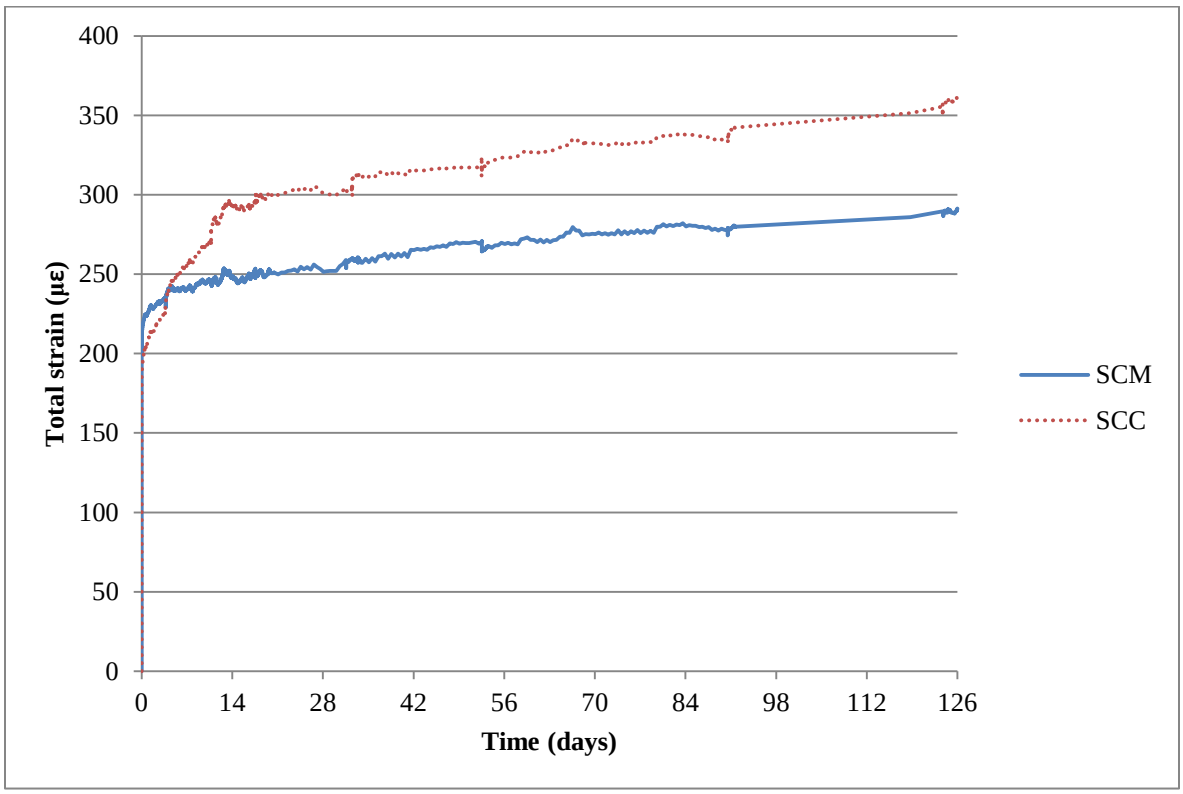

Figure 4.2. Total strains in the concrete cores of the CFT specimens at h = 56 in.

Figure 4.3 shows the total strain in the concrete core of the CFT specimens 32 inches above the surface of the footing. This is a similar behavior as at 56 inches. The SCM curve is almost identical to the one at 56 inches but the SCC curve has lower initial strain than at 56 inches.

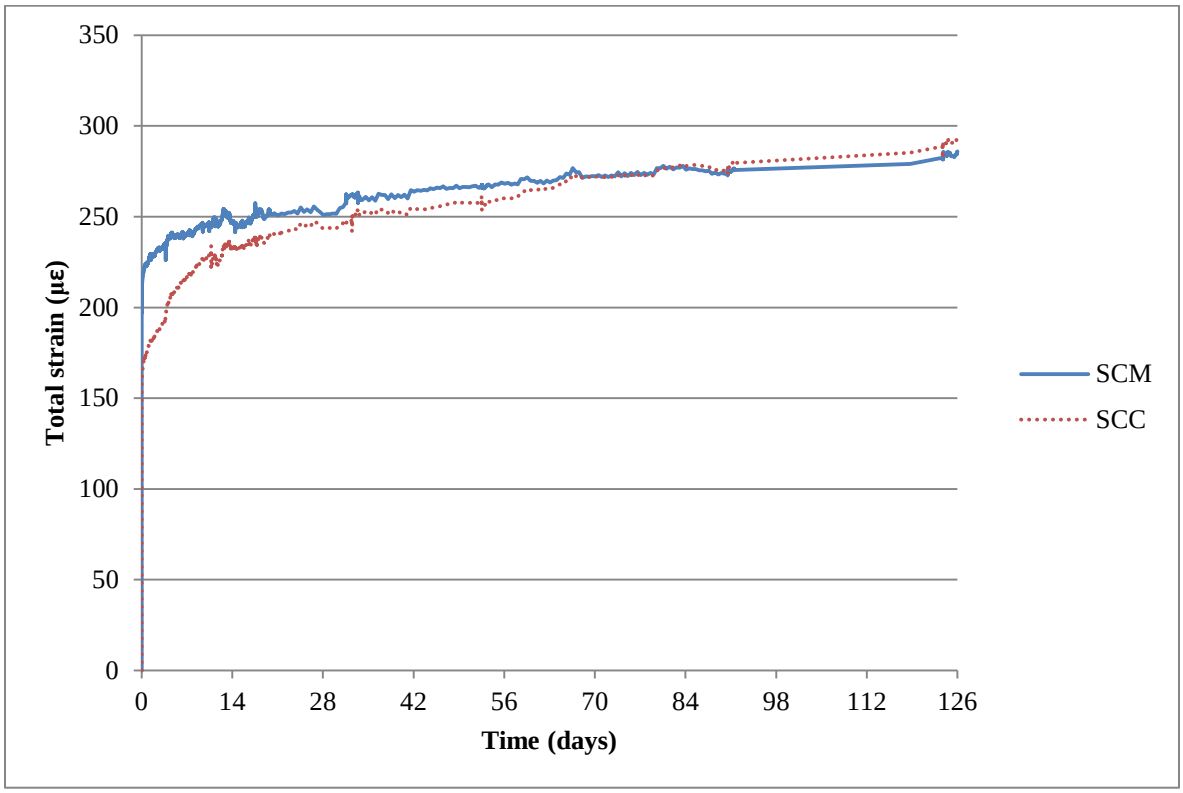

Figure 4.3. Total strains in the concrete cores of the CFT specimens at h = 32 in.

Figure 4.4 shows the total strain in the concrete core of the CFT specimens 8 inches above the surface of the footing. The curves look like what might be expected from a specimen that was loaded uniformly. The SCC is stiffer and therefore had lower initial strain, but the time dependent strain of the SCC was still higher.

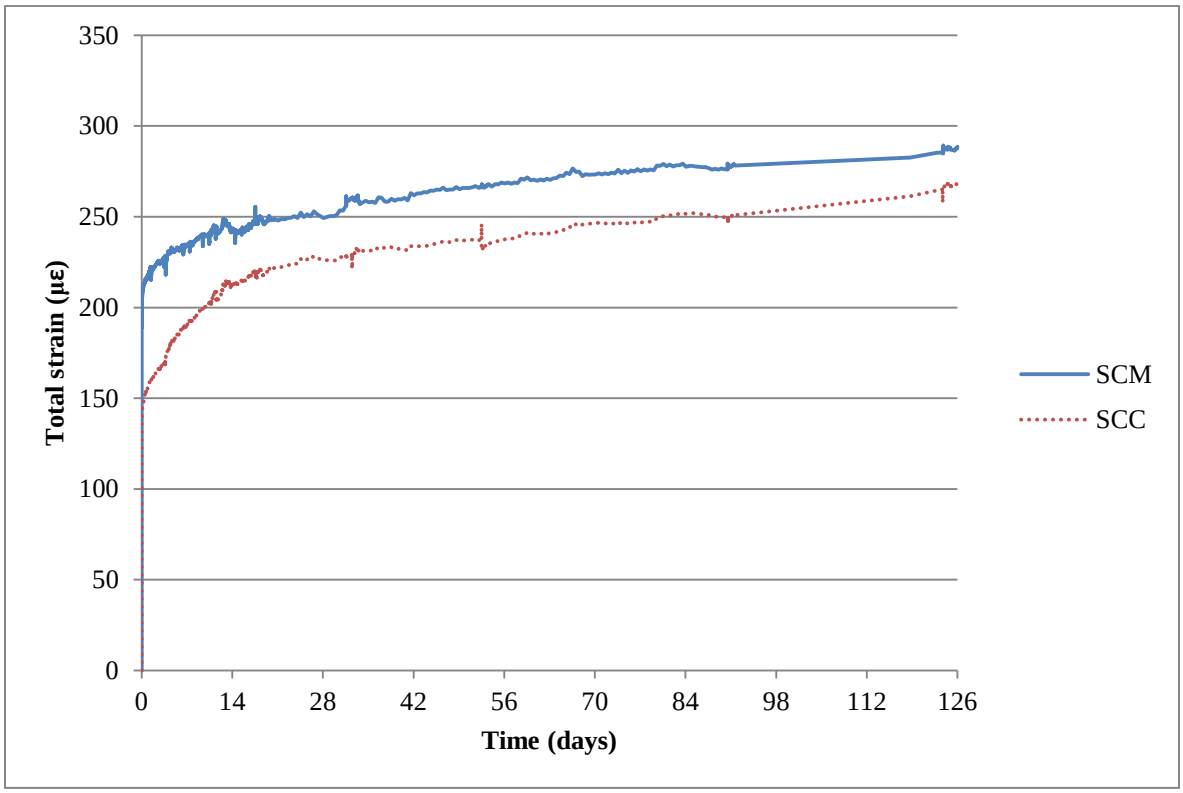

Figure 4.4. Total strains in the concrete cores of the CFT specimens at h = 8 in.

Figure 4.5 shows the average total strain in the concrete core of the CFT specimens tested in this research program. As can be seen, the initial strain in the SCC specimen was lower. The concrete in the SCM specimen sustained on average a higher percentage of the initial load than the SCC specimen, although the plain unsealed SCC concrete is approximately 20% stiffer than the SCM at the time of loading. The difference in stiffness was found by comparing the initial strains of the unsealed cylinders. This implies that initial confinement was higher in the SCC specimen. However, the SCM shed more load to the steel over time, as can be seen in Figure 4.6 to Figure 4.10 which might indicate that the SCM concrete expands more as it creeps and therefore bonds more with the steel over time, as discussed below. At 126 days, the percentage of load that the concrete carried on average had reduced to 68% from the initial value of 79%. Corresponding values for the SCC were 73% and 78%, which shows how much more load was shed to the steel over time in the SCM specimen.

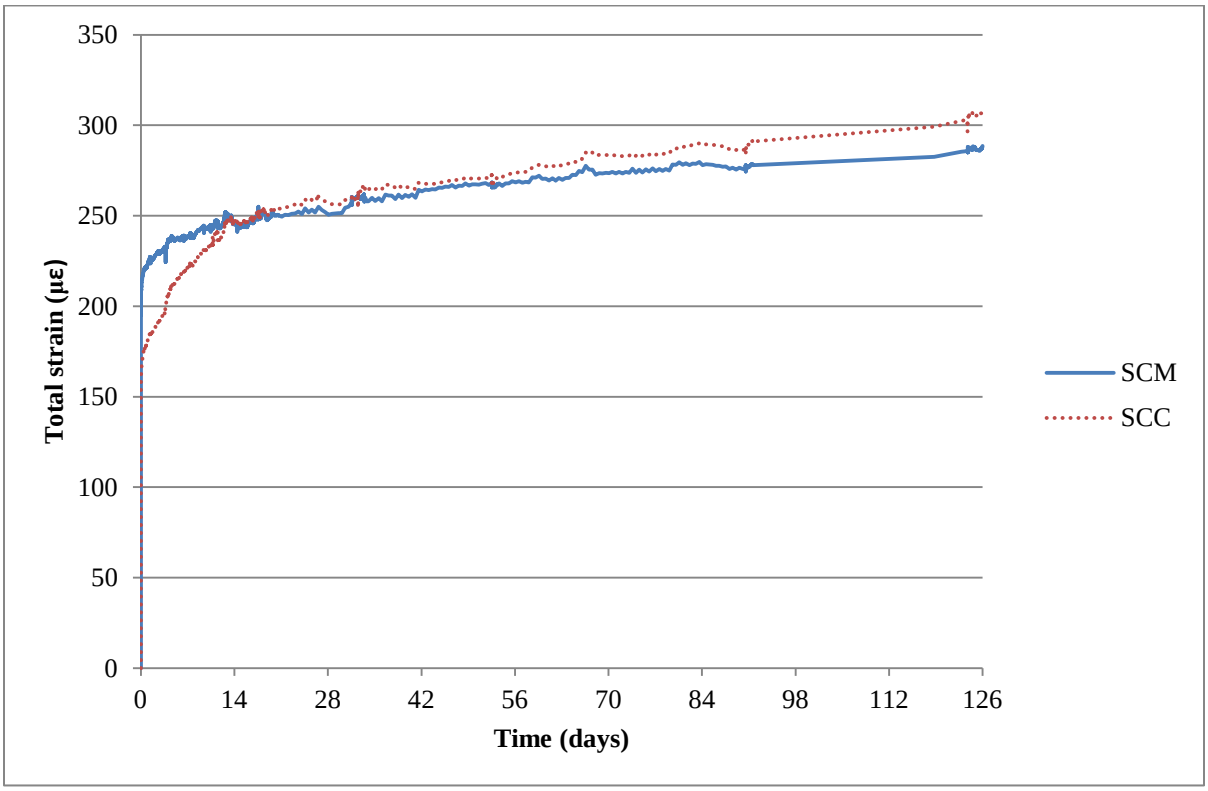

Figure 4.5. Average total strains in the concrete cores of the CFT specimens

The two specimens showed quite a difference in behavior. One might conclude that the SCC suffered more basic creep than the SCM, which is certainly a factor based on the creep coefficient of the sealed cylinders, shown in Figure 4.22. However, this also indicates a difference in slip over time between the concrete and the steel in the two specimens. More of the total load was shed to the steel over time in the SCM specimen, resulting in less total time-dependent strain in the concrete. The smaller initial strain in the SCC specimen is due to its higher stiffness, and perhaps more initial confinement than occurred in the SCM specimen as discussed before. A measurement of hoop strains in the steel or lateral strains in the concrete would have been necessary to confirm this.

Both initial strain and basic creep strain consist of a deviatoric component and volumetric component. The absence of a deviatoric component in a loaded specimen would result in no change in volume, thereby resulting in a lateral strain. The absence of a volumetric component would result in zero lateral strain and therefore no expansion of the concrete. The ratio of these components can be different between initial strain and basic creep strain, and also different between concretes. The results suggest that the SCM concrete expands more over time, which would increase the friction between the steel and the concrete over time and cause higher time-dependent strains in the steel tube, both axial and circumferential. More autogeneous shrinkage in the SCM concrete could explain what seems to be less initial confinement in the SCM specimen. Table 4.1 also implies that there is a difference between the two specimens in initial confinement.

The discussion above will not be considered further in this research due to lack of information on lateral strain, but the influence of these parameters is worth investigating in detail.

4.1.1.3 Total steel strain

Figure 4.6 to Figure 4.10 show the total steel strain at each height level in the steel of both CFT specimens tested in this research program. The difference in behavior between the SCM specimen and the SCC specimen is apparent. Table 4.4 summarizes the initial and final steel stresses and strains in the experiment.

Table 4.4. Total stress and strain results of steel in CFT specimens after 126 days of loading

Specimen (in. above footing)	Initial strain (με)	Initial stress (ksi)	% of total load	126 day strain (με)	126 day stress (ksi)	% of total load
SCM (74”)	150	4.3	20	269	7.8	36
SCC (74”)	118	3.4	16	139	4.0	19
SCM (56”)	140	4.0	19	201	5.8	27
SCC (56”)	136	3.9	18	144	4.2	19
SCM (32”)	175	5.1	23	255	7.4	34
SCC (32”)	197	5.7	26	251	7.3	34
SCM (8”)	181	5.2	24	257	7.5	34
SCC (8”)	203	5.9	27	278	8.1	37
SCM (Avg.)	161	4.7	21	246	7.1	32
SCC (Avg.)	163	4.7	22	203	5.9	27

The initial strain of the steel in the two specimens was similar on average, but differed over the height of the specimens. The steel in the SCM specimen took 20% and 24% of the initial load at top and bottom, respectively, while the corresponding values for the SCC specimen were 16% and 27%. At 126 days these values were 36% and 34% for the SCM but 19% and 37% for the SCC. This difference suggests that the degree of bond over time between the steel and the concrete in the SCM specimen is higher than that of the SCC specimen. The following figures further indicate this.

Figure 4.6 shows the total strains in the steel of both CFT specimens at height 74 inches above the surface of the footing. This location was very close to the top of the tube, which was 84 inches in length. It seems that the SCM specimen had acquired good bond at this height. No concrete gauges were present at this height level, so it cannot be verified whether the concrete strain increased at a similar rate, but it must be likely that this is the case.

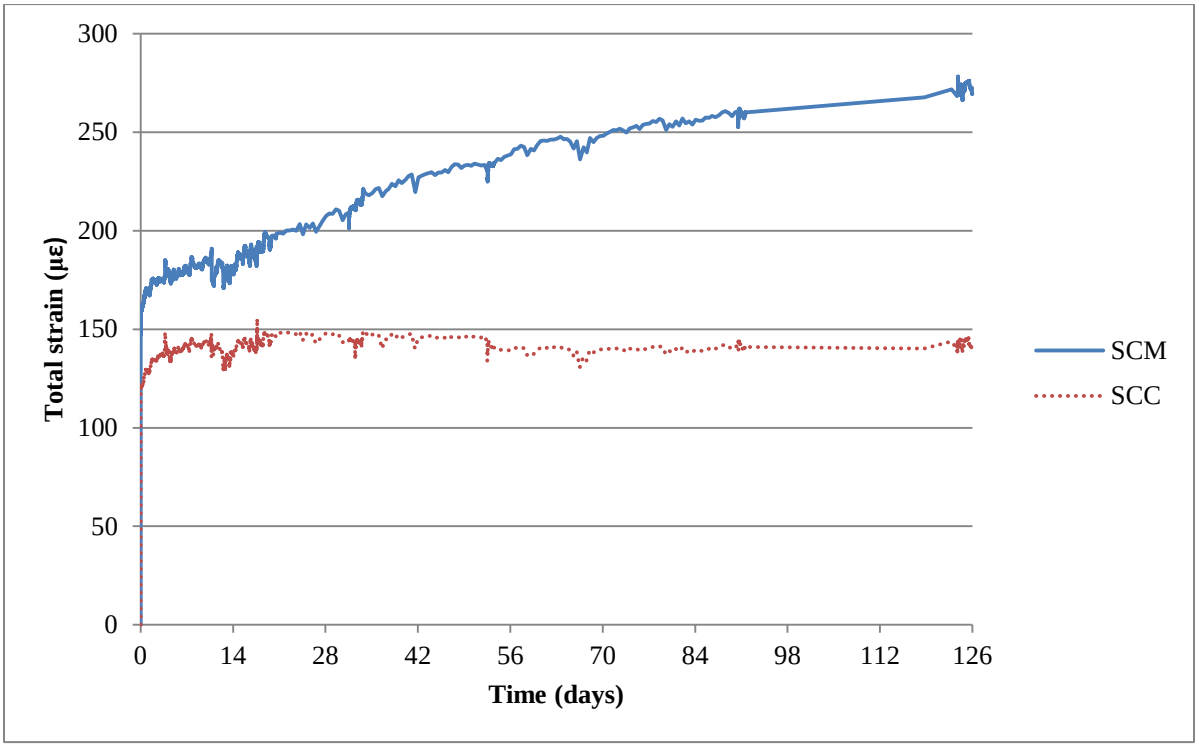

Figure 4.6. Total strains of the steel tubes of the CFT specimens at h = 74 in.

Figure 4.7 shows the total strains in the steel of both CFT specimens at 56 inches above the surface of the footing. This location was very close to the mid-height of the tube, which was at 51 inches. It seems that the SCM specimen still has more bond than the SCC specimen. The increase in steel strain of the SCC specimen was negligible at this height level.

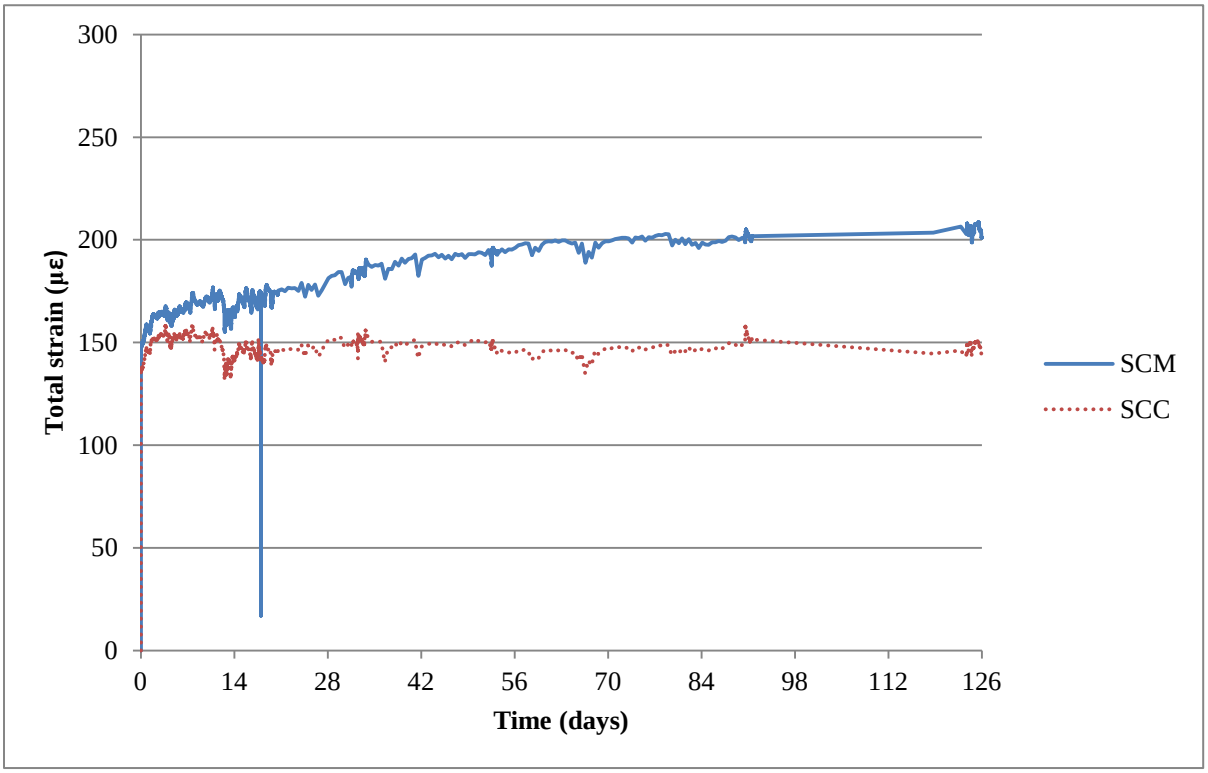

Figure 4.7. Total strains in the steel tubes of the CFT specimens at h = 56 in.

Figure 4.8 shows the total strains in the steel of both CFT specimens 32 inches above the surface of the footing. The SCC concrete seems to be developing more bond with the steel at this height, but the time-dependent strain of the steel in the SCM specimen was still larger.

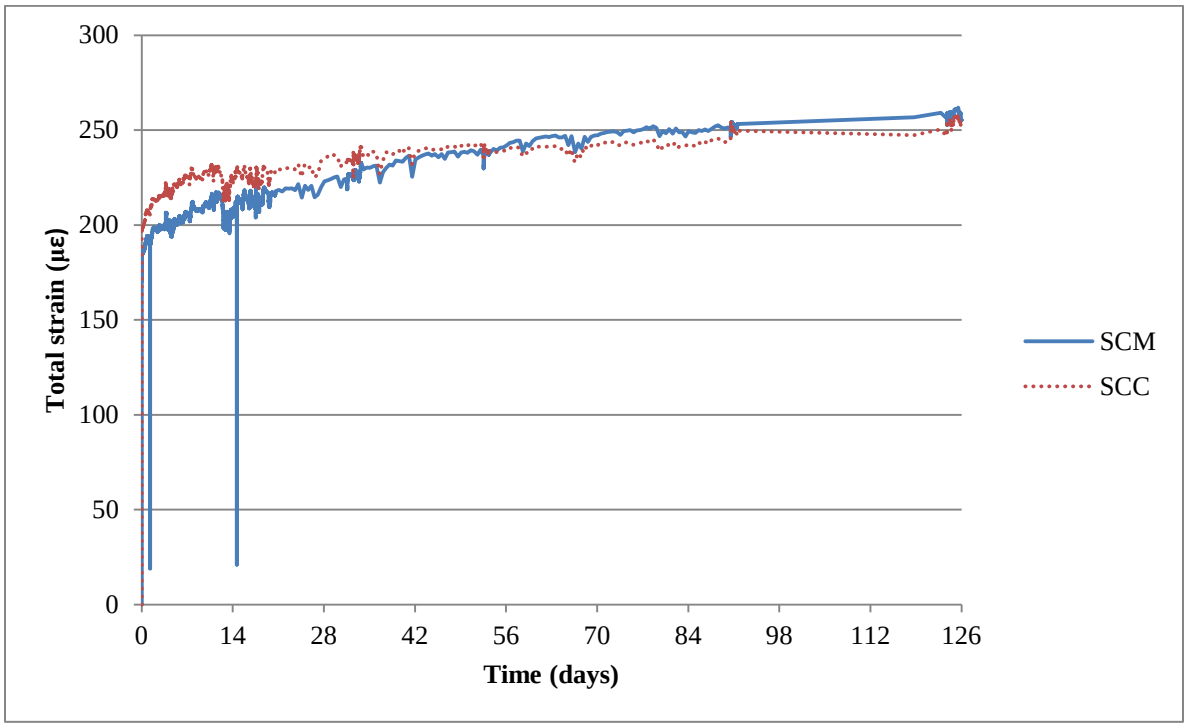

Figure 4.8. Total strains in the steel tubes of the CFT specimens at h = 32 in.

Figure 4.9 shows the total strain in the steel of both CFT specimens at height 8 in. above the surface of the footing. The SCC specimen seems to have developed the same bond between the concrete and the steel as the SCM specimen at this height level.

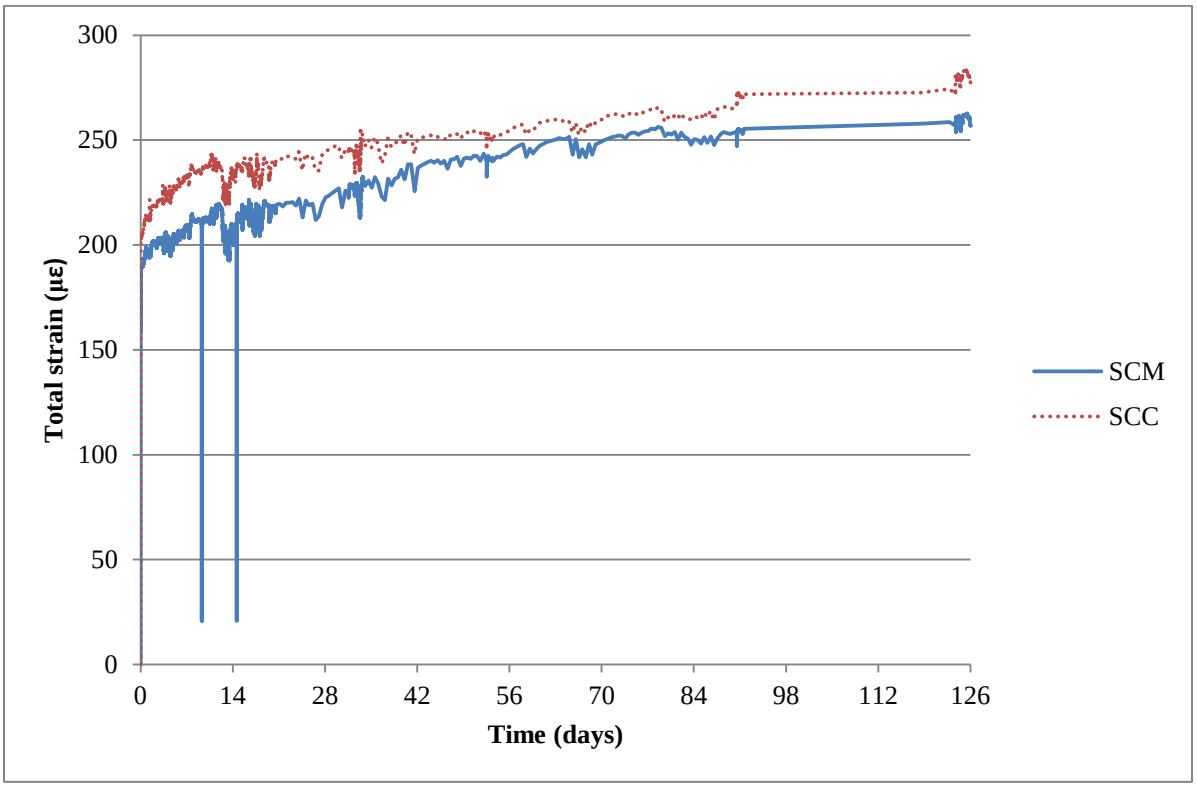

Figure 4.9. Total strains in the steel tubes of the CFT specimens at h = 8 in.

Figure 4.10 shows the average total strains in the steel along the height of both CFT specimens. It can be seen that the concrete in the SCM specimen shed on average more load to the steel than the SCC specimen over time, due the difference in which the two concretes seemed to bond with the steel. The explanation may be smaller volumetric change in the SCM concrete, as discussed earlier in this chapter. The difference in creep of the two concretes seems to be more than it is in reality because of the difference in load shed to the steel. More load in the steel results in less load in the concrete, hence less elastic strain of the concrete. It should not be left unnoted that even though the concrete shed some load to the steel over time, steel strains after 126 days of loading corresponded to a stress of only 7.5 ksi and 8.1 ksi at the critical location at the bottom of the tube (h = 8 in.) for the SCM and SCC specimens, respectively. Even though creep had not completely ceased in the specimens after 126 days, it may be concluded that these stresses will not get very much higher since the majority of the concrete creep had already taken place after 126 days. This is discussed further in Chapter 5.

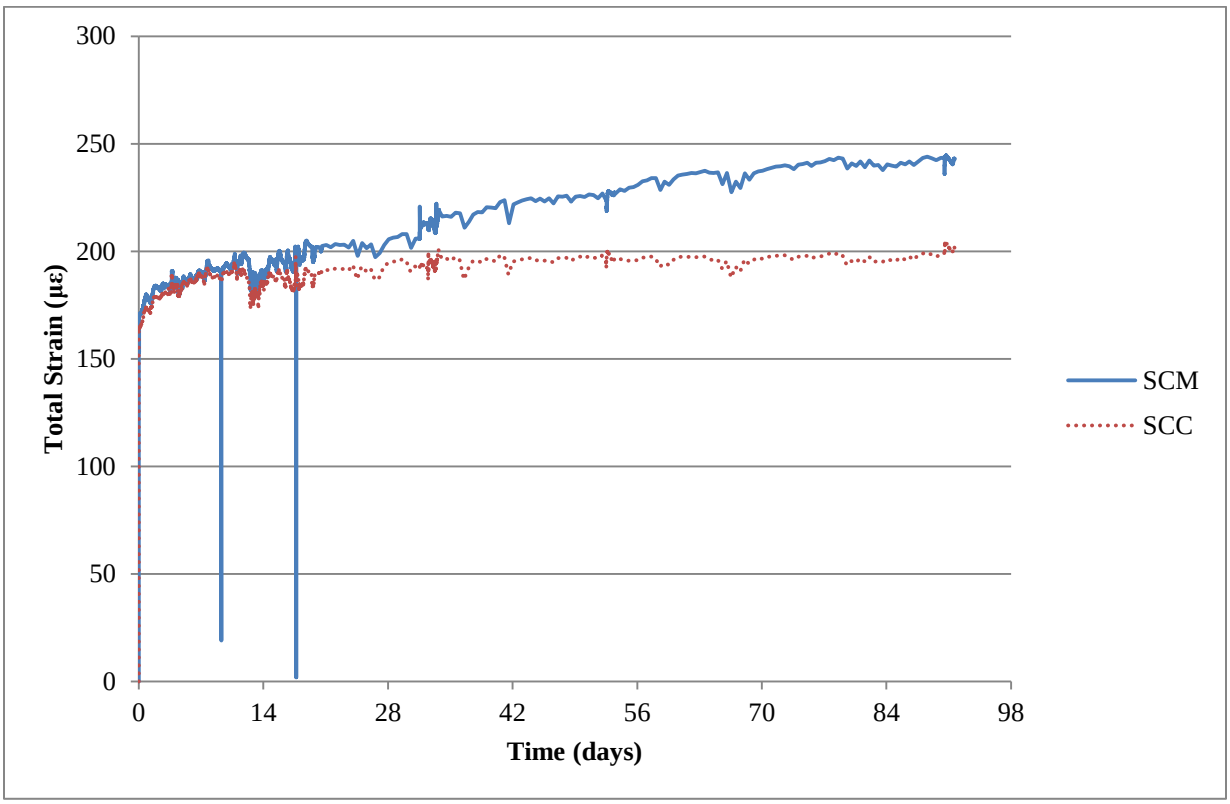

Figure 4.10. Average total strains in the steel tubes of the CFT specimens

Figure 4.11 shows the total steel strain in the SCM specimen along the height of the steel tube at selected time intervals throughout the experiment. The behavior was almost identical at each height level, apart from the behavior at 56 inches above the surface of the footing.

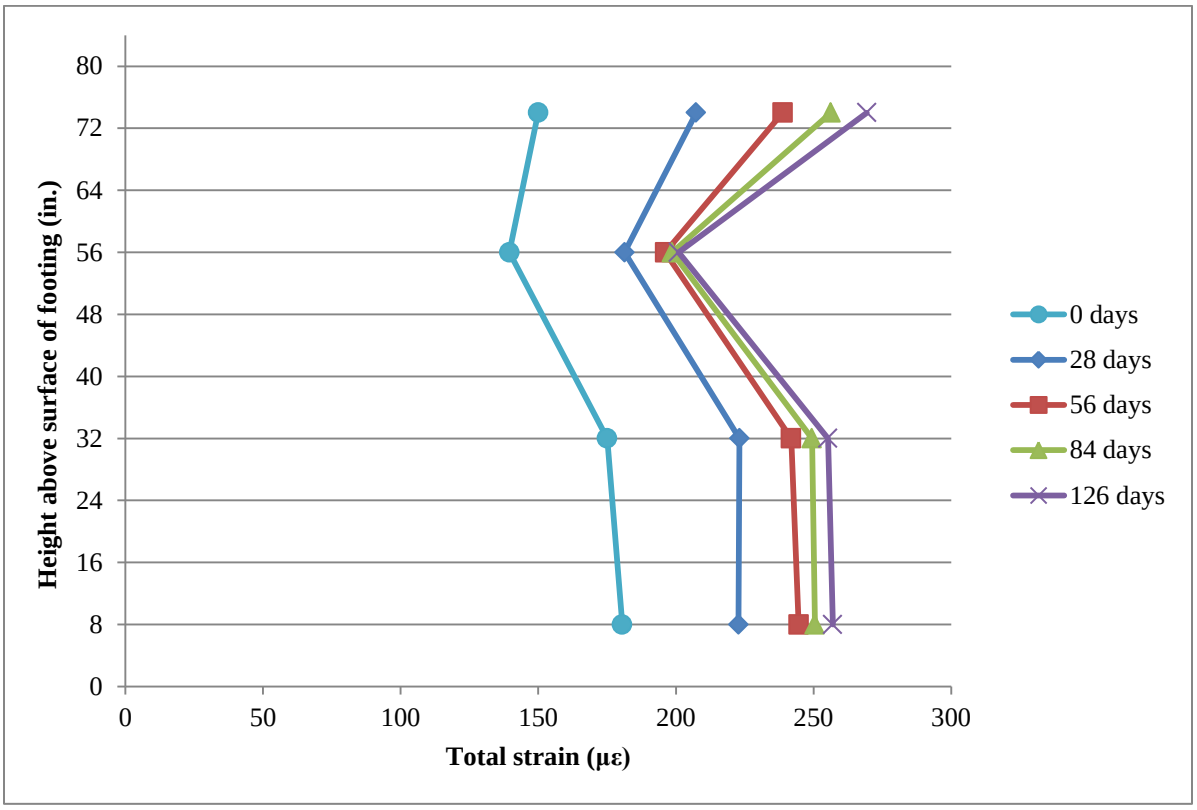

Figure 4.11. Total strains in the steel tube along the height of the SCM specimen

Figure 4.12 shows the total steel strain in the SCC specimen along the height of the steel tube at selected time intervals throughout the experiment. As can be seen in the figure, the bond between the steel and the concrete increased gradually as the height got closer to the footing.

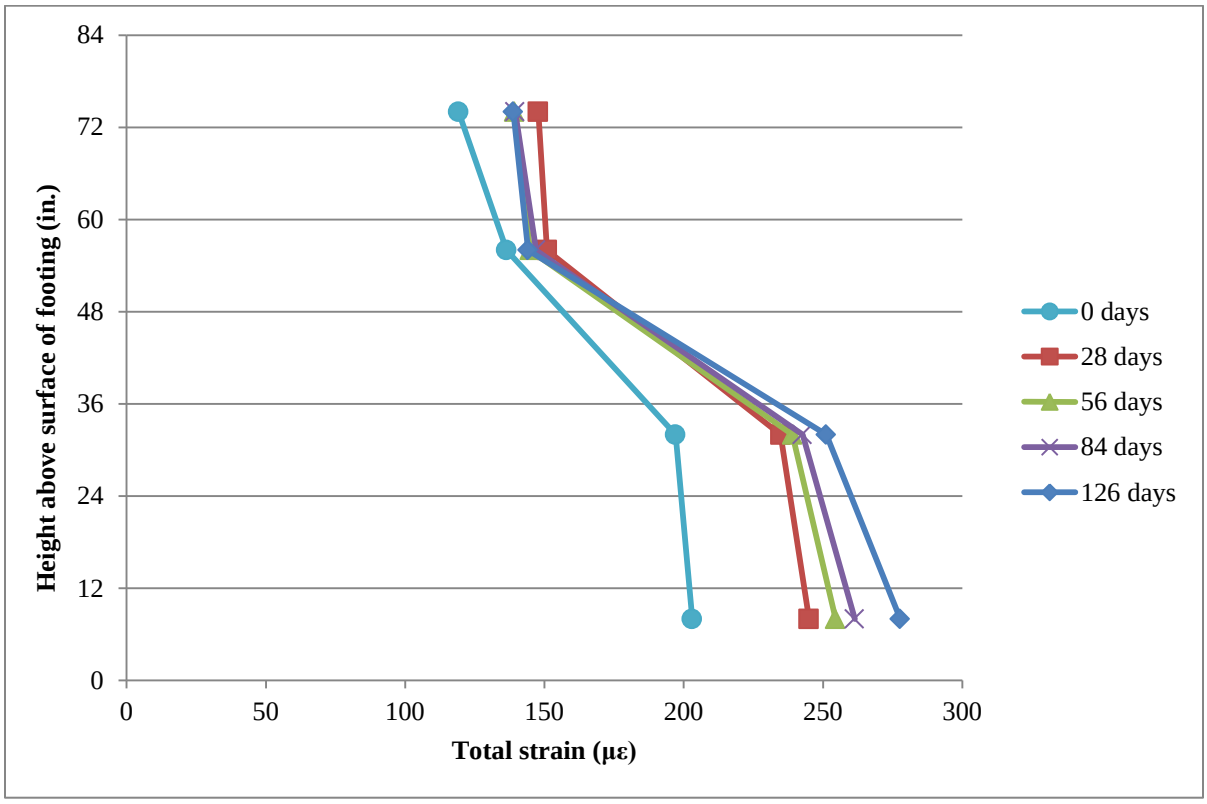

Figure 4.12. Total strains in the steel tube along the height of the SCC specimen

4.1.1.4 Comparison of total concrete strain and total steel strain

Figure 4.13 shows the average total strain of the concrete and the steel in the SCM specimen. The curves are almost identical in shape, suggesting a very similar average time-dependent strain in the concrete as in the steel. The initial strain in the concrete was higher, which indicates that some slip occurred between the steel and the concrete at initial loading.

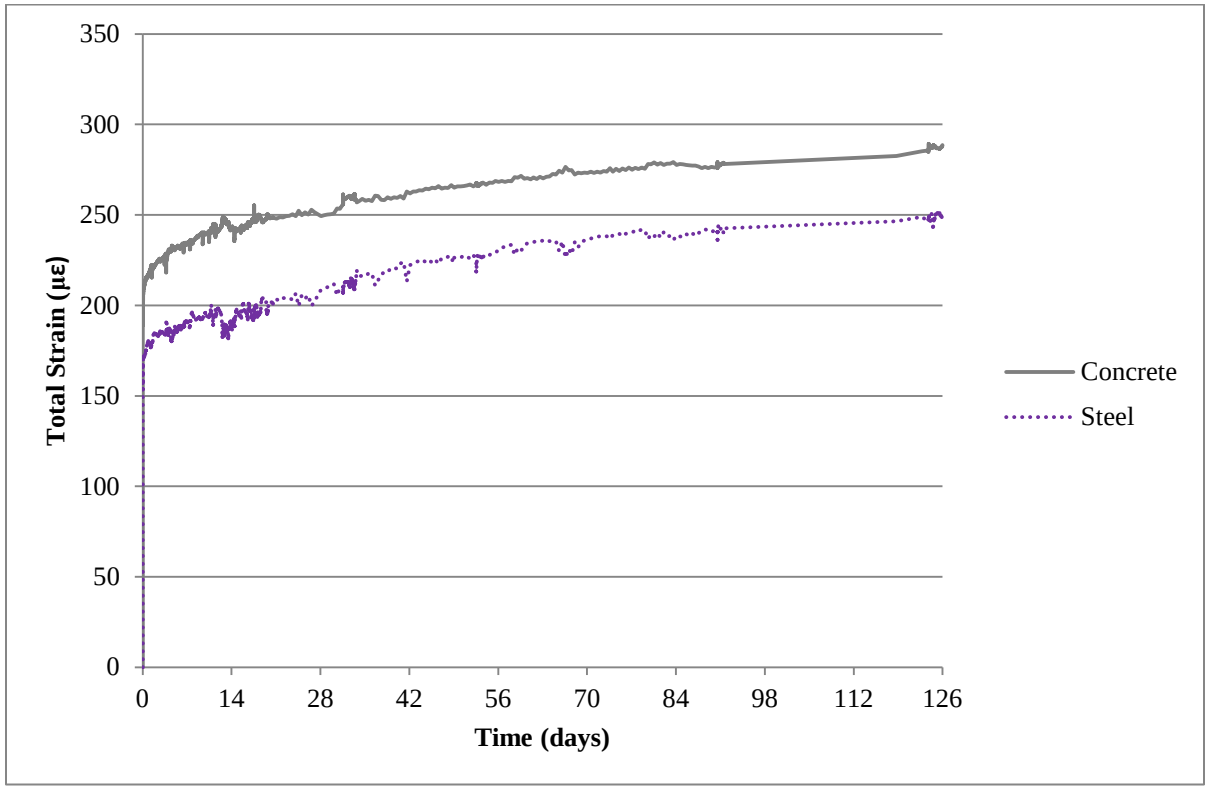

Figure 4.13. Average total strains in concrete and steel in the SCM specimen

Figure 4.14 shows the average total strain of the concrete and the steel in the SCC specimen. Contrary to the SCM specimen, the initial strain was similar for the steel and the concrete but the time dependent strain was higher in the concrete. This indicates that very little slip occurred at initial loading. Slip occurred with time, however, resulting in higher total strain of the concrete than the steel.

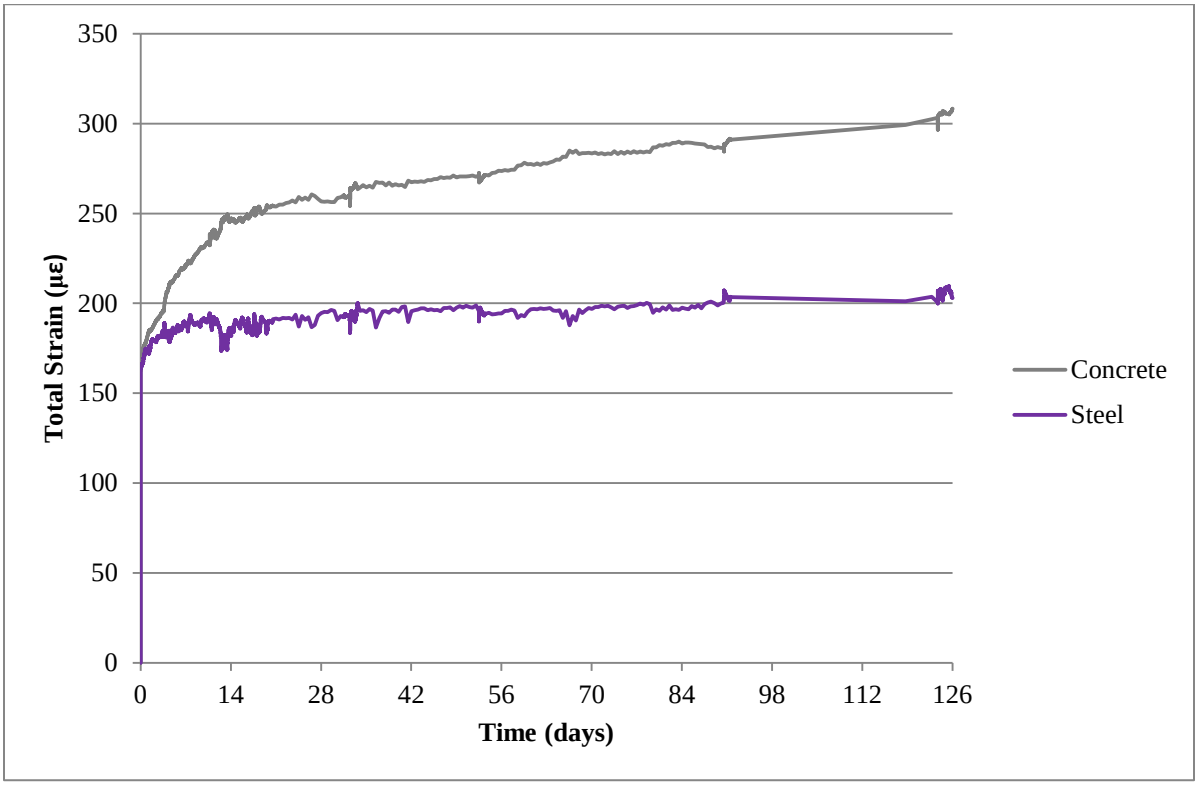

Figure 4.14. Average total strains in concrete and steel in the SCC CFT specimen

4.1.2 Creep strain and creep coefficient

Total creep consists of basic creep and drying creep. Basic creep strain is independent of the relative ambient humidity and is theoretically the same for identical concrete under same load, whether it is sealed from the environment or not. It is not associated with moisture loss. Drying creep also depends on the load applied, but is associated with moisture loss and dependent on the relative ambient humidity. Therefore, concrete that is completely sealed from the environment, or is in 100% humid atmosphere or under water, theoretically experiences no drying creep. The total creep strain in the CFTs was obtained from:

$$\varepsilon(\mathrm{t})_{tc,CFT} = \varepsilon(\mathrm{t})_{t,CFT} - \varepsilon_{i,CFT} \quad \textbf{(4-5)}$$

where:

$\varepsilon(t)_{tc,CFT}$ = Total creep strain of CFT specimen

$\varepsilon(t)_{t,CFT}$ = Total strain of CFT specimen

$\varepsilon_{i,CFT}$ = Initial elastic strain of CFT specimen

The time-dependent creep coefficient, $\varphi(t)$, is unitless and is the ratio of total creep strain to elastic strain. Therefore, the initial time-dependent creep coefficient is zero and when creep strain reaches the same value as the initial elastic strain, the time-dependent creep coefficient has reached a value of 1.0. It is not separated into a basic creep coefficient and a drying creep coefficient, but creep models account for relative ambient humidity, which affects drying creep only. This is discussed further in Chapter 5. The time-dependent creep coefficient for CFTs was obtained from the following equation:

$$\varphi(t)_{CFT} = \frac{\varepsilon(\mathrm{t})_{tc,CFT}}{\varepsilon_i} \quad \textbf{(4-6)}$$

Table 4.5 summarizes the creep measurements of the specimens after 126 days of loading. Specific creep strain is defined as the total creep strain per unit of stress. The value of the time-dependent creep coefficient, $\varphi(t)_{CFT}$, must not be confused with the value of the final creep coefficient, $\varphi_{p,CFT}$, which is a predicted final value of the creep coefficient when creep ceases. The final creep coefficient is discussed further in Chapter 5.

Table 4.5. Creep measurements of the CFT specimens after 126 days of loading

Specimen	Applied Stress (ksi)	Initial strain (με)	Drying creep (με)	Basic creep (με)	Total creep (με)	Specific creep (με/ksi)	Creep coefficient $\varphi(t)_{CFT}$
SCM	0.89	208	-	80	80	90	0.39
SCC	0.87	159	-	150	150	172	0.94

Figure 4.15 shows the creep strains of the CFT specimens. As can be seen, the concrete core of the SCC specimen seemed to creep more than that of the SCM specimen. The two concrete cores were subject to very similar stress at initial loading, as can be seen in Table 4.5. The difference, however, is that the SCM concrete shed more load to the steel tube than the SCC concrete as discussed earlier in this chapter. Therefore, the elastic strain in the SCM decreased more with time. The figure shows that CFTs filled with high-volume SCM concrete should not suffer larger time-dependent strains than CFTs filled with conventional concrete if the stress is the same. In fact, this research shows that this strain is considerably smaller for the SCM. The creep strains at 126 days were 80 με and 150 με for the SCM and SCC, respectively.

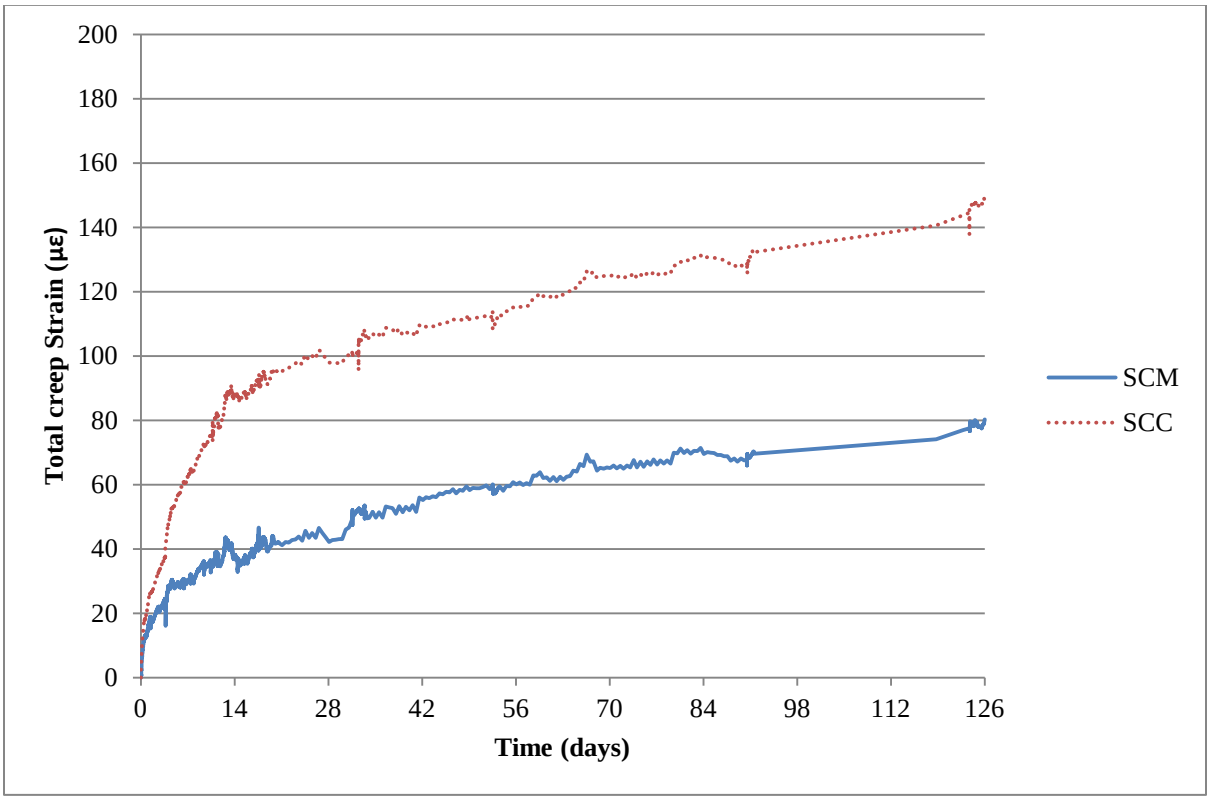

Figure 4.15. Creep strains of the CFT specimens

Figure 4.16 shows the creep coefficient of the CFT specimens. As can be seen, the difference between the SCM and SCC was even greater than the difference in creep strain, even though the stress is almost the same. Creep strain increases linearly with increasing stress, which means that the creep coefficient is independent of loading. The difference between the two figures is due to the fact that the initial strain in the SCC was lower since it is stiffer and likely better confined initially, as discussed earlier in this chapter. Comparing the ratio of creep strain to elastic strain for the two concretes therefore yielded a greater difference than comparing the creep strains. The creep coefficient at 126 days was 0.39 and 0.94 for the SCM and SCC, respectively.

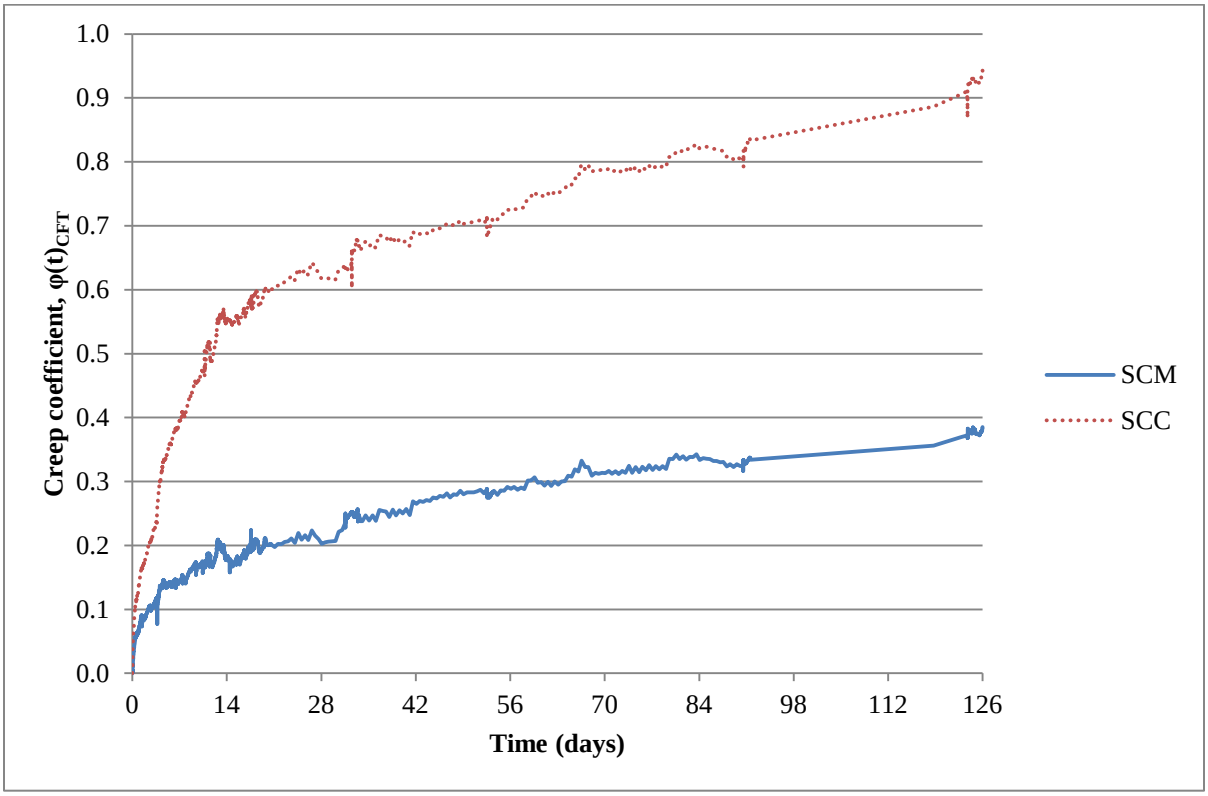

Figure 4.16. Creep coefficients of the CFT specimens

Figure 4.17 shows the ratio of SCM creep coefficient to SCC creep coefficient for the CFT specimens. As can be seen, the ratio became relatively constant after approximately five weeks of loading. The rate of creep is higher for the SCC before that time. At 126 days, the creep coefficient of the SCM was about 40% of the creep coefficient of the SCC.

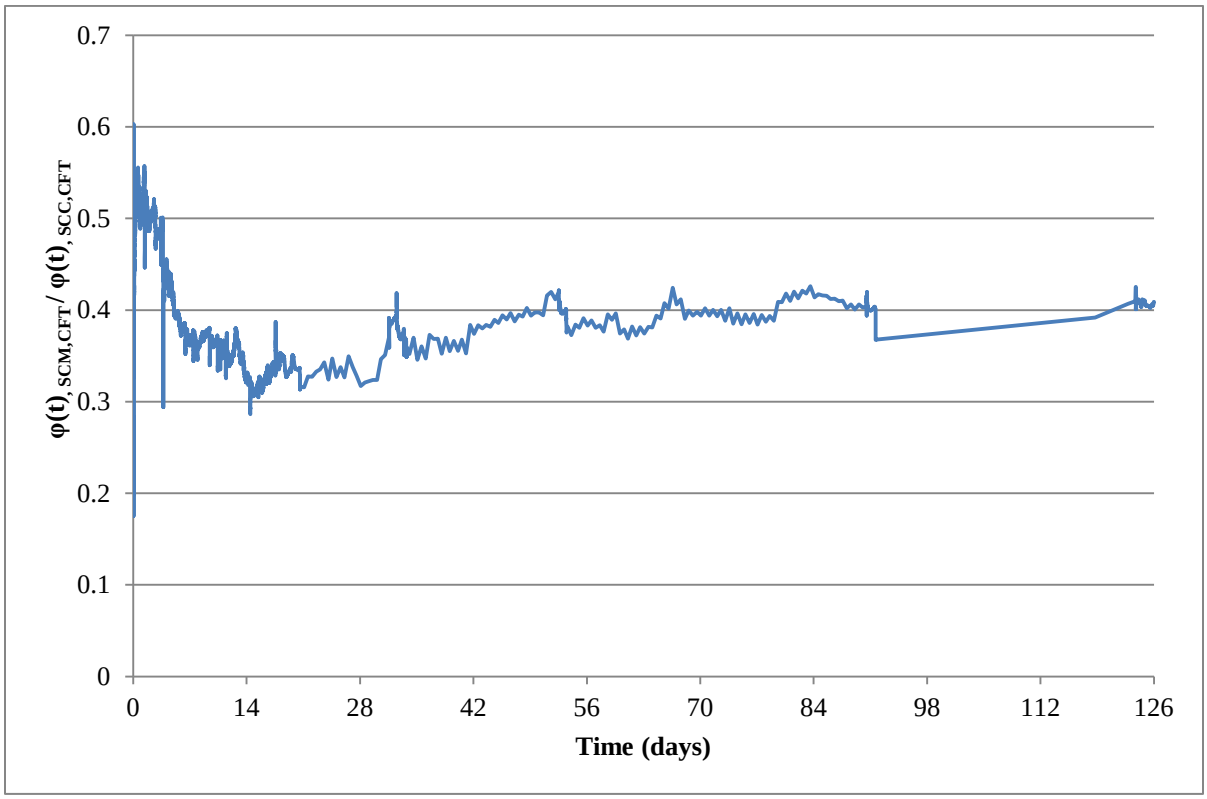

Figure 4.17. Ratio of SCM creep coefficient to SCC creep coefficient for the CFT specimens

4.2 Results from cylinder specimens

Concrete cylinders from the two mixes specified in Table 3.3 and Table 3.4 were tested for shrinkage and creep behavior to compare the results to those of the CFT specimens. Both sealed and unsealed cylinders were tested. All cylinder specimens were loaded after being cured for fourteen days in 100% relative humidity. The tests were performed as described in section 3.3.2. Strain data used was measured with the vibrating wire strain gauges and collected by the Multilogger data acquisition system, as mentioned in Section 4.1.

4.2.1 Total strain

The total strains of all cylinder specimens are displayed in Figure 4.18. The plots for the cylinders show the average total strain of two sets of cylinders. Total strain for each cylinder was obtained by taking the average strain of the two vibrating wire strain gauges attached to the specimen.

As expected, the plots of total strain are characterized by large initial strain followed by a gradual increase in strain with time. The large initial strain is the result of when load was first applied and is the elastic strain of the specimen.

The total strain of the concrete in the cylinder specimens was much higher than that of the CFT specimens. The elastic strain was less because the steel takes about a fifth of the initial load, even though load is applied to the concrete core only. Another reason is that the tube confines the concrete, putting it in a tri-axial stress state that retards lateral expansion and therefore reduces compressive axial strain.

The total strains of the unsealed cylinders were larger than for the sealed cylinders. Much less drying shrinkage occurred in the sealed specimens because very little excess water in the concrete can evaporate in this case. The perimeter of the sealed cylinders was coated with two layers of epoxy to minimize evaporation. However, the ends are only sealed with sulfur caps which may let out some moisture, causing the shrinkage of the sealed specimens to reach values that cannot be considered negligible, although they were very small.

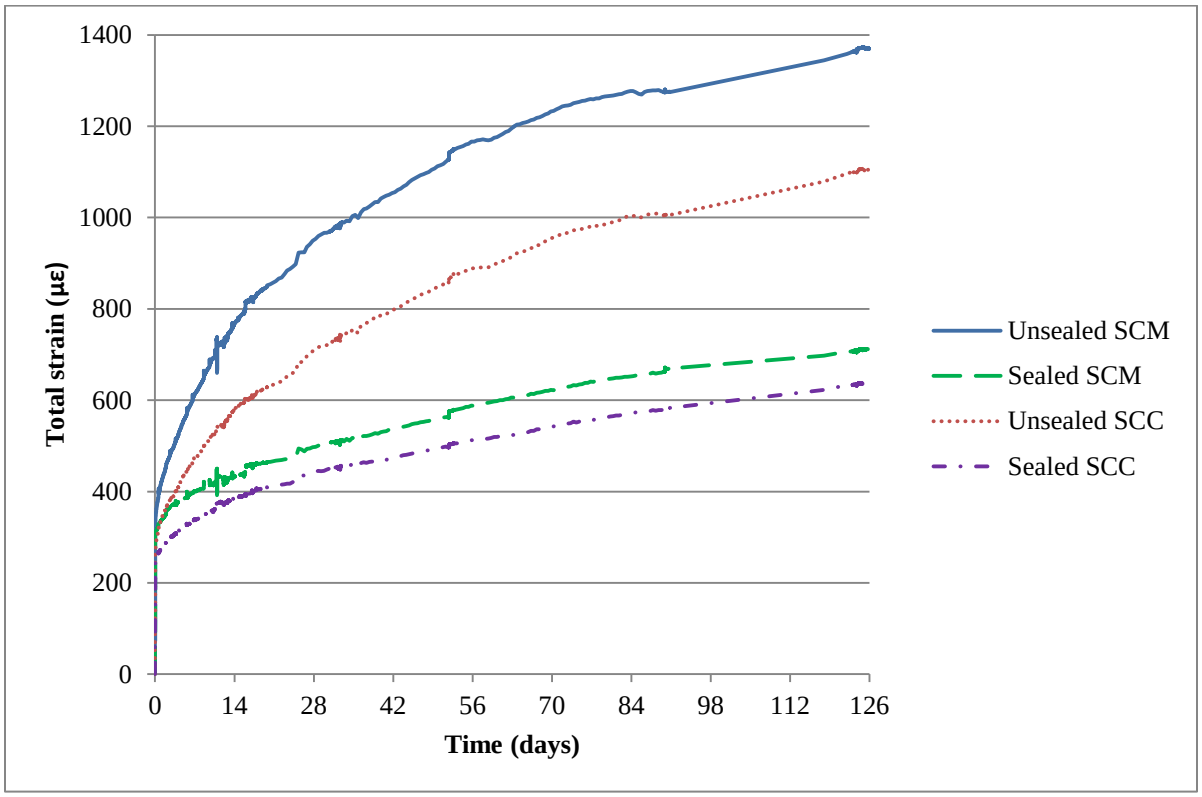

Figure 4.18. Total strains in the cylinder specimens

4.2.2 Shrinkage strain

The shrinkage cylinders were monitored at fourteen days. Data was taken at four-minute intervals for the first few weeks and the time interval was then changed to one hour. Shrinkage strain was the average strain of the two vibrating wire strain gauges attached to each unloaded specimen. The specimens were kept in a fog room at 100% relative humidity and taken out for preparation two days prior to monitoring. Inevitably some shrinkage occurred during those two days. That strain could not be measured.

The shrinkage strain of all cylinder specimens is shown in Figure 4.19. As expected, the shrinkage strain of unsealed specimens was higher than the sealed specimens (the epoxy coating the sealed cylinders prevents most of the free water in the concrete from evaporating). The SCM concrete has larger shrinkage strains than the SCC concrete. This is evident for both sealed and unsealed specimens.

The shrinkage strains of the sealed cylinders after 126 days of monitoring were 231 με 203 με for the SCM and SCC, respectively. Most of the autogenous shrinkage should already have taken place before monitoring started, but that cannot be stated with certainty. In theory, the sealed cylinders should experience no drying shrinkage at all. However, the drying shrinkage is very sensitive to how well the cylinders are sealed. Previous research has shown that only one coating of sealant does little to prevent drying shrinkage (Terrey, Bradford, & Gilbert, 1994). Therefore it is unlikely that two coatings prevent all of it. In addition, some moisture was lost through the sulfur caps, which were not sealed.

The shrinkage strains of the unsealed cylinders after 126 days of monitoring were 527 με 466 με for the SCM and SCC, respectively. Comparing these values to the creep strain of the unsealed concretes shows that it is exactly the same as the creep strain (527 με) for the SCM, and the shrinkage strain in the SCC specimens was actually considerably higher than the creep strain, which was 375 με. It is interesting to see how great of a factor drying shrinkage is in the total strain of unsealed concrete. After 126 days of monitoring, it accounted for about 38% and 42% of the total strain in the SCM and SCC, respectively.

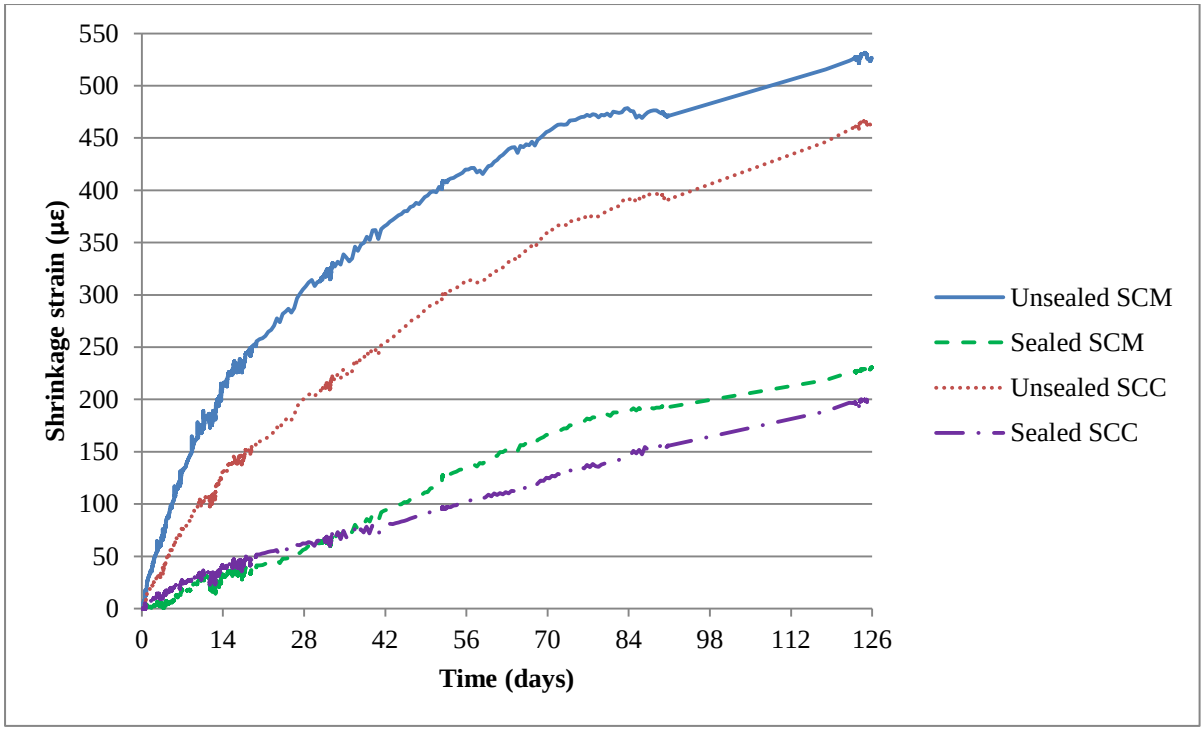

Figure 4.19. Shrinkage strains in the cylinder specimens

Figure 4.20 shows the ratio of SCM shrinkage to SCC shrinkage for the cylinders specimens. As can be seen, the behavior was quite different. For the unsealed cylinders, the SCM had more shrinkage strain than the SCC but the ratio decreased with time. At 126 days, the shrinkage in the SCM was about 14% higher than the shrinkage in the SCC. The sealed cylinders seem to have some sort of a trend, but it is irregular. The shrinkage in the SCC was much greater than the shrinkage in the SCM for the first few days, but after approximately five weeks, the two sealed concretes had the same shrinkage strain. After that, the ratio of SCM shrinkage to SCC shrinkage kept increasing until about two months into the experiment, when the ratio became relatively similar to the ratio for the unsealed cylinders and kept that trend until the end of the experiment.

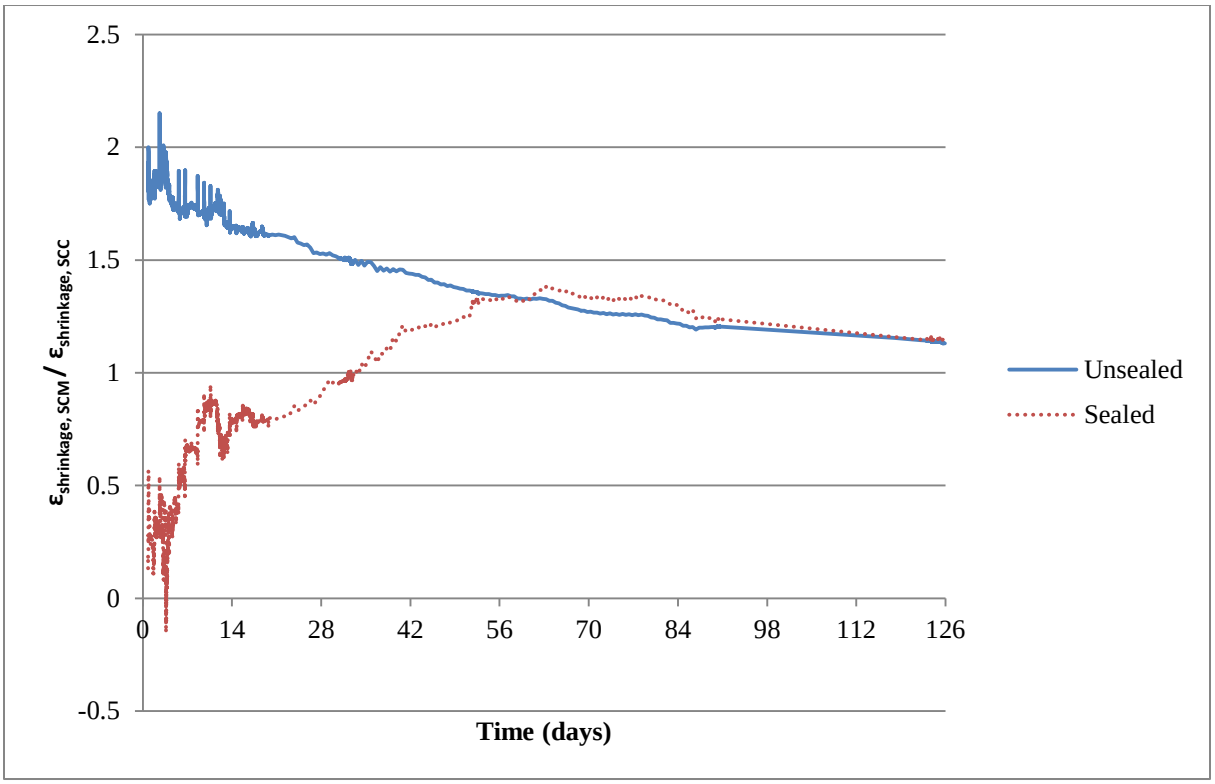

Figure 4.20. Ratio of SCM shrinkage to SCC shrinkage for cylinder specimens

4.2.3 Creep strain and creep coefficient

As mentioned in Section 4.1.2, total creep consists of basic creep and drying creep. Basic creep strain is independent of the relative ambient humidity and is theoretically the same for sealed and unsealed concrete under same load. It is not associated with moisture loss. Drying creep strain also depends on the load applied, but is associated with moisture loss and dependent on the relative ambient humidity. Therefore, sealed concrete theoretically experiences no drying creep. However, the epoxy coating on the sealed cylinders in this experiment did not completely eliminate moisture loss, which was evident from the results of drying shrinkage of the sealed cylinders. Therefore, it cannot be stated that the sealed cylinders experienced no drying creep at all. However, drying creep and basic creep cannot be separated within the sealed specimen. The only way to separate the two is to assume no drying creep in the sealed cylinders and obtain drying creep of the concrete by subtracting creep of sealed cylinders from creep of unsealed cylinders. This was done in this research program. The total creep strains in the cylinders were obtained from the following equations:

Unsealed cylinders:

$$\varepsilon(t)_{tc,u} = \varepsilon(t)_{t,u} - \varepsilon_{i,u} - \varepsilon(t)_{ds,u} \quad \textbf{(4-7)}$$

where:

$\varepsilon(t)_{tc,u}$ = Total time-dependent creep strain of unsealed cylinders in creep rig

$\varepsilon(t)_{t,u}$ = Total time-dependent strain of unsealed cylinders in creep rig

$\varepsilon_{i,u}$ = Initial elastic strain of unsealed cylinders in creep rig

$\varepsilon(t)_{ds,u}$ = Time-dependent drying shrinkage strain of unloaded unsealed cylinders

Sealed cylinders:

$$\varepsilon(\mathrm{t})_{tc,s} = \varepsilon(\mathrm{t})_{t,s} - \varepsilon_{i,s} - \varepsilon(\mathrm{t})_{ds,s} \quad \textbf{(4-8)}$$

where:

$\varepsilon(t)_{tc,s}$ = Total time-dependent creep strain of sealed cylinders in creep rig

$\varepsilon(t)_{t,s}$ = Total time-dependent strain of sealed cylinders in creep rig

$\varepsilon_{i,s}$ = Initial elastic strain of sealed cylinders in creep rig

$\varepsilon(t)_{ds,s}$ = Time-dependent drying shrinkage strain of unloaded sealed cylinders

The drying creep strains in the unsealed cylinders were then obtained from:

$$\varepsilon(\mathrm{t})_{dc,u} = \varepsilon(\mathrm{t})_{tc,u} - \varepsilon(\mathrm{t})_{tc,s} \quad \textbf{(4-9)}$$

The time-dependent creep coefficient, $\varphi(t)$, is unitless and is the ratio of total creep strain to elastic strain. Therefore, the initial time-dependent creep coefficient is zero and when creep strain reaches the same value as the initial elastic strain, the time-dependent creep coefficient has reached a value of 1.0. It is not separated into a basic creep coefficient and drying creep coefficient, but creep models account for relative ambient humidity, which affects drying creep only. This is discussed further in Chapter 5. The time-dependent creep coefficient for the cylinders was obtained from:

$$\varphi(t) = \frac{\varepsilon(\mathrm{t})_{tc}}{\varepsilon_i} \quad \textbf{(4-10)}$$

Table 4.6 summarizes the creep measurements of the cylinder specimens after 126 days of loading. As discussed in Section 4.1.2, specific creep strain is defined as the total creep strain per

unit of stress. The value of the time-dependent creep coefficient, $\varphi(t)$, must not be confused with the value of the final creep coefficient, φ_p, which is a predicted final value of the creep coefficient when creep ceases, based on experimental results. The final creep coefficient is discussed further in Chapter 5.

Table 4.6. Creep measurements of the cylinder specimens after 126 days of loading

Concrete	Specimen	Applied Stress (ksi)	Initial strain (με)	Drying creep (με)	Basic creep (με)	Total creep (με)	Specific creep (με/ksi)	Creep coefficient φ(t)
SCM	Unsealed	1.20	316	345	182	527	439	1.58
	Sealed	1.20	300	-	182	182	152	0.61
SCC	Unsealed	1.20	264	179	196	375	313	1.42
	Sealed	1.20	241	-	196	196	163	0.81

It was anticipated that the total creep strains (unsealed specimens) would be larger than the basic creep strains (sealed specimens), since less water is evaporated in the sealed specimens. The free water in capillary pores increases creep resistance (Mindess, Young, & Darwin, 2003). Thus, less free water leads to less creep resistance. (Hannesson, 2010)

Figure 4.21 shows the total creep strains of the cylinder specimens. As expected, the total creep strain in the unsealed concrete was much higher than that of the sealed concrete, due to the absence of drying creep in the latter. Unsealed SCM concrete had higher total creep strain than unsealed SCC concrete. However, the total creep strain in the sealed SCM specimens was lower than that of the SCC specimens. This suggests that the SCM concrete was actually less affected by basic creep than the SCC, but had a much larger drying creep component as can be seen in Figure 4.24.

Smaller basic creep strain in the SCM than the SCC is probably caused by large portion of fly ash and slag remaining unreacted in the concrete which acts as a fine aggregate, providing higher resistance against creep. (Hannesson, 2010)

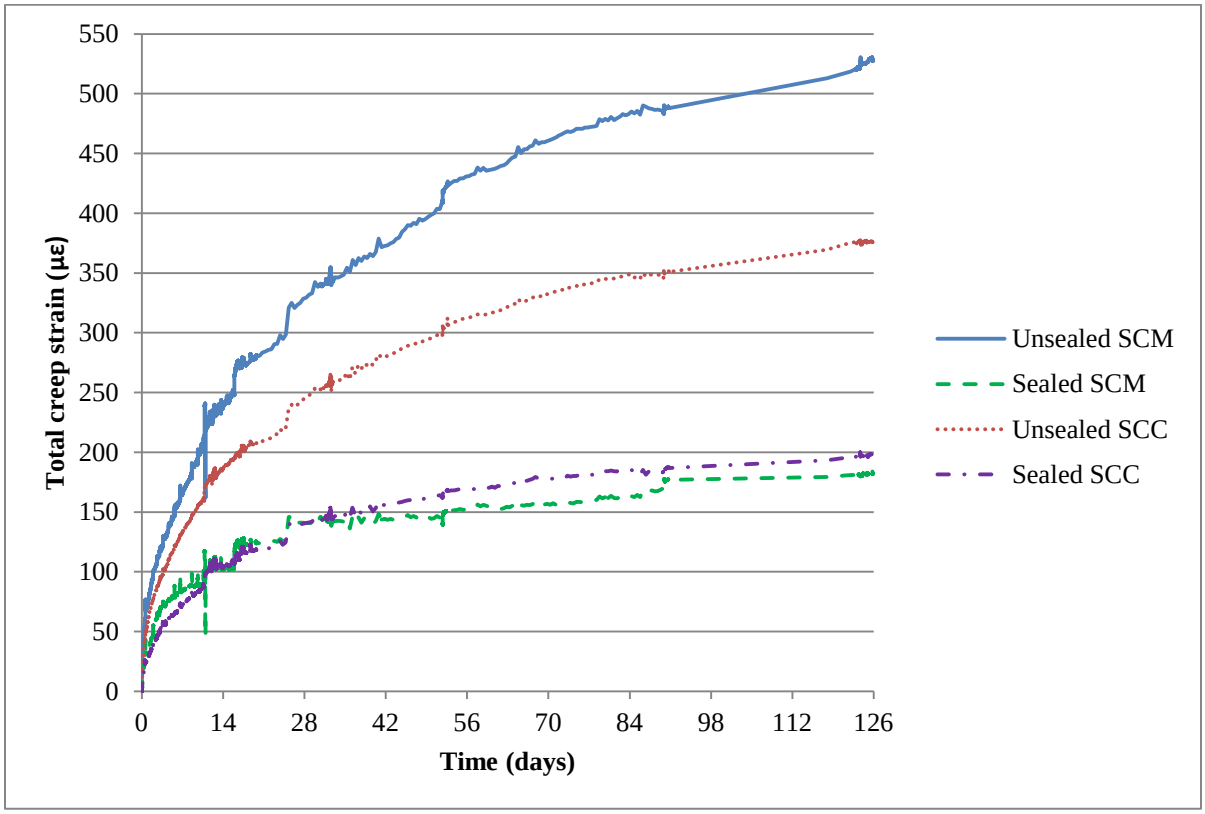

Figure 4.21. Creep strains in the cylinder specimens

Figure 4.22 shows the creep coefficient of the cylinder specimens. The unsealed SCM concrete had a higher creep coefficient than the unsealed SCC concrete. However, the creep coefficient of the sealed SCM concrete was lower than that of the sealed SCC. As mentioned in Section 4.1.2, creep strain increases linearly with increasing stress, which means that the creep coefficient is independent of loading. The difference between the two figures is due to the fact that the initial strain in the SCC was lower since it was stiffer, as discussed earlier in this chapter. Comparing the ratio of creep strain to elastic strain for the two concretes therefore yielded a greater difference than comparing the creep strains. The measured creep coefficient of the unsealed specimens at 126 days was 1.58 and 1.42 for the SCM and SCC, respectively. The measured creep coefficient of the sealed concretes at 126 days was 0.61 and 0.81 for the SCM and SCC, respectively.

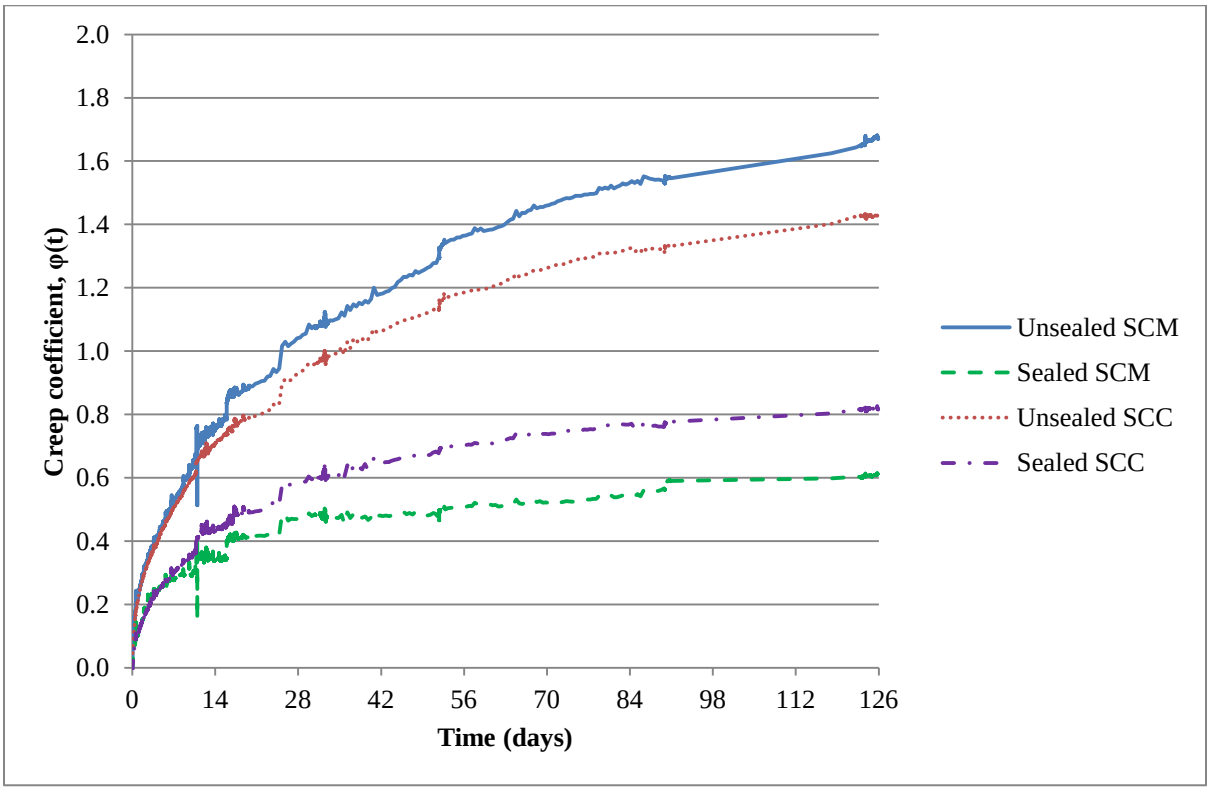

Figure 4.22. Creep coefficients of the cylinder specimens

Figure 4.23 shows the ratio of SCM creep coefficient to SCC creep coefficient for the cylinder specimens. As can be seen, the ratio for the sealed cylinders became relatively constant after approximately five weeks of loading. The rate of creep in sealed cylinders was higher for the SCC before that time. The behavior was very similar to that of CFT specimens throughout the experiment. The ratio for the unsealed cylinders was approximately constant the whole time. At 126 days, the creep coefficient of the sealed SCM was approximately 75% of the creep coefficient of the sealed SCC. The creep coefficient of the unsealed SCM was about 17% higher than that the creep coefficient of the SCC at that time.

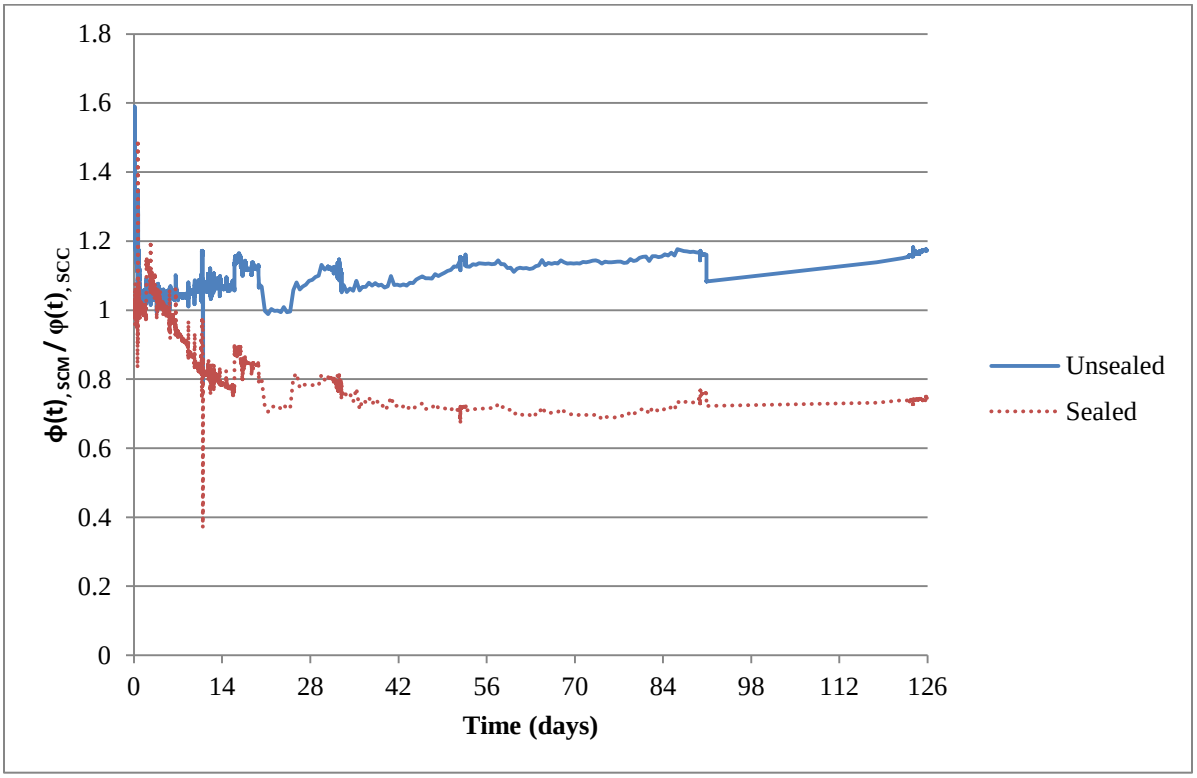

Figure 4.23. Ratio of SCM creep coefficient to SCC creep coefficient for the cylinder specimens

Figure 4.24 shows the drying creep of the unsealed cylinders. As can be seen, the drying creep of the SCM concrete was much higher than that of the regular SCC for the specimens tested in this research program. This illustrates further that SCM is very suitable for CFTs, not only because CFTs do not require high early strength of concrete, but also because drying creep can be considered negligible in CFTs. The measured drying creep of the unsealed concretes at 126 days was 345 με and 179 με for the SCM and SCC, respectively.

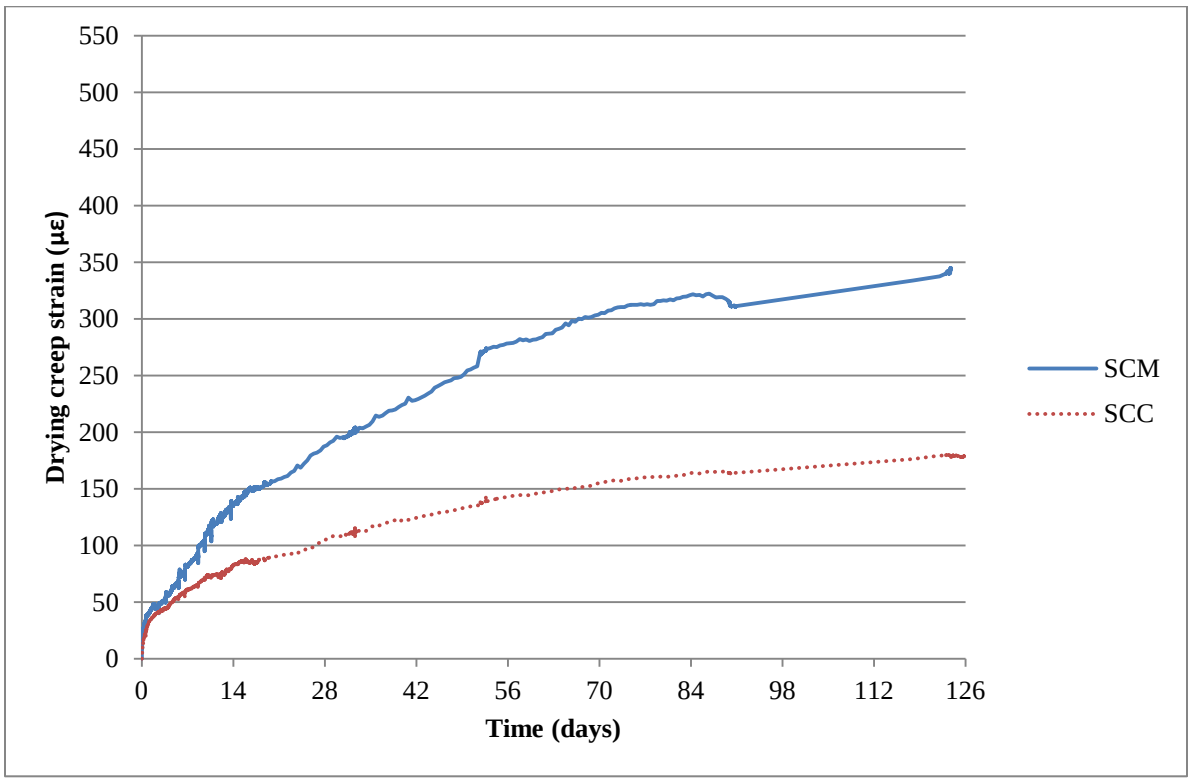

Figure 4.24. Drying creep strains in the unsealed cylinder specimens

4.3 Comparison of CFTs and cylinders

Experimental results of total strain and creep coefficient of unsealed cylinders, sealed cylinders and CFT specimens were compared for the two different concretes. Both showed a similar trend where unsealed concrete suffered much higher time-dependent strain than the sealed specimens and the CFT specimens. As discussed before, this is because concrete that is sealed from the environment suffers much less drying shrinkage than sealed concrete, and experiences negligible drying creep.

4.3.1 Total strain

Figure 4.25 shows the average total strain in the concrete of all SCM specimens tested in this research program. As can be seen, the difference between CFT core, unsealed cylinders and sealed cylinders was large. Some of the difference is due to lower stress in the concrete core of the CFT. Also, the concrete in the CFT transferred some load to the steel over time, which resulted in a decrease in elastic strain of the CFT core over time, as discussed earlier in this chapter.

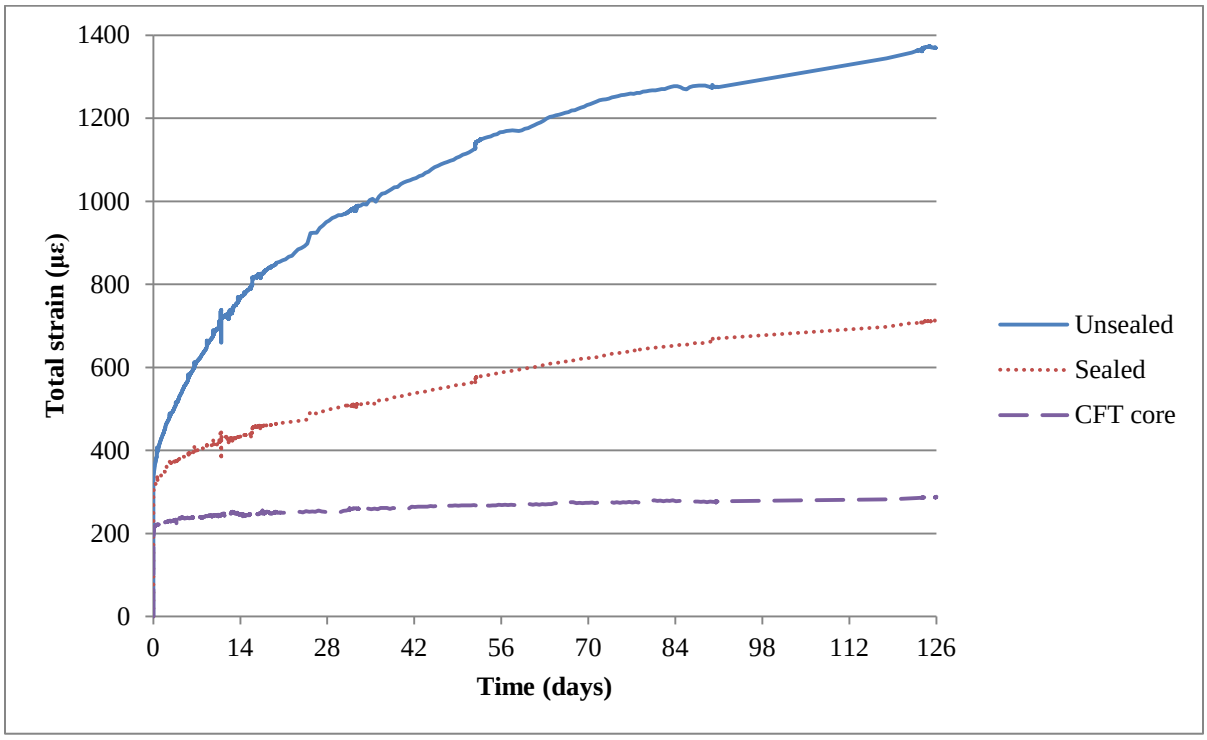

Figure 4.25. Total strains in the concrete for all SCM specimens

Figure 4.26 shows the average total strain in the concrete of all SCC specimens tested in this experiment. The difference between CFT concrete, unsealed cylinders and sealed cylinders was large. As in the SCM specimen, some of the difference is due to lower stress in the concrete core of the CFT. The concrete core in the SCC CFT specimen did not transfer as much load to the steel over time as the SCM specimen. Therefore, the difference between the sealed cylinders and the CFT core was not as great for the SCC specimen as for the SCM specimen.

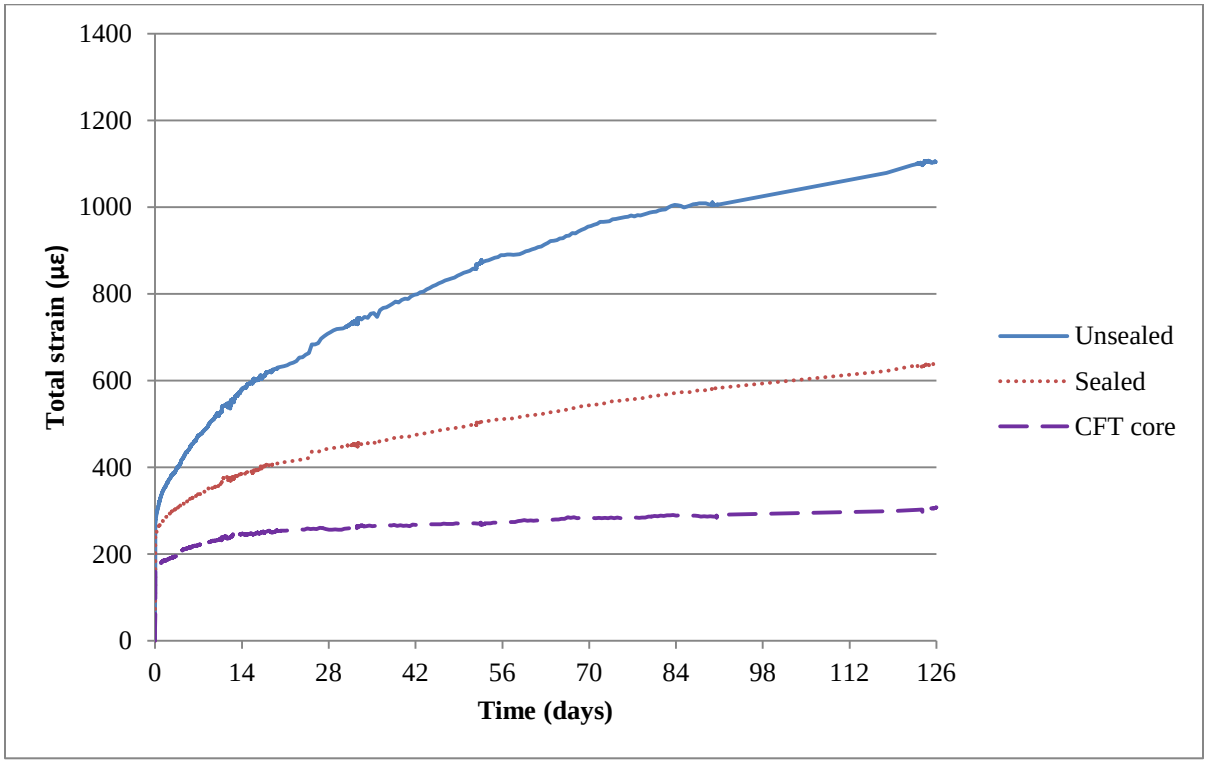

Figure 4.26. Total strains in the concrete for all SCC specimens

4.3.2 Creep coefficient

Figure 4.27 shows the creep coefficient of the concrete in all SCM specimens tested in this research program. As expected, the creep coefficient in the unsealed concrete was much higher than that of the sealed concrete, due to the absence of drying creep in the latter. The creep coefficient in the CFT core was much lower than that of the sealed specimens. This suggests that the SCM concrete expands more than the SCC as it creeps, as discussed before. This would result in more confinement from the steel tube over time, which increases the friction between the steel and the concrete and therefore increases the time-dependent axial steel strain in the tube. As mentioned before, the volumetric changes in the specimens cannot be confirmed in this research because neither hoop strains in the steel tubes nor lateral strains in the concrete cores were measured.

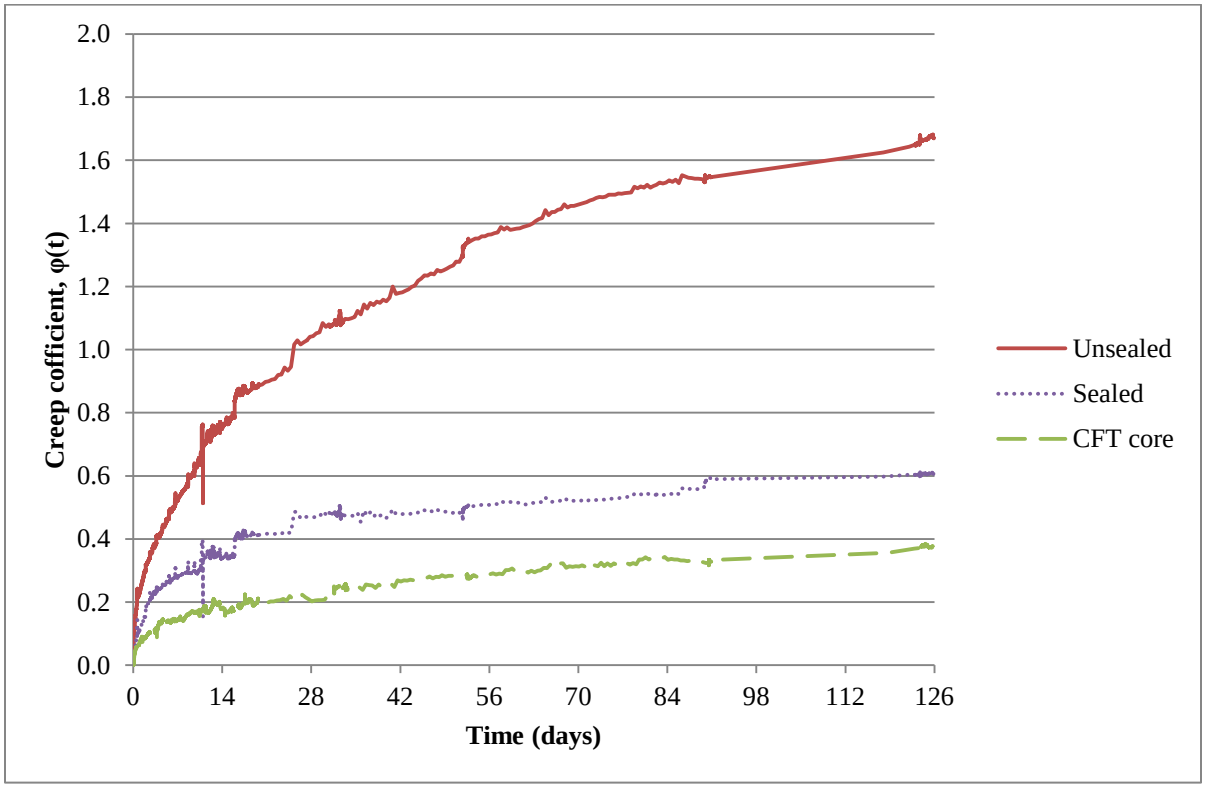

Figure 4.27. Creep coefficient of all SCM specimens

Figure 4.28 shows the creep coefficient of the SCC specimens. As for the SCM concrete, the creep coefficient in the unsealed specimens was much higher than that of the sealed concrete, due to the absence of drying creep in the latter. The creep coefficient in the CFT core, however, was almost identical to that of sealed specimens. This suggests that the basic creep of the SCC concrete consists mostly of the deviatoric component discussed before. This would result in little volume change in the concrete as it creeps, and therefore little confinement from the steel tube over time, as evident from Figure 4.6 to Figure 4.10. Little friction increase between the steel and the concrete would occur and therefore the time-dependent axial steel strain in the tube would be small. As mentioned before, the volumetric changes in the specimens cannot be confirmed in this research due to lack of information on lateral strains.

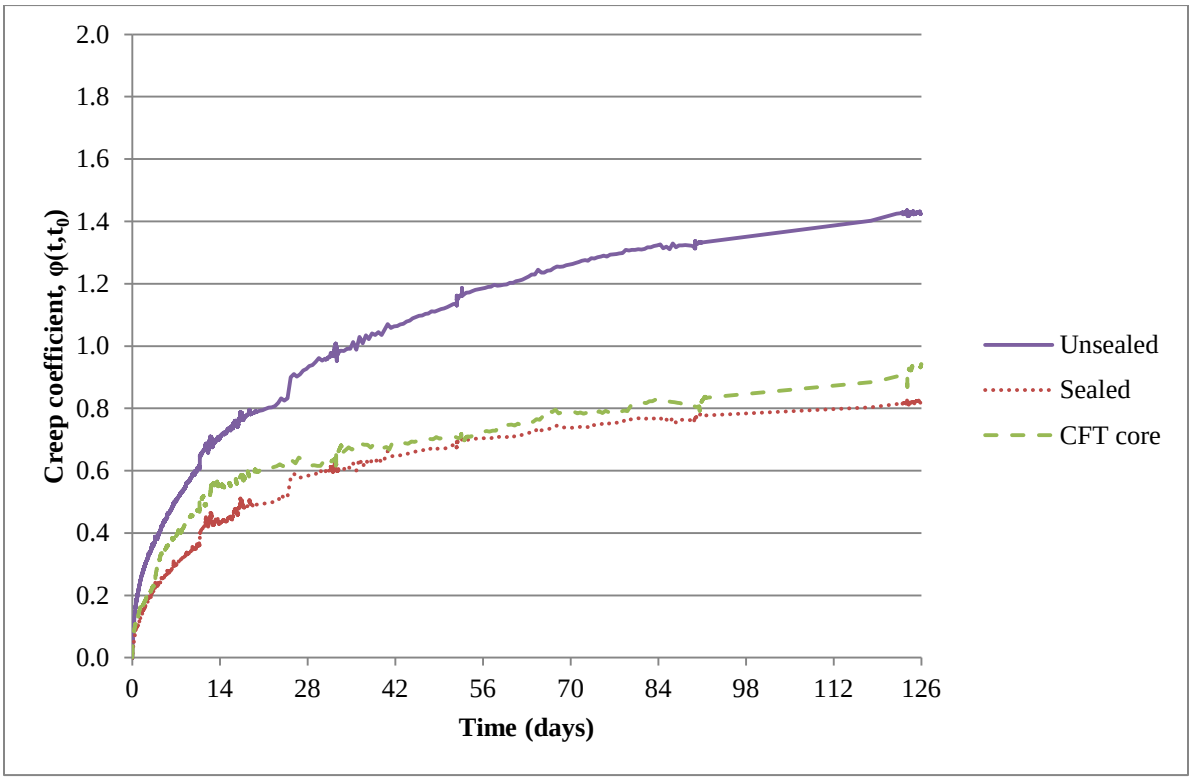

Figure 4.28. Creep coefficient of all SCC specimens

Chapter 5: Creep and shrinkage models

The results from this experiment were compared to existing models for time-dependent strains, both by evaluating and calibrating parameters and by evaluating the shape. The creep coefficient and shrinkage strain were compared with the ACI committee 209 models (ACI Committee 209, 2008), AASHTO 2007 models (AASHTO, 2007), CEB-FIP Model Code 1990 models (CEB, 1990), and GL 2000 models (Gardner & Lockman, 2001).

Time is the only variable in the models. Other parameters are taken as constants, but some models account for strength development of concrete over time. The parameters of the models are: ambient relative humidity, volume-to-surface ratio, age at loading, ambient temperature, concrete composition, compressive strength, rate of strength gain, slump, and air content. None of the models depend on all parameters mentioned.

The models are all very sensitive to relative humidity, but they do not specify how to treat concrete that is sealed from the environment with respect to humidity; higher humidity results in less moisture loss and therefore less drying creep and drying shrinkage. If concrete is completely sealed from the environment it loses no moisture due to drying. In CFTs, drying creep and drying shrinkage were determined negligible and the value of relative ambient humidity was therefore set to 100% when applying the humidity parameter to the models. The sealed cylinders experienced some drying shrinkage so it was difficult to quantify the humidity value to apply for them. The value was set as 95% because that seemed to fit the experimental curves best on average. For the unsealed cylinders, the average measured value of humidity was used; the models do not allow for variations in humidity. This value was found to be 50.3% during the 126 days of testing. The humidity and temperature report can be found in **Error! Reference source not found.**.

When comparing the unsealed and sealed specimens in this research program to the CFT specimens, it must be kept in mind that the v/s ratio is different. For a cylinder, this ratio is the radius divided by 2. The CFT core therefore has a v/s ratio of 4.875 while the value for the cylinders is 1.5. This results in a creep coefficient that is smaller for the CFTs than the cylinders. However, the v/s ratio correction factor is to account for the fact that thicker members shed less moisture over their lifetime and should therefore only apply to drying creep, but the models do

not distinct between drying and basic creep. Since only basic creep is considered in CFTs, the v/s ratio was not considered different when comparing cylinders and CFTs.

5.1 Models and parameters

5.1.1 ACI committee 209

ACI 209 report provides models for time-dependent strain in concrete. The models were developed from data that included normal weight, sand lightweight, and lightweight concrete with Type I and III cement and also takes into accounts for curing conditions; moist cured or steam cured. There are correction factors for concrete composition, age at loading, ambient relative humidity, volume-to-surface ratio, and ambient temperature. The concrete composition correction factors apply to cement content, fine aggregate percentage, and air content.

5.1.1.1 Creep model

The ACI-209 creep model is described by:

$$\varphi(t) = \frac{(t-t')^{0.6}}{10 + (t-t')^{0.6}} \varphi_u \quad \textbf{(5-1)}$$

where:

φ(t) = creep coefficient of concrete at age t, loaded at age t'

t = age of concrete (days)

t' = age of concrete at loading (days)

φ_u = ultimate (final) creep coefficient (value of the creep coefficient when creep ceases).

ACI-209 suggests an average ultimate creep coefficient of 2.35, which is multiplied by six correction factors:

$$\varphi_u = 2.35 * \gamma_{la} * \gamma_\gamma * \gamma_{vs} * \gamma_s * \gamma_\psi * \gamma_\alpha \quad \textbf{(5-2)}$$

where:

φ_u = ultimate (final) creep coefficient

$\gamma_{la} = \begin{cases} 1.25 \cdot t'^{-0.118} & for\ moist\ curing \\ 1.13 \cdot t'^{-0.094} & for\ steam\ curing \end{cases}$; age of loading factor

t' = age of concrete at loading (days)

$\gamma_{\lambda} = \begin{cases} 1.27 - 0.67 \cdot h\ for\ h \geq 0.40 \\ 1.00\ otherwise \end{cases}$; ambient relative humidity factor

h = relative ambient humidity (in decimals)

$\gamma_{VS} = \frac{2}{3}\left(1 + 1.13 \cdot \exp\left\{-0.54 \cdot {}^{V}\!/\!_{S}\right\}\right)$; volume-to-surface ratio factor

V = volume of member (in^3)

S = surface area of member (in^2)

$\gamma_s = 0.82 + 0.067 \cdot s$; slump factor

s = slump (in)

$\lambda_{\psi} = 0.88 + 0.24 \cdot \psi$; fine aggregate content factor

Ψ = fine aggregate-to-total aggregate ratio (decimals)

$\gamma_{\alpha} = 0.46 + 0.09 \cdot \alpha$; air content factor

α = air content (%)

5.1.1.2 Shrinkage model

The ACI-209 shrinkage model is described by:

$$\varepsilon_{sh}(t) = \frac{(t - t_0)}{35 + (t - t_0)} \varepsilon_{sh,u} \quad \textbf{(5-3)}$$

where:

t = age of concrete (days)

t_0 = age of concrete at beginning of drying (days)

$\varepsilon_{sh}(t)$ = shrinkage strain after t - t_0 days of drying

$\varepsilon_{sh,u}$ = ultimate (final) shrinkage strain (value of shrinkage strain when shrinkage ceases)

ACI-209 suggests an average ultimate shrinkage strain of 780 με, which is multiplied by six correction factors:

$$\varepsilon_{sh,u} = 780 * \gamma_\gamma * \gamma_{vs} * \gamma_s * \gamma_\psi * \gamma_c * \gamma_\alpha \quad \textbf{(5-4)}$$

where:

$\varepsilon_{sh,u}$ = ultimate (final) shrinkage strain

$\gamma_\lambda = \begin{cases} 1.40 - 1.0 \cdot h \ for \ 0.40 \le h \le 0.80 \\ 3.00 - 3.0 \cdot h \ for \ h > 0.80 \end{cases}$; ambient relative humidity factor

h = relative ambient humidity (in decimals)

$\gamma_{VS} = 1.2 \cdot \exp\left\{-0.12 \cdot V/S\right\}$; volume-to-surface ratio factor

V = volume of member (in^3)

S = surface area of member (in^2)

$\gamma_s = 0.89 + 0.041 \cdot s$; slump factor

s = slump (in)

$\gamma_\psi = \begin{cases} 0.30 - 1.4 \cdot \psi \ for \ \psi \le 0.50 \\ 0.90 - 0.2 \cdot \psi \ for \ \psi > 0.50 \end{cases}$; fine aggregate content factor

Ψ = fine aggregate-to-total aggregate ratio (decimals)

$\gamma_c = 0.75 + 0.00036 \cdot c$; cementitious materials content factor

c = cementitious materials content (lb/yd^3)

$\gamma_\alpha = 0.95 + 0.08 \cdot \alpha$; air content factor

α = air content (%)

5.1.2 CEB-FIP-MC90

The CEB-FIP model code for concrete structures is the European design code recommended by the Euro-International Concrete Committee and International Federation for Prestressing. It offers a similar concept as the ACI 209 for modeling time-dependent strain in concrete. The CEB-FIP-MC90 models are designed to predict the mean time dependent deformation for normal weight, plane structural concrete. It only considers parameters that are generally known in the design stage of projects. These parameters are: mean or design strength of the concrete, mean ambient relative humidity, age of concrete at loading and member dimensions. The shrinkage model depends on the same parameters, in addition to the cement type used.

5.1.2.1 Creep model

The CEB-FIP-MC90 creep model is described by:

$$\varphi = \varphi_0 * \left[\frac{(t - t')}{\beta_H + (t - t')}\right]^{0.3} \quad \textbf{(5-5)}$$

where:

φ = creep coefficient of concrete at age t, loaded at age t'

t = age of concrete (days)

t' = age of concrete at loading (days)

$$\phi_0 = \left[1 + \frac{(1-h)}{0.367 \cdot \left(A_c/u\right)^{1/3}}\right] \cdot \frac{5.3}{\sqrt{\frac{f_c'}{1.45}}} \cdot \frac{1}{0.1 + t'^{0.2}} \text{ ; notional creep coefficient}$$

h = relative ambient humidity (in decimals)

A_c = cross sectional area (in^2)

u = exposed perimeter (in)

f'_c = compressive strength at 28 days (ksi)

$$\beta_H = 150 \cdot \left[1 + (1.2 \cdot h)^{18}\right] \cdot 0.508 \cdot A_c/u + 250 \le 1{,}500 \quad \text{; constant depending on size and humidity}$$

If strength gain of the concrete is expected to be different from normal, the following corrections are used:

$$t' = t'_T \left[\frac{9}{2 + (t'_T)^{1.2}} + 1\right]^{\alpha} \ge 0.5 \; days$$

$$t'_T = \sum \Delta t_i \cdot \exp\left\{-\left[\frac{4{,}000}{273 + T(\Delta t_i)/T_0} - 13.65\right]\right\}$$

t' = age of concrete at loading (days)

t'_T = adjusted age of concrete at loading (days)

$$\alpha = \begin{cases} -1 \text{ for slowly hardening cement} \\ 0 \text{ for normal / rapid hardening cement} \\ +1 \text{ for rapid hardening high early strength cement} \end{cases}$$; cement type parameter

Δt_i = period of time at temperature T(Δt_i) (°C = 0.556*°F – 17.78)

T_0 = 1°C

5.1.2.2 Shrinkage model

The CEB-FIP-MC90 shrinkage model is described by:

$$\varepsilon_s(t, t_0) = \varepsilon_{s0} * \beta_s * (t - t_0) \quad \textbf{(5-6)}$$

where:

t = age of concrete (days)

t_0 = age of concrete at beginning of drying (days)

$$\varepsilon_{s0} = \left[160 + 10 \cdot \beta_{sc} \cdot \left(9 - \frac{f_c'}{1{,}450}\right)\right] \cdot \beta_{RH}$$; notional shrinkage coefficient

$$\beta_{sc} = \begin{cases} 4 \text{ for slowly hardening cement} \\ 5 \text{ for normal / rapid hardening cement} \\ 8 \text{ for rapid hardening high early strength cement} \end{cases}$$; cement type parameter

$$\beta_{RH} : \begin{cases} -1.55 \cdot \left[1 - h^3\right] & \text{for} \quad 0.40 \le h \le 0.99 \\ 0.25 & \text{for} \quad h \ge 0.99 \end{cases}$$; relative humidity factor

h = relative ambient humidity (in decimals)

f'_c = compressive strength at 28 days (ksi)

$$\beta_s(t,t_0)=\left[\frac{(t-t_0)}{\beta_{sH}+(t-t_0)}\right]^{0.5}$$; shrinkage-time function

$$\beta_{sH}=350\cdot\left(5.08\cdot A_c/u\right)^2$$; geometric factor

A_c = cross sectional area (in^2)

u = exposed perimeter (in)

5.1.3 AAHSTO 2007

The AASHTO 2007 models for long-term deflections of concrete resemble the ACI 209 method, in that it too uses an ultimate creep coefficient which is corrected with several factors based on the materials, the environment and the loading age. It is based on results of research documented in NCHRP Report 496 (2003), which was sponsored by the National Cooperative Highway Research Program (NCHRP). The AASHTO 2007 models have correction factors for relative ambient humidity, the volume-to-surface ratio, 14-day concrete strength, and time development which depends on the 14-day concrete strength.

5.1.3.1 Creep model

The AASHTO 2007 creep model is described by:

$$\psi(t,t_i)=1.9*k_s*k_{hc}*k_f*k_{td}*t_i^{-0.118} \quad \textbf{(5-7)}$$

where:

$\Psi(t,t_i)$ = time-dependent creep coefficient

k_s = 1.45-0.13(V/S) ≥ 1.0 ; volume-to-surface area factor

V = volume of member (in^3)

S = surface area of member (in^2)

k_{hc} = 1.56 – 0.008H ; relative humidity factor for creep

h = relative ambient humidity (in %)

$$k_f = \frac{5}{1+f'_{ci}}$$; concrete strength factor

f'_{ci} = compressive strength at time of loading

$$k_{td} = \frac{t}{61-4f'_{ci}+t}$$; time development factor (time-dependent)

t = age of concrete (days)

t_i = age of concrete at loading (days)

5.1.3.2 Shrinkage model

AASTO 2007 suggests the following model for shrinkage:

$$\varepsilon_{sh}(t,t_i) = 480 * k_s * k_{hs} * k_f * k_{td} * t_i^{-0.118} \quad \textbf{(5-8)}$$

where:

k_{hs} = 2.0 – 0.014H ; relative humidity factor for shrinkage

all other factors are the same as for the creep model

5.1.4 GL 2000

The GL2000 models were developed by N. J. Gardner and M. J. Lockman as a design office procedure to predict creep and shrinkage in concrete structures. The predicted values can be improved by measuring the compressive strength and modulus of elasticity. When the modulus of elasticity is not measured, as was the case in this research, the measured initial elastic strain can be used with the creep coefficient to develop the curve, as done for previously discussed

models. The creep coefficient is predicted with correction factors for the time at loading, volume-to-surface ratio, ambient relative humidity and the time at the beginning of moisture loss. Shrinkage strain prediction takes into account cement type used, volume-to-surface ratio, relative ambient humidity and mean 28-day compressive strength.

5.1.4.1 Creep model

The GL2000 creep model proposes a creep coefficient in an equation which shows all the variables on which it is dependent:

$$\Phi(t,t_0) = \Phi(t_c)\left[2\left(\frac{(t-t_0)^{0.3}}{(t-t_0)^{0.3}+14}\right)+\left(\frac{7}{t_0}\right)^{0.5}\left(\frac{t-t_0}{t-t_0+7}\right)^{0.5}+2.5(1-1.086h^2)\left(\frac{t-t_0}{t-t_0+77\cdot(v/s)^2}\right)^{0.5}\right] \quad \textbf{(5-9)}$$

where:

$\Phi(t_c) = \left[1-\left(\frac{t_0-t_c}{t_0-t_c+77\cdot(v/s)^2}\right)^{0.5}\right]^{0.5}$; correction factor for drying before loading

t_c = age of concrete at beginning of drying (days)

h = relative ambient humidity (in decimals)

t = age of concrete (days)

t_0 = age of concrete at loading (days)

v = volume of member (in^3)

s = surface area of member (in^2)

5.1.4.2 Shrinkage model

The GL 2000 shrinkage model is described by:

$$\varepsilon_s(t, t_0) = \varepsilon_{shu} * \beta(h) * \beta(t) \quad \textbf{(5-10)}$$

where:

$\varepsilon_{shu} = 900K\left(\frac{30}{f_{cm28}}\right)^{1/2} \times 10^{-6}$; ultimate shrinkage strain

$\beta(h) = 1\text{-}1.18h^4$; correction term for the effect of time on shrinkage

$\beta(t) = \left(\frac{t - t_c}{t - t_c + 77(v/s)^2}\right)^{0.5}$; correction factor for drying before loading

h = relative ambient humidity (in decimals)

t_c = age of concrete at beginning of drying (days)

t = age of concrete (days)

v = volume of member (in^3)

s = surface area of member (in^2)

K = 1 for type I cement, 0.75 for type II cement, and 1.15 for type III cement

f_{cm28} = compressive strength at 28 days

5.2 Models compared with experimental results

Experimental results from the long-term experiment of the CFTs, sealed cylinders and unsealed cylinders for both types of concrete were plotted with the creep and shrinkage models discussed above. The model curves were developed using the equations for each model, using theand known parameters of the materials and surroundings.

5.2.1 Creep models compared with experimental results

Table 5.1 shows a comparison between the creep models and experimental results after 126 days of loading.

Table 5.1. Creep models compared with experimental results after 126 days of loading

Concrete	Specimen	Experiment	ACI 209		CEB-FIP-MC90		AASHTO 2007		GL 2000	
		$\varphi(t)$	$\varphi(t)_p$	%	$\varphi(t)_p$	%	$\varphi(t)_p$	%	$\varphi(t)_p$	%
SCM	Unsealed	1.58	1.30	-17	1.93	22	1.30	-18	2.34	48
	Sealed	0.61	0.88	45	0.68	11	0.90	47	1.19	95
	CFT	0.39	0.84	115	0.49	25	0.85	119	1.02	160
SCC	Unsealed	1.42	1.30	-8	1.73	22	0.91	-36	2.34	65
	Sealed	0.81	0.88	9	0.61	-25	0.63	-23	1.19	47
	CFT	0.94	0.84	-11	0.44	-53	0.60	-37	1.02	8

Figure 5.1 to Figure 5.6 display the experimental curves of creep coefficient plotted with the creep models. On each plot, all the creep models considered are plotted with one experimental curve. This is done for unsealed cylinders, sealed cylinders, and CFTs for both types of concrete.

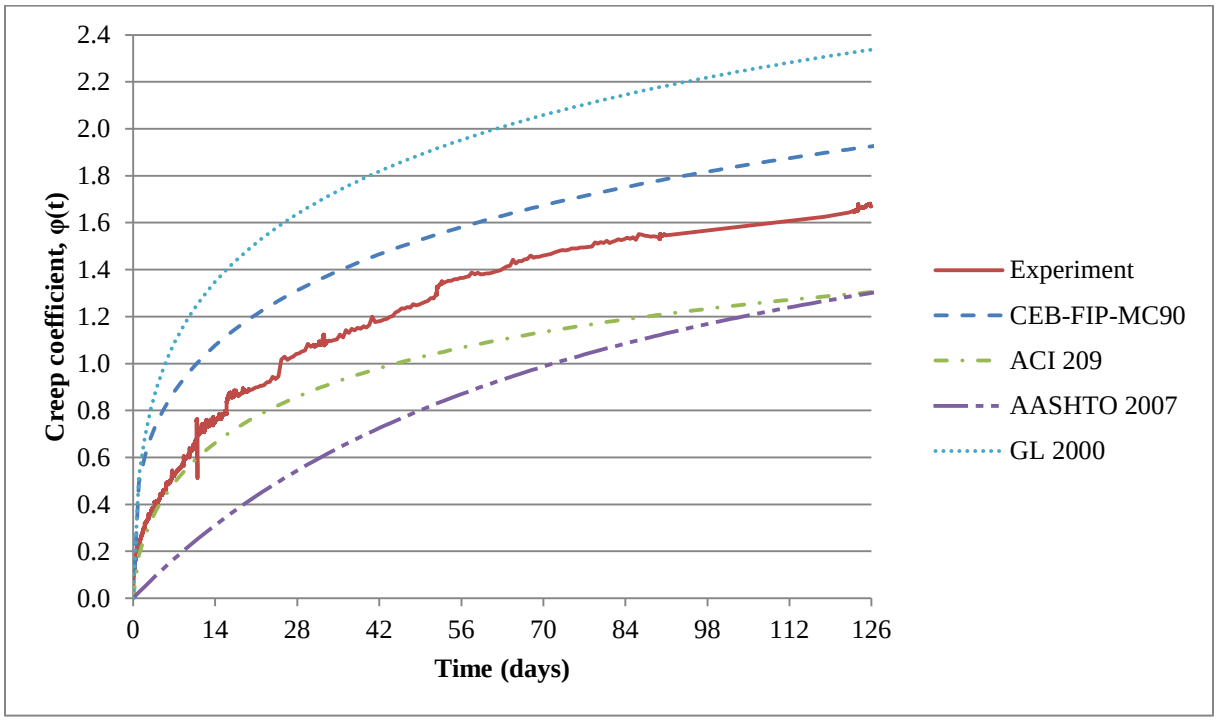

Figure 5.1. Creep models for unsealed SCM cylinders compared with experimental results

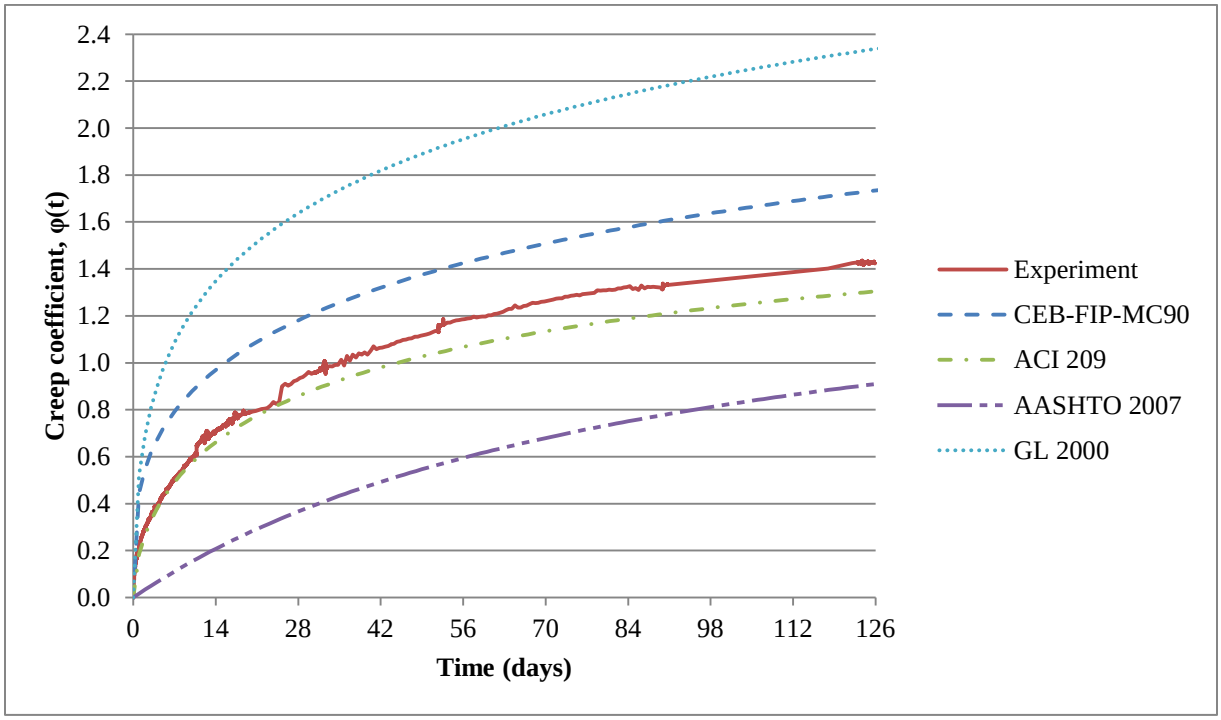

Figure 5.2. Creep models for unsealed SCC cylinders compared with experimental results

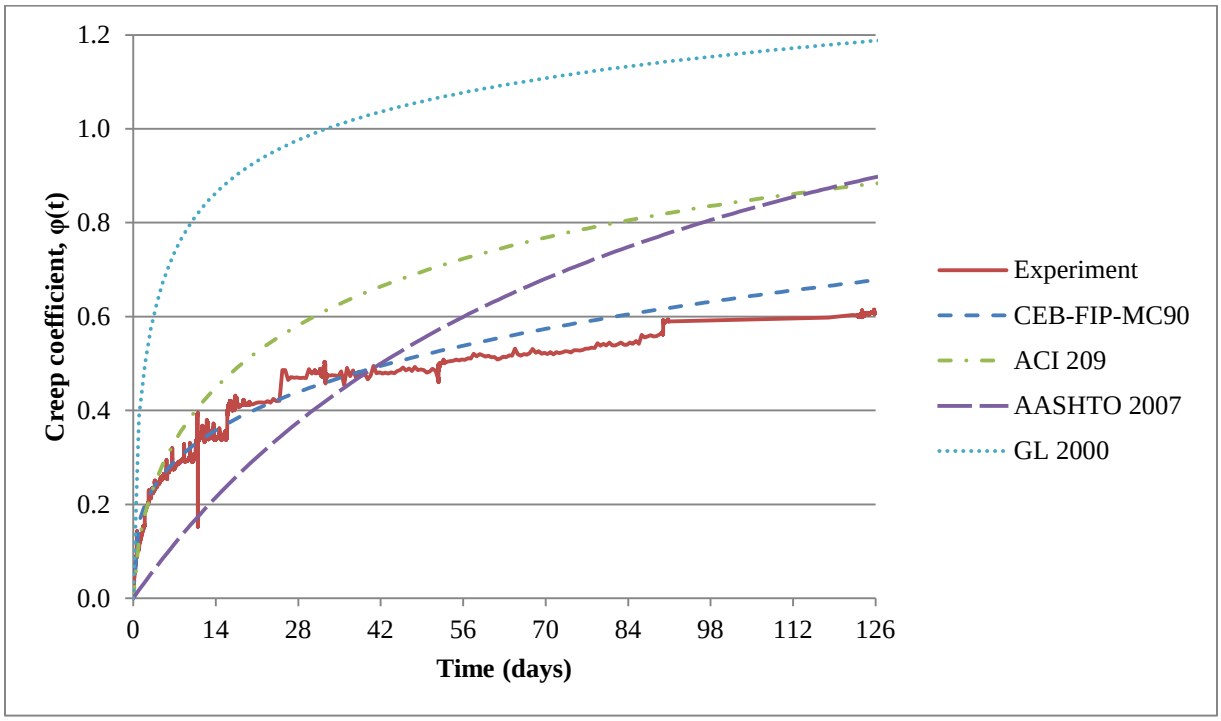

Figure 5.3. Creep models for sealed SCM cylinders compared with experimental results

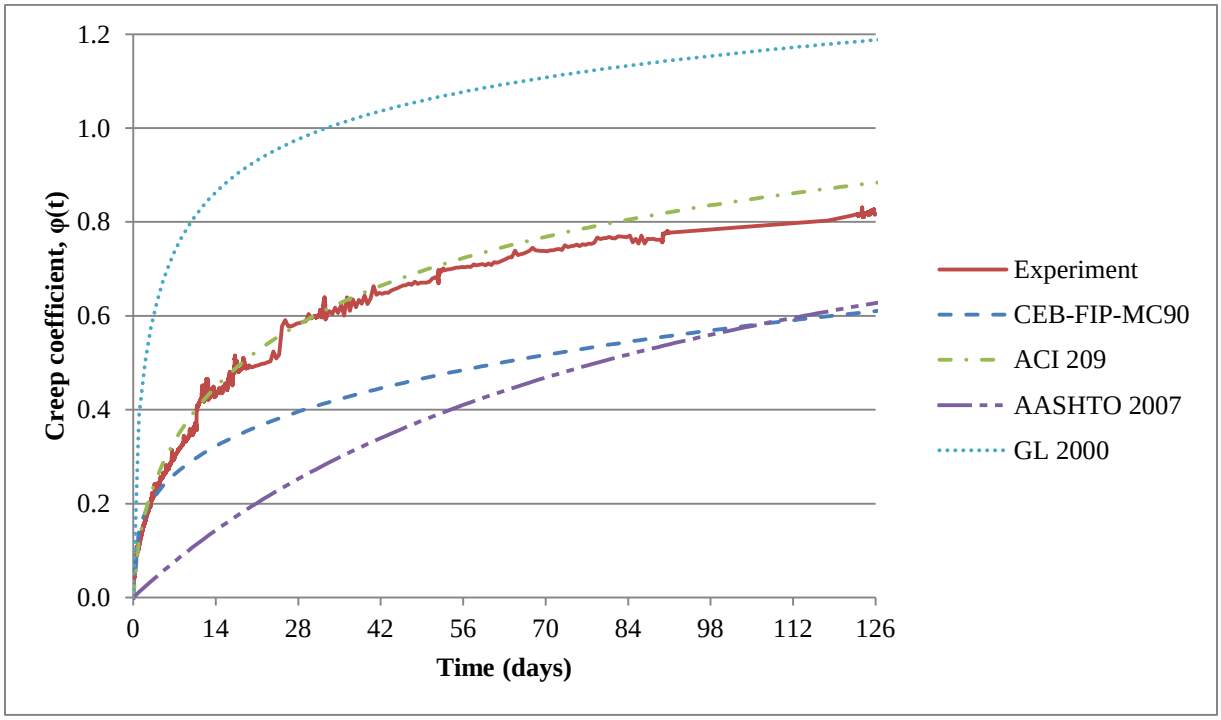

Figure 5.4. Creep models for sealed SCC cylinders compared with experimental results

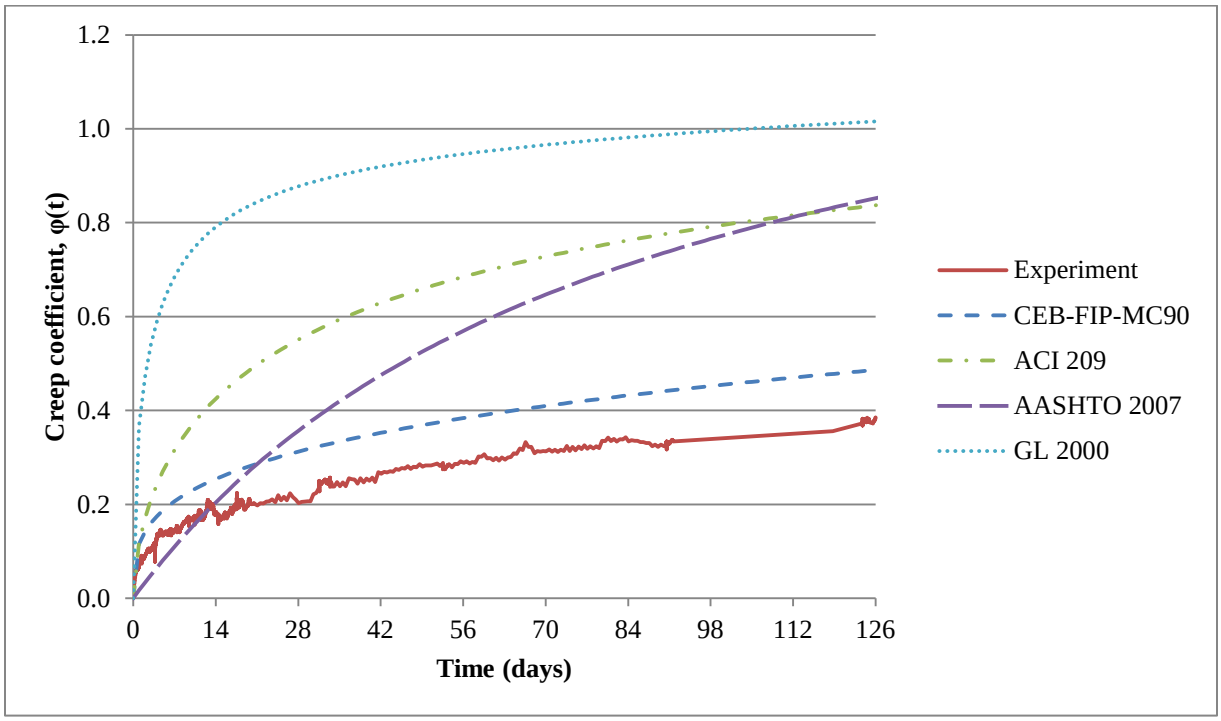

Figure 5.5. Creep models for SCM CFT core compared with experimental results

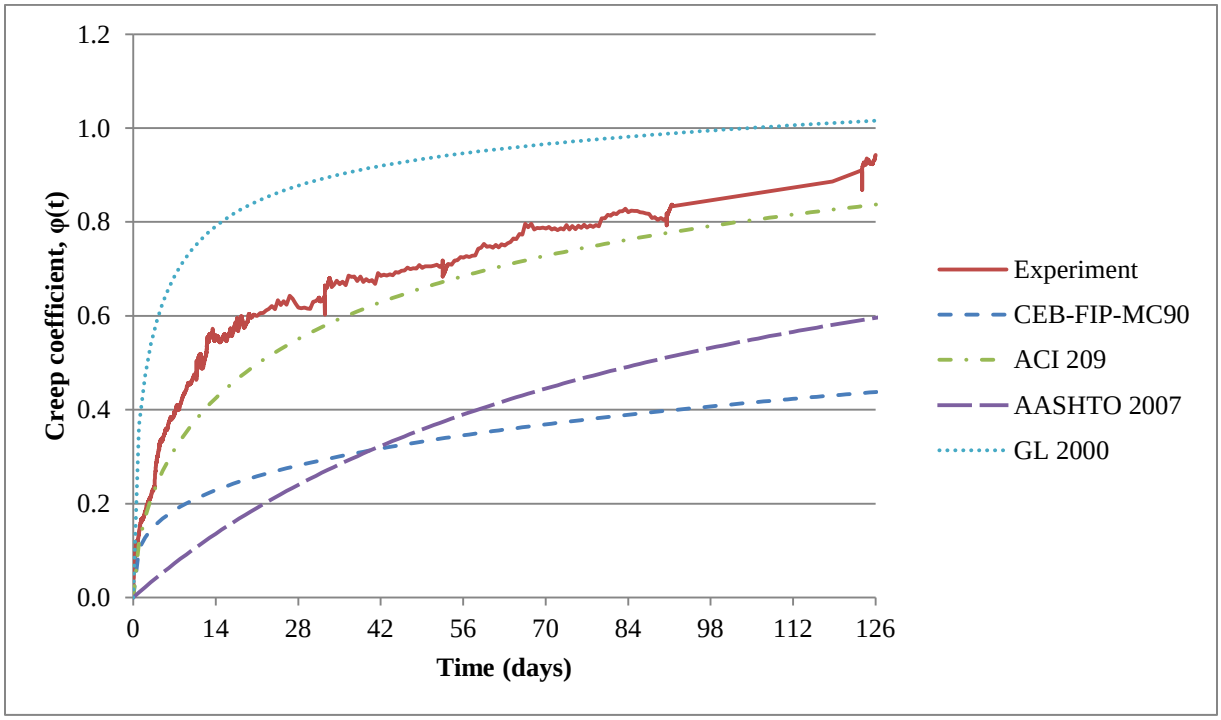

Figure 5.6. Creep models for SCC CFT core compared with experimental results

5.2.2 Shrinkage models compared with experimental results

Table 5.2 shows a comparison between the shrinkage models and experimental results after 126 days of loading.

Table 5.2. Shrinkage models compared with experimental results after 126 days of loading

Concrete	Specimen	Experiment $\varepsilon_{sh}(t)$	ACI 209		CEB-FIP-MC90		AASHTO 2007		GL 2000	
			$\varepsilon_{sh}(t)_{,p}$	%	$\varepsilon_{sh}(t)_{,p}$	%	$\varepsilon_{sh}(t)_{,p}$	%	$\varepsilon_{sh}(t)_{,p}$	%
SCM	Unsealed	527	533	1	269	-49	368	-30	419	-20
	Sealed	231	262	14	44	-81	190	-18	18	-92
SCC	Unsealed	466	533	14	326	-30	258	-45	378	-19
	Sealed	203	262	29	53	-74	133	-35	16	-92

Figure 5.7 to Figure 5.10 display the experimental curves of shrinkage strains plotted with the shrinkage models. On each plot, all the shrinkage models considered are plotted with one experimental curve. This is done for unsealed cylinders and sealed cylinders for both types of concrete.

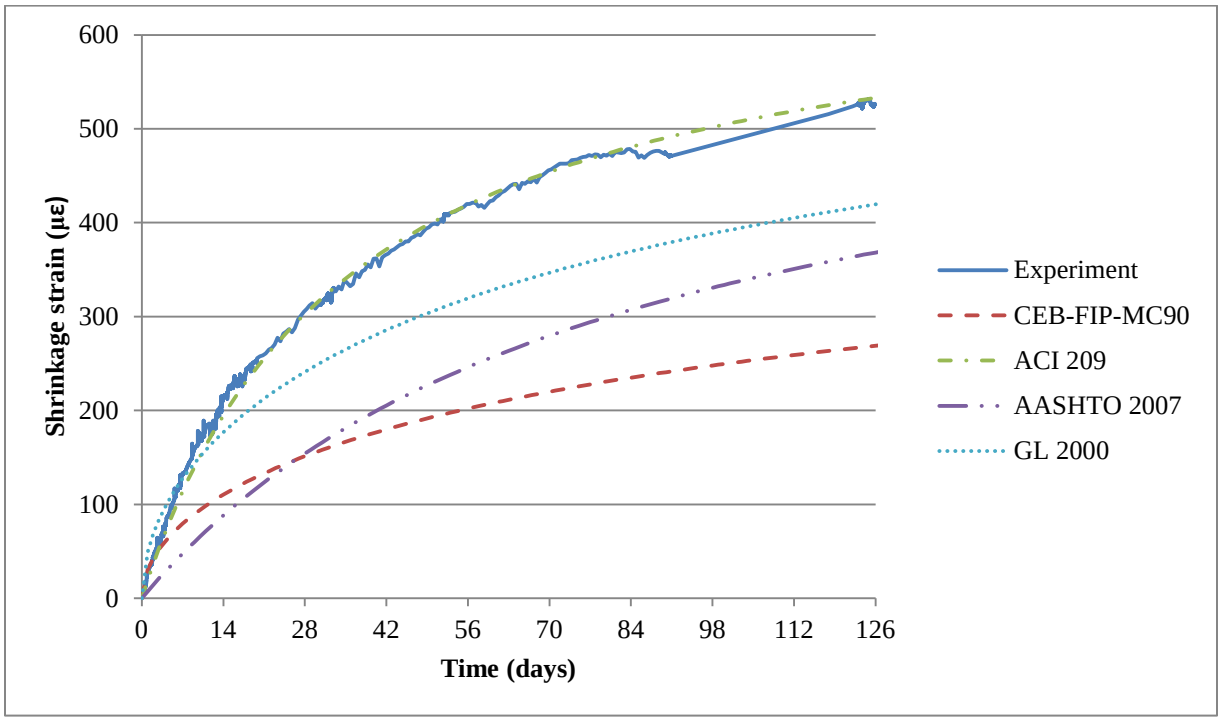

Figure 5.7. Shrinkage models for unsealed SCM cylinders compared with experimental results

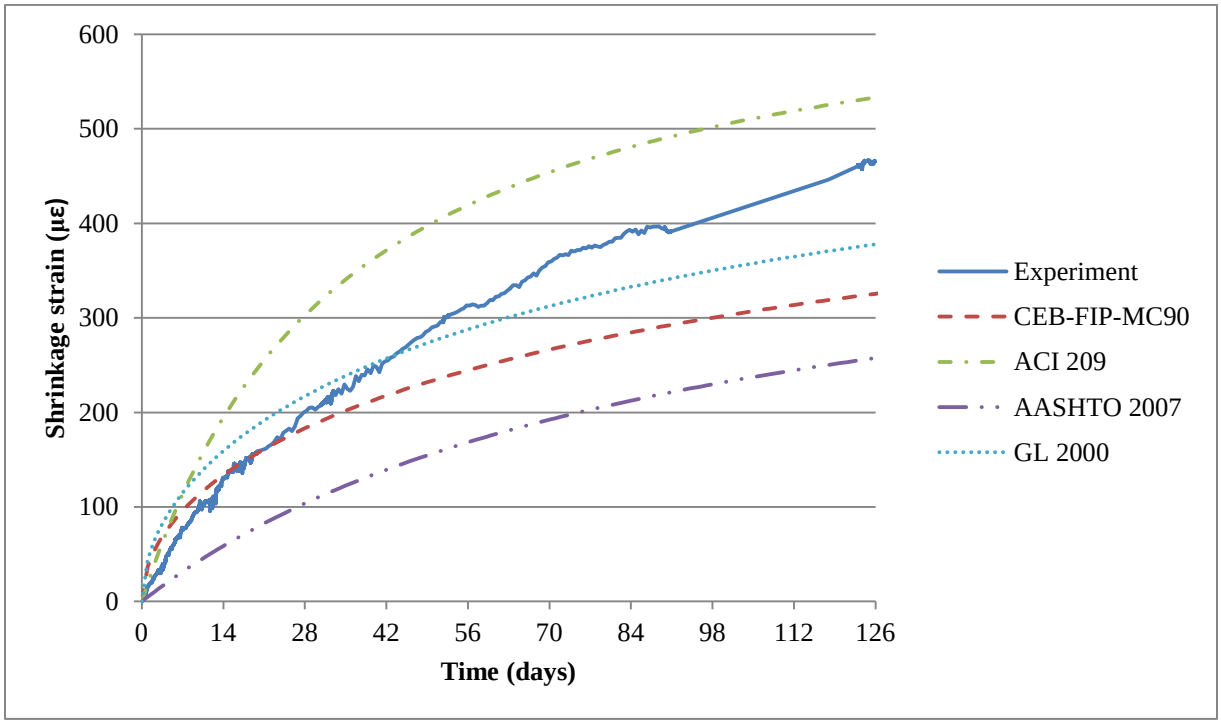

Figure 5.8. Shrinkage models for unsealed SCC cylinders compared with experimental results

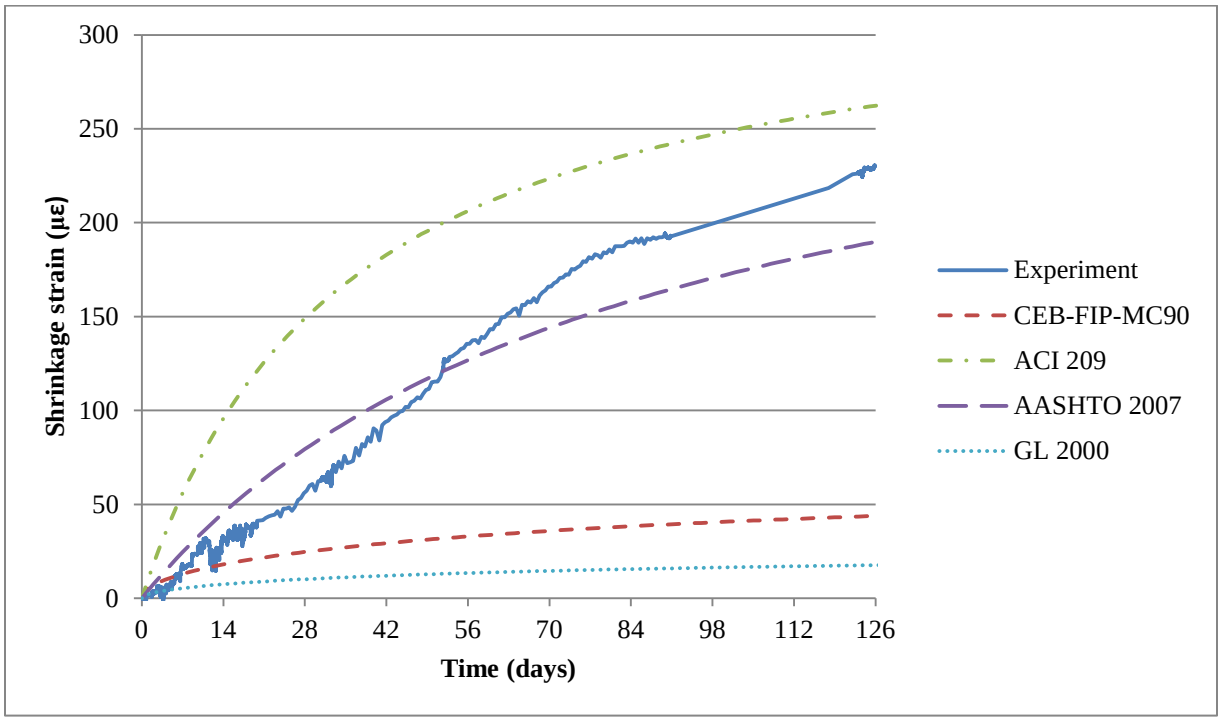

Figure 5.9. Shrinkage models for sealed SCM cylinders compared with experimental results

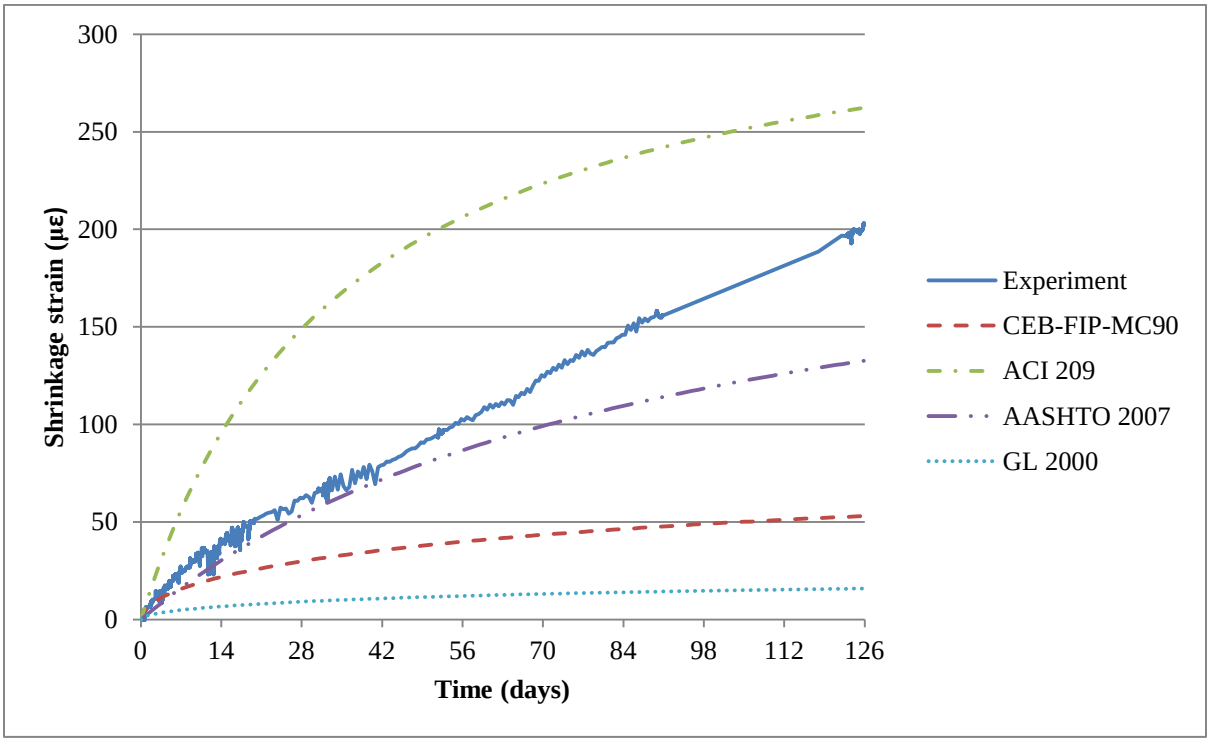

Figure 5.10. Shrinkage models for sealed SCC cylinders compared with experimental results

The ACI 209 model provides a good estimation of the creep coefficient of unsealed SCM for the first week of loading, but then the curve predicts a faster rate of ceasing than observed in the experiment. The CEB-FIP-MC 90 model seems to provide the best estimation for the unsealed SCM concrete, although it slightly overestimates the deflection. This overestimation is largely occurring in the first few days of loading. The AASHTO 2007 model predicts about the same creep coefficient as the ACI model at 126 days. However, the fit is much better in the ACI model, since the AASHTO model does not capture the early creep as well. For example, the creep coefficient at fourteen days is more than double that observed in the experiment. The GL 2000 model predicts high values, especially in the first few weeks of loading.

The ACI 209 model provides the best estimation of the creep coefficient of the plain unsealed conventional concrete, especially for the first two weeks of loading. The CEB-FIP-MC 90 is a rather good indicator as well, but again it overestimates the deflection occurring in the beginning. The AASHTO 2007 model underestimates grossly the development of creep. The model is quite sensitive to the 14-day compressive strength and seems to overestimate the effect that high early strength has on creep. Again, the AASHTO model does not capture early creep as well as the ACI 209 model. The GL 2000 model predicts high values, especially in the first few weeks of loading.

For the sealed SCM concrete, the ACI 209 model again predicts the early creep well. However, it ceases much faster than the model assumes. The CEB-FIP-MC 90 creep model is the best predictor for the sealed SCM concrete but creep seems to slow down a bit faster than the model presumes. The AASHTO 2007 model does not capture the creep behavior well. The prediction of early creep is much too low and the creep rate ceases more slowly than the experiment indicates. The GL 2000 model grossly overestimates creep during the first month of loading but captures the creep rate rather well after that.

The ACI 209 creep model is the best predictor of creep in the sealed SCC concrete. The experimental curve follows the model very closely for the first 10 weeks and after that the difference is small, as the creep model starts to slightly overestimate the creep rate. The CEB-FIP-MC 90 model underestimates creep of sealed SCC concrete despite capturing the behavior well during the first week. Again, the AASHTO 2007 model does not capture the creep behavior

of sealed concrete well, although the curve approaches the experimental one over time. The GL 2000 model again grossly overestimates creep during the first month of loading but captures the creep rate rather well after that.

All models overestimate creep for the SCM CFT specimen. This is due to the fact that it sheds some of its load to the steel over time, which means that the stress in the concrete decreases. Therefore, the elastic deflection decreases, which makes the creep coefficient, as a function of the initial elastic strain, smaller. None of the models account for decreasing load although it would not be complex. However, it is not practical since total deflection and deflection after initial loading are generally the parameters of interest in design. The CEB-FIP-MC90 model captures the behavior better than the other models, but overestimates early creep as before. The model has the best fit largely due to the fact that it is more sensitive to relative ambient humidity than the other models. Since the moisture loss in CFTs was assumed negligible, humidity was set as 100% when modeling the behavior of the CFT specimens.

As discussed in Chapter 4, the main difference in behavior between the SCC CFT and the SCM CFT specimens is the amount of load shed to the steel during the 18 weeks of loading. The SCC specimen sheds almost no load to the steel and therefore the stress in the concrete does not change much.. As a result, the creep of the SCC CFT core is much higher than that of the SCM specimen and very similar to the creep of the SCC sealed cylinders. The ACI 209 model provides the best prediction in this case. It follows the experimental curve closely, but is slightly below it. The CEB-FIP-MC90 and The AASHTO 2007 models underestimate the development of creep due to sensitivity to humidity and 14-day compressive strength, respectively, while the GL 2000 model overestimates it. However, this is the best prediction that GL 2000 creep model made for the specimens in this experiment. This model, like the CEB-FIP-MC90 model is sensitive to humidity, which benefits the estimation in this case. Shrinkage models compared with experimental results

The ACI 209 model provides an estimation of the shrinkage strain of unsealed SCM that is almost identical to the experimental curve. The CEB-FIP-MC 90 model seems to provide good estimation for the first few days since the cylinders were removed from the fog room, but the rate after that is too slow. The AASHTO 2007 model predicts too low shrinkage as well, but it is

closer to the experimental curve in shape. The GL 2000 model predicts high values of early shrinkage but the rate decreases faster than observed in the experiment.

The ACI 209 model overestimates the shrinkage strain somewhat for unsealed SCC, but the curves are still similar. Other models underestimate the shrinkage, as was the case with the SCM specimens.

The experimental curve of the sealed SCM is quite unpredictable and cannot be represented well with a single function as all the shrinkage models are comprised of. The ACI 209 model overestimates the shrinkage strain greatly in the beginning but the error becomes less with time. The AASHTO 2007 model predicts too low shrinkage but is closer to the experimental curve overall. The other two models are too far from the experimental curve to be compared to it directly. They are both very sensitive to the relative ambient humidity, even more so than the corresponding creep models since all drying shrinkage is associated with moisture loss while this is true only for drying creep, not for basic creep.

This experimental curve is rather unpredictable, as was the case for the sealed SCM specimens, but seems almost linear. The ACI 209 model again overestimates the shrinkage strain of sealed concrete greatly in the beginning. The AASHTO 2007 model predicts too low shrinkage but is again closer to the experimental curve overall. The other two models are again too far from the experimental curve to be compared to it directly.

5.3 Model calibrations

All creep and shrinkage models considered in this research program were calibrated to get the best agreement with the experimental data. This was done to estimate a value of the final creep coefficient and final shrinkage strain for the specimens tested.

The models are very sensitive to relative ambient humidity, but they do not specify how to treat concrete that is sealed from the environment. Humidity is probably the parameter which is most difficult to measure in this experiment. In addition, it was very fluctuating throughout the experiment but the models do not account for changes in humidity. For these reasons, the models were calibrated by changing the value of the relative humidity until a good fit with the

experimental curve was found. For the ACI 209 and AASHTO 2007 models it does not matter which parameter is changed; the value of the final creep coefficient and the shape of the curve will be the same. For the CEB-FIP-MC90 and GL 2000 models it matters to a certain extent, but it has minimal effect on the final creep coefficient and the shape of the curve.

5.3.1 Creep model calibrations

Table 5.3 presents the final creep coefficient ($\varphi_{u,p}$) for all specimens, predicted by the models. The value of the final creep coefficient after calibration ($\varphi_{u,c}$) is shown as a comparison.

Table 5.3. Model predictions of ultimate creep coefficient before and after calibration

Concrete	Specimen	ACI 209		CEB-FIP-MC90		AASHTO 2007		GL 2000	
		$\varphi_{u,p}$	$\varphi_{u,c}$	$\varphi_{u,p}$	$\varphi_{u,c}$	$\varphi_{u,p}$	$\varphi_{u,c}$	$\varphi_{u,p}$	$\varphi_{u,c}$
SCM	Unsealed	2.02	2.60	2.89	2.52	2.16	2.75	4.50	3.44
	Sealed	1.37	0.97	1.48	1.42	1.49	0.98	2.73	1.43
	CFT	1.30	0.57	1.32	1.00	1.41	0.60	2.46	0.84
SCC	Unsealed	2.02	2.21	2.61	2.18	1.58	2.41	4.50	3.17
	Sealed	1.37	1.27	1.33	1.50	1.09	1.38	2.73	2.02
	CFT	1.30	1.43	1.19	1.56	1.03	1.56	2.46	2.27

Figure 5.11 to Figure 5.16 display the experimental curves of creep coefficient plotted with the creep models. On each plot, all the creep models considered are plotted with one experimental curve. This is done for unsealed cylinders, sealed cylinders, and CFTs for both types of concrete.

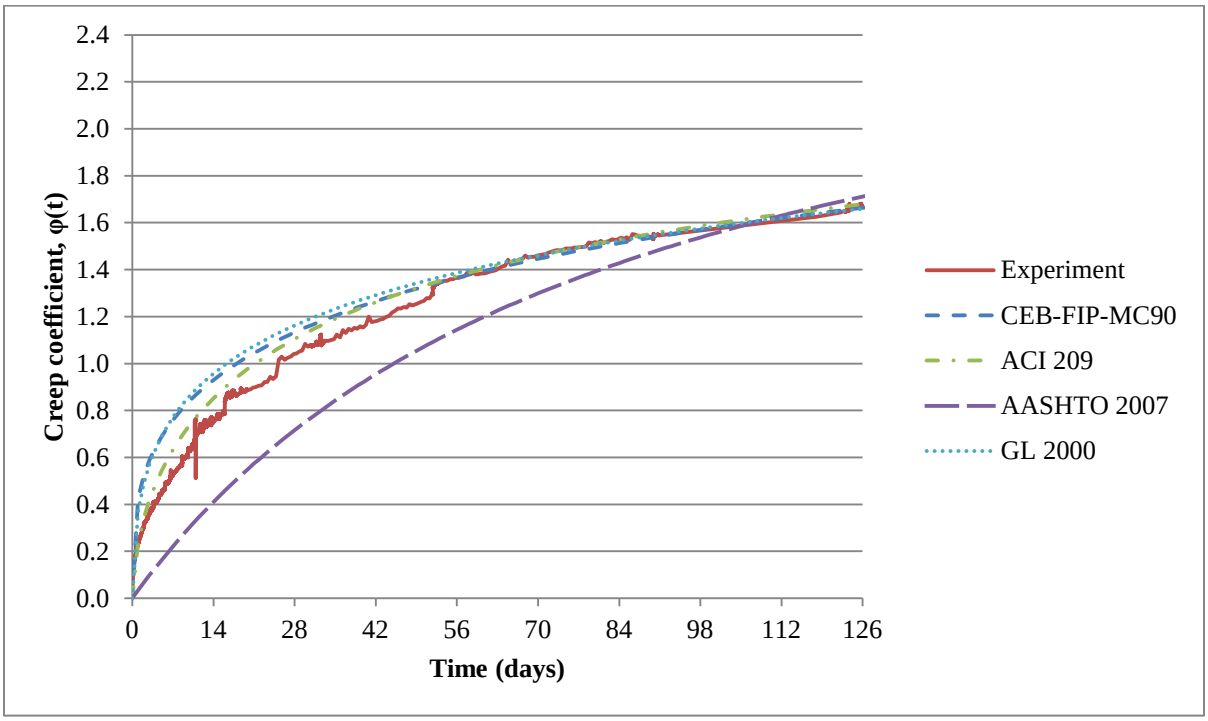

Figure 5.11. Creep models for unsealed SCM cylinders calibrated to fit experimental results

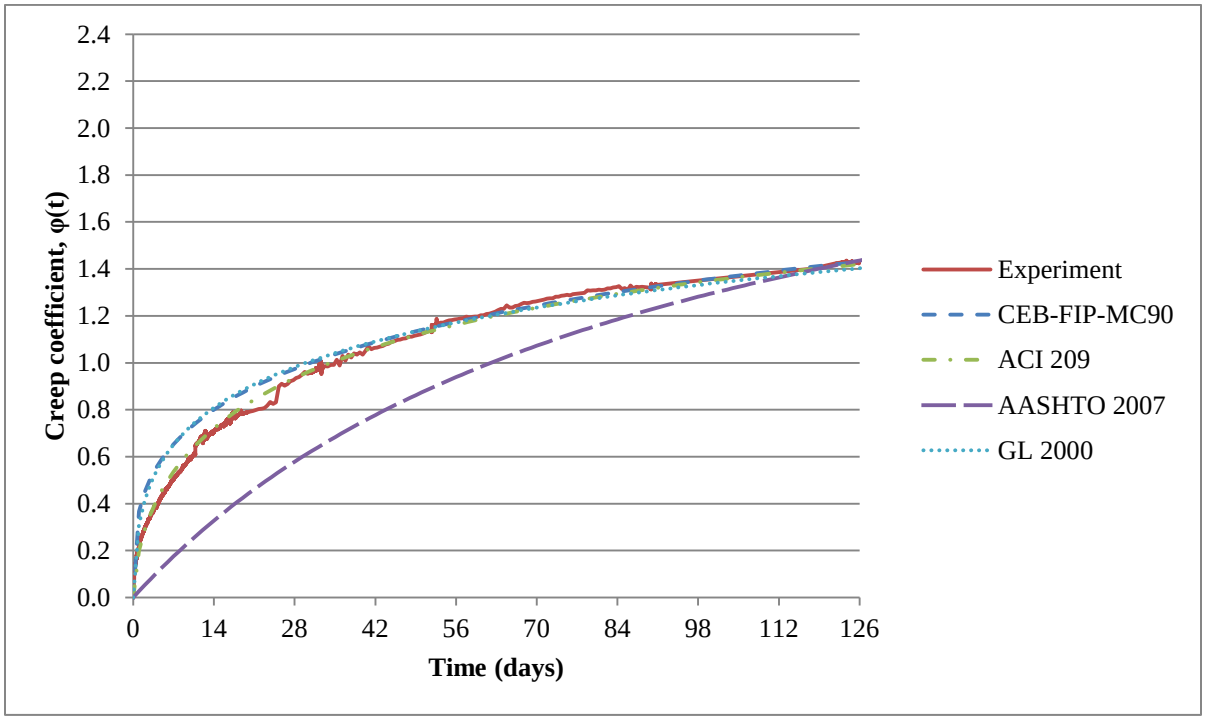

Figure 5.12. Creep models for unsealed SCC cylinders calibrated to fit experimental results

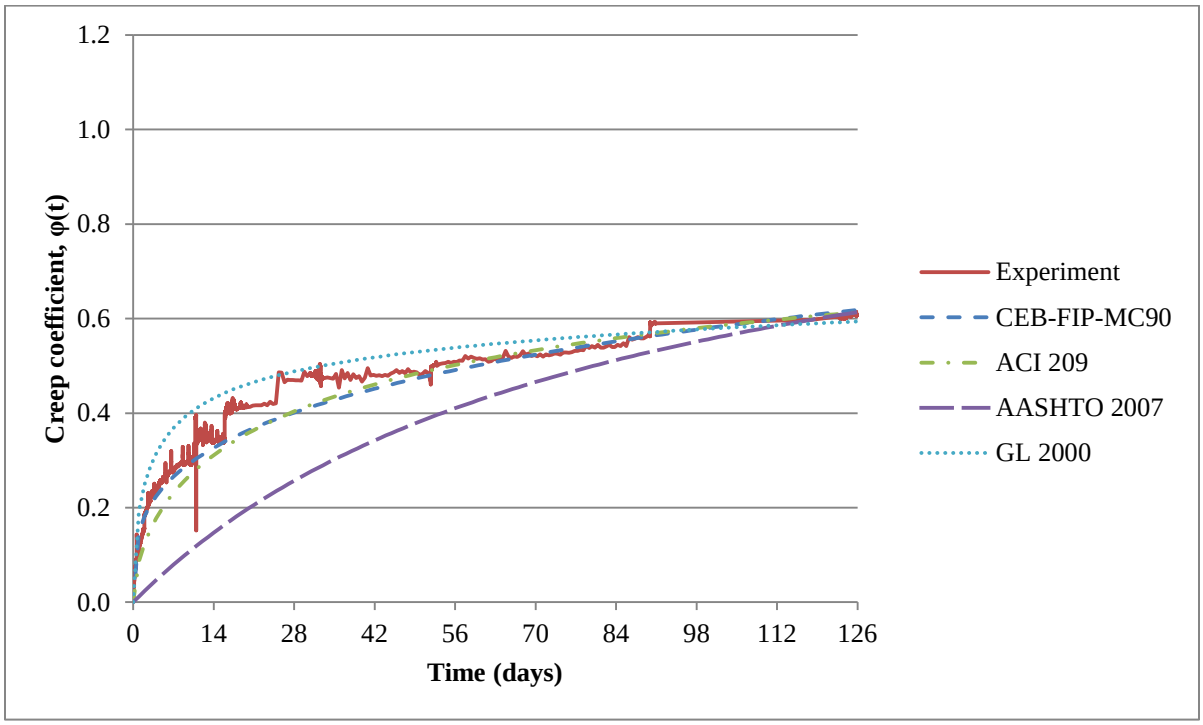

Figure 5.13. Creep models for sealed SCM cylinders calibrated to fit experimental results

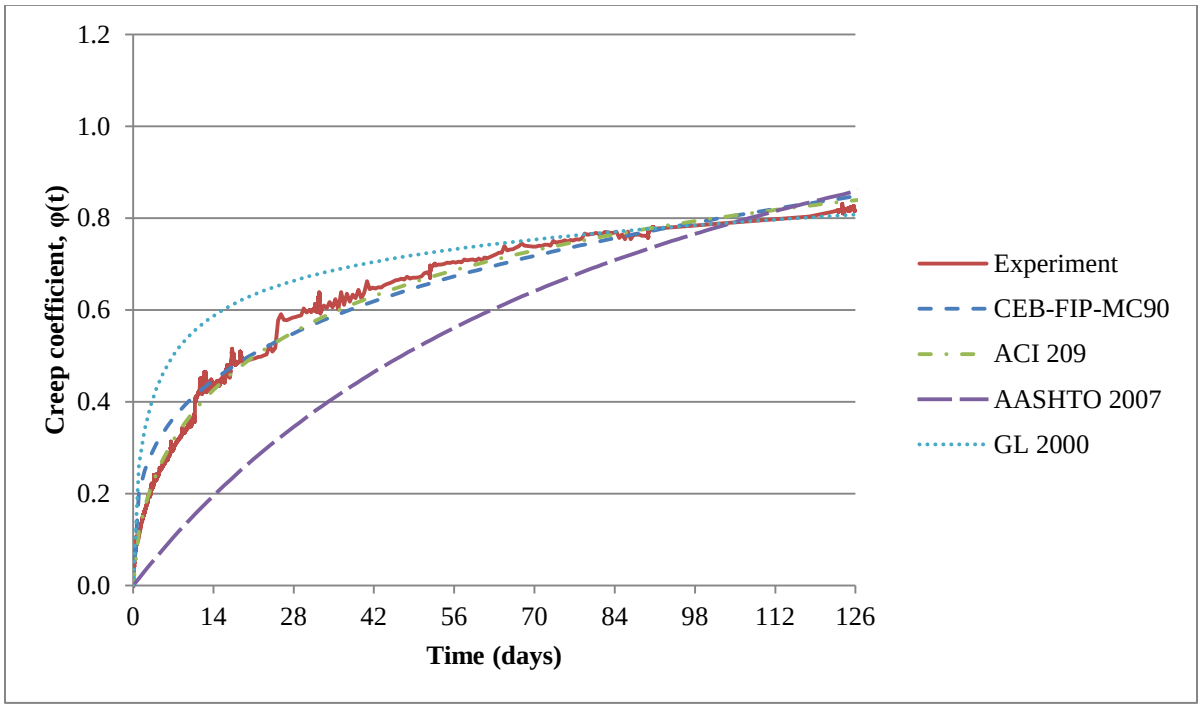

Figure 5.14. Creep models for sealed SCC cylinders calibrated to fit experimental results

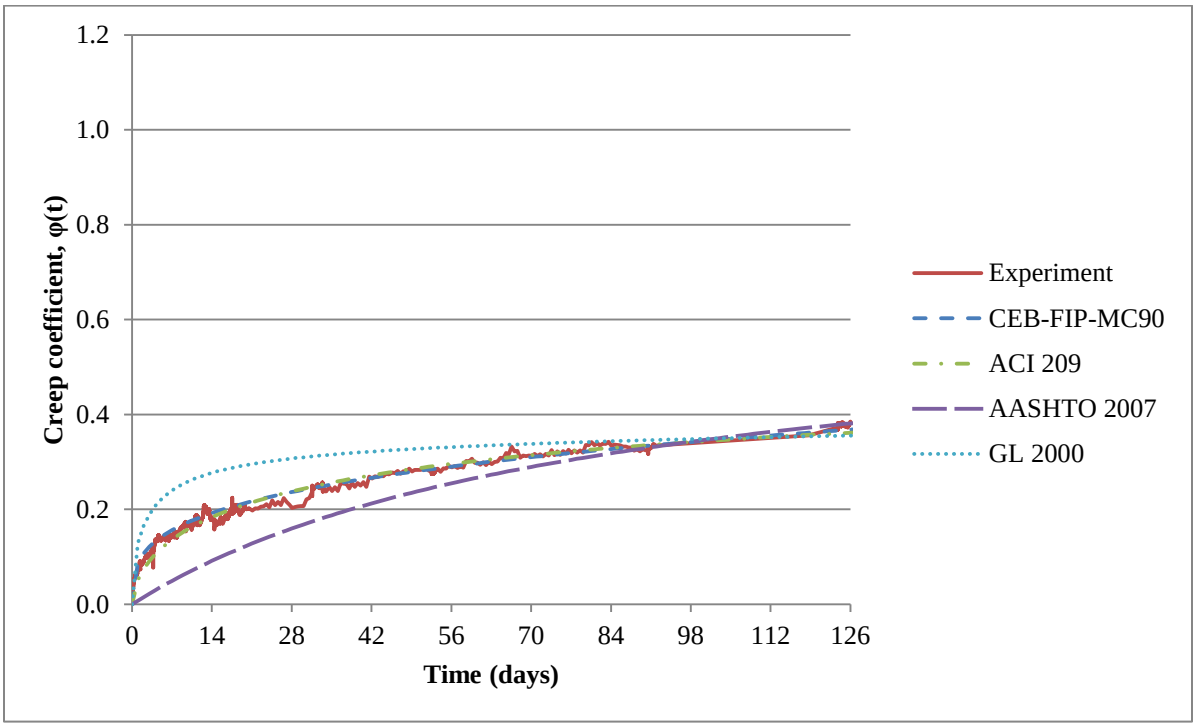

Figure 5.15. Creep models for SCM CFT core calibrated to fit experimental results

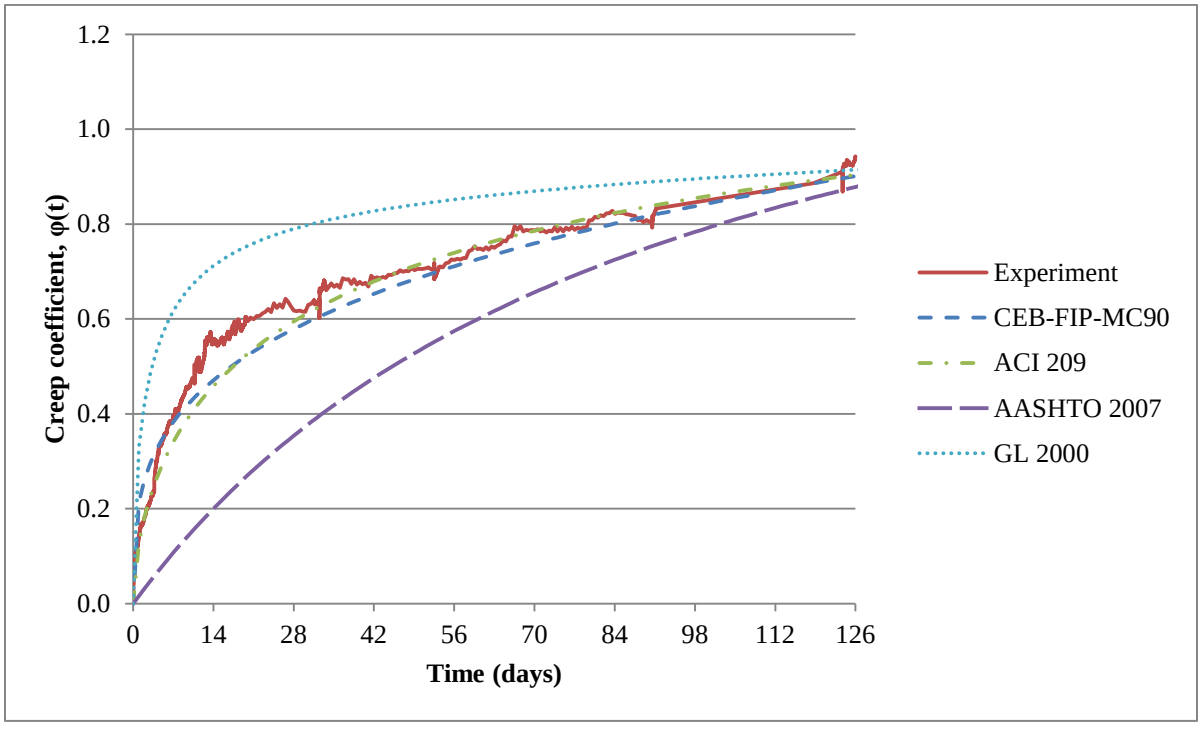

Figure 5.16. Creep models for SCC CFT core calibrated to fit experimental results

5.3.2 Shrinkage model calibrations

Table 5.4 presents the final shrinkage strains ($\varepsilon_{sh,p}$) for the cylinder specimens, predicted by the models. The value of the final shrinkage strain after calibration ($\varepsilon_{sh,c}$) is shown as a comparison.

Table 5.4. Model predictions of ultimate shrinkage strain before and after calibration

Concrete	Specimen	ACI 209		CEB-FIP-MC90		AASHTO 2007		GL 2000	
		$\varepsilon_{sh,p}$	$\varepsilon_{sh,c}$	$\varepsilon_{sh,p}$	$\varepsilon_{sh,c}$	$\varepsilon_{sh,p}$	$\varepsilon_{sh,c}$	$\varepsilon_{sh,p}$	$\varepsilon_{sh,c}$
SCM	Unsealed	681	681	435	875	611	887	646	850
	Sealed	335	297	71	378	315	378	27	361
SCC	Unsealed	681	604	526	770	447	807	582	730
	Sealed	335	266	86	337	230	360	24	325

Figure 5.17 to Figure 5.20 display the experimental curves of the shrinkage strains plotted with the creep models. On each plot, all the shrinkage models considered are plotted with one experimental curve. This was done for unsealed and sealed cylinders, for both types of concrete.

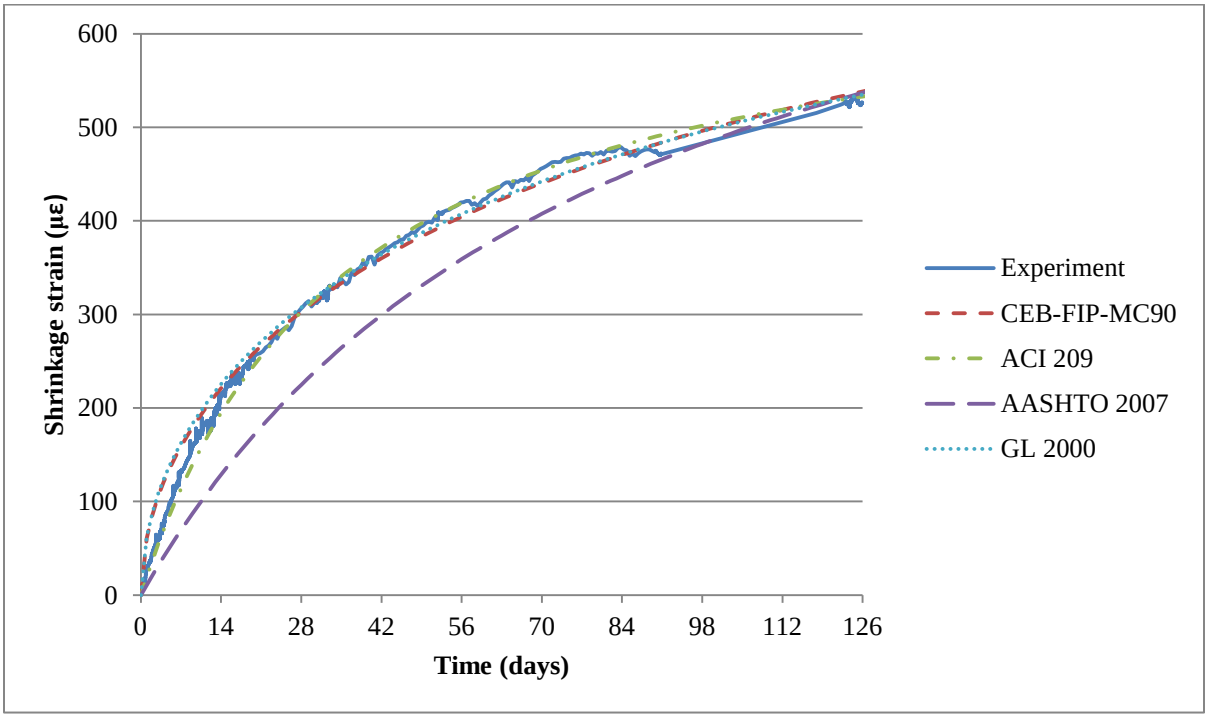

Figure 5.17. Shrinkage models for unsealed SCM cylinders calibrated to fit experimental results

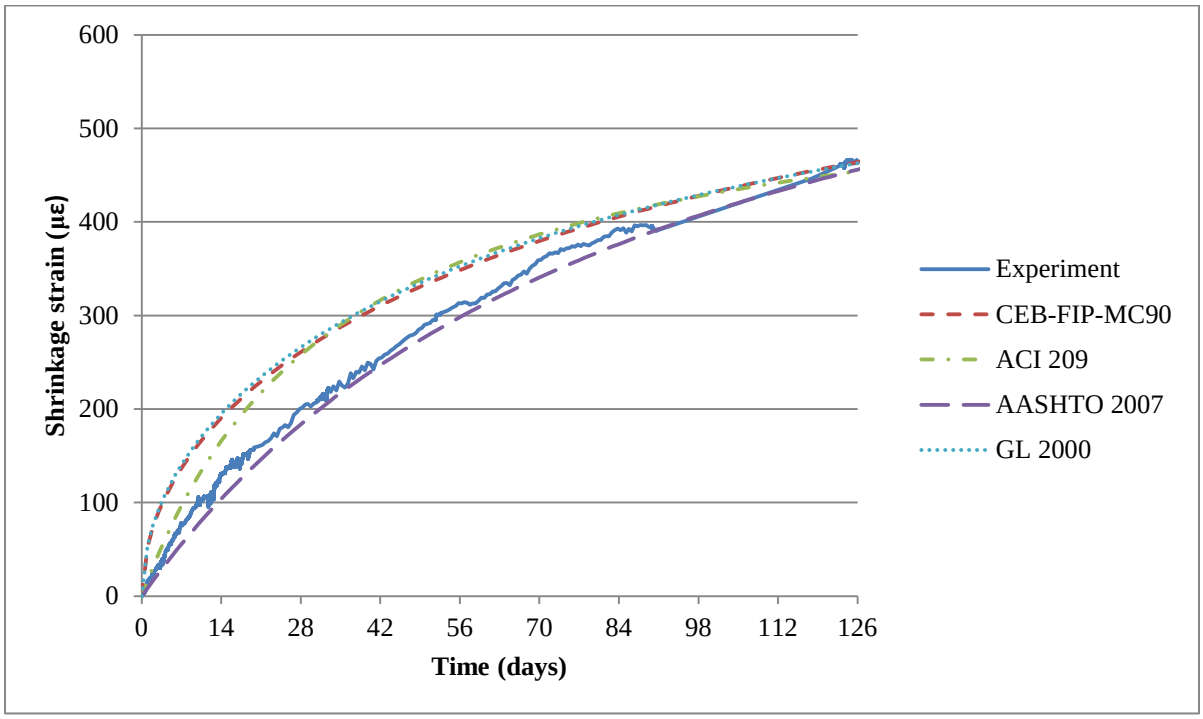

Figure 5.18. Shrinkage models for unsealed SCC cylinders calibrated to fit experimental results

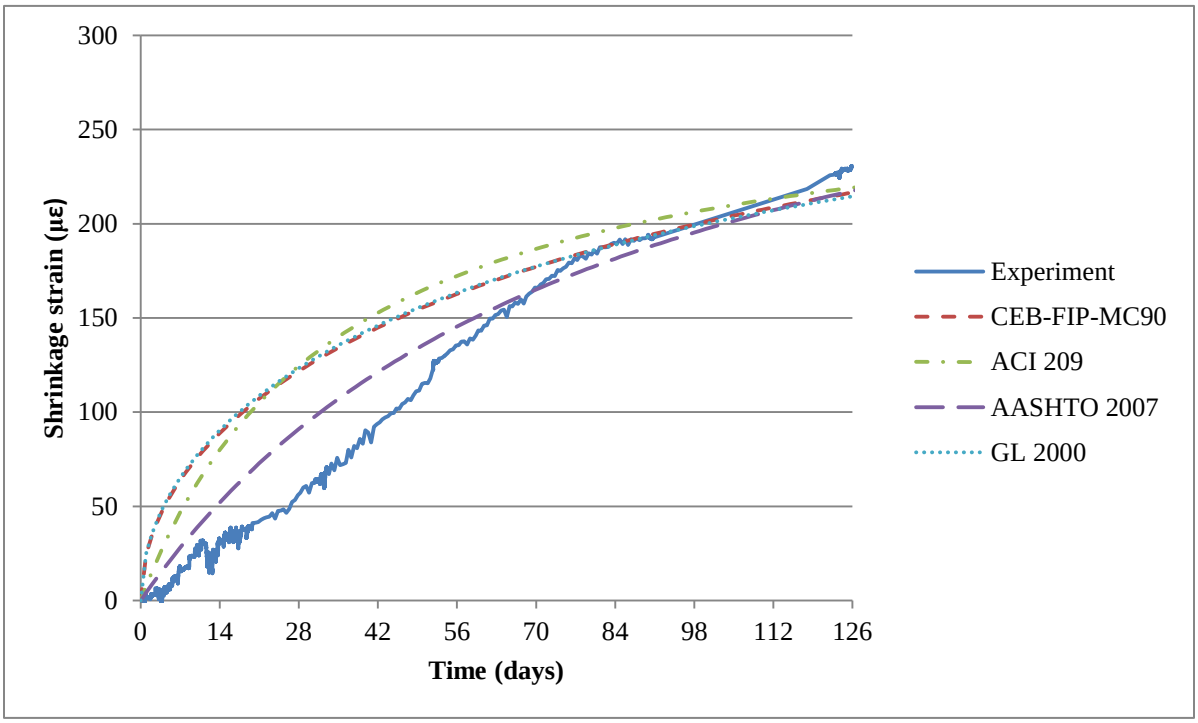

Figure 5.19. Shrinkage models for sealed SCM cylinders calibrated to fit experimental results

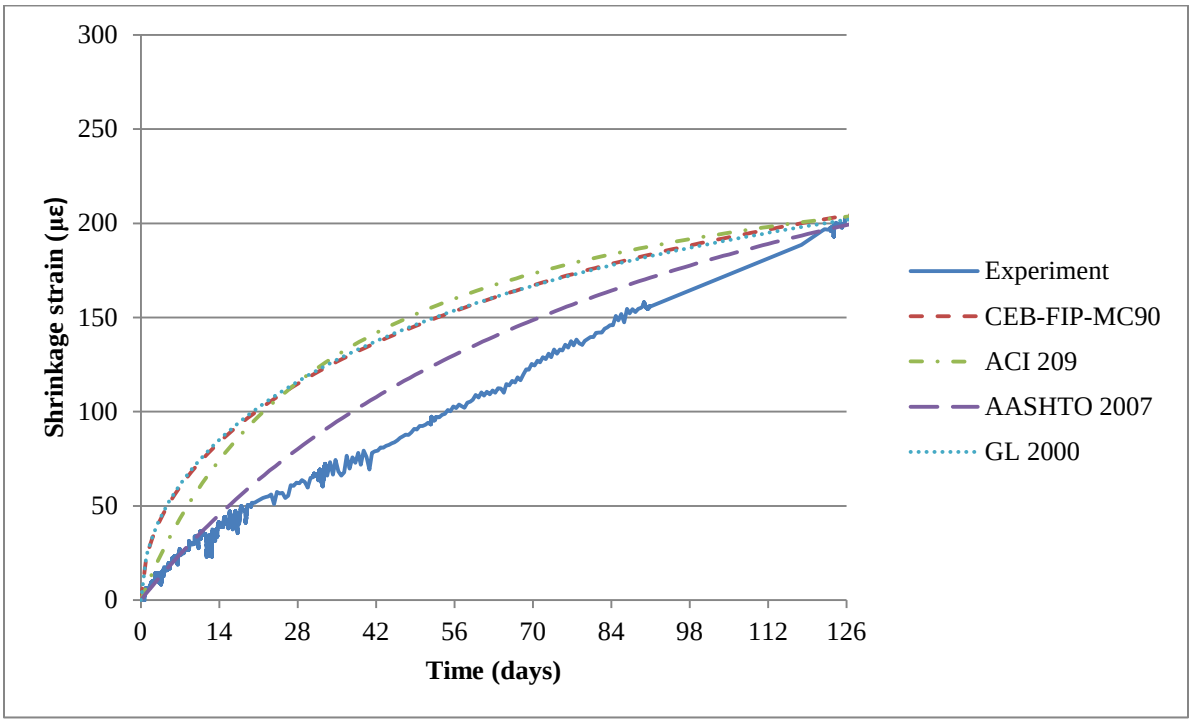

Figure 5.20. Shrinkage models for sealed SCC cylinders calibrated to fit experimental results

In general, all creep models except the AASHTO 2007 model can be calibrated to fit the experimental curves rather well, but the final calibrated creep coefficients obtained are quite different. The calibrated ACI 209 model provides the best fit overall, since the CEB-FIP-MC90 and GL 2000 models still overestimate early creep after calibration in most cases.

All shrinkage models can generally be calibrated to fit the experimental curves quite well for both unsealed concretes, but the final calibrated shrinkage strains obtained are different. For both sealed concretes, however, none of the models capture the shrinkage behavior well, since the experimental curves are not shaped like shrinkage curves for unsealed concrete.

Chapter 6: Results from seismic performance tests

After 126 days of sustained loading, the CFT specimens were tested for seismic performance. A combined load consisting of a constant axial force and an increasing cyclic lateral force was applied and the specimens loaded until failure. The results were then compared to see if the SCM specimen had seismic performance comparable to specimens with conventional SCC concrete. The specimens were compared to two specimens previously tested; a 20-inch diameter specimen tested by Lee (Lee, 2011) which was identical to the SCC specimen tested in this research, and a 30-inch diameter specimen tested by O'Neill (O'Neill, 2011). All data in this chapter was processed by O'Neill.

6.1 Experimental results

6.1.1 Specimen 8-50-SCM

This specimen had a grouted-recessed connection and the embedment length was 14 in. The specimen was subjected to 24 complete cycles in the load protocol. The global specimen performance of this specimen consisted of approximately linear-elastic behavior prior to measurement of compression tube yielding. Following the measurement of the compression yield strain in cycle 7, the tension yield strain was measured in cycle 10. Steel tube local buckling was visually observed in cycle 16 on both the north and south sides of the column. Finally, tearing of the steel tube occurred in cycle 22 and resulted in a significant reduction in the CFT resistance to lateral load. Tearing of the steel tube occurred on the respective tension sides of the column near the apex of the buckle. A summary of the 20 in. diameter preloaded SCM test from recorded measured data can be seen in Table 6.1. (O'Neill, 2011)

Table 6.1. 20-inch diameter preloaded SCM test summary (O'Neill, 2011)

Cycle Number	Target Drift Ratio (%)		Achieved Drift Ratio (%)		Achieved Drift (inches)		Moment at Peak Displacement (k-in)		Performance
	Max	Min	Max	Min	Max	Min	Max	Min	
1-2	0.21	-0.21	0.01	-0.31	0.01	-0.22	2681	-2641	Approximately Linear-Elastic
3-4	0.42	-0.42	0.17	-0.50	0.12	-0.36	4210	-4103	
5-6	0.62	-0.62	0.35	-0.70	0.25	-0.50	5387	-5311	
7-9	0.83	-0.83	0.55	-0.89	0.39	-0.64	6336	-6406	Compression Tube Yield Strain Measured
10-12	1.25	-1.25	0.89	-1.30	0.64	-0.94	7746	-7806	Tension Yield Strain Measured
13-15	1.66	-1.66	1.26	-1.74	0.91	-1.25	8544	-8692	
16-17	3.32	-3.32	2.74	-3.32	1.97	-2.39	9929	-9691	Local Buckling Observed
18-19	4.98	-4.98	4.41	-4.87	3.18	-3.51	9932	-9733	
20-21	6.64	-6.64	6.12	-6.51	4.41	-4.69	9800	-9395	
22	8.30	-8.30	7.77	-8.21	5.59	-5.91	8841	-6415	Tube Tearing
23	8.30	-8.30	8.04	-8.30	5.79	-5.98	5730	-5306	
24	9.96	-9.96	9.78	-9.83	7.04	-7.08	5136	-4810	

Cracking at the grout to concrete footing interface initiated in cycle 2 with a min drift ratio value of -0.31%. Radial cracking in the footing initiated in cycle 7 at a min drift ratio value of -0.88%. New footing cracks and crack propagation continued to occur in following cycles. In cycle 10, the maximum crack width in the concrete footing was 0.4 mm and the maximum crack width at the grout to concrete footing interface was 0.3 mm, while the CFT was displaced. At zero displacement at the end of cycle 10, the maximum crack width in the footing was hairline and the maximum crack width at the grout to concrete footing interface was 0.2 mm. An image of footing cracking, with the cracks highlighted in black, can be seen in Figure 6.1. (O'Neill, 2011)

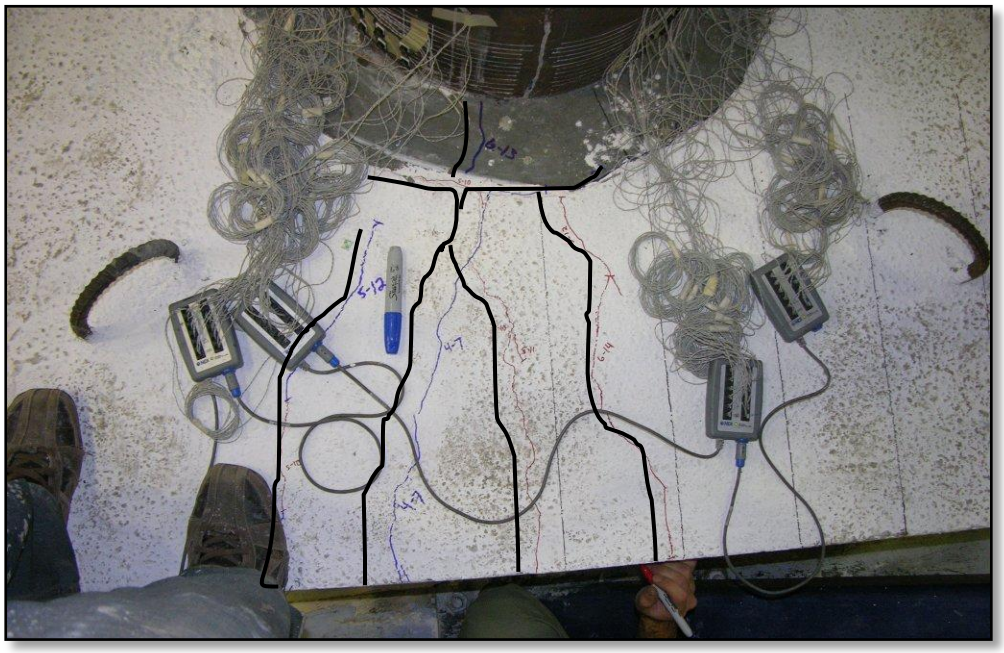

Figure 6.1. Footing cracking on west side of footing, cycle 14, drift ratio of 1.25% to south (O'Neill, 2011)

The compression yield strain was measured in tube strain gauges located 3.5 in. above the footing surface in cycle 7 on both the north and the south side of the steel tube when the respective side was in compression. The compression yield strain was measured on the south side of the steel tube at a drift ratio value of 0.4%. The compression yield strain was measured on the north side of the steel tube at a drift ratio value of -0.8%. (O'Neill, 2011)

Tension yield strain was measured in the tube strain gauges 3.5 in., 8 in. and 12 in. above the footing surface on the north side of the steel tube first in cycle 10 at a drift ratio value of 0.8%. Following this, the tension yield strain was measured in the tube strain gauges 4 in. below the footing surface and 3.5 in. above the footing surface on the south side of the steel tube in cycle 10 at a drift ratio value of -1.0%. (O'Neill, 2011)

Local buckling occurred on the south side of the steel tube in cycle 16 at a peak drift ratio value of 2.7% and can be seen in Figure 6.2. The apex of the buckle on the south side of the steel tube was approximately 2.5 in. above the surface of the footing. In the subsequent half cycle, local buckling occurred on the north side of the steel tube in cycle 16 at a minimum drift ratio value

of -3.3%. The apex of the buckle on the north side of the steel tube was approximately 2.5 in. above the footing surface. (O'Neill, 2011)

Figure 6.2. Onset of local buckling on south side of tube, cycle 16, drift ratio of 2.7% to south (O'Neill, 2011)

The magnitude of the out of surface deformation increased in each cycle, even in cycles with the same specimen displacement magnitude as the previous cycle. An image of local buckling in cycle 21 can be seen in Figure 6.3. (O'Neill, 2011)

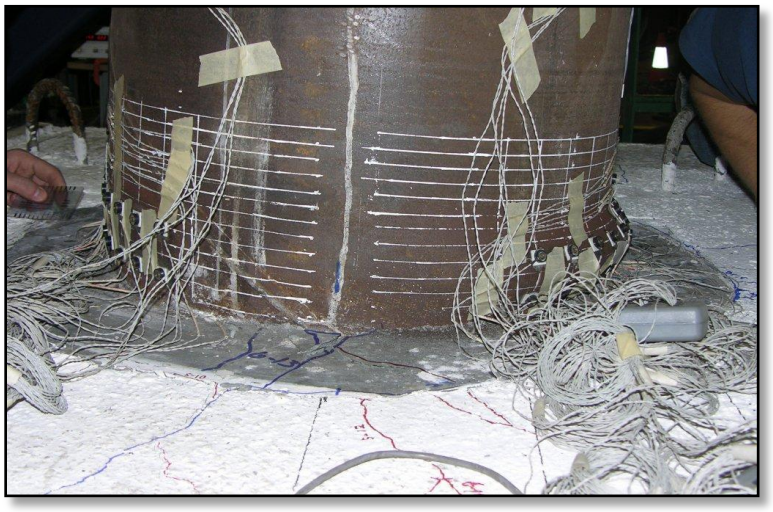

Figure 6.3. Local buckling on southside of tube, cycle 21, drift ratio of 6.1% to south (O'Neill, 2011)

The maximum residual crack width when the CFT was at zero displacement at the end of cycle 16 in the top surface of the concrete footing was 0.35 mm and the maximum residual crack width at the grout to concrete footing interface was 0.4 mm. (O'Neill, 2011)

Progressive footing crack propagation and new cracking ceased following the completion of cycle 18 with a max drift ratio value achieved of 4.36%. (O'Neill, 2011)

Steel tube tearing initiated on the north side of the steel tube as the CFT was displaced to the south in the first quarter cycle of cycle 22 at a drift ratio value of 7.27% as the tube was displaced to a max drift ratio value of 7.77%. An image of this tearing can be seen in Figure 6.4. Steel tube tearing occurred on the tension side of the steel tube. The tear occurred approximately 2.25 in. above the surface of the footing. The tear extended 1.5 in. to the west and 4.5 in. to the east circumferentially around the tube for a total tear length of 6 in. or 10% of the steel tube circumference. (O'Neill, 2011)

Figure 6.4. Steel tube tearing on north side of tube, cycle 22, drift ratio of 7.77% to south (O'Neill, 2011)

In the subsequent half cycle of cycle 22, steel tube tearing occurred on the south side of the steel tube, as the CFT was displaced to the north, at a drift ratio value of -4.47% as the tube was displaced to a min drift ratio value of -8.21%. Steel tube tearing occurred on the tension side of the steel tube. The tear occurred approximately 2.25 in. above the surface of the footing. The tear extended 7.5 in. to the west and 8 in. to the east circumferentially around the tube for a total tear length of 15.5 in. or 25% of the steel tube circumference. (O'Neill, 2011)

When the CFT returned to zero displacement following the completion of cycle 22, the length of the tear on the north side of the steel tube was 8 in. and the length of the tear on the south side of the steel tube was 17.5 in. The combination of these tear lengths equals 25.5 in., or 41% of the circumference of the steel tube. (O'Neill, 2011)

In cycle 23, the tear on the north side of the steel tube extended 8.75 in. to the west and 9 in. to the east circumferentially for a length of 17.75 in. or 28% of the tube circumference. Tearing on the south side of the steel tube extended 9 in. to the west and 10.5 in. to the east for a length of 19.5 in. or 31% of the tube circumference as shown in Figure 6.5. So, the combination of the tear length on the north side and the south side of the steel tube was 37.25 in. or 59% of the tube circumference. (O'Neill, 2011)

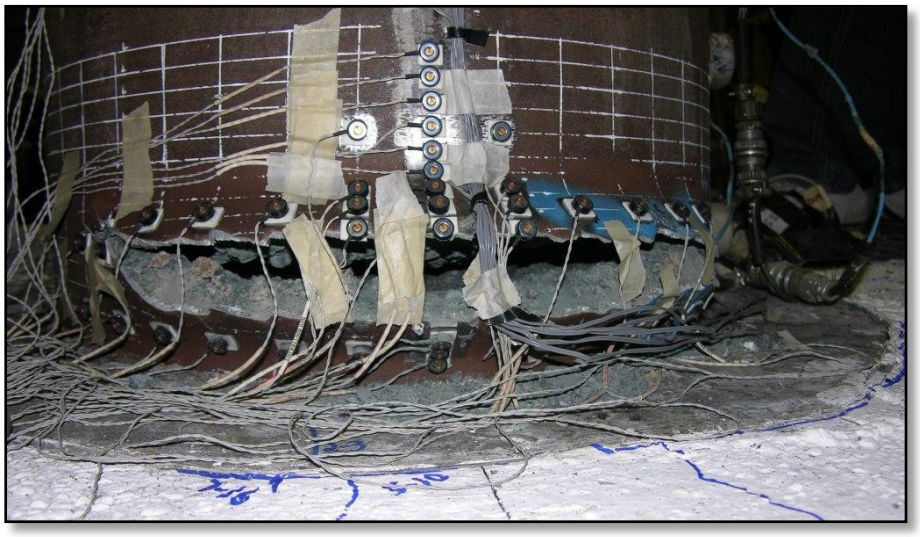

Figure 6.5. South side tear length increase, cycle 23, drift ratio of -8.20% to north (O'Neill, 2011)

6.1.2 Specimen 7-50

This specimen had a grouted-recessed connection and the embedment length was 14 in. The specimen was subjected to 24 complete cycles in the load protocol. The global specimen performance of this specimen consisted of approximately linear-elastic behavior prior to measurement of compression tube yielding. Following the measurement of the compression yield strain in cycle 5, the tension yield strain was measured in cycle 10. Steel tube local buckling was visually observed in cycle 16 on both the north and south sides of the column. Finally, tearing of the steel tube occurred in cycle 22 on the south side of the column while that side was in compression. That is, initial tearing did not occur on the tension side of the column. In the subsequent half cycle of cycle 22 the size of the tear on the south side grew larger but tearing did not occur on the north side of the column. Tearing on the north side of the column occurred in cycle 24. Tearing resulted in significant reduction in the CFT resistance to lateral load. A summary of the 20 in. diameter preloaded SCC test from recorded measured data can be seen in Table 6.2. (O'Neill, 2011)

Table 6.2. 20-inch diameter preloaded SCC test summary (O'Neill, 2011)

Cycle Number	Target Drift Ratio (%)		Achieved Drift Ratio (%)		Achieved Drift (inches)		Moment at Peak Displacement (k-in)		Performance
	Max	Min	Max	Min	Max	Min	Max	Min	
1-2	0.21	-0.21	0.12	-0.20	0.09	-0.14	2819	-2735	Approximately Linear-Elastic
3-4	0.42	-0.42	0.30	-0.40	0.22	-0.29	4213	-4088	
5-6	0.62	-0.62	0.48	-0.58	0.35	-0.42	5287	-5212	Compression Tube Yield Strain Measured
7-9	0.83	-0.83	0.66	-0.78	0.48	-0.56	6244	-6154	
10-12	1.25	-1.25	1.04	-1.18	0.75	-0.85	7827	-7753	Tension Yield Strain Measured
13-15	1.66	-1.66	1.41	-1.59	1.02	-1.14	8768	-8670	
16-17	3.32	-3.32	3.06	-3.18	2.20	-2.29	10161	-9731	Local Buckling Observed
18-19	4.98	-4.98	4.70	-4.73	3.38	-3.41	10329	-9726	
20-21	6.64	-6.64	6.39	-6.32	4.60	-4.55	10003	-9726	
22	8.30	-8.30	7.95	-8.05	5.72	-5.80	9952	-6018	Tube Tearing
23	8.30	-8.30	8.25	-8.11	5.94	-5.84	5872	-5225	Tube Tearing
24	9.96	-9.96	10.00	-9.70	7.20	-6.98	5123	-4819	

Radial cracking in the concrete footing started in cycle 3 at a minimum drift ratio value of -0.39%. Cracking at the grout to concrete footing interface initiated in cycle 6 with a max drift ratio value of 0.48%. New footing cracks and crack propagation continued to occur in following cycles. (O'Neill, 2011)

In cycle 12, while the CFT was displaced to the south, the maximum crack width at the grout to concrete footing interface was 0.5 mm. In cycle 12, while the CFT was displaced to the north, the maximum crack width at the grout to concrete footing interface was 1.0 mm. At zero displacement at the end of cycle 12, the radial cracks in the top surface of the footing were closed to hairline and the maximum crack width at the grout to concrete footing interface was 0.2 mm. An image of footing cracking while the CFT was displaced to the north in cycle 10 can be seen in Figure 6.6. (O'Neill, 2011)

Figure 6.6. Footing cracking on west side of footing, cycle 10, drift ratio of -1.17% to north (O'Neill, 2011)

The compression yield strain was measured in a tube strain gauge located 8 in. above the footing surface in cycle 5 on the south side of the specimen when the side was in compression at a drift ratio value of 0.45%. In cycle 7, the compression yield strain was measured in a tube strain gauge located 3.5 in. above the footing surface on the south side of the specimen when the side was in compression at a drift ratio value of 0.63%. In the following half cycle of cycle 7, the compression yield strain was measured in a tube strain gauge located 3.5 in. above the footing surface on the north side of the specimen when the side was in compression at a drift ratio value of -0.74%. (O'Neill, 2011)

The tension yield strain was measured in the tube strain gauges 3.5 in. and 8 in. above the footing surface on the north side of the steel tube first in cycle 10 at a drift ratio value of 0.81%. Following this, the tension yield strain was measured in the tube strain gauges 4 in. below the

footing surface and 3.5 in., 8 in., 12 in. and 18 in. above the footing surface on the south side of the steel tube in cycle 10 at a drift ratio value of -0.86%. (O'Neill, 2011)

Local buckling occurred on the south side of the steel tube in cycle 16 at a peak drift ratio value of 2.9% as shown in Figure 6.7. The apex of the buckle on the south side of the steel tube was approximately 1.5 in. above the surface of the footing. In the subsequent half cycle, local buckling occurred on the north side of the steel tube in cycle 16 at a minimum drift ratio value of -3.2%. The apex of the buckle on the north side of the steel tube was approximately 2.0 in. above the footing surface. (O'Neill, 2011)

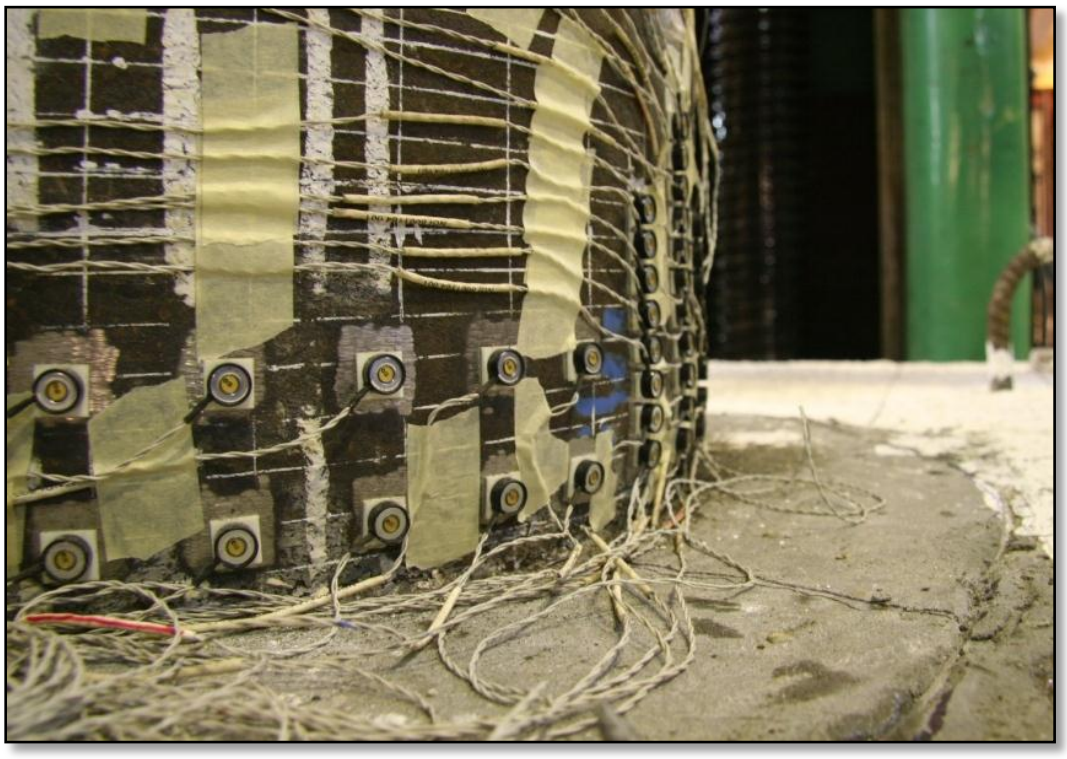

Figure 6.7. Onset of local buckling to South side of tube, cycle 16, drift ratio of 2.9% to south (O'Neill, 2011)

The magnitude of the out of surface deformation increased in each cycle, even in cycles with the same specimen displacement magnitude as the previous cycle. An image of local buckling in cycle 21 as the CFT was displaced to the north can be seen Figure 6.8. (O'Neill, 2011)

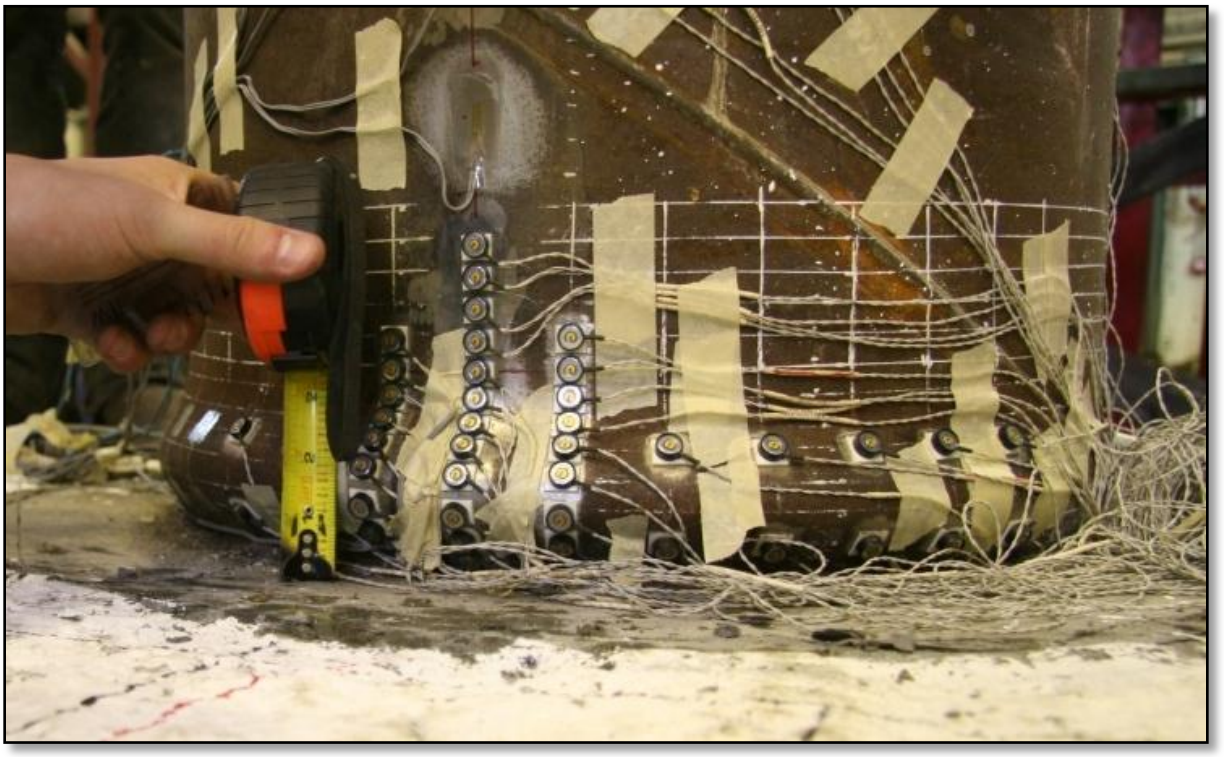

Figure 6.8. Local buckling on North side of tube, cycle 21, drift ratio of -6.32% to north (O'Neill, 2011)

The maximum residual crack width when the CFT was at zero displacement at the end of cycle 16 in the top surface of the concrete footing was 0.15 mm and the maximum residual crack width at the grout to concrete footing interface was 0.6 mm. (O'Neill, 2011)

Progressive footing crack propagation and new cracking ceased following the completion of cycle 20 with a max drift ratio value achieved of 6.33%. (O'Neill, 2011)

Steel tube tearing initiated on the south side of the steel tube as the CFT was displaced to the south in the first quarter cycle of cycle 22 at a drift ratio value of 7.95% as the tube was displaced to a max drift ratio value of 7.95% as seen in Figure 6.9. It is important and interesting to note that steel tube tearing occurred on the compression side of the steel tube near the apex of the buckle while the buckle was in compression. The tear occurred approximately 1.5 in. above the surface of the footing. The tear extended 2.5 in. to the west and 0.5 in. to the east

circumferentially around the tube for a total tear length of 3 in. or 5% of the steel tube circumference. (O'Neill, 2011)

Figure 6.9. Steel tube tearing on South side of tube, cycle 22, drift ratio of 7.95% to south (O'Neill, 2011)

In the subsequent half cycle of cycle 22, the tear length of the steel tube tear on the south side of the CFT grew longer to extend 10 in. to the west and 8.5 in. to the east for a total length of 18.5 in. or 29% of the steel tube circumference. However, tearing did not initiate on the north side of the steel tube. (O'Neill, 2011)

In the first quarter cycle of cycle 23, steel tube tearing occurred on the north side of the steel tube at a drift ratio value of 5.16% as the tube was displaced to a max drift ratio value of 8.25%. The tear occurred approximately 1.75 in. above the surface of the footing. The north side tear extended 9.5 in. to the west and 7 in. to the east circumferentially around the tube for a total tear length of 16.5 in. or 26% of the steel tube circumference. (O'Neill, 2011)

When the specimen was cycled the opposite direction in cycle 23, the length of the tear on the south side of the tube grew longer as shown in Figure 6.10. The south side tear extended 11.5 in. to the west and 10 in. to the east circumferentially around the tube for a total tear length of 21.5 in. or 34% of the steel tube circumference. At the end of cycle 23, the total sum of the tear lengths on the north and the south side of the steel tube equaled 38 in. or 60% of the steel tube circumference. (O'Neill, 2011)

Figure 6.10. South side tear length increase, cycle 23, drift ratio of -8.11% to North (O'Neill, 2011)

6.1.3 Specimen 5-50 (tested by Lee)

Specimen 5-50 had a grouted-recessed connection type with an embedment length of 14 inches (Le/D = 0.7). The steel tube had a diameter of 20 inches and a thickness of 0.25 inches (D/t = 80). The design was identical to Specimen IV (Specimen Number 4) tested by Kingsley except for the use of a steel tube with differing material properties and differing embedment length. (O'Neill, 2011)

As reported by Lee, cracking was observed in the concrete footing at a drift ratio of 0.8%. The yield strain of the steel tube was measured at a drift ratio of 0.8% above the surface of the footing. Local buckling of the steel tube was observed at a drift ratio of 3.2%. Progressive footing damage ceased at a drift ratio of 3.2%. Steel tube tearing occurred at a drift ratio of 7.4%. (Lee, 2011) A summary of results of the test, as reported by Lee, can be seen in Table 6.3.

Table 6.3. Results of 5-50 experimental test as reported by Lee (Lee, 2011)

5-50 Results									
Drift Range	Cycle		Drift (in)		Drift Ratio (%)		Peak Base Moment (k-in)		Performance
	From	To	Min (South)	Max (North)	Min (South)	Max (North)	Min (South)	Max (North)	
1	1	2	-0.050	0.022	-0.07	0.03	-1405	1002	
	3	4	-0.158	0.122	-0.22	0.17	-3112	2718	
	5	6	-0.310	0.252	-0.43	0.35	-4340	4009	
	7	8	-0.490	0.418	-0.68	0.58	-5723	5134	
	9	11	-0.691	0.598	-0.96	0.83	-6967	6539	Yielding is Measured
	13	15	-1.12	0.950	-1.55	1.32	-9020	8409	
	16	18	-1.58	1.41	-2.19	1.96	-9696	9301	Local Buckling is Observed
2	20	21	-2.52	2.33	-3.50	3.24	-11048	9970	
	22	23	-3.46	3.36	-4.81	4.66	-10140	9943	
3	25	26	-5.42	5.41	-7.53	7.51	-9309	9964	Tearing of tube at apex of buckled region
	27	28	-7.42	7.68	-10.30	10.66	-4971	5844	

6.2 Force-Displacement response

6.2.1 Specimen 8-50-SCM

The force-displacement response for the 20 in. diameter preloaded SCM specimen can be seen in Figure 6.11. The maximum and minimum lateral loads occur in the same cycle that local buckling of the steel tube is observed. Similar to the 20 in. diameter specimen tested by Lee (5-50), this specimen experiences a greater decrease in lateral load resistance capacity, after the specimen experiences maximum lateral load, than the 30 in. diameter specimen. Once steel tube tearing occurs, there is a significant decrease in the specimen resistance to lateral load. (O'Neill, 2011)

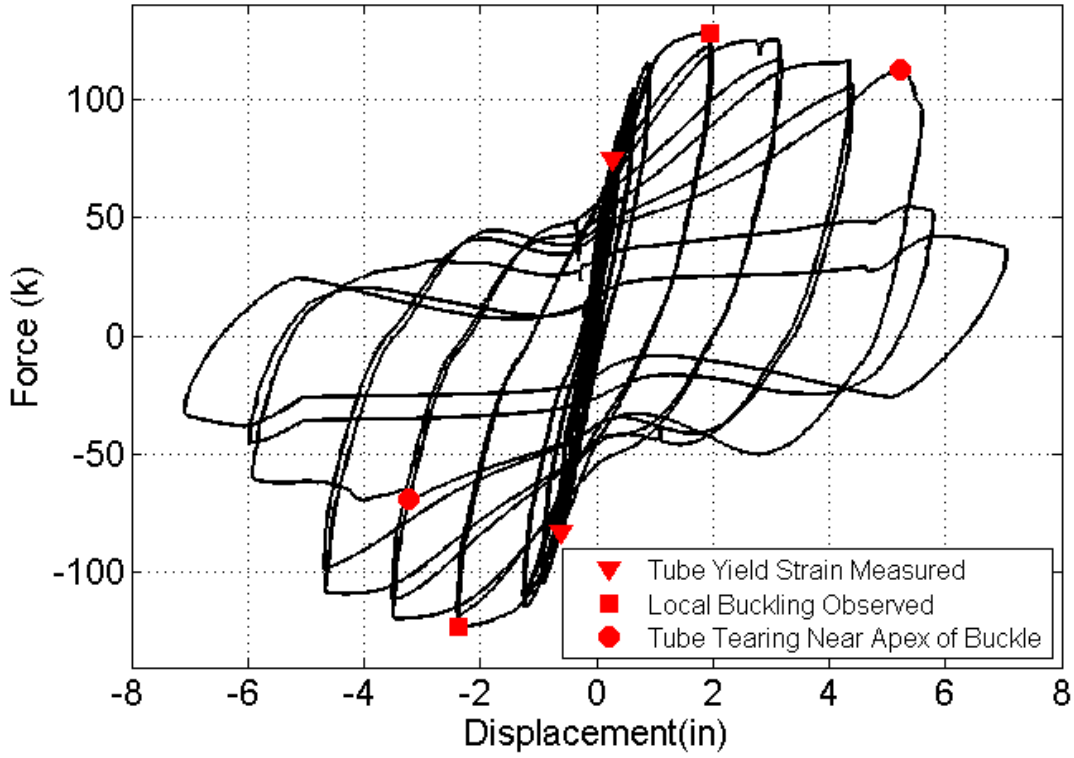

Figure 6.11. Force-Displacement response of preloaded SCM specimen (O'Neill, 2011)

6.2.2 Specimen 7-50

The force-displacement response for the 20 in. diameter preloaded SCC specimen can be seen in Figure 6.12. The maximum and minimum lateral loads occur in the same cycle that local buckling of the steel tube is observed. Similar to the 20 in. diameter specimen tested by Lee (5-50) and the 20 in. diameter preloaded SCM specimen, this specimen experiences a greater decrease in lateral load resistance capacity after the specimen experienced maximum lateral load than the 30 in. diameter specimen. Once steel tube tearing occurs, there is a significant decrease in the specimen resistance to lateral load. (O'Neill, 2011)

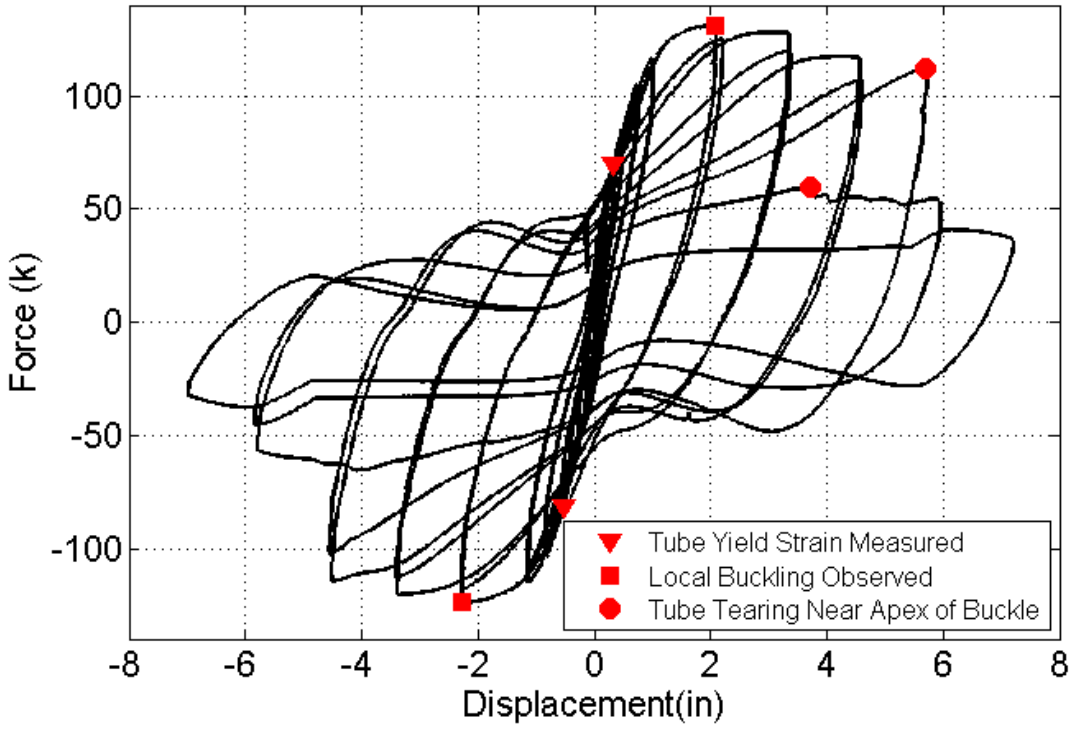

Figure 6.12. Force-Displacement response of preloaded SCC specimen (O'Neill, 2011)

6.2.3 Specimen 5-50 (tested by Lee)

The force-drift ratio response for the 20 in. diameter SCC specimen experimentally tested by Lee (Lee, 2011) can be seen in Figure 6.13. As reported by Lee, the minimum force occurred at a drift ratio of -3.40% and had a value of -135 kips. The maximum and minimum lateral loads occur in the same cycle that local buckling of the steel tube is observed. In comparison to the 30 in. diameter specimen, the 5-50 specimen experienced a much greater decrease in lateral load resistance capacity after the specimen experienced maximum lateral load than the 30 in. diameter specimen. Once steel tube tearing occurs there is a significant decrease in the specimen resistance to lateral load. (O'Neill, 2011)

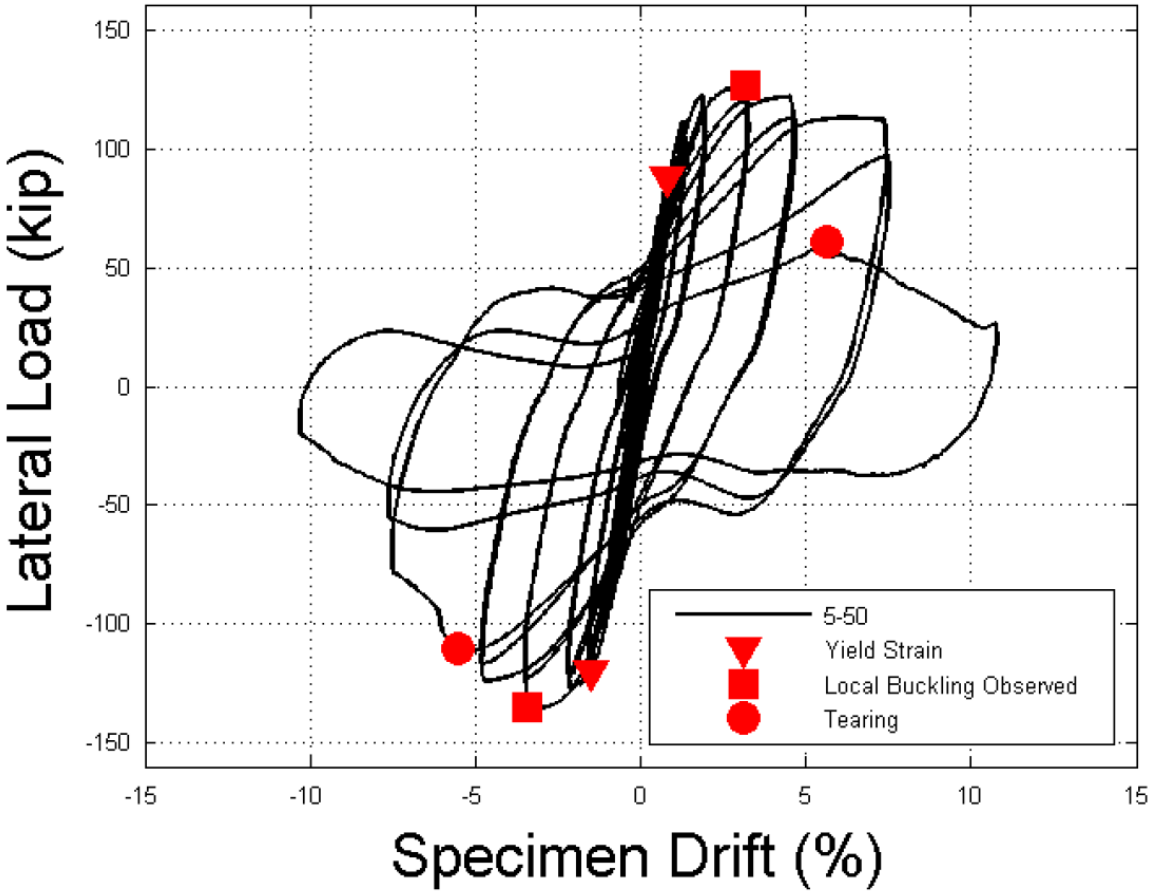

Figure 6.13. Force-Drift ratio of specimen 5-50 (Lee, 2011)

6.2.4 Specimen 30”-50 (tested by O’Neill)

The force-displacement response in the 30-inch diameter specimen tested by O’Neill is shown in Figure 6.14. A rigid body rotation of the self-reaction frame was measured during the test. This rigid body rotation was added to the measured displacement. (O'Neill, 2011)

An important note is that the force displayed in Figure 6.14 is not an effective horizontal force (additional effective force due to P-Delta effects). At larger displacement, P-Delta effects are larger than at smaller displacements. The presence of these larger P-Delta effects at larger displacement contributes to the decrease in lateral load as the displacement increases. (O'Neill, 2011)

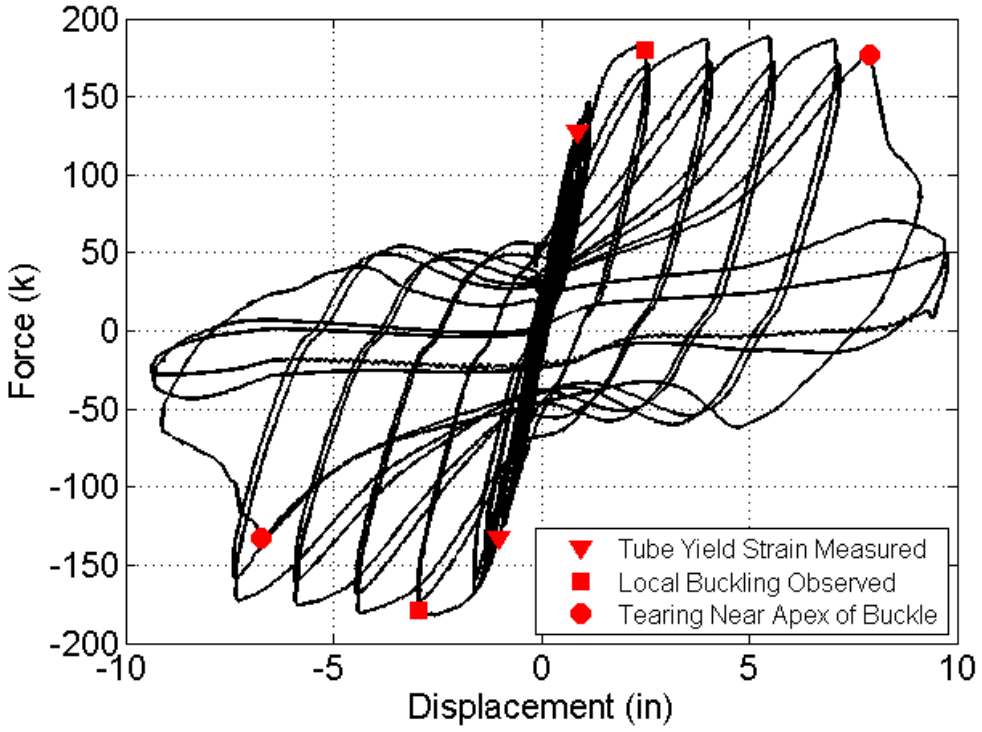

Figure 6.14. Force-Displacement response of 30-inch diameter specimen (O'Neill, 2011)

The force at which the yield strain was measured in the positive displacement direction was 127.7 kips. The force at which the yield strain was measured in the negative displacement direction was -132.7 kips. In this manner, the specimen was nearly symmetric in both the positive and negative displacement direction for the measurement of yield strain. (O'Neill, 2011)

Several cycles after steel tube yielding, local buckling of the steel tube occurred. The force measured in the positive displacement direction was 180.3 kips and the force measured in the negative displacement direction was -179.3 kips. The magnitude of the measured lateral load was nearly the same in both the positive and negative displacement directions. (O'Neill, 2011)

Steel tube tearing occurred on the north side of the tube while the tube was displaced in the positive direction with a measured lateral load of 176.8 kips first. This lateral load is only slightly less than the test measured maximum of 188 kips. Once the specimen was cycled into the negative displacement direction, tearing occurred on the south side of the steel tube. The

force measured when tearing occurred on the south side was -133.1 kips due to the tearing damage already existing on the opposite side of the tube. (O'Neill, 2011)

6.2.5 Comparison between specimens

Each specimen discussed previously in this section experiences similar force-displacement responses. However, the 20 in. diameter specimens seem to experience more deterioration in lateral load capacity than the 30 in. diameter specimen after the specimens experience maximum lateral load. Additionally, the 20 in. diameter specimens experience the maximum lateral load in the same cycle as the observation of steel tube local buckling. In the 30 in. diameter specimen, the maximum lateral load and the observation of local buckling do not necessarily coincide. The decrease in lateral load capacity at larger displacements is probably due to the larger relative axial load on the 20 in. diameter columns than the 30 in. diameter column. As mentioned previously, the 30 in. diameter column had 5% of the gross axial capacity of axial load applied to the specimen but the 20 in. diameter columns had 10% of the gross axial capacity of axial load applied. So, as the displacements become larger the lateral load capacity decreases due to increased P-Delta effects. (O'Neill, 2011)

6.3 Moment-Drift ratio response

The specimen base moment was calculated by equation (6-1). This equation adds the moment due to P-Delta effects to the moment due to multiplying the force applied by the horizontal actuator by the moment arm from the horizontal load height to the base of the column. The base moment was considered positive when the column was displaced towards the south. (O'Neill, 2011)

$$M = HL + P\Delta \quad \textbf{(6-1)}$$

where

M = column base moment
H = horizontal actuator applied load
L = distance from horizontal load height to base of column
P = applied axial load
Δ = horizontal displacement

The column drift ratio was calculated by equation (6-2). In this section this drift ratio value was displayed in percent. The column displacement was considered positive when the column was displaced towards the south.

$$\text{Drift Ratio} = \frac{\Delta}{L} \tag{6-2}$$

where

Δ = horizontal displacement

L = distance from horizontal load height to base of column

6.3.1 Specimen 8-50-SCM

The moment-drift ratio response for the 20 in. diameter preloaded SCM specimen can be seen in Figure 6.15. The approximately linear elastic portion of the plot is followed by a portion of the plot where the moment capacity of the specimen does not increase or decrease much with an increase in displacement from the previous cycle. Local buckling of the steel tube does not lead to a significant reduction in moment capacity at the instance when local buckling occurs. Once steel tube tearing occurs, there is a significant decrease in the specimen moment capacity. (O'Neill, 2011)

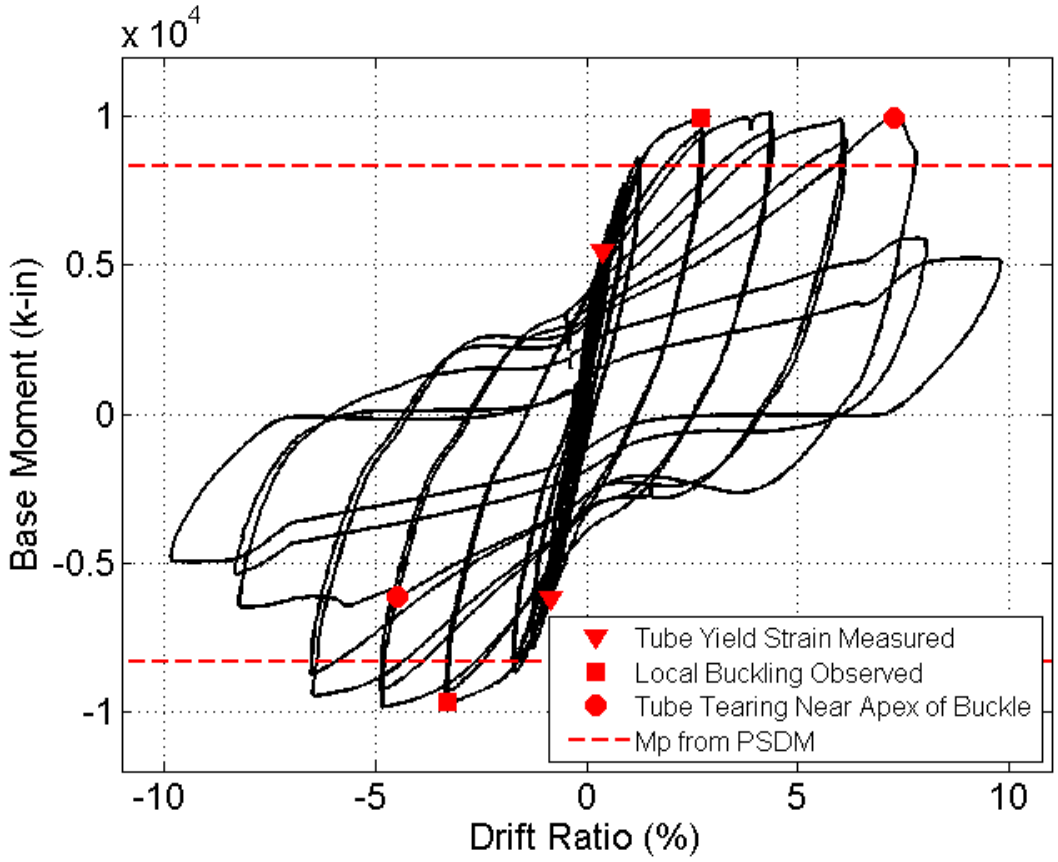

Figure 6.15. Moment-Drift ratio response of preloaded SCM specimen (O'Neill, 2011)

6.3.2 Specimen 7-50

The moment-drift ratio response for the 20 in. diameter preloaded SCC specimen can be seen in Figure 6.16. The approximately linear elastic portion of the plot is followed by a portion of the plot where the moment capacity of the specimen does not increase or decrease much with an increase in displacement from the previous cycle. Local buckling of the steel tube does not lead to a significant reduction in moment capacity at the instance when local buckling occurs. Once steel tube tearing occurs, there is a significant decrease in the specimen moment capacity. (O'Neill, 2011)

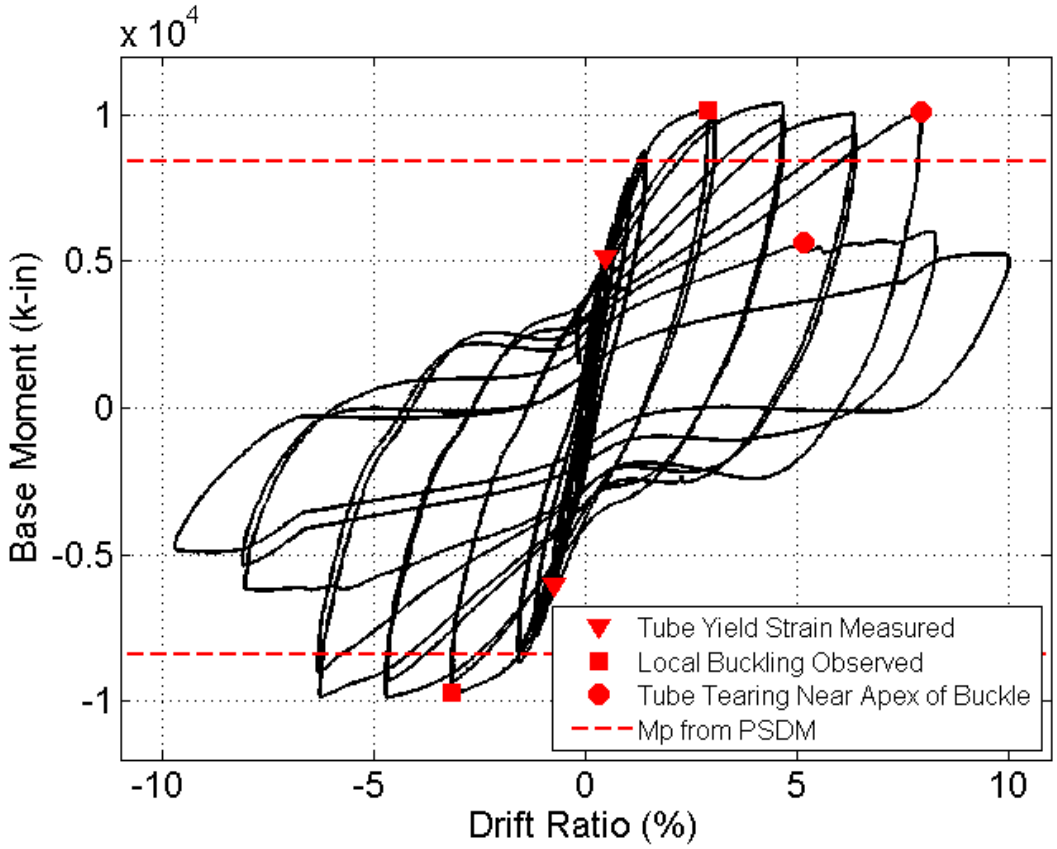

Figure 6.16. Moment-Drift ratio response of preloaded SCC specimen (O'Neill, 2011)

6.3.3 Specimen 5-50 (tested by Lee)

The moment-drift ratio response for the 20 in. diameter SCC specimen experimentally tested by Lee (Lee, 2011) can be seen in Figure 6.17. As reported by Lee, the minimum moment occurred at a drift ratio of -3.40% and had a value of -11048 k-in. Once steel tube tearing occurs there is a significant decrease in the specimen resistance to lateral load. (O'Neill, 2011)

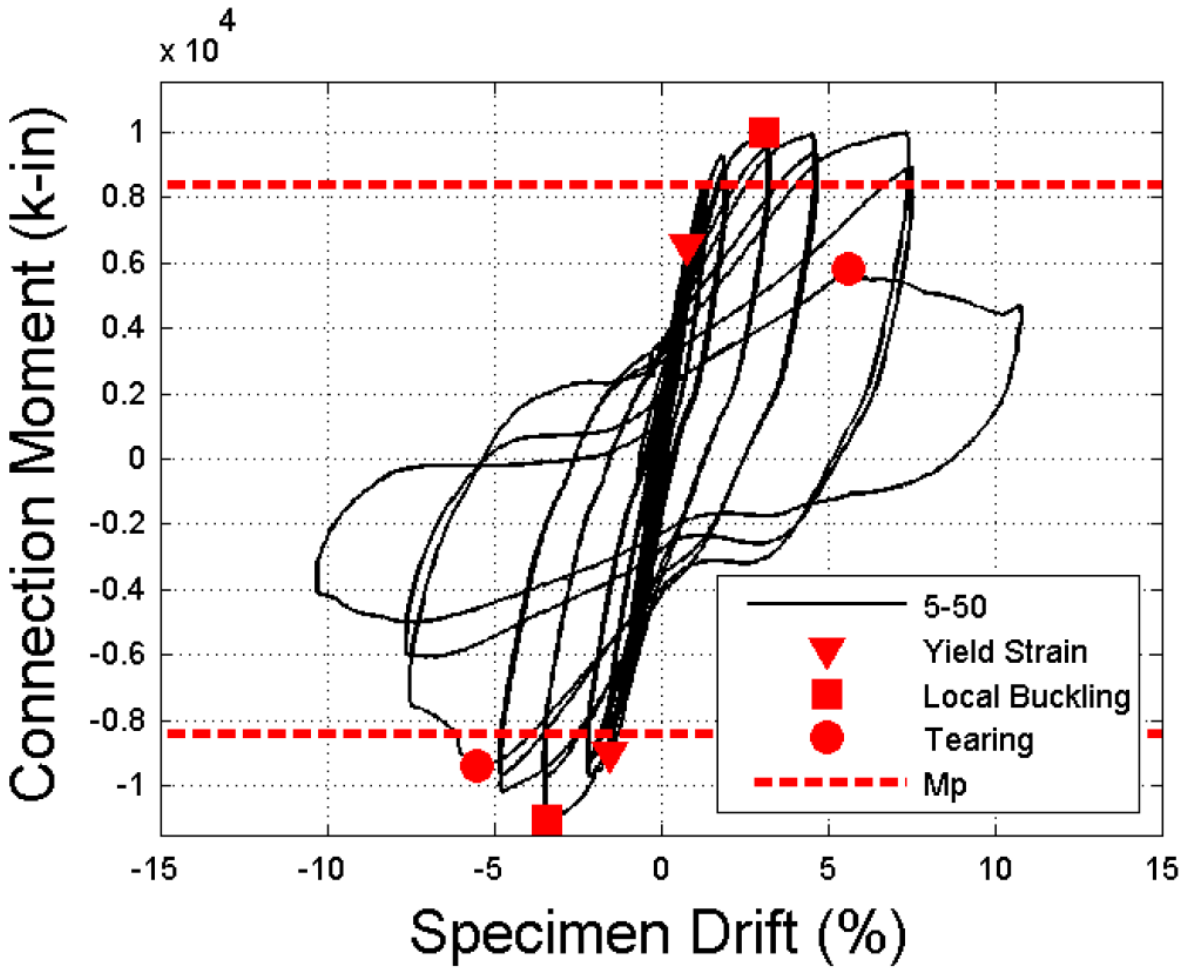

Figure 6.17. Moment-Drift ratio response of specimen 5-50 (Lee, 2011)

6.3.4 Specimen 30”-50 (tested by O’Neill)

The moment for the 30 in. diameter SCC specimen experimentally tested by Lee, when the yield strain was measured in the positive displacement direction, was 14,590 kip-in. The moment when the yield strain was measured in the negative direction was -15,205 kip-in. (O'Neill, 2011)

Several cycles after steel tube yielding, local buckling of the steel tube occurred. The moment measured in the positive displacement direction at buckling was 21,040 kip-in and the moment measured in the negative displacement direction was -21,080 kip-in. The magnitude of the measured moment was nearly the same in both the positive and negative displacement directions. (O'Neill, 2011)

Tube tearing initiated on the north side of the tube near the apex of the buckle in cycle 24 at a moment of 22,440 k-in and a drift ratio of 7.06%. In the subsequent half-cycle of cycle 24, tube tearing occurred on the south side of the tube near the apex of the buckle at a moment of -17,164 k-in and a drift ratio of -6.03%. When tearing occurred on the south side of the tube, the column had been significantly damaged from previous cycles and tearing of the tube on the north side. This is why the magnitude of the moment and the drift ratio are less in the negative direction when tube tearing occurs. (O'Neill, 2011)

The moment-drift ratio response with markers indicating the measurement of tube yield strain, the observation of local buckling and tearing near the apex of the buckle can be seen in Figure 6.18. (O'Neill, 2011)

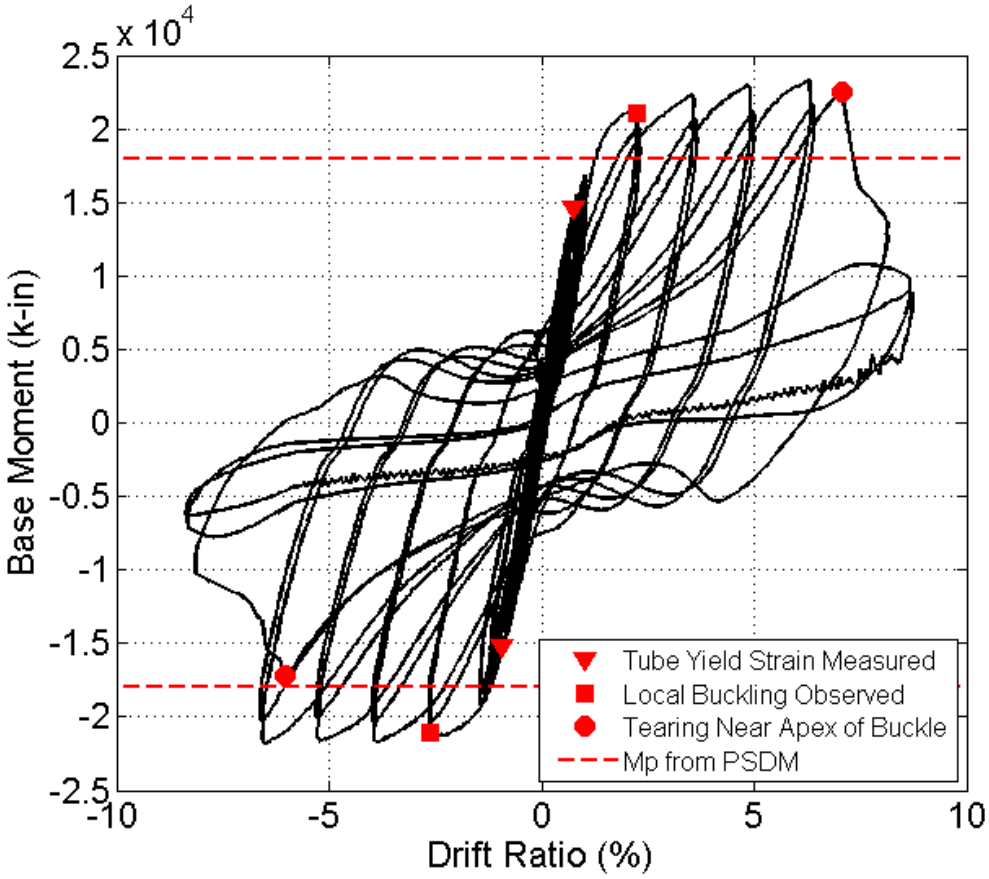

Figure 6.18. Moment-Drift ratio response of 30-inch diameter specimen (O'Neill, 2011)

6.3.5 Comparison between specimens

Each specimen discussed previously in this section experienced similar moment-drift ratio responses. In order to better compare the responses of the specimens, Figure 6.19 shows a normalized moment envelope of the four specimens. The moment capacity of the specimens was normalized by dividing the measured moment by the plastic moment capacity (Mp) of the specimen predicted from the plastic stress distribution method. The reported material properties were used to determine Mp for the 5-50 specimen. For the preloaded specimens and the 30 in. diameter specimen, the measured cylinder concrete strength was used for the CFT concrete strength and the yield stress of the steel tube was assumed equal to 50 ksi to determine Mp. Even though the axial load on the specimens did vary slightly throughout the tests, the target axial load was used to determine Mp because most of the variations throughout the test were +/- 5 kips. One exception to this was in one half-cycle of the 20 in. diameter SCC 5-50 experimental test. During one half-cycle, the applied axial load increased to 520 kips (target axial load was 360 kips). (Lee, 2011) So, for this one half-cycle, the normalized moment envelope was normalized by Mp calculated using the increased axial load of 520 kips. (O'Neill, 2011)

Additionally, the plot in Figure 6.19 shows an envelope of the specimen normalized moment capacity. This means that only the minimum and maximums of cycles with an increase in displacement from the previous cycle are plotted on the graph. (O'Neill, 2011)

All of the specimens display similar normalized moment capacities in Figure 6.19. However, there are some subtle differences between the 30 in. diameter specimen and the 20 in. diameter specimens. There are little or no differences between the three 20 in. diameter specimens up until steel tube tearing. Once steel tube tearing occurred the specimens exhibited slight differences in their reduction of moment capacity. (O'Neill, 2011)

In contrast, the 30 in. diameter specimen had an increase in moment capacity in the positive displacement direction at drift ratio values up to 6.30%. However, the moment capacity in the negative displacement direction nearly matches all of the 20 in. diameter specimens. Steel tube tearing occurred in the 30 in. diameter specimen at a slightly smaller drift ratio than the 20 in. diameter specimens, and following steel tube tearing, the reduction in moment capacity was

much quicker than the 20 in. diameter specimens. This is evidenced by the steeper slope of the normalized moment envelope line after steel tube tearing occurred. (O'Neill, 2011)

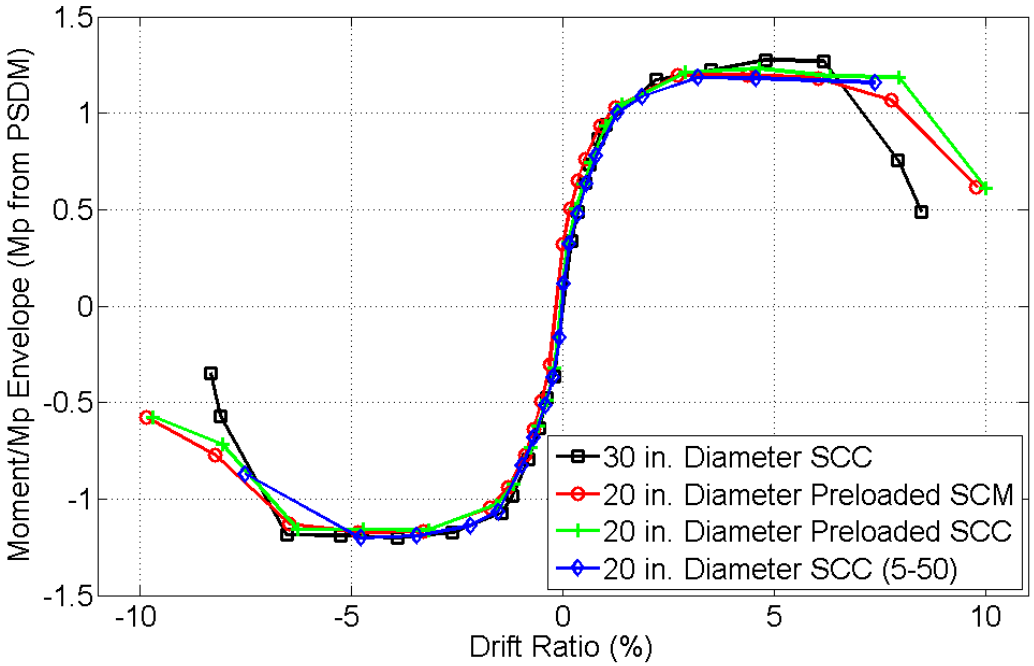

Figure 6.19. Moment-Drift ratio envelope comparison (O'Neill, 2011)

Chapter 7: Conclusions and recommendations

A research program was undertaken to compare creep, shrinkage and seismic performance of two 20-inch diameter steel tubes; one filled with self-consolidating SCM concrete with an 80% cement replacement and the other filled with conventional SCC concrete. In addition, standard ASTM cylinders were tested for creep and shrinkage comparison and to determine the compressive strength development of the mixtures. Literature review revealed that very little research has been done on the creep and shrinkage of CFTs and none on such large scale specimens. One of the objectives was to determine if high-replacement SCM concrete performed as well as conventional concrete. The replacement percentage and the ratio of fly ash to slag causes the early compressive strength to be less than that of conventional concrete, particularly at ages less than 28 days. An objective was to determine if this fact would be an issue in CFTs. Another objective was to determine if the concrete inside CFTs sheds much load to the steel due to creep. Four existing analytical models for creep and shrinkage (ACI committee 209, CEB-FIP-MC90, AASHTO 2007 and GL 2000 models) were also compared to the experimental results. Finally, the models were calibrated to estimate the error between the models and the results and to predict a likely final value of the creep coefficient and the shrinkage strain for each of the specimens.

7.1 Conclusions

7.1.1 Compressive strength

- The early-age compressive strength of the self-consolidating SCM concrete used in this research program was less than that of the conventional SCC concrete. This trend was expected since pozzolanic reaction associated with SCMs is slower than the hydraulic reaction associated with Portland Cement.

- The SCM concrete gains more strength and increases in strength for a longer time than does the conventional SCC concrete. After approximately 170 days of curing, the strength is virtually the same for the two mixtures. This agrees with results obtained by Hannesson (Hannesson, 2010) for a similar SCM mixture which included 20% cement, 40% fly ash and 40% slag. This research concluded that ternary mixes (cement, fly ash

and slag being the three components) with 50:50 fly ash to slag ratio, had the most reliable strength development of the different mix proportions tested.

7.1.2 Creep and shrinkage

7.1.2.1 Creep strains and creep coefficient

- The creep strain of the sealed cylinder specimens was less than that of the unsealed cylinder specimens, which was expected since less water evaporation occurs in concrete that is coated with sealant, resulting in less drying creep.

- Creep strain of the conventional SCC concrete was considerably less than that of the SCM concrete for the unsealed cylinder specimens. However, the sealed SCC cylinders had both less creep strain and a smaller creep coefficient than the SCC CFT specimen, even though it has a higher ratio of applied stress to measured compressive strength at the day of loading. This was is probably due to a large portion of fly ash and slag acting as fine aggregate by remaining unreacted in the concrete, providing higher resistance to creep.

- The SCM CFT specimen had both less creep strain and a smaller creep coefficient than the SCC CFT specimen, agreeing with the results obtained from the sealed cylinders. The difference between the two mixtures in this case, however, was greater. Some of the difference can be attributed to the unreacted fly ash and slag mentioned above, but it is also due to the fact that the SCM CFT specimen sheds more load to the steel over time than the SCC CFT specimen does, which results in less stress in the concrete.

- The difference in time dependent strain in the steel between the two specimens may be explained by difference in behavior between the two concretes. In the SCM CFT specimen, the excess water resulting from the unreacted fly ash and slag has no way to go since it cannot evaporate. On the contrary, all of the water in the SCC reacts with all of the cement over time. This may cause a larger volumetric change in the SCC than the SCM, which would result in less expansion of the SCC over time and therefore less engagement with the steel tube.

7.1.2.2 Shrinkage strain

- Drying shrinkage of the sealed cylinders was considerably less than that of the unsealed cylinders for both concretes, which was expected since less water evaporation occurs in sealed concrete.

- Shrinkage strain of the conventional SCC concrete was slightly less than that of the SCM concrete for both sealed and unsealed specimens.

- The shrinkage strain of the sealed cylinder specimens could not be used to represent shrinkage of CFTs. This was apparent from the fact that the total time-dependent strain in the CFTs was less than the shrinkage strain of the sealed cylinders for both concretes. From this observation and results from previous research, drying shrinkage was assumed to be negligible in CFTs.

7.1.3 Creep and shrinkage models

7.1.3.1 Creep models

- The CEB-FIP-MC90 creep model captured the creep behavior of the SCM specimens better than any other model in all cases. After 126 days of loading, the model predicted values that were 11-25% higher than the experimental value. Calibration of the model resulted in a very good fit with the experimental curves in most cases.

- The ACI committee 209 creep model a better indicator of the creep behavior of the SCC specimens than any other model in all cases. After 126 days of loading, the model predicted values that were 11% lower to 9% higher than the experimental value. Calibration of the model generally provided a very good fit with the experimental curves.

- The AASHTO 2007 model underestimated creep in most cases, especially for the first weeks of loading. It could generally not be calibrated to fit the experimental curves well.

- The GL 2000 model overestimated creep in all cases, which was mostly due to its general assumption of rapid rate of creep in the early stages. It could not be calibrated to fit the experimental curves well in most cases.

7.1.3.2 Shrinkage models

- The ACI committee 209 shrinkage model captured the shrinkage behavior of the unsealed cylinders better than any other model for both concretes. For the SCM concrete, the experimental value of the shrinkage strain after 126 days of loading was exactly what the model predicted and the curves had almost identical shapes. For the SCC concrete, the model predicted a values that was 14% higher than the experimental value. Calibration of the model was not needed for the SCM concrete but resulted in a rather good fit with the data from the unsealed SCC specimens.

- None of the models captured the shrinkage behavior of the sealed specimens well, since the experimental curves were irregular in shape (SCM) or almost linear (SCC). Calibrations of the models improved the fit, but did not capture the behavior as well

7.1.4 Seismic performance

7.1.4.1 Experimental results

- Yield strains, local buckling and tube tearing occurred at very similar drifts for the SCM CFT specimen as for the 20 in. comparison specimens with conventional SCC concrete. No effect of sustained loading was observed for the two preloaded specimens.

7.1.4.2 Force-Drift response

- The SCM CFT specimen displayed a very similar Force-Drift response as the 20 in. comparison specimens with conventional SCC concrete. Sustained loading seemed to have no effect on this response.

7.1.4.3 Moment-Drift response

- The normalized Moment-Drift ratio envelope of the three 20 in. CFT specimens was almost identical. The type of concrete inside the steel tube seemed to have no impact on this response. Sustained loading prior to the lateral test also proved to have no notable effect.

7.2 Recommendations for further research

Creep of CFTs should be investigated under different loading conditions. The CFT columns in this research were loaded through the concrete only, as has been done in a few previous research programs, but in most of them, the load has been applied to the steel and concrete uniformly. This would be difficult to do for large scale specimens but is certainly achievable for smaller scale CFTs.

Lateral strain should be measured during creep testing to quantify the volumetric change in the concrete at initial loading and over time. This may be important in determining how well the concrete engages with the tube under axial loading. Less volumetric change would result in more expansion of the concrete, leading to more confinement provided by the steel tube, and therefore more friction, larger steel strain and less creep.

Autogenous shrinkage of different SCMs may be of significance and is worth examining further. Embedded vibrating wire strain gauges are ideal instruments for such measurements since they can measure deformations even before the concrete has cured. Autogeneous shrinkage is mostly completed a few days after casting, so surface gauges would not capture the initial shrinkage. Drying shrinkage was considered negligible for CFTs in this research, but this assumption should be confirmed with experimental testing. Results could be obtained from the same gauges that measure autogeneous shrinkage, but care must be taken when distinguishing between autogeneous and drying shrinkage.

The use of SCM concrete in prestressed concrete structures would be worthwhile investigating, especially in composite structures such as CFTs. If the SCM concrete creeps less due to less volumetric change, as mentioned above and in Section 7.1.2.1, it could for example mean that prestressed composite structures filled with SCM concrete may suffer less prestressing losses due to creep than those filled with conventional concrete.

Further research should also be done on the creep and shrinkage behavior of concrete containing high volume of SCMs. Concrete mixes should be at different replacement levels and at different stress levels. Development of analytical expressions that predict creep and shrinkage of SCM concretes without performing tests are also needed.

Reference

AASHTO. (2007). *AASHTO LRFD Bridge Design Specifications, fourth edition.* American Association of State Highway and Transportation Officials.

ACI Committee 209. (2008). *209R-92: Prediction of Creep, Shrinkage, and Temperature Effects in Concrete Structures (Reapproved 2008).* Farmington Hills: American Concrete Institute.

Applied Technology Council (ATC). (1992). ATC-24 Guidelines for Testing Steel Components. Redwood City, CA, USA.

ASTM 1018 SS. (2007). *Standard Specification for Steel, Sheet and Strip, Heavy-Thickness Coils, Hot-Rolled, Carbon, Commercial, Drawing, Structural, High-Strength Low-Alloy, High-Strength Low-Alloy with Improved Formability, and Ultra-High Strength.* American Society for Testing and Materials.

ASTM A325. (2009). *Standard Specification for Structural Bolts, Steel, Heat Treated, 120/105 ksi Minimum Tensile Strength.* American Society for Testing and Materials.

ASTM A370. (2011). *tandard Test Methods and Definitions for Mechanical Testing of Steel Products.* American Society for Testing and Materials.

ASTM C 39. (2009). *Standard Test Method for Compressive Strength of Cylindrical Concrete Specimens.* PA, USA: American Society for Testing and Materials.

ASTM C 512. (2010). *Standard Test Method for Creep of Concrete in Compression.* American Society for Testing and Materials.

ASTM C1107. (2008). *Standard Specification for Packaged Dry, Hydraulic-Cement Grout (Nonshrink).* American Society for Testing and Materials.

Cambell, T. I., & Kong, W. L. (1988). *Laboratory Study of Friction on TFE Sliding Surfaces for Bridge Bearings.* Ministry of Transportation, Downsview, Ontario, Canada.

CEB. (1990). *CEB-FIP Model Code 1990.* London: Comite Euro-International du Beton.

CEMBUREAU. (2009). *Activity Report 2008.* Brussels: CEMBUREAU.

Chronister, A. (2007). *Experimental Investigation of High Strength Concrete Filled Steel Tubes in Embedded Column Base Foundation Connections.* MSCE Thesis, University of Washington, Civil and Environmental Engineering, Seatte.

Gardner, N. J., & Lockman, M. J. (2001). Design Provisions for Drying Shrinkage and Creep of Normal-Strength Concrete. *ACI Materials Journal , 98*, 159-167.

Geokon, I. (2010). Instruction Manual - Model 4000 (and 4050) Vibrating Wire Strain Gage. Lebanon, NH, USA.

Geokon, I. (2010). Instruction Manual - Model 4200 Vibrating Wire Strain Gage. Lebanon, NH, USA.

Gilbert, R. (1988). *Time effects in concrete structures.* Amsterdam: Elsevier.

Han, L., & Yang, Y. (2003). Analysis of thin-walled steel RHS columns filled with concrete under long-term sustained loads. *Thin-Walled Structures 41* , 849-870.

Han, L., Zhong, T., & Liu, W. (2004). Effects of Sustained Load on Concrete-Filled Hollow Structural Steel Columns. *Journal of Structural Engineering, V. 130, No.9* , 1392-1404.

Hannesson, G. (2010). *Mechanical Properties of High-Volume SCM Concretes.* MSCE Thesis, University of Washington , Civil and Environmental Engineering, Seattle.

Ichinose, L., Watanabe, E., & Nakai, H. (2001). An experimental study on creep of concrete filled steel pipes. *Journal of Constructional Steel Research, V. 57, No. 4* , 453-466.

Kingsley, A. (2005). *Experimental and Analytical Investigation of Embedded Column Base Connections for High Strength Concrete Filled Steel Tubes.* MSCE Thesis, University of Washington, Civil and Environmental Engineering, Seattle.

Lee, J. R. (2011). *Experimental Investigation of Embedded Connections for Concrete-Filled Steel Tube Columns.* MSCE Thesis, University of Washington, Civil and Environmental Engineering, Seattle.

Lehman, D. E., Roeder, C. W., Larson, R., & Curtin, K. (2003). *Cotton Duck Bearing Pads: Engineering Evaluation and Design Recommendations.* University of Washington, Civil and Environmental Engineering. Seattle: Washington State Transportation Center.

Mindess, S., Young, J. F., & Darwin, D. (2003). *Concrete - Second Edition.* Upper Saddle River: Pearson Education, Inc.

Morino, S., Kswaguchi, J., & Cao, Z. (1997). Creep behavior of concrete-filled steel tubular members. *Composite construction in steel and concrete III, Proceedings of an Engineering Foundation Conference,* (pp. 514-525). Irsee, Germany.

O'Neill, K. A. (2011). *Experimental Investigation of Circular Concrete Filled Steel Tube Geometry on Seismic Performance.* MSCE Thesis, University of Washington, Civil and Environmental Engineering, Seattle.

Terrey, P., Bradford, M., & Gilbert, R. (1994). Creep and shrinkage in concrete-filled steel tubes. *Tubular Structures IV* (pp. 293-298). Rotterdam, Netherlands: Grundy, Holgate & Wong (eds).

Uy, B. (2001). Static Long-Term Effects in Short Concrete-Filled Steel Box Columns under Sustained Loading. *ACI Structural Journal, V. 98, No.1* , 96-104.

Wang, Y., Geng, Y., Ranzi, G., & Zhang, S. (2011). Time-dependent bahoviour of expansive concrete-filled steel tubular columns. *Journal of Constructional Steel Research 67* , 471-483.

Williams, T. (2006). *Experimental Investigation of High Strength Concrete Filled Steel Tubes in Embedded Column Base Foundation Connections.* MSCE Thesis, University of Wasington, Civil and Environmental Engineering, Seattle.

Yang, Y., Han, L., & Wu, X. (2008). Concrete Shrinkage and Creep in Recycled Aggregate Concrete-Filled Steel Tubes. *Advances in Structural Engineering, V. 11, No. 4* , 383-394.

Zhou, X., Cao, G., He, R., & Liu, X. (2009). Study on Long-Term Behavior and Ultimate Strength of CFST Columns. *ICCTP 2009: Critical Issues in Transportation Systems Planning, Development, and Management* , 2239-2248.